UNIVERSITY OF LIVERPOOL

Polymers and Covalent Organic Frameworks as Positive Electrodes for Lithium-ion Cells

Hui Gao

Department of Chemistry and Materials Innovation Factory,
University of Liverpool

Thesis submitted in accordance with the requirements of

The University of Liverpool for the degree of Doctor in Philosophy

July 2021

Supervisors: Professor Andrew I. Cooper
Professor Laurence J. Hardwick

ABSTRACT OF THESIS

Polymers and Covalent Organic Frameworks as Positive Electrodes for Lithium-ion Cells

Hui Gao

Rechargeable lithium-ion (Li-ion) cells are widely used within portable electronics and increasingly for electric vehicles. With the increasing performance demand of Li-ion cells for today's applications, the use of organic materials as electrodes in rechargeable Li-ion cells has become increasingly attractive for the following reasons: (1) Organic electrode materials have lower environmental footprints and greater safety as compared to inorganic metal oxide electrodes; (2) organic electrode materials allow eco-efficient production and disposal; (3) organic electrode materials afford high energy storage capabilities as their structures can be engineered at the molecular level to support multiple redox reactions. However, organic small molecules suffer from dissolution in organic electrolytes leading to poor cyclic stability.

To suppress the solubility of organic electrode materials, a polyimide material (PI) was synthesised by the polycondensation reaction and investigated the electrochemical performance. One of the problems of polymeric electrode materials is that they often exhibit low utilisation of the redox-active sites. In Chapter 3, to improve the electrochemical performance of PI, a series of PIX ("X" value refers to either 10, 30 and 50 = wt.% of reduced graphene oxide (rGO)) composites were synthesised through *in situ* polycondensation on rGO. By optimising the content of rGO in the composite, it was found that the composite with 50 wt.% rGO exhibited the largest specific capacity. All the PI and PIX composites showed good cyclic stability and rate performance. The redox mechanism was studied by *ex situ* FT-IR.

In Chapter 4 and 5, the utilisation of redox-active sites in two covalent organic framework materials (COFs), DAPQ-COF and PT-COF, were improved using a similar strategy. The COF composites (DAPQ-COFX and PT-COFX, where X = 10, 30, and 50 wt.% of carbon nanotubes, CNT) were synthesised by *in situ* polycondensation on CNTs. These COF composites feature an abundance of redox-active units, *β*-ketoenamine linkages, and well-defined pores. The optimised composites possess tube-type core-shell structures with intimately grown COF layers on the CNT surface. This synergistic structural design enables superior electrochemical performance. DAPQ-COF50 showed 95% utilisation of redox-active sites, long cycling stability (76% retention after 3000 cycles at 2000 mA g^{-1}), and ultra-high rate capability, with 58% capacity retention at 50 A g^{-1}. This rate translates to charging times of *ca.* 11 seconds (320 C), implying that DAPQ-COF50 holds great promise for high-power cells. The rate capability

outperformed all previous reports for carbonyl-contained organic electrodes by an order of magnitude; indeed, this power density and the rapid charge/discharge time are competitive with electrochemical capacitors. In addition, as the COFs contained an abundance of electron-withdraw groups, the COFs based electrode has relatively high discharge voltage as compared to other carbonyl-functionalised polymer electrode materials. What is more, by designing the electrochemically redox-active building block to increase the number of active redox sites, the capacity of the PT-COF50 composite achieved 280 mAh g^{-1} at 200 mA g^{-1}, with an average discharge capacity of 2.55 V.

Acknowledgments

How time flies! I cannot believe it is four years already. I am so lucky that I met numerous nice people, who support me from different aspects in the Ph.D. journey.

Firstly, I would like to express my sincere gratitude to Professor Andy Cooper for the opportunity to study in his fantastic lab and his strong support throughout my Ph.D. His foresight and perseverance in doing pioneer work inspired me imperceptibly. I would like to thank Professor Laurence Hardwick for his huge support and guidance throughout my Ph.D. project from the many meetings to discuss the results and outlook for the project.

I would like to thank Dr. Michael Briggs for the valuable discussions and his encouragement since I started the project. “Keep reading, keep thinking, keep talking to people and keep trying” is what I learned from Briggs. This is proved to be very useful to me and I will keep the “four keeping” in my future career. Big thanks go to Dr. Bingbing Tian (Shenzhen University) for the very useful training courses he provided on lithium-organic batteries, which established the foundation of this thesis. Thanks must go to Dr. Marc Little, Dr. Reiner Sebastian Sprick and Dr. Alex Neale for the helpful data discussions, patient guidance and valuable suggestions on the thesis and paper manuscripts.

I would also like to thank the past and present members of the Cooper group and Hardwick group for their help, advice, events and lively atmosphere throughout the four years. There are truly too many to list but Guohong, Ming, Xiaofeng, Yang, Xiaoyan, Xiaobo, Kewei, Yue, Linjiang, Hongjun, John, Ai, Haofan, Peng, Qiang, Lunjie, Hongmei, Zhiwei, Zhongfu, Tom, Craig, Duncan, Cath, Christian, Ammar, Andy, Alex, Rich, Megan, Xue, Yongjie, Aiting, Donglin, Weiwei, Wei, Tom, Jinchao, Jose, Iain, Julia, Leo, Yundong, Marianna, David, Jungwoo and Winston all deserve a mention. Special thanks to Rob for fixing all the instruments and Bonnie for taking care of me since the Ph.D. application. I extend my thanks to my friends, Ni, Dingyue, Yan, Charlie and Bowen. Thanks all for helping me a lot on science and enriching my life in Liverpool.

Lastly, huge thanks must go to my elder brother, my parents and my grandparents for their unconditional love, support and encouragement throughout my life. I also must thank my boyfriend, Mr. Lei Ding, who is doing his Ph.D. in Australia. It is not easy for us, especially in this difficult time. Thanks Lei for his huge support and love during the years.

A big thanks to all again. I couldn’t have made it through this challenging experience without your help and support. With hope in my heart, I'll never walk alone!

List of Publications

I. **Hui Gao**, Bingbing Tian, Haofan Yang, Alex R. Neale, Marc A. Little, Reiner Sebastian Sprick, Laurence J. Hardwick, and Andrew I. Cooper. Crosslinked Polyimide and Reduced Graphene Oxide Composites as Long Cycle Life Positive Electrode for Lithium-Ion Cells. *ChemSusChem,* **2020**, 13(20), 5571.

II. **Hui Gao**, Qiang Zhu, Alex R. Neale, Mounib Bahri, Xue Wang, Haofan Yang, Lunjie Liu, Rob Clowes, Nigel D. Browning, Reiner Sebastian Sprick, Marc A. Little, Laurence J. Hardwick, and Andrew I. Cooper. Integrated Covalent Organic Framework/Carbon Nanotube Composite as Li-ion Positive Electrode with Ultra-high Rate Performance. *Advanced Energy Materials,* **2021**, 11, 2101880

III. **Hui Gao**, Qiang Zhu, Alex R. Neale, Mounib Bahri, Haofan Yang, Xue Wang, Yongjie Xu, Rob Clowes, Nigel D. Browning, Laurence J. Hardwick, and Andrew I. Cooper. A Pyrene-4,5,9,10-tetraone-based Covalent Organic Framework as Positive Electrode for Li-ion Batteries with High Specific Capacity. *In preparation.*

IV. **Hui Gao**, Alex R. Neale, Yang Bai, Bowen Zhang, Marc A. Little, Reiner Sebastian Sprick, Laurence J. Hardwick, and Andrew I. Cooper. Recent Progress of Carbonyl-containing Conjugated Polymers as Electrode Materials for Rechargeable Lithium-ion Batteries. *In preparation.*

List of Abbreviations

2D	Two dimensional
3D	Three dimensional
AC	Alternating current
ADALS	Azobenzene-4,4'-dicarboxylic acid lithium salt
BJH	Barrett, Joyner, and Halenda
CNT	Multi-walled carbon nanotubes
COFs	Covalent organic frameworks
CPE	Constant phase element
CP-MAS	Cross-polarization magic angle spinning
DAPQ	2,7-Diamino-9,10-phenanthrenequinone
DAPT	2,7-Diaminopyrene-4,5,9,10-tetraone
DFT	Density functional theory
DMAc	Dimethylacetamide
DMC	Dimethyl carbonate
DME	Dimethoxyethane
DMF	Dimethylformamide
DMSO	Dimethyl sulfoxide
DNPT	2,7-Dinitropyrene-4,5,9,10-tetraone
DOL	1,3-Dioxolane
EC	Ethylene carbonate
EIS	Electrochemical impedance spectroscopy
FT-IR	Fourier-transform infrared spectroscopy
GCD	Galvanostatic charge/discharge
HOMO	Highest occupied molecular orbital
HR-TEM	High-resolution transmission electron microscopy
Li-ion	Lithium-ion
$LiPF_6$	Lithium hexafluorophosphate
LiTFSI	Lithium bis(trifluoromethanesulfonyl)imide
LUMO	Lowest unoccupied molecular orbital
N_2	Nitrogen
NL-DFT	Nonlocal density functional theory

NMP	*N*-methyl-2-pyrrolidone
NMR	Nuclear magnetic resonance spectroscopy
OCP	Open circuit potential
o-DCB	1,2-Dichlorobenzene
PBQS	Poly(benzoquinonyl sulfide)
PDTTA	Poly(5,8-dihydro-1*H*,4*H*-2,3,6,7-tetrathia-anthracene)
PI	Polyimide
PMDA	Pyromellitic dianhydride
PPy	Polypyrene
PQ	9,10-Phenanthrenequinone
PT	Pyrene-4,5,9,10-tetraone
PTMA	Poly(2,2,6,6-tetramethylpiperidinyloxy-4-yl methacrylate)
PVDF	Polyvinylidene fluoride
PXRD	Powder X-ray diffraction
rGO	Reduced graphene oxide
SA_{BET}	BET surface area
SEM	Scanning electron microscope
TAPM	Tetra-(4-aminophenyl)methane
TBPD	7,8,10-Trimethylbenzo[g]pteridine-2,4(3H,10H)-dione
TCNQ	Tetracyanoquinodimethane
TEGDME	Tetraethylene glycol dimethyl ether
TEM	Transmission electron microscopy
TFG	1,3,5-Triformylphloroglucinol
TGA	Thermogravimetric Analysis
THF	Tetrahydrofuran

Contents

Chapter 1

Introduction and Background of Rechargeable Li-organic Batteries

Some of the contents in Chapter 1 are taken from Paper IV.

Recent Progress of Carbonyl-containing Conjugated Polymers as Electrode Materials for Rechargeable Lithium-ion Batteries, Hui Gao, Alex R. Neale, Yang Bai, Bowen Zhang, Marc A. Little, Reiner Sebastian Sprick, Laurence J. Hardwick* and Andrew I. Cooper*

1.1 Introduction

To meet the demand for efficient and clean energy sources, corresponding high-performance energy storage devices must be developed and, for this regard, new and improved battery technologies are under intense investigation.[1,2] During the past 30 years, the comprehensive battery performance of Li-ion batteries has been improved significantly compared to other kinds of batteries such as lead-acid, nickel-cadmium and nickel-metal hydride batteries. However, Li-ion cells are limited by conventional inorganic solid-state positive electrode materials (*e.g.* $LiCoO_2$ and $LiFePO_4$) with limited theoretical specific capacity and structural stability. Second, the environmental and resource issues caused by the large-scale production and use of transition metal (*e.g.* Co, Ni) based positive electrode materials are gaining more attention. These challenges inspire the development of high-capacity positive (*e.g.*, $xLi_2MnO_3 \cdot (1 - x)LiMO_2$)[3] and negative electrodes (*e.g.*, Si)[4], in addition to exploring other alternative battery technologies such as Li–organic cells.[5,6]

Li-organic cells have the potential for lower environmental pollution and greater safety compared to inorganic metal oxide electrodes and allow eco-efficient production and disposal.[1] As such Li-organic cells are a strong candidate energy storage technology for large-scale power systems, such as smart grids.[2,3]

The history of the Li-organic battery can be traced back to 1969 when a tricarbonyl compound (dichloroisocyanuric acid) was used as the cathode for a primary Li-ion cell.[7] Afterwards, the use of carbonyl compounds in rechargeable Li-ion batteries was successfully demonstrated.[8] However, the high solubility of carbonyl compounds in non-aqueous electrolytes often limits their performance, which results in a rapid decay in capacity during charge/discharge cycling.[9–11] Recently, growing attention has been given to organic electrodes due to the potential advantages of high theoretical capacity and structural diversity. Organic materials can also in principle be obtained from biomass-derived resources using low-temperature synthesis routes. For instance, dilithium rhodizonate ($Li_2C_6O_6$), an electrochemically redox-active material, can be produced from the natural sugar *myo*-inositol, which exists in plants such as corn in the hexaphosphate form, phytic acid. Since the first report of organic electrode materials for Li-ion batteries was published in 1969,[7] several kinds of organic materials have been explored for Li-ion batteries during the last few decades including conductive polymers,[12–18] organosulfur compounds,[19–22] organic radicals,[23–27] carbonyl compounds,[28–32] and other molecules based on C=N,[33] cyano,[34] and N=N.[35–37] The reaction mechanisms of organic compounds are

summarised in Table 1-1. Conductive polymers show low capacity because the doping level of conductive polymers is typically below 50%, which means that less than half of the redox-active groups undergo charging/discharging. The organosulfur compounds generally suffer from sluggish reaction kinetics and, additionally, the self-discharge that occurs with organic radicals generally impedes their practical application. Encouragingly, however, carbonyl and imine compounds can exhibit relatively high specific capacities, thus are the focus of current research in organic electrode materials. For example, cyclohexanehexone (C_6O_6) with a high capacity of 902 mAh g^{-1} at 20 mA g^{-1} in lithium-ion batteries was reported by Chen *et al.* [38]

Carbonyl organic materials have been widely investigated in Li-ion cells though some issues remain to be resolved, such as the dissolution of small molecules in organic electrolytes, poor electronic conductivity, and low working potentials (*ca.* 1.5 to 3.2 V). For example, cyclohexanehexone has a high capacity (902 mAh g^{-1}), but the average voltage of cyclohexanehexone redox reactions occurs at 1.7 V, and its cycling stability is still far away from practical use. For example, cyclohexanehexone showed a capacity decrease of 12% after 100 cycles at 50 mA g^{-1}. The dissolution of the small organic active materials in electrolytes can be suppressed by various strategies, including grafting the electroactive molecule to a conductive backbone, forming a salt with organic compounds, and forming polymers. To increase the conductivity of organic materials, the primary method is to incorporate conductive additives, which are relatively simple and easy to apply at large scales. Also, increasing the conjugation carbonyl compounds or reducing the bandgap of the material would contribute to improving the electronic conductivity of the materials.

Table 1-1. Electrochemical storage mechanisms in redox-active organics together with examples.

Reversible redox-active moiety	Classification	General mechanism	Examples of electrode reaction	Ref
Conjugated carbonyls	n-type	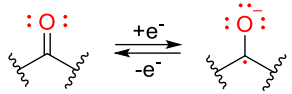	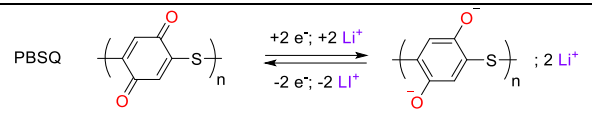	32
Organodisulfides	n-type	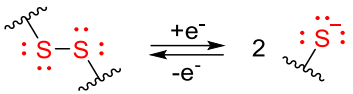	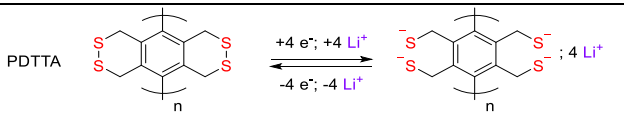	21
Conjugated azo groups	n-type	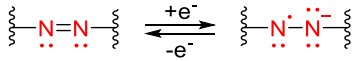	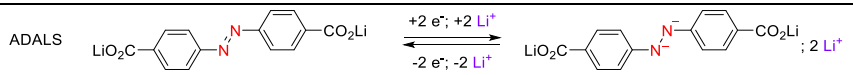	36
Conjugated nitriles	n-type	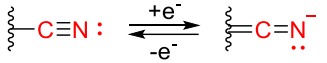	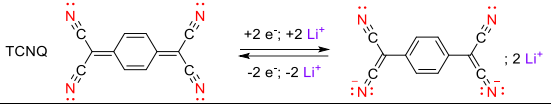	34
Conjugated imines	n-type	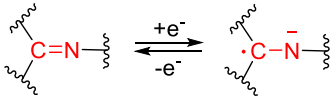	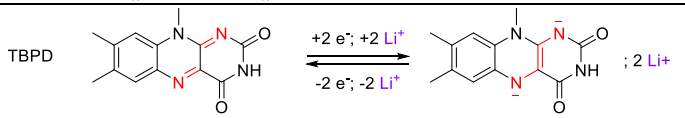	39
Conjugated amines	p-type	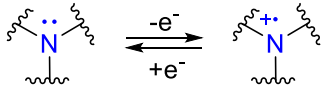	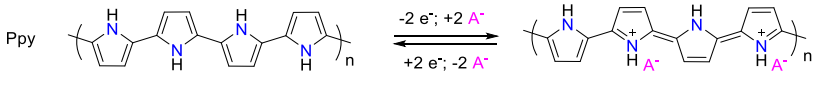	17
Conjugated ether oxides	p-type	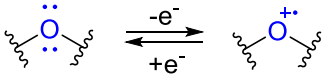	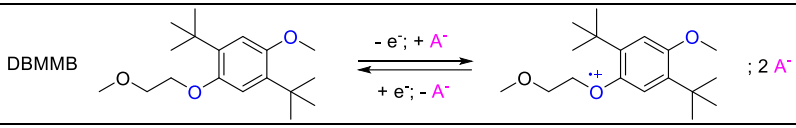	26
Conjugated thioethers	p-type	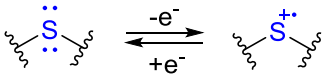	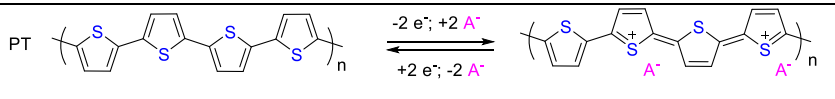	18
Nitroxide radical	n/p-type (bipolar)	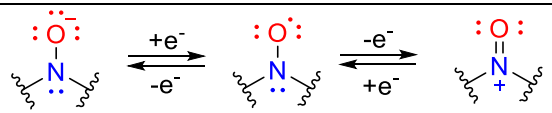	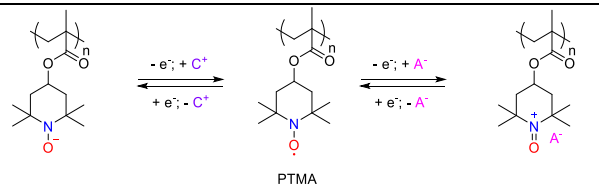	27

1.2 Working Principle of Organic Electrode Materials

Generally, organic electrode materials can be divided into three categories (n-type, p-type, and bipolar) depending on their different redox reactions (Figure 1-1). the concept of n-type and p-type categories has its origins from semiconductors. Also, these categories can be used in the classification of organic electrode materials. N-type organics are reduced during electrochemical reactions, which results in negatively charged anions. By contrast, p-type organics are oxidised in the redox reaction to positively charged cations. Bipolar organics can be reduced and oxidized; therefore, they are a combination of n- and p-type.

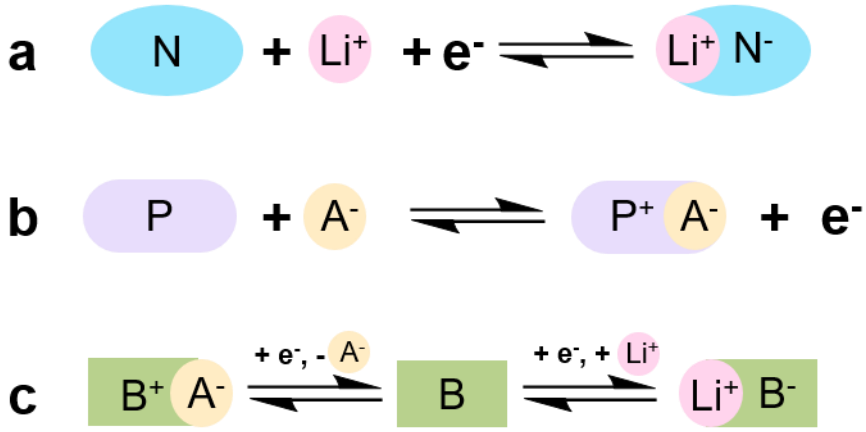

Figure 1-1. The redox reaction of three types of electroactive organics: (a) n-type; (b) p-type; (c) bipolar. A^- means anion of the electrolyte and Li^+ can be replaced by other alkali ions.

Almost all carbonyl compounds are n-type organics that can be reduced when discharging the corresponding electrode. The negatively charged carbon-oxygen groups require other surrounding functional moieties to stabilise them. According to the different stabilisation mechanisms of the reduced anion, the materials can be categorised into three different groups (Types I, II and III, Figure 1-2).[30,40] Compounds in group I use the neighbour carbonyls to form stable enolates during reduction (*e.g.*polymer-bound pyrene-4,5,9,10-tetraone).[41] This enolate can be further stabilised by neighbour aromatic systems. Carbonyl compounds in type II are aromatic carbonyl derivates. The carbonyl groups are directly connected to an aromatic core, which can stablise the negative charge by delocalization. The third group of compounds (type III) normally consists of quinone sub-structures, sharing some features with type I and II compounds, but the main stabilisation force is the formation of an additional aromatic system

after electron injection. Also, the anions formed in the redox reaction should be balanced by a suitable cation (*i.e.*, Li^+) derived from the electrolyte salt that will go back to the electrolyte upon oxidation.

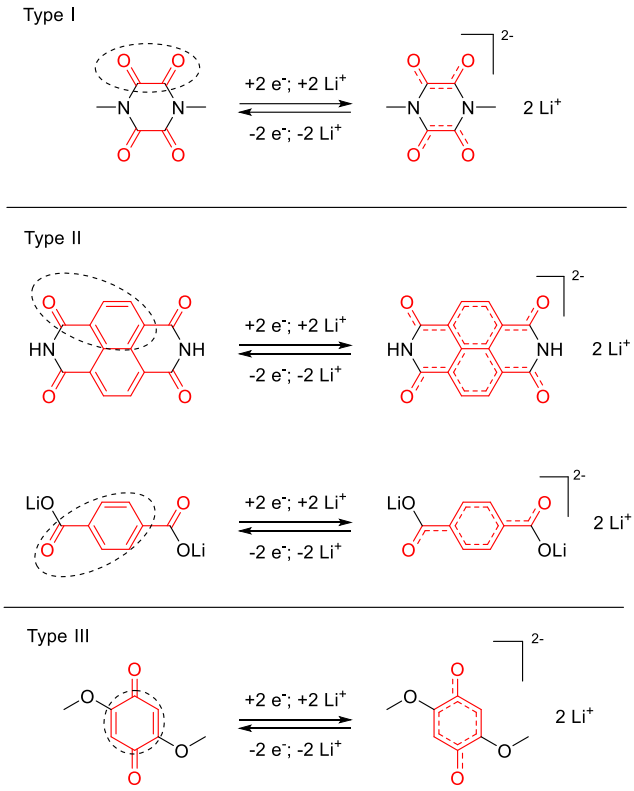

Figure 1-2. Illustration of the carbonyl-based electrode of three groups.

To date, most carbonyl-containing polymeric electrodes are used as positive electrodes, and lithium metal or lithiated silicon or tin alloys are typically used as the negative electrode materials. The representation of the discharge and charge process of a rechargeable lithium-ion battery with the n-type organic material as the cathode is shown in Figure 1-3. Due to the reverse nature of the redox reaction of n-type materials, the n-type organic positive electrode is in an oxidised state in a fresh cell. This means the battery is already charged after assembly. Therefore, the first step of charge/discharge cycling is discharging the cell (Figure 1-3a). When both electrodes are connected electrically, the n-type organic material (positive electrode) is reduced (accepting electrons) and the lithium cations are transported from the electrolyte to the positive electrode. Meanwhile, the Li metal is oxidised (releasing electrons) to form lithium cations, which are transported through the electrolyte. During the charging process, the positive electrode releases the accepted electrons and lithium cations, and Li is plated back onto the

lithium metal (Figure 1-3b). Some carbonyl-containing polymeric electrodes exhibit a low redox potential (< 1.5 V) and can, therefore, in principle be utilised as the negative electrode. In this case, different compounds with higher redox potentials (> 2.5V), such as metal alloys, organic compounds, or oxygen, can be used as the positive electrode. To provide comparable test systems for organic electrode materials, the majority of new materials are not tested in a full cell, but in a metal-organic battery (half cells). In this case, the metal serves as the negative electrode and metal ion source and both p- and n-type organic materials are tested as the positive electrode.[42]

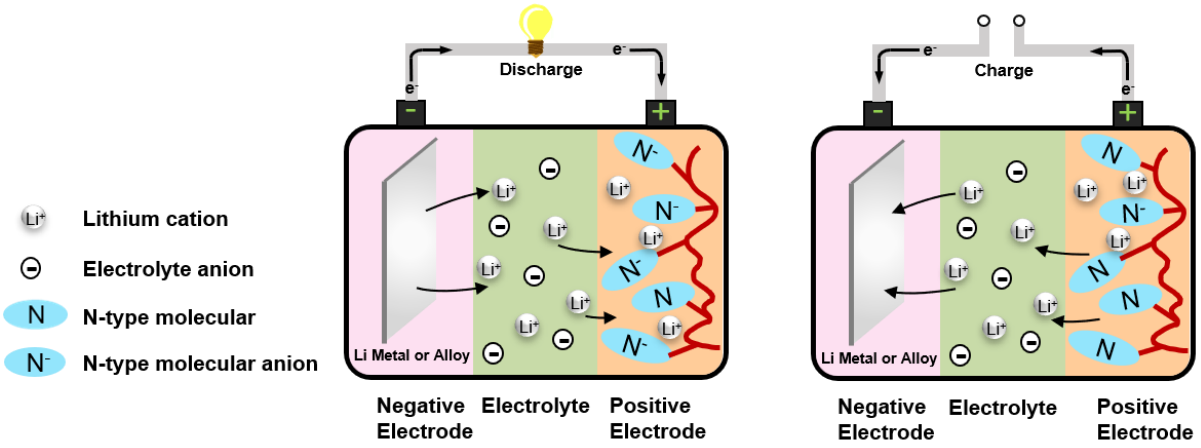

Figure 1-3. Schematic representation of the processes during (a) discharging and (b) charging of a Lithium-organic cell. The red curved line in the figure represents the polymer backbone. Redrawn from reference [43].

1.3 Characteristics of Electrochemical Cells

Some of the basic characteristics and main parameters (*i.e.* voltage, capacity, specific energy) relating to organic batteries are defined and introduced in Section 1.3.[42]

Negative electrode: the electrode of an electrochemical cell that is oxidised and releases electrons to the external circuit during discharge.

Positive electrode: the electrode of an electrochemical cell that is reduced and acquires electrons from the external circuit during discharge.

Electrolyte: the electrolyte is the medium that only allows the conduction of ions between the electrodes of a cell (*i.e.*, the electrolyte is ionically conductive but electronically insulating). The liquid electrolytes used herein consist of salts dissolved in solvents.

Theoretical voltage (V (V)): The theoretical cell voltage of a battery can be calculated from the potentials of the respective electrodes:

Positive electrode potential (V) – Negative electrode potential (V) = cell voltage (V)

(**Equation 1-1**)

Specific capacity (C_{spec} (Ah kg^{-1})): the capacity of electrodes is usually provided per mass of active material. The specific capacity of a single electrode can be calculated as follows:

$$C_{spec} = \frac{n \times F}{M_w} = \frac{n \times 26.8\ (\text{Ah mol}^{-1})}{M_w\ (\text{kg mol}^{-1})} \qquad \textbf{(Equation 1-2)}$$

Where n is the number of electrons transferred per redox reaction. F represents the Faraday constant, and M_w is the molar weight of the repeat unit of the organic component.

Theoretical Energy (E_{theo} (Wh)): An even more important parameter is the energy of the electrochemical cell. The theoretical energy is the maximum energy that can be delivered by a given system with a theoretical voltage V and a theoretical capacity C_{theo}. Meanwhile, specific energy (E_{spec} (Wh kg^{-1})) is the energy of the cell that can be utilized per mass of the active materials. In like manner, energy density (E_{dens} (Wh dm^{-3})) means the maximum energy that can be used per volume of the active materials.

$$E_{theo} = C_{theo} \times V\,(\text{V}) \qquad \textbf{(Equation 1-3)}$$

$$E_{spec} = \frac{\text{E (Wh)}}{\text{m (kg)}} \qquad \textbf{(Equation 1-4)}$$

$$E_{dens} = \frac{E\ (\text{Wh})}{\text{volume}(\text{dm}^{-3})} \qquad \textbf{(Equation 1-5)}$$

Coulombic efficiency (η_c (%)): the ratio of the obtained discharging and charging capacity.

$$\eta_c = \frac{C_{discharge}}{C_{charge}} \qquad \textbf{(Equation 1-6)}$$

C-rate: a character for the charging/discharging current of a cell.

$$C = \frac{i_{applied}}{i_{1h}} \qquad \textbf{(Equation 1-7)}$$

Where i_{1h} is the current that is used to fully charge/discharge the cell in 1 h based on the theoretical capacity.

The most commonly used housing for a lab-scale test cell is the coin cell (Figure 1-4a). In coin cells, low masses of active material can be tested. The positive electrode is separated from the negative electrode by a porous separator wetted with a liquid electrolyte. The cell housing is crimp sealed under an inert atmosphere with the presence of the spacer and spring to apply uniform compression to the electrode stack during cycling. A so-called Swagelok cell (Figure 1-4b) is also used in an alternate cell configuration, which is conceptually similar to that of coin cells. These consist of two stainless steel rods as the current collectors sealed in a straight union using compression fittings also loaded with a spring to apply compression to the electrode stack. The main benefits of the Swagelok configuration are its reusability and straightforward cell disassembly, enabling the *ex situ* investigations of the electrodes after charge/ discharge cycling by, for example, scanning electron microscope (SEM) to visualize structural changes.

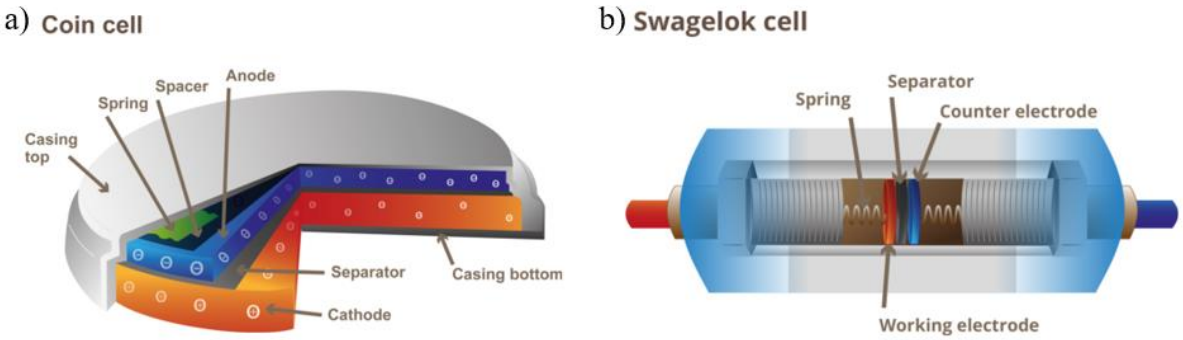

Figure 1-4. Schematic representation of (a) coin cell and (b) Swagelok cell. Reprinted with permission from reference 42. Copyright 2016, American Chemical Society.[42]

1.4 Requirements for Electrochemical Performance

The basic requirement for an organic rechargeable battery is that the electrodes can undergo reversible electrochemical redox reactions. For polymeric electrode candidates, some basic requirements for electrochemical performance are summarised as follows:

1.4.1 Reaction Reversibility

Reversibility means chemical reversibility and thermodynamic reversibility. It is an important factor determining the electrochemical polarisation and rate capability of the electrode materials. Carbonyl-containing polymer electrodes have the potential for very fast reaction kinetics and high rate performance. By contrast, organosulfides show slow reaction kinetics, since the working principle of organosulfides involves the bonds breaking/forming of the S-S and S=O, which needs high activation energy.

1.4.2 Cell Energy

As stated above, the energy that is stored in the cell is calculated from the capacity and the cell voltage (Equation 1-3). The cell potential of a battery can be calculated by the difference between the potentials of the positive and negative electrodes. Therefore, to obtain a battery with high potential, a cathode with high redox potential and an anode with low redox potential are required. In general, carbonyl functionalized polymer electrodes have a low redox potential (< 3.0 V *vs.* Li^+/Li), which is lower than that of inorganic cathode materials (around 3.2-4.0 V).[44–49] However, the redox potential of organic materials can be adjusted by introducing different functional groups. The introduction of electron-withdrawing groups (e.g., $–CF_3$, –CN, –F, –Cl, –Br) or electron-donating groups (e.g., $–NH_2$, $–CH_3$, $–OCH_3$) can expand or shrink the voltage difference between the anode and cathode materials (Figure 1-5). The electron-withdrawing groups (like C=O)decrease the lowest unoccupied molecular orbital (LUMO) level and in turn raise the reduction potential.[50] For the theoretical capacity, as in the formula shown above (in the section on characteristics of batteries Equation 1-2), two approaches can be used to improve the theoretical specific capacity: one is to reduce the molar weight of the structural unit, the other is to introduce more redox groups into the structural unit.

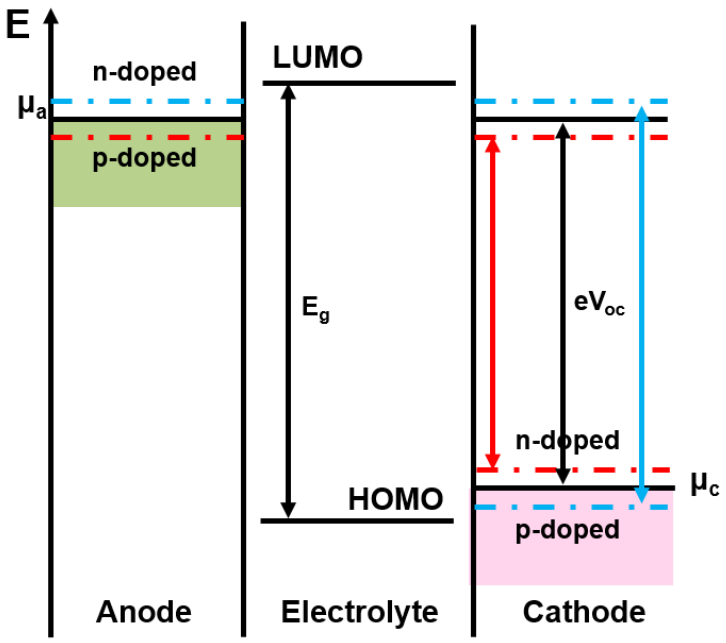

Figure 1-5. Schematic open-circuit energy diagram of a lithium-ion battery. μ_a and μ_c are the electrochemical potential (Fermi energy of electrons) of the anode and cathode, respectively. E_g is the electrochemical window of the electrolyte for thermodynamic stability. V_{OC} is the open-circuit voltage of the lithium-ion cell. Redrawn from reference [51].

1.4.3 Synthesis and Cost

Facile synthesis routes and cheap raw materials are required for organic Li-ion batteries if considering the scale-up practical application. As reported, many carbonyls functionalised organic electrode materials can be produced from biomass and bulk industrial chemicals. For instance, electrochemically redox-active polyquinones can be synthesised by polycondensation of malic acid, which is a natural product found in apples.[2]

1.5 Aspects Affecting the Electrochemical Performance for Positive Polymeric Electrodes

The redox potential of the carbonyl-containing polymeric electrode is tuneable by the introduction of electron-donating or electron-withdrawing functional groups surrounding the active carbonyl groups. However, the introduction of substituents that are not directly taking part in the redox reaction increases the component mass and thus decreases the theoretical capacity of the carbonyl-containing polymers. The capacity depends on the molecular mass

and the number of electrons involved in the redox reaction in the structure unit. The charge/discharge cycling stability is affected by several factors such as solubility of the active material, side reactions, and relative stabilities of the formed anions. For carbonyl-containing polymers, the solubility is not the most crucial factor resulting in capacity drop as most polymers show poor dissolution in the electrolyte. For example, Xu *et al.* reported the solubility of cis-exo-2,3-Bis(hydroxymethyl)bicyclo[2.2.1]hept-5-ene (monomer 1) and linear polymers of monomer 1 with molecular weight of 4200, 36200 and 91500 g mol^{-1}, and a cross-linked polymer (Figure 1-6a). The polymers are named P10, P100, P500 and CP100, respectively.[52] The solubility was examined by immersing three pieces of the corresponding electrodes in 2 ml of 1,3-dioxolane (DOL)/ dimethoxyethane (DME) (1/1, v/v) solvent. It showed that the solvents with Monomer 1 and P10 electrodes became yellow after one week of soaking, while the solvent with P100, P500, and CP100 remained clear (Figure 1-6b). The results indicated that the solubility of high molecular weight linear polymers and cross-linked polymers is much lower than the monomer and low molecular weight linear polymers. The conductivity of the polymeric electrode is one of the factors that hinder the electrochemical performance of polymeric active materials. So conductive additives are necessary because of the poor conductivity of the polymers. Conductive coatings and the incorporation of conductive additives like carbon nanotubes, graphene, or reduced graphene oxide, have been used to enhance charge transport in polymeric electrochemical active materials, and these methods have been shown to improve rate capability. For example, a 2D microporous poly(imide-benzoquinone) covalent-organic framework (COF) was synthesised by *in situ* polymerization on graphene (PIBN-G).[53] At the current density of 10 C, PIBN-G delivered reversible specific capacities of 193 mAh g^{-1}, while PIBN delivered a capacity of around 80 mAh g^{-1}. Compared with redox-active small molecules (*i.e.* non-polymeric form), the utilization of the electrochemical redox-active sites in the polymeric electrode is lower because of polymer chains resulting in poor access of redox-active groups by Li^+ or electrons. Making polymer carbon composite materials by this *in situ* method reduces the particle size, which enhances the utilization of the redox-active site and improves conductivity at the same time.[54] Also, there are other methods to promote the accessibility of redox-active sites including improving the surface area, as well as the synthesis of nanostructured polymer or polymer/carbon nanocomposites.[55]

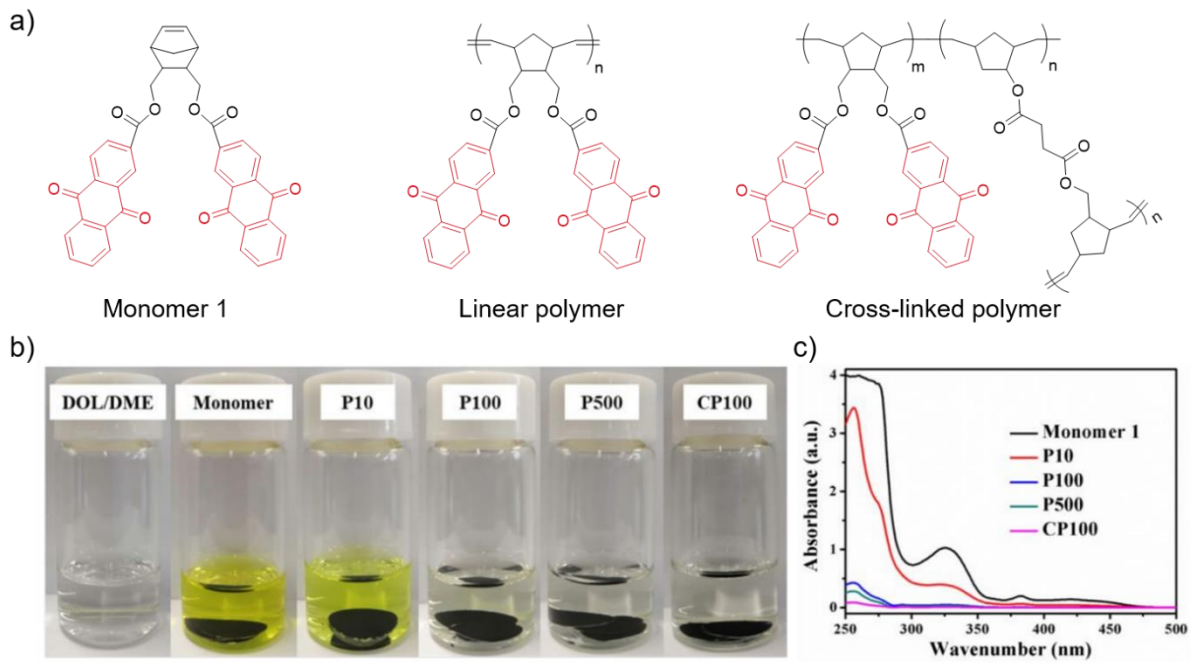

Figure 1-6. (a) Structure of monomer 1, linear polymer and cross-linked polymer; solubility test of Monomer 1, P10, P100, P500, and CP100 electrodes, (b) photographs and (c) UV/Vis spectra of the immersed solvents (DOL/DME, 1/1, v/v, total 2 mL) for a week. Reprinted with permission from reference 52. Copyright 2019, American Chemical Society.[52]

1.6 Advantages of Polymeric Electrode

As discussed at the beginning of the chapter, conjugated carbonyl groups have the advantages of high reversibility in electrochemical reactions and fast kinetics. Hence materials containing conjugated carbonyl groups are considered one of the most promising electrodes candidates.[56]

1.6.1 High Gravimetric Energy Density

Although the organic cathode electrodes have relatively low redox potential, which can be offset by their much higher theoretical capacity, thus it is still possible for them to obtain high energy density. Lithium-organic batteries have higher gravimetric energy densities compared to commercial batteries. For example, poly (pyrene-4,5,9,10-tetraone) electrode possesses a theoretical specific energy of 980 Wh kg^{-1}, calculated from its redox potential of 2.4 V vs

lithium metal and theoretical capacity of 412 mAh g^{-1}.[57] This is higher than that of and $LiFePO_4$ (540 W h kg^{-1}) $LiCoO_2$ (about 740 W h kg^{-1}).[58]

1.6.2 Structure Diversity

For organic carbonyl-containing polymers, there are huge possibilities in both the structures and properties. Carbonyl-containing polymers with different porous networks can be prepared by using different precursors to promote the transportation of electrolyte ions.[59] Besides, by the introduction of electron-donating/withdrawing groups, the redox potential of organic carbonyl-containing polymers can be adjusted.

1.6.3 Flexibility

To achieve fully stretchable electronics such as wearable electronics and roll-up displays, flexible power supplies are required.[60,61] Organic materials, especially polymers, are flexible and do not sustain structural failure during bending or deformation.

1.6.4 Insolubility

The solubility of small organic molecules in electrolytes leads to poor cycling stability when small organic molecules are used as the electrode. Compared with organic small molecules, organic polymers always have much lower solubility in the non-aqueous electrolyte, especially highly polymerised materials or cross-linked polymers.[32,62–64] Therefore, polymerisation should be a good strategy to improve cycling stability.

1.7 Introduction of Covalent Organic Frameworks

Covalent organic frameworks (COFs) were first reported by the Yaghi group in 2005 (Figure 1-7).[65] COF are a class of 2D or 3D structures formed by connecting organic precursors with strong, covalent bonds to afford porous crystalline materials. By choosing different building blocks, the geometry and pore size of the COFs can be easily adjusted, which enables fine-

tuning of physical and chemical properties. The well-defined porous channels facilitate the mass transfer, beneficial to the COFs' application in catalysis, separation, sensing, and electrode materials. Moreover, the diversity of building blocks and synthesis reactions allow us to design COFs with abundant electrochemical redox-active groups.

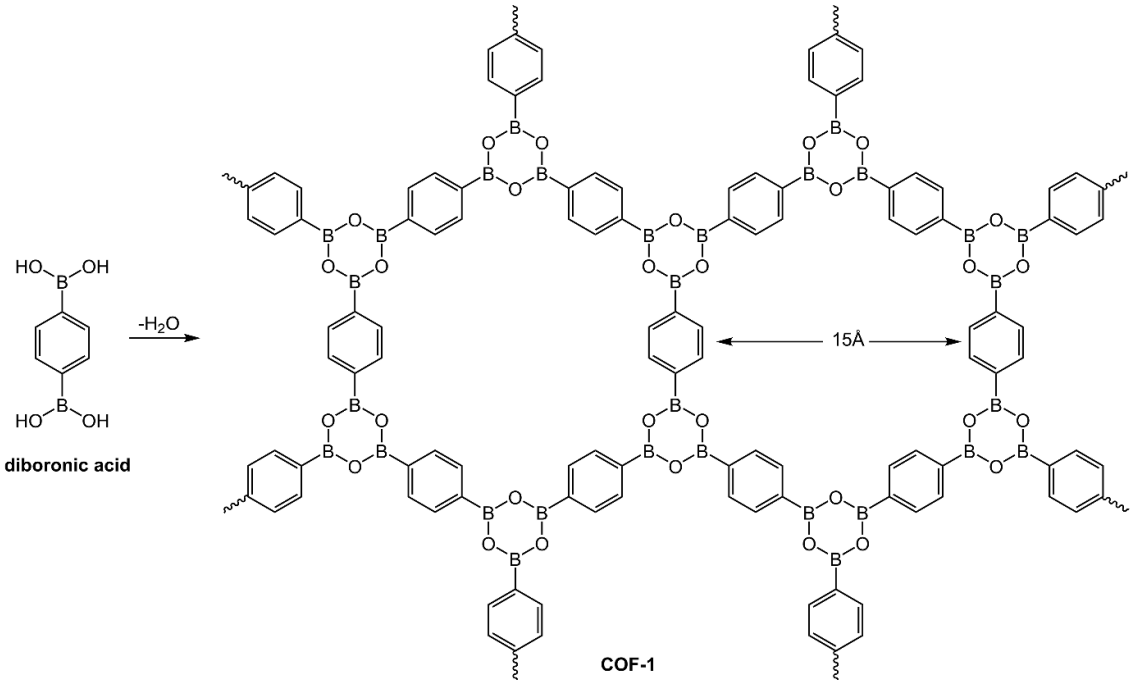

Figure 1-7. Synthesis of the first COF (COF-1) by self-condensation of 1,4-benzenediboronic acid**.** Redrawn from reference [65]**.**

Since the first COF was synthesised by the self-condensation of boronic acids (Figure 1-7), a variety of the synthesis routes have been developed to afford COFs (Figure 1-8), providing the possibility to synthesise the COFs that meet different requirements. To ensure a clear direction for each covalent bond, the monomers are required to have relatively rigid backbones in which the reactive sites are distributed in a distinct geometry. Figure 1-9 shows the simplified design concept of the geometry of the COFs with hexagonal pores. Generally, when synthesising COFs, a mixture of polar solvent and the nonpolar solvent is used as a reaction medium for the reversible covalent bond formation reaction. The combinations of solvents, catalyst, reaction temperature, and reaction time are major factors to be considered for the thermodynamic control of the reaction. These factors determine the crystallinity and porosity of the resulting COFs. With the efforts of researchers all over the world, COFs synthesis has been extended from the first boroxine and boronate-ester,[65–67], linked COFs to a variety of other linkages

including borosilicate,[68] triazine,[69] imine,[70–72] hydrazone,[73] borazine,[74] squaraine,[75] azine,[76] phenazine,[77] imide,[78] double-stage,[79,80] spiroborate,[81] C=C,[82–85] amide,[86] viologen,[87] hypercoordinate silicon,[88] urea,[89] and 1,4-dioxin linkages[90,91] (Figure 1-8). The size of the π systems and the type of the reactive units determine the solubility of the COFs. For example, the boroxine-based COFs easily decompose in water and Schiff-base linked COFs are not stable in basic conditions generally. On the other hand, the imide-based COFs structures are more robust.

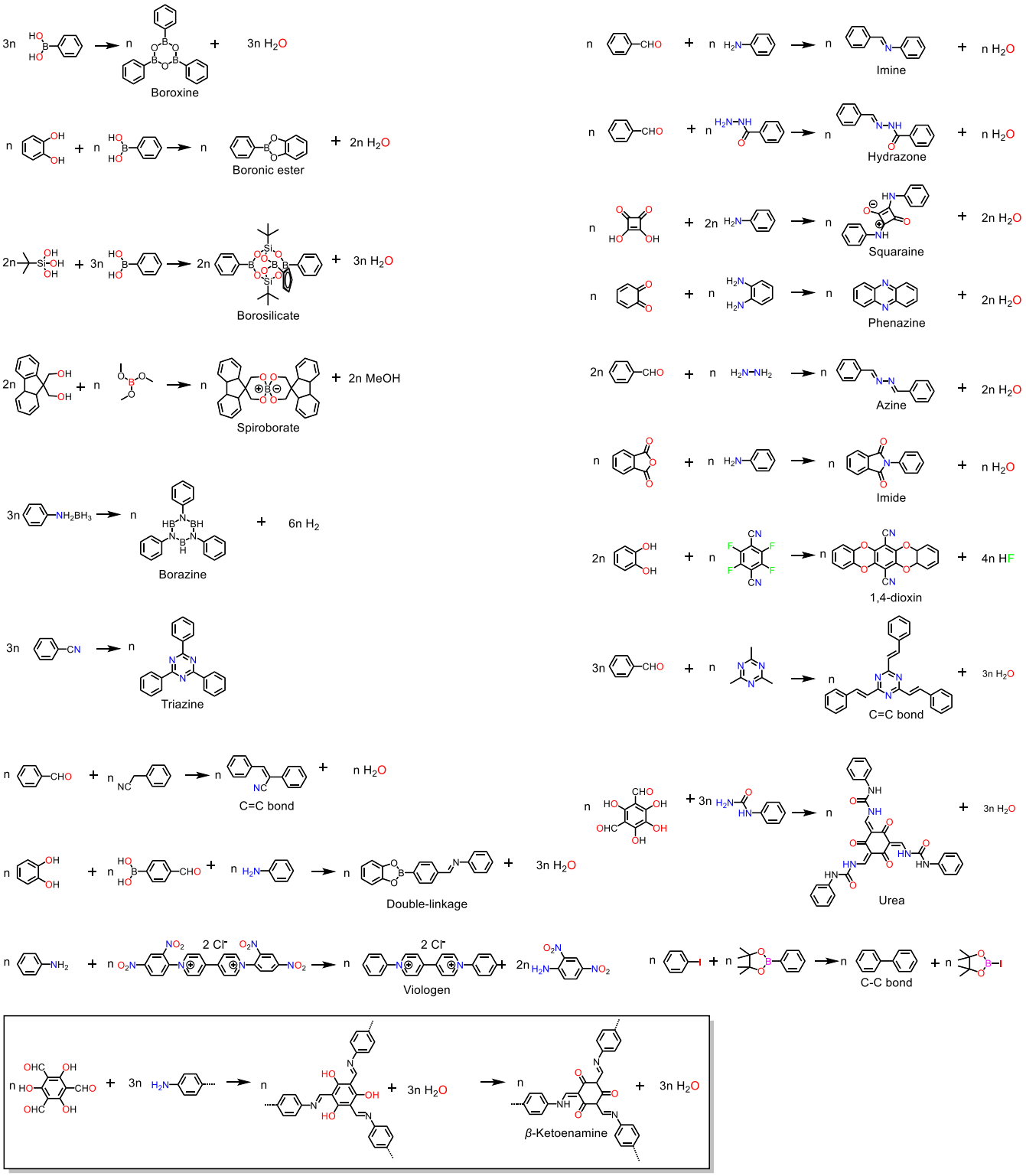

Figure 1-8. Synthesis routes for the COFs. Redrawn from reference [92].

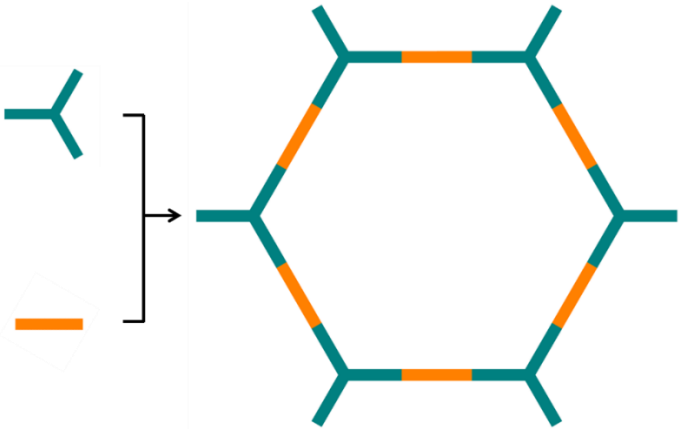

Figure 1-9. Basic topological diagrams for the COFs with hexagonal pores.

1.7.1 Boroxines and Boronic Esters

COF-1 was synthesised by self-condensation of 1,4-benzenediboronic acid.[65] The condensation of diboronic acid and hexahydroxy triphenylene to synthesize boronic esters crystalline frameworks was also reported (Figure 1-10).[65]

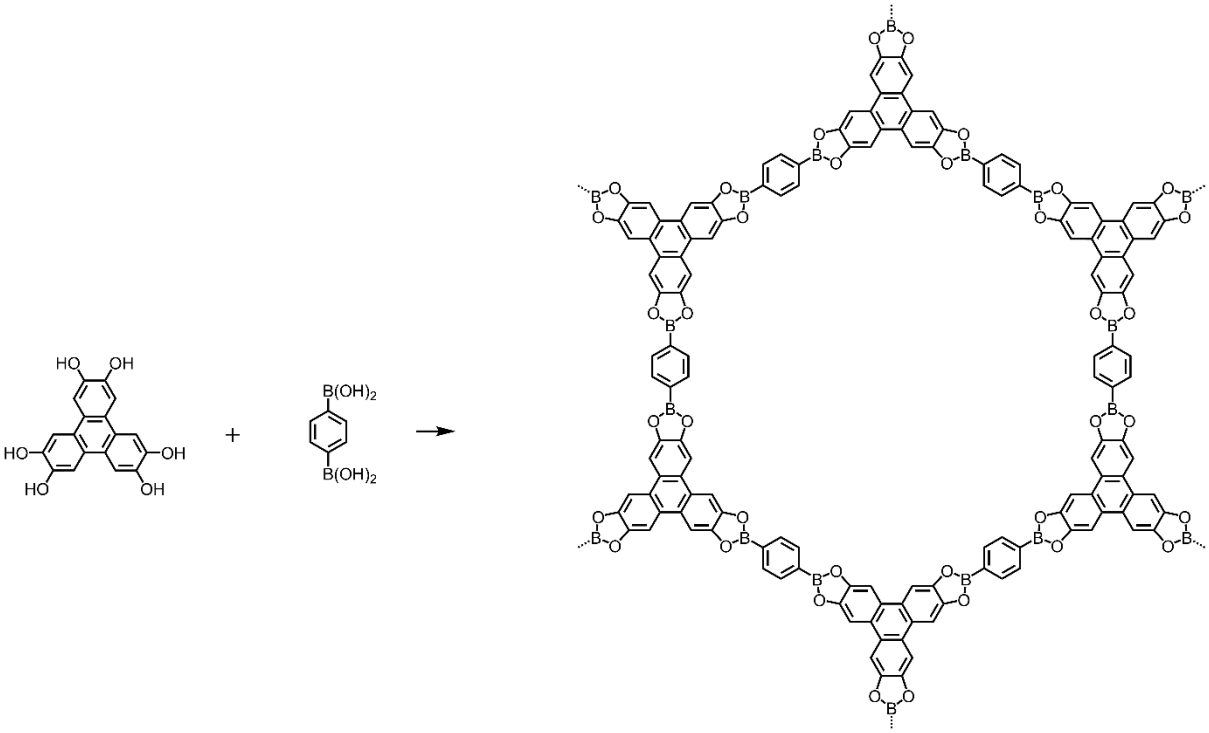

Figure 1-10. Synthesis of COF-5 by condensation of diboronic acid and hexahydroxy triphenylene. Redrawn from reference [65].

The usage of boroxine and boronic ester linkages was extended from 2D COFs to 3D COFs by Yaghi and co-workers. By self-condensation of tetrahedral boronic acid tetra(4-dihydroxyborylphenyl) methane and tetra(4-dihydroxyborylphenyl)silane or co-condensation with hexahydroxy triphenylene, they formed 3D COFs which have high surface area and crystallinity.[93] Instead of using a two-component condensation system consisting of one knot and one linker, Jiang *et al* reported a general strategy to form tetragonal and hexagonal multiple-component COFs based on the boroxines and boronic ester linkage by using one knot and two or three linkers.[94] Although boroxine and boronic esters chemistry shows good reversibility and form crystalline frameworks, the poor hydrolytic stability of these linkages hinders the applications of the materials. These linkages also break the extended conjugation in the materials.

1.7.2 Imine

Imine-linked COF is formed by Schiff base condensation of aldehydes and amines. Compared to boroxines and boronic esters linkages, the imine linkage is more much stable, which allows imine COFs can be applied in a wide range of applications. What is more, unlike boroxine and boronic ester linkages, imine linkages extend conjugation over whole 2D layers. This has made imine coupling the most common synthesis method to form COFs to date. The first imine-linked COF was reported by Yaghi *et al*. in 2009 (Figure 1-11).[70] The tetrahedral 3D COF was synthesised through co-condensation of tetra-(4-anilyl)methane and terephthalaldehyde.[70]

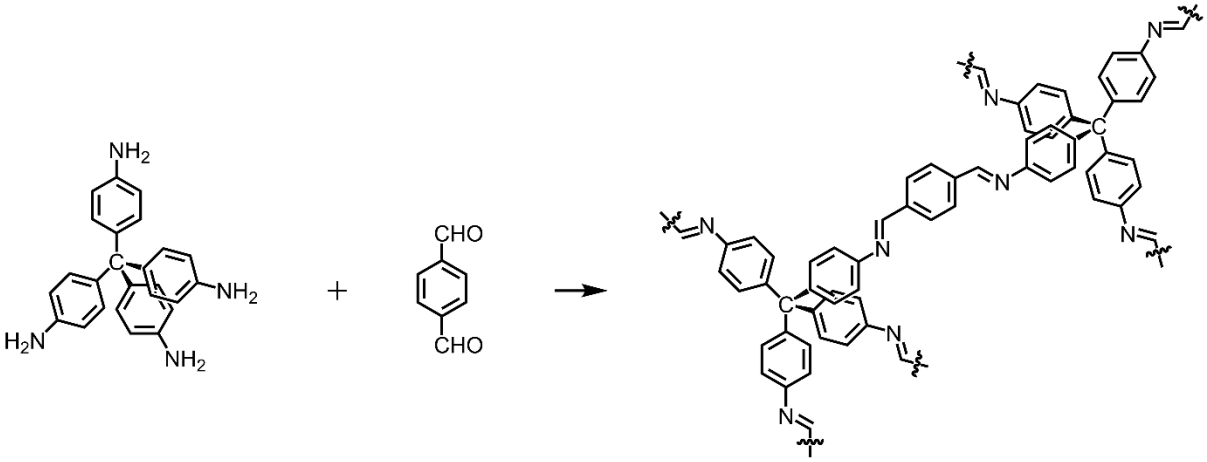

Figure 1-11. Synthesis of 3-D imine-linked COF. Redrawn from reference [70].

The first 2-D imine-linked COF (COF-LZU1) was reported by Wang *et al*. in 2011.[95] COF-LZU1 with hexagonal channels was made by condensation of 1,3,5-triformylbenzene and 1,4-phenylenediamine. COF-LZU1 is robust and stable showing great potential for heterogeneous catalysis.

1.7.3 Ketoenamine

The stability of COFs is a critical issue to widen the application of COFs. enhancing the stability of COFs has been a challenge since the first COF was reported. In 2012, a chemically stable COF with *β*-ketoenamine linkages was reported by Banerjee *et al*.[96] 1,3,5-Triformylphloroglucinol and *p*-phenylenediamine were used for COF synthesis. An enol-imine COF was formed initially, followed by an irreversible enol-keto tautomerization to form a *β*-ketoenamine-linked COF (Figure 1-12). The resulting ketoenamine-linked COF showed good acid stability (9 N HCl) and boiling water for 7 days. For battery applications, the stability of the electrode in the electrolyte affects the cycling life of the cell.

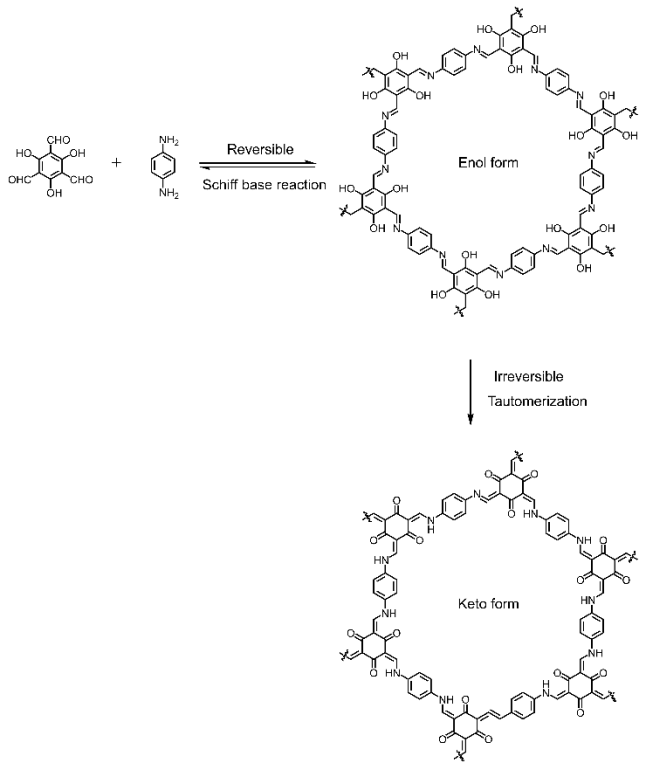

Figure 1-12. Synthesis of ketoenamines COFs (TpPa-1) by the combined reversible and irreversible reaction of 1,3,5-triformylphloroglucinol with p-phenylenediamine. Redrawn from reference [96].

1.7.4 Imide

A series of large pore crystalline polyimide COFs was reported by Yan *et al.* by using a reversible imidization reaction (Figure 1-13).[78] These polyimide COFs show remarkable thermal stability and Brunauer-Emmett-Teller surface areas (SA_{BET}) up to 2346 m^2 g^{-1}. As the polyimide is electrochemically redox-active, Huang *et al.* explored the application of PI-COFs as cathode materials in Li-ion cells.[97]

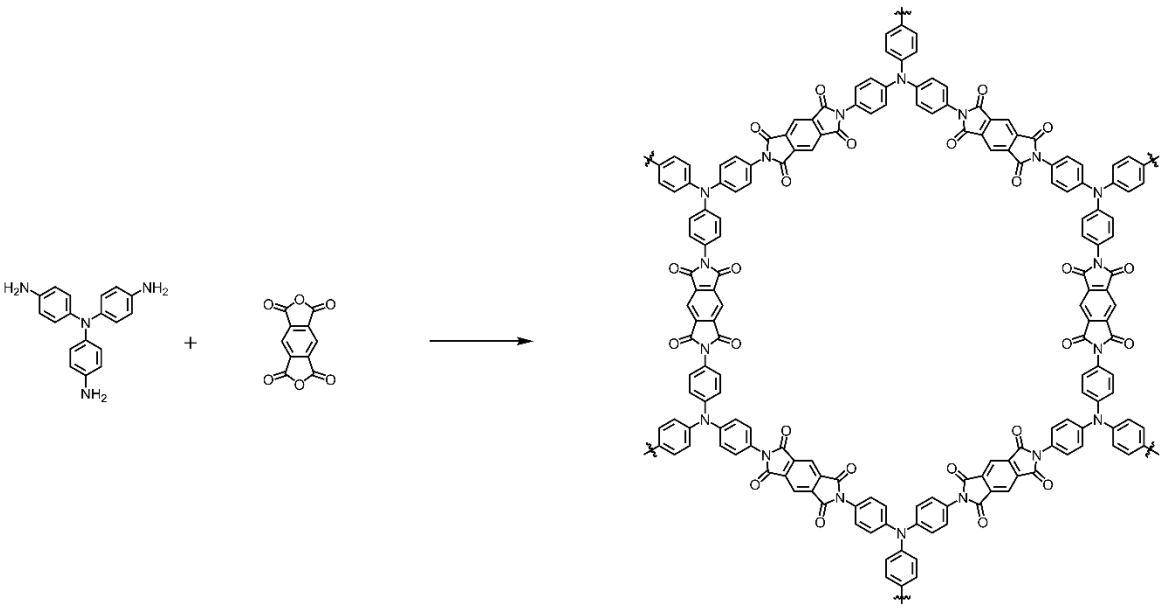

Figure 1-13. Synthesis of polyimide PI-COF-1 by imidization. Redrawn from reference [78].

1.7.5 Olefin

In 2017, Jiang *et al.* synthesised a 2-D sp^2c-COF by C=C condensation reactions of tetrakis(4-formylphenyl)pyrene and 1,4-phenylenediacetonitrile (Figure 1-14).[83] The sp2c-COF was fully p-conjugated and constructed from all sp2 carbons to form extended conjugation along with both x and y directions. sp^2c-COFs are of interest in terms of their high chemical stability and enhanced delocalized electronic structures. In 2019, Feng *et al.* reported an olefin-linked nitrogen-rich hexaazatrinaphthalene based COF and explored their application in a Li-ion cell.[98]

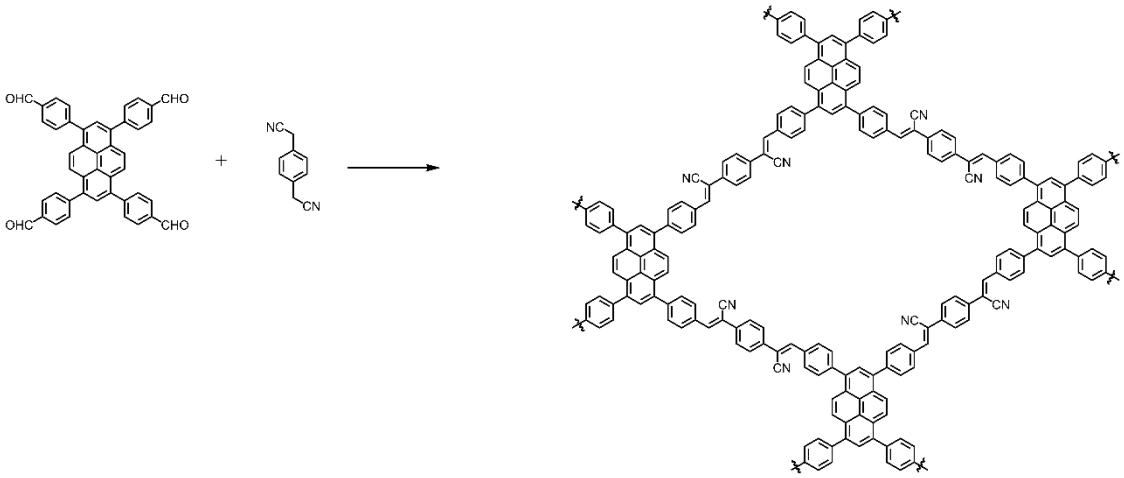

Figure 1-14. Synthesis of olefin-linked sp^2 c-COF. Redrawn from reference [83].

Other coupling reactions have been used to build COFs as described in the literature, but at present, only boroxine, imine, ketoenamine, and olefin-linked COFs have been studied as electrode materials in Li-ion cells.

1.8 Preparation Methods of Polymer and Reduced Graphene Oxide/Carbon Nanotube Composites

Reduced graphene oxide (rGO) is made from graphene oxide by chemical, thermal and other methods to reduce the oxygen content, while graphite oxide is a material produced by oxidation of graphite which leads to increased interlayer spacing and functionalisation of the basal planes of graphite.[99] The electrical conductivity of rGO is 10^2 to 10^3 S m^{-1}.[100] Carbon nanotubes (CNTs) are cylindrical large molecules consisting of a hexagonal arrangement of hybridized carbon atoms, which may be formed by rolling up a single sheet of graphene (single-walled carbon nanotubes) or by rolling up multiple sheets of graphene (multiwalled carbon nanotubes).[101] The electrical conductivity of CNT can be as high as 10^6 to 10^7 S m^{-1}.[102] Therefore, rGO/CNT has been widely used to prepare composites with organic materials to improve conductivity. To maximise the advantage of rGO/CNTs in the composites, the rGO/CNTs should not form aggregates and must be well dispersed to enhance the interfacial interaction with the matrix. Several processing methods have been used to fabricate polymer including solution mixing, bulk mixing, sonication mixing, melting mixing, and *in situ* polymerisation.

1.8.1 Solution Mixing

Solution mixing is the most common method to fabricate the polymer and rGO/CNT composites. This technique involves mixing both components into a certain solvent and evaporating the solvent to form a composite film. rGO/CNT powders are dispersed into a suitable solvent by vigorous stirring and/or sonication while applying mechanical energy to unbundle the rGO/CNT. The rGO/CNT dispersion is then mixed with a polymer solution, followed by controlled evaporation of the solvent with or without vacuum conditions. Finally, the dispersed rGO/CNT and polymer matrix are mixed and form a composite film.

The choice of solvent is key, as it depends on the solubility of the polymer matrix. The solvents for both components (rGO/CNT) can be the same or different, but they must be miscible. Additionally, the boiling point of the solvent has a great influence on the property of the formed composite. High-boiling point solvents are hard to be removed and tend to get trapped in the composite. The trapped solvent may deteriorate the electrical, thermal, or mechanical properties. Low-boiling points solvents are generally preferred for they are easily removed from the solution-made composites.

1.8.2 Bulk Mixing

Bulk mixing is a mechanical process that leads to local generation of high pressure as a result of collisions throughout the grinding media. For example, ball milling was employed to incorporate rGO/CNTs into polymer matrices.[97,103] In this way, a satisfactory level of dispersion of rGO/CNTs was introduced into the polymer matrix, resulting in an improvement of the physical and electrical properties of the samples.

1.8.3 Sonication Mixing

Sonication mixing is widely used for the fabrication of polymer and rGO/CNT composites. In this method, the rGO/CNT powers are dispersed in a solvent solution and ultrasound before the addition of the polymer matrix. The rGO/CNT bundles are broken down to individual rGO/CNT during sonication and the polymers are adsorbed to the surface of the rGO/CNT.

The power of sonication, the solvent, the rGO/CNT geometry are the factors that influence the final composite structure.

1.8.4 Melt Mixing

Melt mixing is a fast, inexpensive, and industry-friendly process for thermoplastic-based composites. This method is suitable for insoluble polymers which can not be processed with solution techniques. In general, melt mixing involves the blending of melt polymer with rGO/CNT powders by application of intense shear forces at elevated temperatures. Depending on the final shape of the composites, the bulk products can then be prepared by several techniques, such as extrusion.[104] This technique requires no solvents/chemicals and has a low cost with the least effect on the environment. This method is suitable for large-scale industrial applications.

1.8.5 *In situ* Polymerisation

In situ polymerisation method is based on the dispersion of rGO/CNT powder into the monomer mixture, then followed by a standard polymerisation procedure. The advantage of this method is that the dispersion can be improved if the rGO/CNT are modified with functional groups compatible with the monomer.[105] What is more, owing to the small size of monomeric molecules, the homogeneity of the resulting composite is much higher than mixing rGO/CNT and polymer chains in solution/bulk. Therefore, in situ method allows the preparation of homogenous composites with high CNT weight fractions.

1.9 Carbonyl-containing Polymeric Electrode Materials

Only a few examples of carbonyl compounds as electrode materials were studied in the 1970s and 80s.[8,106–112] The development of the carbonyl-compound electrodes was limited by the dissolution of carbonyl compounds in aprotic electrolytes, which leads to fast capacity fading. However, carbonyl-containing polymers attracted a lot of attention for their application in energy storage during the last ten years. As the carbonyl group is a common organic

functionality, a variety of synthetic routes can be chosen to design new active materials, like quinone-based polymers, polyimides, and other polymeric carbonyl derivatives.

1.9.1 Polyquinone

Quinone compounds were included in the earliest materials to be investigated for use in Li-ion cells.[7,8] In 1986, a polymeric quinone, which has a high theoretical capacity (505 mAh g^{-1}), energy density, and insolubility in organic electrolytes, used as the positive electrode for Li-ion cell was reported by Foos *et al.*[113] However, the practical capacity of the polymeric quinone is 25% of its theoretical capacity with poor cycle performance, which may result from the synthetic techniques, the electrolyte used and non-optimised electrode construction. These earlier works demonstrated the potential of carbonyl-containing polymers for organic batteries. During the last few decades, numerous attempts have been made to synthesize and use carbonyl-containing polymers as the electrode for Li-ion cells.

A quinone-based polymer electrode, poly(anthraquinonylsulfide), was made from the polycondensation of 1,5-dichloranthraquinone with sodium sulphide, which exhibited a reversible redox reaction at 2.33 V (*vs* Li^+/Li) which is similar to anthraquinone.[114] Poly(anthraquinonylsulfide) electrode achieved a capacity of 185 mAh g^{-1} (at 50 mA g^{-1}) and showed better cycling stability compared to anthraquinone. However, it still cannot meet the requirements for practical application. A follow-up study systematically investigated the factors influencing the performance of batteries containing this active material.[115]

2D COFs also can be used as electrode materials in Li-ion cells. For 2D COFs, however, because 2D extended layers tend to close pack in an eclipsed arrangement in COFs due to the strong interlayer π−π interactions, inside the 1D channels the deeply buried active sites are difficult to access due to the long ion transportation path, especially at a high charge/discharge rates. The sluggish Li^+ migration in 1D channels will inevitably lead to the insufficient utilization of the redox-active sites and thus reduce their capacity and rate performance.[69] To solve this challenge, Wang *et al*. first reported a general strategy to exfoliate COFs into few-layer nanosheets (Figure 1-15).[118] The exfoliated COF was prepared by a facile and scalable mechanical milling procedure. It was demonstrated that the ball milling method just changes the thickness of the COF particles without destroying the chemical structure. And the thickness of the exfoliated COFs is tunable by varying vibration frequency and time. At the same current

density, the exfoliated COF showed a higher capacity than the raw COFs. The exfoliation strategy opens up a new avenue for preparing the next generation of sustainable and high-performance Li-ion electrode materials.

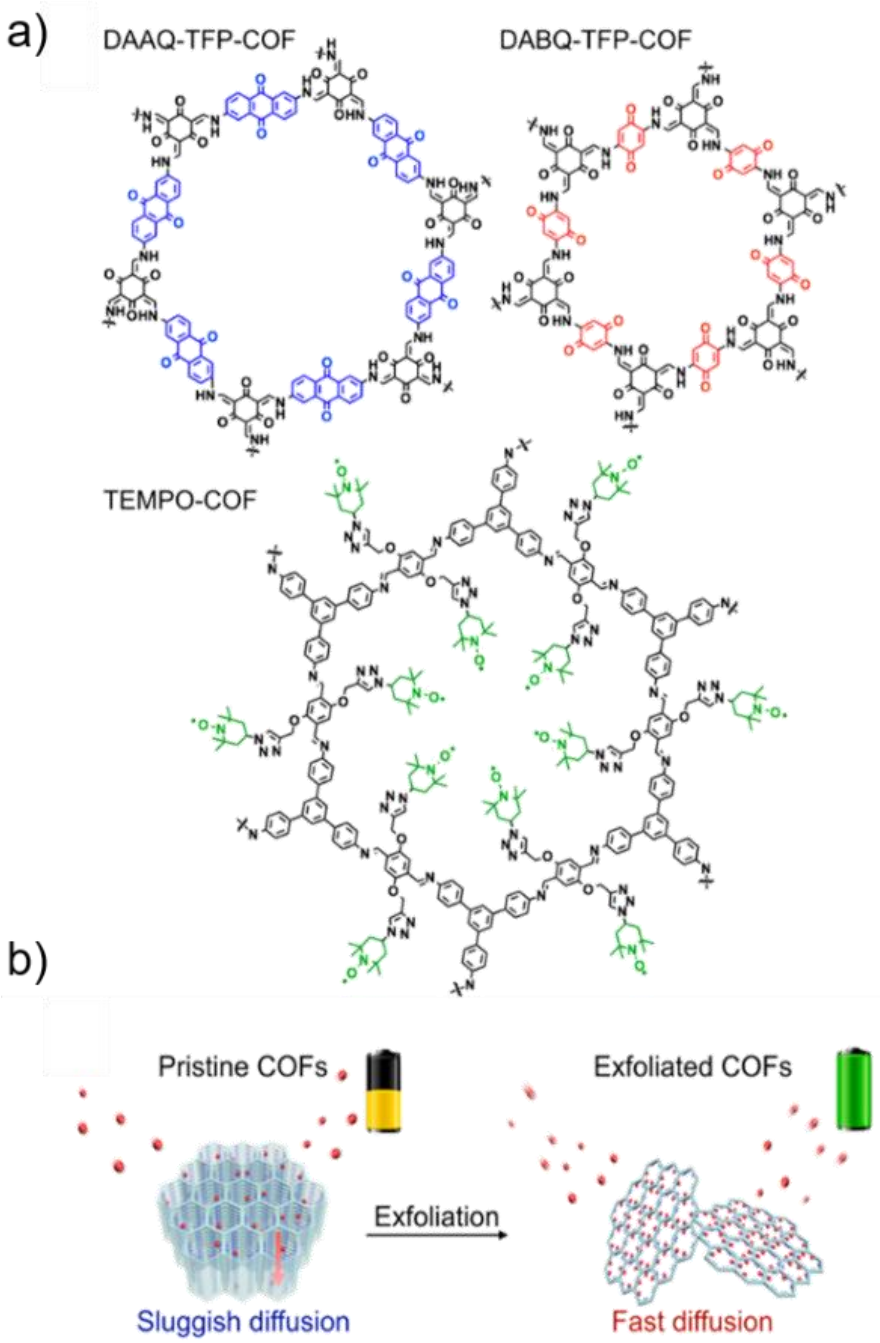

Figure 1-15. (a) Chemical structures of DAAQ-TFP-COF, DABQ-TFP-COF, and TEMPO−COF, (b) Schematic illustration for the exfoliation of 2d redox-active COSs into exfoliated COFs as cathodes for lithium-ion batteries. Reprinted with permission from reference 118. Copyright 2017, American Chemical Society.[118]

Polymerisation often introduces electrochemically inactive motifs into the structure, leading to a reduced theoretical specific capacity. To improve the theoretical specific capacity, the generation of extra redox-active sites by self-polymerisation has also been reported.[119] 2,7-dianitropyrene-4,5,9,10-tetraone (PT-$2NO_2$) was self-polymerised by electrochemical reduction and then applied as the positive electrode for Li-ion cells. The nitro groups in the PT-$2NO_2$ could be electrochemically reduced to azo groups, which also can serve as a redox-active site. Besides the high irreversible capacity of the first cycle, PT-$2NO_2$ showed discharge capacities of 301 mAh g^{-1} at 50 mA g^{-1} and the highest reversible capacity of 82 mAh g^{-1} after 500 cycles. Furthermore, PT-$2NO_2$ showed high specific energy of 1047 Wh kg^{-1} and specific power of 2246 W kg^{-1}. Self-polymerisation to introduce an extra redox-active site is a good way to solve the poor cycling performance of small molecules and to reduce the capacity loss after polymerisation at the same time.

To improve the energy density of an electrode, less non-active material should be included in its formulation. Zhang *et al.* reported 2D COFs as cathodes for binder-free lithium-ion batteries (Figure 22).[120] A 2D boroxine-linked chemically-active pyrene-4,5,9,10-tetraone (PTO) covalent organic framework (PPTODB) was synthesised and a binder-free organic cathode electrode was prepared by the mixing of 70% PPTODB with 30% carbon nanotube (CNT). At 20 mA g^{-1}, PPTODB based electrode has a capacity of 198 mAh g^{-1} at the second discharge process and an average output voltage of 2.8 V. PPTODB based electrode also showed good capacity retention of 68.3% after 150 cycles with a stable Coulombic efficiency of ~99.6%. The capacity at 1000 mA g^{-1} is 76% of the capacity at 100 mA g^{-1}.

The high theoretical specific capacity of the organic electrode is because of the lightweight of the organic molecule. However, the lightweight also leads to a low density, which results in low volumetric energy density. To solve this problem, Marcilla *et al.* reported polymer nanostructures to make the polymeric electrode packing better.[121] Anthraquinone-based conjugated microporous polymers (IEP-11) were prepared by Sonogashira cross-coupling reaction with 2,6-dibromoanthraquinone and 1,3,5-triethynylbenzene following two different synthetic protocols. IEP-11-E made from mini emulsion polymerisation exhibited enhanced specific surface area, enhanced solution dispersibility, and increased tap density compared to IEP-11-C synthesised from the conventional polymerization. IEP-11-E12 which has the same chemical structure as IEP-11, is synthesised by mini emulsion polymerization followed by 12 h solvothermal treatment. The IEP-11-E12 based electrode has triple the density of IEP-11-C. This is directly related to the volumetric capacity, for example, IEP- 11-E12 delivered a

volumetric capacity of 23 mAh cm^{-3} at 5 C, 7 times higher than that for IEP-11-C. For the same materials, the improved volumetric capacity would lead to a higher volumetric energy density.

1.9.2 Polyimides

The research on polyimides represents a relatively young field in the development of redox-active polymers for electrochemical energy storage. Generally, polyimides are synthesised through a simple polycondensation reaction of dianhydrides and diamines. The imide functionalities undergo two one-electron reduction steps, one carbonyl group can undergo fully reversible reduction. While the second carbonyl group required deep discharging to below 1.5 V, which leads to the decomposition of the redox-active structure. Therefore, only the first redox stage can be utilized in a rechargeable battery application.[42,122]

In 2010, Song *et al.* investigated the battery application of five polyimides.[122] The polyimides were prepared by the condensation of different combinations of pyromellitic dianhydride and 1,4,5,8-naphthalenetetracarboxylic dianhydride with 1,4-phenylenediamine and 1,2-ethanediamine. The five polyimide samples are all electrochemically active and exhibited output voltages in the range from 2.0 to 2.5 V *vs* Li^+/Li. They delivered specific capacities of around 200 mAh g^{-1} with Coulombic efficiencies close to 100% and a moderate loss after 100 cycles. In general, the naphthalene diimides reveal higher potentials because of their larger delocalized system, resulting in easier reducibility. To optimize the rate performance, the same group developed a nanocomposite combining graphene with polyimide which was made through the polycondensation of 1,4,5,8-naphthalenetetracarboxylic dianhydride and ethylenediamine.[55] At a charging rate of 10 C, a capacity of 135 mAh g^{-1} was obtained. A significant drawback of this material is a large voltage gap of 0.9 V between the charge and discharge plateaus.

Jiang *et al.* reported a redox-active, crystalline, mesoporous COF on carbon nanotubes (D_{TP}-A_{NDI}-COF@CNTs) used as electrodes.[123] The composite was made by *in situ* polycondensation of D_{TP}-A_{NDI}-COF on CNT wires under solvothermal conditions (Figure 1-16e). In the D_{TP}-A_{NDI}-COF@CNTs composite electrode, only the naphthalene diimide (NDINA) units are electrochemically redox-active and experience the reversible two-electron redox reaction. the triphenylene knots and boronate linkages are electrochemically inactive (Figure 1-16a-c). The charge/discharge capacity of D_{TP}-A_{NDI}-COF@CNTs cathode was stable upon cycling and

delivered a capacity of 67 mAh g^{-1} at the current density of 200 mA g^{-1} (corresponding to a rate of 2.4 C). under the same conditions, D_{TP}-A_{NDI}-COF exhibited a capacity of 42 mAh g^{-1}, and about 50% capacity decrease after the 50 cycles. D_{TP}-A_{NDI}-COF@CNTs delivered a capacity of 58 mAh g^{-1} when increasing the current density to 12 C, which corresponds to a retention of 85% (relative to that of 2.4 C) and shows much better rate performance compared to the electrode without CNTs. With the current rate increasing, the charge/discharge plot always remained stable and displayed a small voltage polarization, indicating that the electronic or ionic transport is fast enough to respond to the charge/discharge reaction at a high current density.

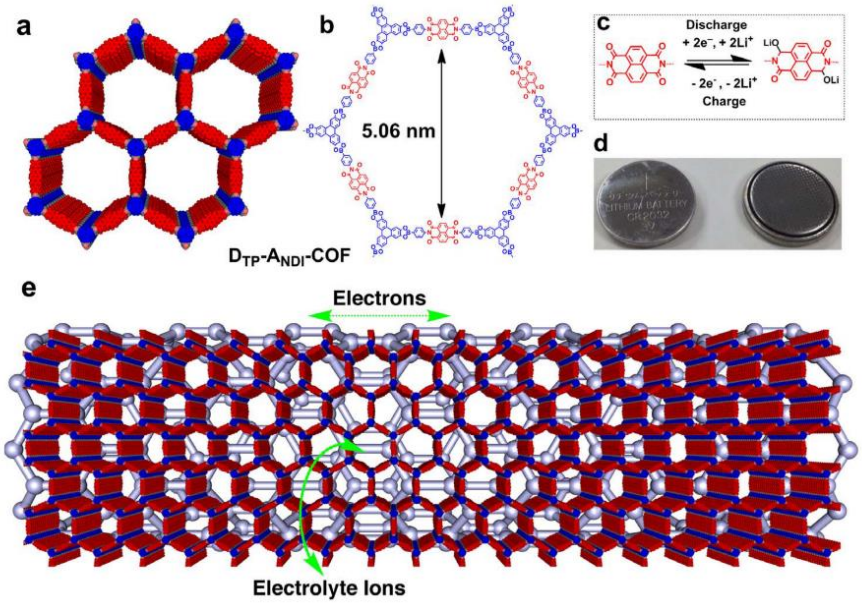

Figure 1-16. Structure of redox-active organic electrode materials. (a) Schematic of the AA-stacking of D_{TP}-A_{NDI}-COF with redox-active naphthalene diimide walls (red) and one-dimensional mesoscale channels; (b) Chemical structure of one pore in D_{TP}-A_{NDI}-COF; (c) Electrochemical redox reaction of a naphthalene diimide unit. (d) Photographs of a coin-type battery. (e), Graphical representation of D_{TP}-A_{NDI}-COF@CNTs (grey for CNTs) and electron conduction and ion transport. Reprinted with permission from reference 123. Copyright 2012 John Wiley & Sons.[123]

Another example of improving the utilization of the redox-active site by the cooperation of CNT is a crystalline 2D-PAI@CNT, which was synthesised by the *in situ* polycondensation reaction between tris(4-aminophenyl)amine (TAPA) and 1,4,5,8-naphthalenetetracarboxylic

dianhydride (NTCDA) in the presence of CNTs (Figure 1-17a).[124] The 2D-PAI@CNT was used as the positive electrode in lithium-ion batteries. At a current density of 100 mA g^{-1}, the 2D-PAI cathode exhibited a limited capacity of 29 mAh g^{-1}, corresponding to low utilization of active sites (22.6%). With the presence of CNTs, under 100 mA g^{-1} 2D-PAI@CNT delivered a capacity of 104 mAh g^{-1} with the utilization of the redox-active site improved to 82.9%, indicating the introduction of CNT beneficial to make the most use of the redox-active site. Further, 2D-PAI@CNT exhibited the state of art long-term cycling performance with 100% capacity retention after 8000 cycles at 500 mA g^{-1} (Figure 1-17d).

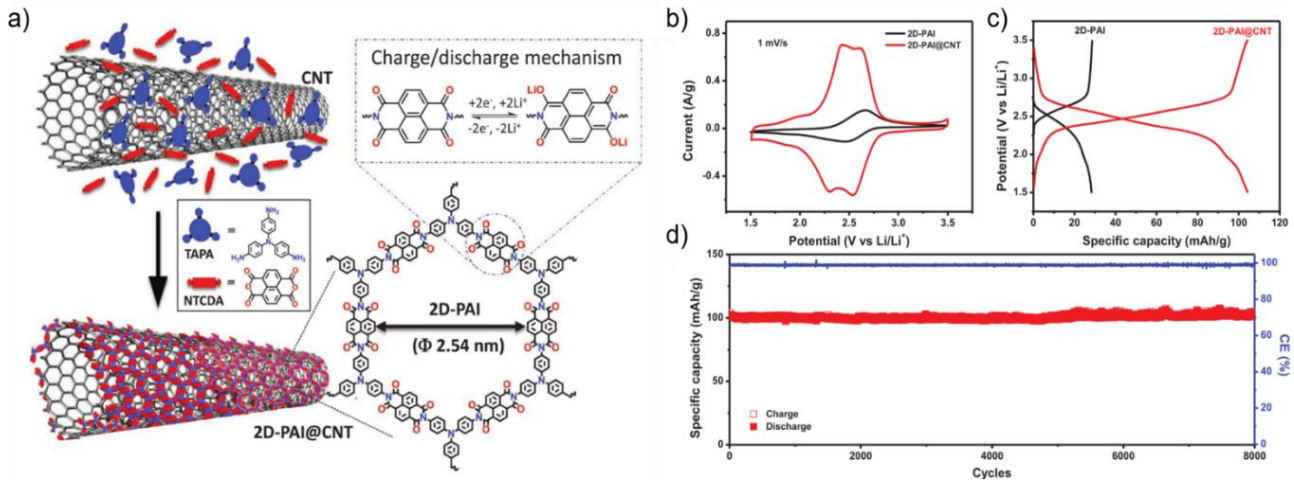

Figure 1-17. (a) Schematic illustration of the synthesis of crystalline 2D-PAI@CNT and energy storage process, (b) CV curves at 1 mV s^{-1}, (c) galvanostatic charge-discharge curves, (d) long-term cycling stability of 2D-PAI@CNT at 0.5 A g^{-1}. Reprinted with permission from reference 54. Copyright 2019 WILEY‐VCH Verlag GmbH & Co. KGaA, Weinheim.[54]

Bu *et al*. reported the synthesis of crystalline porous polyimide-based COFs (Tp-DANT-COF) by reacting 1,3,5-triformylphloroglucinol (Tp) and 2,7-diaminobenzo[*lmn*][3,8]phenanthroline-1,3,6,8(2H,7H)-tetraone (DANT).[125] Tp-DANT-COF has a capacity of 78.9 mAh g^{-1} (corresponding to the 59% utilization of the redox-active site) at the current density of 1.5 C (corresponding to 200 mA g^{-1}) and kept the capacity for more than 200 cycles. Tp-DANT-COF delivered a capacity of 66.3 mAh g^{-1} at a current density of 14.9 C corresponding to 84% retention of the capacity at 1.5 C, implying a good rate performance.[125] In addition, when the monomer Tp is replaced by 1,3,5-triformylbenzene, the resultant Tb-DANT-COF exhibited a lower polarization value (the gap between the oxidation and reduction potential) and higher initial discharge capacity compared to Tp-DANT-COF.

This result reveals that the extension of the conjugation in the backbone is a fundamental strategy to improve the intrinsic electrical conductivity of COFs.

Besides CNTs, reduced graphene oxide (rGO) is also employed to optimise the utilisation of the electrochemically redox-active sites in the polymeric electrodes.[97] Huang and co-workers reported a composite of polyimide COF (PI-COFs) and rGO as positive electrode for Li-ion cells. It was found that the electrochemical capability of PI-COFs could be enhanced by rGO via the ball-milling strategy.

For most cases, polymerisation would introduce electrochemically inactive components into the polymer, which will increase the molecular mass of the repeating unit leading to a reduced theoretical capacity. A feasible way to alleviate this issue is to use electrochemically redox-active linkers to polymerize the monomer. Polyquinoneimines (PQIs), which were synthesised by hydrothermal polymerization reactions of 1,4,5,8-naphthalene tetracarboxylic anhydride and 2,6-diaminoanthraquinone, are used as cathode materials in lithium-ion batteries.[62] Because both quinones and anhydrides are electrochemically active, the direct polymerization of these two monomers did not introduce additional inactive monomers. Therefore, it did not sacrifice the theoretical specific capacity. Furthermore, the increased molar mass effectively suppresses the dissolution of the active materials in the electrolyte. Compared to polymeric precursors, a PQI-1 based electrode has a higher specific capacity of 210 mAh g^{-1} and better cycling performance (136 mAh g^{-1} after 200 cycles).

Chen *et al.* synthesised 2D microporous poly(imide-benzoquinone) (PIBN) COFs by *in situ* polymerization on graphene (PIBN-G).[126] (Due to the similar 2D features of PIBN COF and graphene, there exists a strong interaction between them in the PIBN-G composite and charge transfer through the conjugation of π–π stacking. The structure benefits from the charge transfer from graphene to PIBN and full access of both electrons and Li^+ ions to the abundant redox-active carbonyl groups. At a current rate of 0.1 C, PIBN-G and PIBN exhibited a discharge capacity of 271.0 and 244.8 mAh g^{-1}, corresponding to 96.8% and 86.1% of their theoretical capacity (Figure 1-18). With the help of graphene, the utilization of the redox-active site is improved. Facilitated by the incorporation of graphene, fast Li^+ and electron transport were achieved. When tested at the same current rate, the specific capacity of PIBN-G was always higher than that of PIBN, the capacity showing a larger difference with increasing of current density. For example, PIBN-G exhibited large reversible specific capacities of 193 mAh g^{-1} at 10 C, while PIBN delivered a capacity of around 80 mAh g^{-1}. Also, PIBN-G presented good

cycling stability with capacity retention of more than 86% after 300 cycles with Coulombic efficiencies approaching 100%.

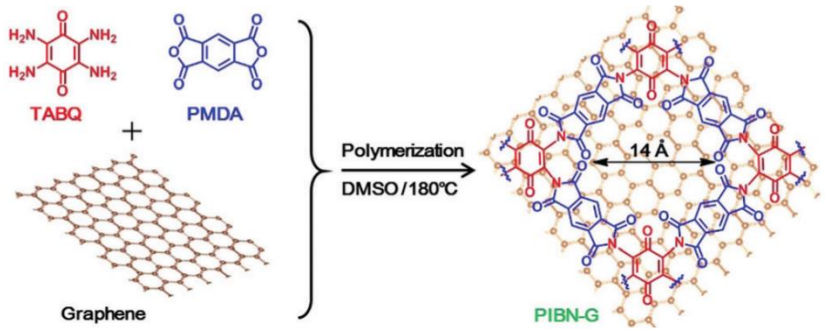

Figure 1-18. Synthesis route of PIBN and PIBN-G. Reprinted with permission from reference 53. Copyright 2018 Wiley‐VCH Verlag GmbH & Co. KGaA, Weinheim.[53]

The electrode composition, electrolyte, electrochemical performance of Li-ion coin cells, in which carbonyl-containing polymers and frameworks work as positive electrodes, were summarised in Table 1-2. High theoretical specific capacity can be achieved by designing the structure of the polymer. For example, a series of (2,7-dianitropyrene-4,5,9,10-tetraone based polymers has a theoretical capacity higher than 400 mAh g^{-1}.[119] However, the utilisation of the redox-active sites of the polymer electrode are often poor, for example, a crystalline 2D polyarylimide COF (2D-PAI) only exhibits 23% utilisation of its redox-active sites.[54]

Table 1-2. Carbonyl-containing polymeric cathode materials for Li-ion batteries in the recent literature.

Sample	Electrode composition (active materials/conductive additive/binder)	Electrolyte	Theoretical capacity (mAh g^{-1})	Maximum discharge capacity; utilisation of the active sites	Capacity retention (%)	Rate performance	Ref.
NDI-O	6/3/1; (AM/CB/PVDF)	1 M $LiPF_6$ in EC and DMC (v: v = 1: 1)	257	227 mAh g^{-1} at 0.1 C; 88.3%	55% after 100 cycles at 0.5 C	135 mAh g^{-1} at 20 C	[127]
NDI-BQ	5/4/1; (AM/Timical Super C65/PVDF)	1 M $LiPF_6$ in DOL and DME (v: v = 2: 1)	289	165 mAh g^{-1} at 0.1 C; 57%	50% after 200 cycles at 0.1 C	125 mAh g^{-1} at 0.5 C	[128]
PT-NO_2	4/5/1; (AM/acetylene black/PVDF)	1 M LiTFSI in DOL and DME (v: v = 1: 1)	490	301mAh g^{-1} at 50 mA g^{-1}; 61.4%	51.1% after 120 cycles at 50 mA g^{-1}	104 mAh g^{-1} at 1000 mA g^{-1}	[119]
PT	4/5/1; (AM/acetylene black/PVDF)	1 M LiTFSI in DOL and DME (v: v = 1: 1)	408	190 mAh g^{-1} at 50 mA g^{-1}; 46.6%	26.3% after 120 cycles at 50 mA g^{-1}	25 mAh g^{-1} at 1000 mA g^{-1}	[119]
PT-Br	4/5/1; (AM/acetylene black/PVDF)	1 M LiTFSI in DOL and DME (v: v = 1: 1)	255	250 mAh g^{-1} at 50 mA g^{-1}; 98%	44% after 120 cycles at 50 mA g^{-1}	55 mAh g^{-1} at 1000 mA g^{-1}	[119]
PT-NH_2	4/5/1; (AM/acetylene black/PVDF)	1 M LiTFSI in DOL and DME (v: v = 1: 1)	366	310 mAh g^{-1} at 50 mA g^{-1}; 84.7%	29% after 120 cycles at 50 mA g^{-1}	50 mAh g^{-1} at 1000 mA g^{-1}	[119]
PAQI-B14	4/4/2; (AM/Ketjen black/PVDF)	1 M LiTFSI in DOL and DME (v: v = 1: 1)	252	210 mAh g^{-1} at 0.2C; 83%	67% after 200– cycles at 0.2 C	55 mAh g^{-1} at 4 C	[129]
PAQI-B15	4/4/2; (AM/Ketjen black/PVDF)	1 M LiTFSI in DOL and DME (v: v = 1: 1)	252	189 mAh g^{-1} at 0.2C; 75%	65% after 200 cycles at 0.2 C	45 mAh g^{-1} at 4 C	[129]

PAQI-N14	4/4/2; (AM/Ketjen black/PVDF)	1 M LiTFSI in DOL and DME (v: v = 1: 1)	230	202 mAh g^{-1} at 0.22C; 88%	80% after 200 cycles at 0.22 C	137 mAh g^{-1} at 4.35 C	[129]
PAQI-N15	4/4/2; (AM/Ketjen black/PVDF)	1 M LiTFSI in DOL and DME (v: v = 1: 1)	230	190mAh g^{-1}at 0.22C; 83%	77% after 200 cycles at 0.22 C	130 mAh g^{-1} at 4.35 C	[129]
DAAQ-ECOF	6/3/1; (AM/Super P/PVDF)	1M LiTFSI in TEGDME	151	145 mAh g^{-1} at 0.13 C; 96%	97% after 1800 cycles at 3.3 C	76 mAh g^{-1} at 19.9 C	[118]
DAAQ-TFP-COF	6/3/1; (AM/Super P/PVDF)	1M LiTFSI in TEGDME	151	110 mAh g^{-1} at 0.13 C; 73%	-	25 mAh g^{-1}at 19.9 C	[118]
D_{TP}-A_{NDI}-COF@CNTs	7/2/2; (AM/Super P/PVDF)	1 M $LiPF_6$ in EC and DMC (w: w = 1: 1)	83	67 mAh g^{-1} at 2.4 C; 81%	100% after 700– cycles at 2.4 C	58 mAh g^{-1} at 12 C	[123]
D_{TP}-A_{NDI}- COF	7/2/2; (AM/Super P/PVDF)	1 M $LiPF_6$ in EC and DMC (w: w = 1: 1)	83	42 mAh g^{-1} at 2.4 C; 51%	34% after 50 cycles– at 2.4 C	4 mAh g^{-1} at 12 C	[123]
2D-PAI@CNT	8/1/1; (AM/Super P/Alginate sodium)	1 M LiTFSI in DOL and DME (v: v = 1: 1)	126	104 mAh g^{-1} at 0.8 C; 83%	100% after 8000 cycles at 15.9 C	100mAh g^{-1} at 15.9 C	[54]
2D-PAI	8/1/1; (AM/Super P/Alginate sodium)	1 M LiTFSI in DOL and DME (v: v = 1: 1)	126	28 mAh g^{-1} at 0.8 C; 23 %	100% after 50cycles at 0.8 C	-	[54]
IEP-11-C	5/4/1; (AM/MWCNTs/PVDF)	1 M LiTFSI in DOL and DME (v: v = 1: 1)	149	40 mAh g^{-1} at 1 C; 26%	89% after 100 cycles at 0.1 C	About 18 mAh g^{-1} at 30C	[121]
IEP-11-E6	5/4/1; (AM/MWCNTs/PVDF)	1 M LiTFSI in DOL and DME (v: v = 1: 1)	149	79 mAh g^{-1} at 1 C; 53%	-	About 39 mAh g^{-1} at 30C	[121]
IEP-11-E12	5/4/1; (AM/MWCNTs/PVDF)	1 M LiTFSI in DOL and DME (v: v = 1: 1)	149	104 mAh g^{-1} at 1 C; 70%	58% after 8000 cycles at 30 C	47 mAh g^{-1} at 30 C	[121]

PMAQ	6/3/1; (AM/Ketjen black/PVDF)	1 M LiTFSI in DOL and DME (v: v = 1: 1)	214	170mAh g^{-1} at 0.1 C; 79%	45% after 100 cycles at 0.2 C	80 mAh g^{-1} at 1 C	[130]
NTAQ	6/3/1 (AM/Kentjen black/PVDF)	1 M LiTFSI in DOL and DME (v: v = 1: 1)	195	145 mAh g^{-1} at 0.1 C; 74%	80.3% after 1000 cycles at 0.5 C	108 mAh g^{-1} at 1 C	[130]
Tp-DANT-COF	6/2/2; (AM/Super P/PVDF)	1 M LiPF6 in DMC, EC and EMC (v: v: v = 1: 1: 1)	133	78.9 mAh g^{-1} at 1.5 C; 59%	90.5% after 600 cycles at 7.5 C	66.3 mAh g^{-1} at 14.9 C	[126]
Tb-DANT-COF	4/4/2; (AM/Ketjen black/PVDF)	1 M LiPF6 in DMC, EC and EMC (v: v: v = 1: 1: 1)	147	135mAh g^{-1} at 0.34 C; 92%	76% after 300 cycles at 3.4 C	66.6 mAh g^{-1} at 13.7 C	[126]
PIBN-G	8/1/1; (AM/Ketjen black/PVDF)	1 M LiTFSI in DOL and DME (v: v = 1: 1)	280	271 mAh g^{-1} at 0.1 C; 96.8%	86% after 300 cycles at 1 C	193 mAh g^{-1} at 10 C	[53]
PIBN	6/3/1; (AM/Ketjen black/PVDF)	1 M LiTFSI in DOL and DME (v: v = 1: 1)	280	244.8mAh g^{-1} at 0.1 C; 86.1%	-	80 mAh g^{-1} at 10 C	[53]
PI-COF-1	6/3/1; (AM/Ketjen black/PVDF)	1 M LiTFSI in DOL and DME (v: v = 1: 1)	142	103 mAh g^{-1} at 0.1 C; 72%	75% after 300 cycles at 1 C	60 mAh g^{-1} at 10 C	[97]
PI-ECOF1/rGO50	6/3/1; (AM/Ketjen black/PVDF)	1 M LiTFSI in DOL and DME (v: v = 1: 1)	142	167 mAh g^{-1} at 0.1 C; 100%	73% after 300 cycles at 1 C	90 mAh g^{-1} at 10 C	[97]
PI-COF-2	6/3/1; (AM/Ketjen black/PVDF)	1 M LiTFSI in DOL and DME (v: v = 1: 1)	128	103 mAh g^{-1} at 0.1 C; 80%	50% after 300 cycles at 1 C	10 mAh g^{-1} at 5 C	[97]
PI-COF-2/rGO50	6/3/1; (AM/Ketjen black/PVDF)	1 M LiTFSI in DOL and DME (v: v = 1: 1)	128	124 mAh g^{-1} at 0.1 C; 97%	56% after 300 cycles at 1 C	37 mAh g^{-1} at 5 C	[97]
PTNDI	4/5/1; (AM/acetylene black/PVDF)	1 M $LiPF_6$ in EC, DMC and EMC	143	140 mAh g^{-1} at 0.1 C;	89% after 100 cycles at 0.1 C	43 mAh g^{-1} at 2C	[131]

		(v: v: v = 1: 1: 1)		98%			
PQ	5/2/2/1 (AM/colloidal graphite/acetylene black/ PVDF)	1 M LiTFSI in DOL and DME (v: v = 1: 1)	228	228 mAh g^{-1} at 50 mA g^{-1}; 100%	45% after 1000 cycles at 50 mA g^{-1}	85 mAh g^{-1} at 5000 mA g^{-1}	[132]
PQ	5/2/2/1 (AM/colloidal graphite/acetylene black/ PVDF)	1 M LiTFSI in DOL and DME (v: v = 1: 1)	228	170 mAh g^{-1} at 50 mA g^{-1}; 100%	77% after 500 cycles at 50 mA g^{-1}	-	[132]
PPTODB	7/3 (AM/CNT)	1 M $LiPF_6$ in EC and DMC (v: v = 1: 1)	-	198 mAh g^{-1} at 20 mA g^{-1}; -	68.3% after 150 cycles at 20 mA g^{-1}	98 mAh g^{-1} at 5000 mA g^{-1}	[120]

1.10 Project Overview and Aims

The aim of this project is to synthesise polymers and COFs with electrochemical redox-active functional groups for application as positive electrodes in Li-ion cells. Strategies for improving the utilization of redox-active sites in the polymers, enhancing the average discharge potential of the organic electrode, and promoting rate performance and achieving high capacity are investigated.

Using carbonyl containing-polymers as positive electrodes solved the problem of the dissolution of small organic molecules in the electrolyte. However, the utilisation of the redox-active site of the polymers is often limited because some redox-active sites are not always accessible. In **Chapter 3**, a redox-active polyimide (**PI**) and composites of PI and rGO (**PI10, PI30**, and **PI50**, where 10, 30 and 50 = wt.% of rGO) were synthesised and studied as the cathode materials in Li-ion cells (Figure 1-19). The relationship of the particle size of **PI**, SA_{BET} of the polymer and the PI composites, in addition to the effect on the utilisation of the redox-active sites was studied.

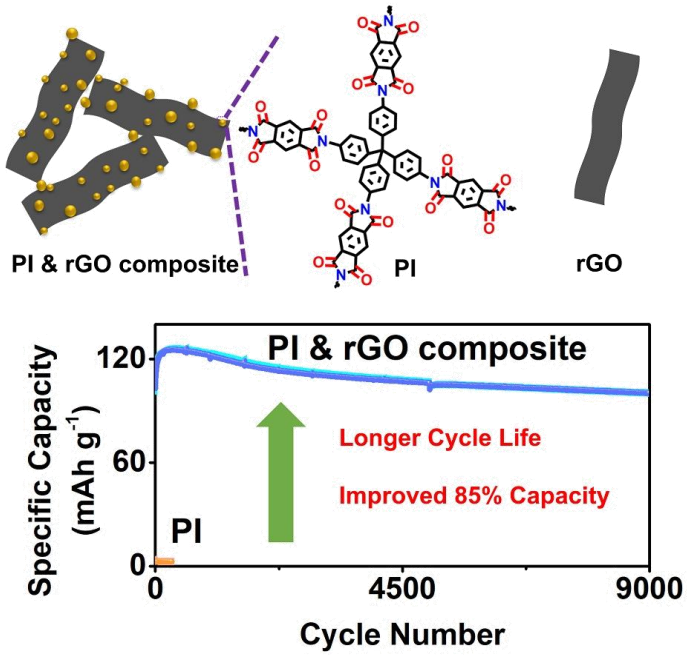

Figure 1-19. The highlight of Chapter 3.

The results described in Chapter 3 show that it is difficult to generate intimate contacts between the polyimide particles and rGO sheets in the composites. Instead, to generate composites with intimate contact between the active materials and the conductive additives, a *β*-ketoenamine

COF with quinone redox-active functional groups was synthesised by *in situ* growth on the surface of CNTs. In **Chapter 4**, the battery application of these *in situ* grown COFs on CNTs is reported. Following the discussion in **Chapter 3**, structure-performance relationships are probed and interpreted so that fundamental insights and design principles can be drawn to help guide future studies and developments of COF electrode materials. Compared to the polyimide structure, the COF described in **Chapter 4** has more electron-withdrawing groups, which leads to a high average discharge potential. By optimizing the proportions of the COF and the CNTs in the reaction mixture, thinner layers of crystalline COF on the CNT surfaces were fabricated, thus dramatically improving the electrochemical accessibility required to drive these redox reactions through ultrafast charge/discharge cycles with only a small drop in performance while also significantly improving the rate performance (Figure 1-20).

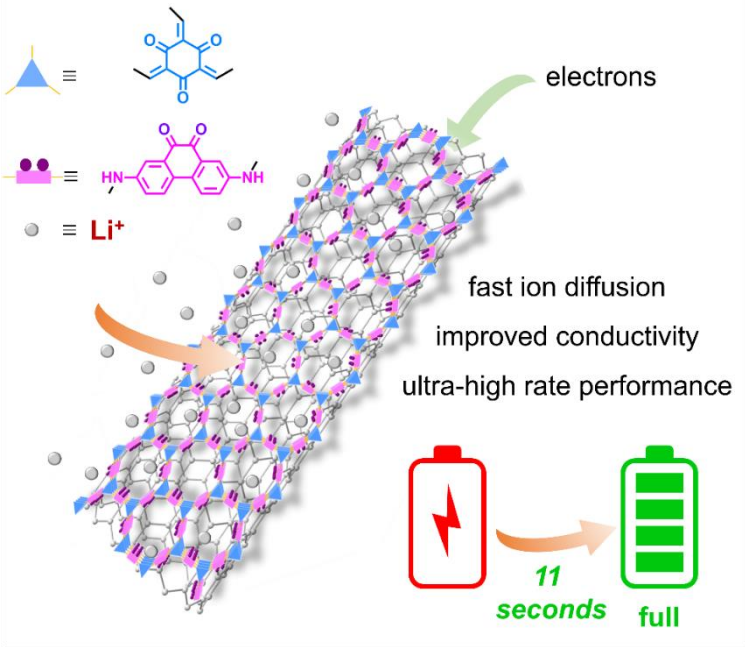

Figure 1-20. The highlight of Chapter 4.

Based on the knowledge gained from Chapter 3 and Chapter 4, a *β*-ketoenamine COF with abundant conjugated carbonyl groups was designed and explored for battery applications in **Chapter 5**. The electrochemical performance of the COF was optimised by the growth of the COF on the CNT. This composite has the highest capacity of the reported COF-based electrode materials.

1.11 Reference

(1) Tarascon, J. M.; Armand, M. Issues and Challenges Facing Rechargeable Lithium Batteries. *Nature* **2001**, *414* (6861), 359–367.

(2) Armand, M.; Tarascon, J.-M. Building Better Batteries. *Nature* **2008**, *451* (7179), 652–657.

(3) Thackeray, M. M.; Kang, S. H.; Johnson, C. S.; Vaughey, J. T.; Benedek, R.; Hackney, S. A. Li_2MnO_3-Stabilized $LiMO_2$ (M = Mn, Ni, Co) Electrodes for Lithium-Ion Batteries. *J. Mater. Chem.* **2007**, *17* (30), 3112–3125.

(4) Kasavajjula, U.; Wang, C.; Appleby, A. J. Nano- and Bulk-Silicon-Based Insertion Anodes for Lithium-Ion Secondary Cells. *J. Power Sources* **2007**, *163* (2), 1003–1039.

(5) Bruce, P. G.; Freunberger, S. A.; Hardwick, L. J.; Tarascon, J. M. Li-O_2 and Li-S Batteries with High Energy Storage. *Nat. Mater.* **2012**, *11* (1), 19–29.

(6) Liang, Y.; Tao, Z.; Chen, J. Organic Electrode Materials for Rechargeable Lithium Batteries. *Adv. Energy Mater.* **2012**, *2* (7), 742–769.

(7) Williams, D. L.; Electrochem, J.; Williams, D. I.; Byrne, J. J.; Driscoll, J. S. High Energy Density Lithium/Dichloroisocyanuric Acid Battery System. *J. Electrochem. Soc.* **1969**, *116* (1), 2–4.

(8) Alt, H.; Binder, H.; Köhling, A.; Sandstede, G. Investigation into the Use of Quinone Compounds-for Battery Cathodes. *Electrochim. Acta* **1972**, *17* (5), 873–887.

(9) Ai, W.; Zhou, W.; Du, Z.; Sun, C.; Yang, J.; Chen, Y.; Sun, Z.; Feng, S.; Zhao, J.; Dong, X.; Huang, W.; Yu, T. Toward High Energy Organic Cathodes for Li-Ion Batteries: A Case Study of Vat Dye/Graphene Composites. *Adv. Funct. Mater.* **2017**, *27* (19), 1603603.

(10) Ai, W.; Du, Z.; Fan, Z.; Jiang, J.; Wang, Y.; Zhang, H.; Xie, L.; Huang, W.; Yu, T. Chemically Engineered Graphene Oxide as High Performance Cathode Materials for Li-Ion Batteries. *Carbon.* **2014**, *76*, 148–154.

(11) Nokami, T.; Matsuo, T.; Inatomi, Y.; Hojo, N.; Tsukagoshi, T.; Yoshizawa, H.; Shimizu, A.; Kuramoto, H.; Komae, K.; Tsuyama, H.; Yoshida, J. I. Polymer-Bound Pyrene-4,5,9,10-Tetraone for Fast-Charge and -Discharge Lithium-Ion Batteries with High Capacity. *J. Am. Chem. Soc.* **2012**, *134* (48), 19694–19700.

(12) Shi, Y.; Peng, L.; Ding, Y.; Zhao, Y.; Yu, G. Nanostructured Conductive Polymers for Advanced Energy Storage. *Chem. Soc. Rev.* **2015**, *44* (19), 6684–6696.

(13) Zhu, L. M.; Lei, A. W.; Cao, Y. L.; Ai, X. P.; Yang, H. X. An All-Organic Rechargeable

Battery Using Bipolar Polyparaphenylene as a Redox-Active Cathode and Anode. *Chem. Commun.* **2013**, *49* (6), 567–569.

(14) Yang, L.; Wang, S.; Mao, J.; Deng, J.; Gao, Q.; Tang, Y.; Schmidt, O. G. Hierarchical MoS_2/Polyaniline Nanowires with Excellent Electrochemical Performance for Lithium-Ion Batteries. *Adv. Mater.* **2013**, *25* (8), 1180–1184.

(15) Zhang, Z. J.; Wang, J. Z.; Chou, S. L.; Liu, H. K.; Ozawa, K.; Li, H. J. Polypyrrole-Coated $LiFeO_2$ Nanocomposite with Enhancedelectrochemical Properties for Lithium-Ion Batteries. *Electrochim. Acta* **2013**, *108*, 820–826.

(16) Lyu, H.; Liu, J.; Mahurin, S.; Dai, S.; Guo, Z.; Sun, X. G. Polythiophene Coated Aromatic Polyimide Enabled Ultrafast and Sustainable Lithium-Ion Batteries. *J. Mater. Chem. A* **2017**, *5* (46), 24083–24090.

(17) Naegele, D.; Bittihn, R. Electrically Conductive Polymers as Rechargeable Battery Electrodes. *Solid State Ionics* **1988**, *28–30* (PART 2), 983–989.

(18) Kaneto, K.; Yoshino, K.; Inuishi, Y. Characteristics of Polythiophene Battery. *Japanese J. Appl. Physics, Part 2 Lett.* **1983**, *22* (9), 567–568.

(19) Sotomura, T.; Tatsuma, T.; Oyama, N. An Organosulfur Polymer Cathode with a High Current Capability for Rechargeable Batteries. *J. Electrochem. Soc.* **1996**, *143* (10), 3152–3157.

(20) Visco, S. J.; DeJonghe, L. C. Ionic Conductivity of Organosulfur Melts for Advanced Storage Electrodes. *J. Electrochem. Soc.* **1988**, *135* (12), 2905.

(21) Deng, S.-R.; Kong, L.-B.; Hu, G.-Q.; Wu, T.; Li, D.; Zhou, Y.-H.; Li, Z.-Y. Benzene-Based Polyorganodisulfide Cathode Materials for Secondary Lithium Batteries. *Electrochim. Acta* **2006**, *51*, 2589–2593.

(22) Wang, D. Y.; Guo, W.; Fu, Y. Organosulfides: An Emerging Class of Cathode Materials for Rechargeable Lithium Batteries. *Acc. Chem. Res.* **2019**, *52* (8), 2290–2300.

(23) Nishide, H.; Suga, T. Organic Radical Battery. *Electrochem. Soc. "Interface"* **2005**, *14* (4), 32–36.

(24) Oyaizu, K.; Nishide, H. Radical Polymers for Organic Electronic Devices: A Radical Departure from Conjugated Polymers? *Adv. Mater.* **2009**, *21* (22), 2339–2344.

(25) Janoschka, T.; Hager, M. D.; Schubert, U. S. Powering up the Future: Radical Polymers for Battery Applications. *Adv. Mater.* **2012**, *24* (48), 6397–6409.

(26) Wei, X.; Duan, W.; Huang, J.; Zhang, L.; Li, B.; Reed, D.; Xu, W.; Sprenkle, V.; Wang, W. A High-Current, Stable Nonaqueous Organic Redox Flow Battery. *ACS Energy Lett.* **2016**, *1* (4), 705–711.

(27) Nakahara, K.; Iwasa, S.; Satoh, M.; Morioka, Y.; Iriyama, J.; Suguro, M.; Hasegawa, E. Rechargeable Batteries with Organic Radical Cathodes. *Chem. Phys. Lett.* **2002**, *359* (5–6), 351–354.

(28) Peng, H.; Yu, Q.; Wang, S.; Kim, J.; Rowan, A. E.; Nanjundan, A. K.; Yamauchi, Y.; Yu, J. Molecular Design Strategies for Electrochemical Behavior of Aromatic Carbonyl Compounds in Organic and Aqueous Electrolytes. *Adv. Sci.* **2019**, *6* (17).

(29) Lv, M.; Zhang, F.; Wu, Y.; Chen, M.; Yao, C.; Nan, J.; Shu, D.; Zeng, R.; Zeng, H.; Chou, S. L. Heteroaromatic Organic Compound with Conjugated Multi-Carbonyl as Cathode Material for Rechargeable Lithium Batteries. *Sci. Rep.* **2016**, *6* (1), 1–8.

(30) Liang, Y.; Zhang, P.; Chen, J. Function-Oriented Design of Conjugated Carbonyl Compound Electrodes for High Energy Lithium Batteries. *Chem. Sci.* **2013**, *4* (3), 1330–1337.

(31) Wu, H. P.; Yang, Q.; Meng, Q. H.; Ahmad, A.; Zhang, M.; Zhu, L. Y.; Liu, Y. G.; Wei, Z. X. A Polyimide Derivative Containing Different Carbonyl Groups for Flexible Lithium-Ion Batteries. *J. Mater. Chem. A* **2016**, *4* (6), 2115–2121.

(32) Song, Z.; Qian, Y.; Zhang, T.; Otani, M.; Zhou, H. Poly(Benzoquinonyl Sulfide) as a High-Energy Organic Cathode for Rechargeable Li and Na Batteries. *Adv. Sci.* **2015**, *2* (9), 1–9.

(33) Wang, J.; Chen, C. S.; Zhang, Y. Hexaazatrinaphthylene-Based Porous Organic Polymers as Organic Cathode Materials for Lithium-Ion Batteries. *ACS Sustain. Chem. Eng.* **2018**, *6* (2), 1772–1779.

(34) Hanyu, Y.; Honma, I. Rechargeable Quasi-Solid State Lithium Battery with Organic Crystalline Cathode. *Sci. Rep.* **2012**, *2* (1), 1–6.

(35) Luo, C.; Ji, X.; Hou, S.; Eidson, N.; Fan, X.; Liang, Y.; Deng, T.; Jiang, J.; Wang, C. Azo Compounds Derived from Electrochemical Reduction of Nitro Compounds for High-Performance Li-Ion Batteries. *Adv. Mater.* **2018**, *30* (23), 1706498.

(36) Luo, C.; Borodin, O.; Ji, X.; Hou, S.; Gaskell, K. J.; Fan, X.; Chen, J.; Deng, T.; Wang, R.; Jiang, J.; Wang, C. Azo Compounds as a Family of Organic Electrode Materials for Alkali-Ion Batteries. *Proc. Natl. Acad. Sci.* **2018**, *115* (9), 2004–2009.

(37) Zhao, G.; Zhang, Y.; Gao, Z.; Li, H.; Liu, S.; Cai, S.; Yang, X.; Guo, H.; Sun, X. Dual Active Site of the Azo and Carbonyl-Modified Covalent Organic Framework for High-Performance Li Storage. *ACS Energy Lett.* **2020**, *5* (4), 1022–1031.

(38) Lu, Y.; Hou, X.; Miao, L.; Li, L.; Shi, R.; Liu, L.; Chen, J. Cyclohexanehexone with Ultrahigh Capacity as Cathode Materials for Lithium-Ion Batteries. *Angew. Chem. Int.*

Ed. **2019**, *58* (21), 7020–7024.

(39) Matsunaga, T.; Kubota, T.; Sugimoto, T.; Satoh, M. High-Performance Lithium Secondary Batteries Using Cathode Active Materials of Triquinoxalinylenes Exhibiting Six Electron Migration. *Chem. Lett.* **2011**, *40* (7), 750–752.

(40) Häupler, B.; Wild, A.; Schubert, U. S. Carbonyls: Powerful Organic Materials for Secondary Batteries. *Adv. Energy Mater.* **2015**, *5* (11), 1402034.

(41) Nokami, T.; Matsuo, T.; Inatomi, Y.; Hojo, N.; Tsukagoshi, T.; Yoshizawa, H.; Shimizu, A.; Kuramoto, H.; Komae, K.; Tsuyama, H.; Yoshida, J. I. Polymer-Bound Pyrene-4,5,9,10-Tetraone for Fast-Charge and -Discharge Lithium-Ion Batteries with High Capacity. *J. Am. Chem. Soc.* **2012**, *134* (48), 19694–19700.

(42) Muench, S.; Wild, A.; Friebe, C.; Häupler, B.; Janoschka, T.; Schubert, U. S. Polymer-Based Organic Batteries. *Chem. Rev.* **2016**, *116* (16), 9438–9484.

(43) Song, Z.; Zhou, H. Towards Sustainable and Versatile Energy Storage Devices: An Overview of Organic Electrode Materials. *Energy Environ. Sci.* **2013**, *6* (8), 2280–2301.

(44) Cai, Y.; Huang, Y.; Wang, X.; Jia, D.; Pang, W.; Guo, Z.; Du, Y.; Tang, X. Facile Synthesis of LiMn2O4 Octahedral Nanoparticles as Cathode Materials for High Capacity Lithium-Ion Batteries with Long Cycle Life. *J. Power Sources* **2015**, *278*, 574–581.

(45) Huang, X.; Yao, Y.; Liang, F.; Dai, Y. Concentration-Controlled Morphology of $LiFePO_4$ Crystals with an Exposed (100) Facet and Their Enhanced Performance for Use in Lithium-Ion Batteries. *J. Alloys Compd.* **2018**, *743*, 763–772.

(46) Cho, J.; Kim, Y. J.; Park, B. Novel $LiCoO_2$ Cathode Material with Al_2O_3 Coating for a Li-Ion Cell. *Chem. Mater.* **2000**, *12* (12), 3788–3791.

(47) Ju, S. H.; Kang, I.; Lee, Y.; Shin, W.; Kim, S.; Shin, K.; Kim, D. Improvement of the Cycling Performance of $LiNi_{0.6}Co_{0.2}Mn_{0.2}O_2$ Cathode Active Materials by a Dual-Conductive Polymer Coating Seo. *ACS Appl. Mater. Interfaces* **2014**, *6* (2014), 2546−2552.

(48) Lu, C.; Yang, S.; Wu, H.; Zhang, Y.; Yang, X.; Liang, T. Enhanced Electrochemical Performance of Li-Rich Vanadium Doping. *Electrochim. Acta* **2016**, *209*, 448–455.

(49) Zhang, J.; Cheng, F.; Chou, S.; Wang, J.; Gu, L.; Wang, H.; Yoshikawa, H.; Lu, Y.; Chen, J. Tuning Oxygen Redox Chemistry in Li-Rich Mn-Based Layered Oxide Cathodes by Modulating Cation Arrangement. *Adv. Mater.* **2019**, *31* (42), 1–7.

(50) Lee, S.; Kwon, J. E.; Hong, J.; Park, S. Y.; Kang, K. The Role of Substituents in Determining the Redox Potential of Organic Electrode Materials in Li and Na

Rechargeable Batteries: Electronic Effects: Vs. Substituent-Li/Na Ionic Interaction. *J. Mater. Chem. A* **2019**, *7* (18), 11438–11443.

(51) Bhosale, M. E.; Chae, S.; Kim, J. M.; Choi, J. Y. Organic Small Molecules and Polymers as an Electrode Material for Rechargeable Lithium-Ion Batteries. *Journal of Materials Chemistry A.* 2018, pp 19885–19911.

(52) Yang, J.; Shi, Y.; Sun, P.; Xiong, P.; Xu, Y. Optimization of Molecular Structure and Electrode Architecture of Anthraquinone-Containing Polymer Cathode for High-Performance Lithium-Ion Batteries. *ACS Appl. Mater. Interfaces* **2019**, *11* (45), 42305–42312.

(53) Luo, Z.; Liu, L.; Ning, J.; Lei, K.; Lu, Y.; Li, F.; Chen, J. A Microporous Covalent–Organic Framework with Abundant Accessible Carbonyl Groups for Lithium-Ion Batteries. *Angew. Chem. Int. Ed.* **2018**, *57* (30), 9443–9446.

(54) Wang, G.; Chandrasekhar, N.; Biswal, B. P.; Becker, D.; Paasch, S.; Brunner, E.; Addicoat, M.; Yu, M.; Berger, R.; Feng, X. A Crystalline, 2D Polyarylimide Cathode for Ultrastable and Ultrafast Li Storage. *Adv. Mater.* **2019**, *31* (28), 1901478.

(55) Song, Z.; Xu, T.; Gordin, M. L.; Jiang, Y. B.; Bae, I. T.; Xiao, Q.; Zhan, H.; Liu, J.; Wang, D. Polymer-Graphene Nanocomposites as Ultrafast-Charge and -Discharge Cathodes for Rechargeable Lithium Batteries. *Nano Lett.* **2012**, *12* (5), 2205–2211.

(56) Iordache, A.; Delhorbe, V.; Bardet, M.; Dubois, L.; Gutel, T.; Picard, L. Perylene-Based All-Organic Redox Battery with Excellent Cycling Stability. *ACS Appl. Mater. Interfaces* **2016**, *8* (35), 22762–22767.

(57) Xie, J.; Chen, W.; Long, G.; Gao, W.; Xu, Z. J.; Liu, M.; Zhang, Q. Boosting the Performance of Organic Cathodes through Structure Tuning. *J. Mater. Chem. A* **2018**, *6* (27), 12985–12991.

(58) Lyu, Y.; Wu, X.; Wang, K.; Feng, Z.; Cheng, T.; Liu, Y.; Wang, M.; Chen, R.; Xu, L.; Zhou, J.; Lu, Y.; Guo, B. An Overview on the Advances of $LiCoO_2$ Cathodes for Lithium-Ion Batteries. *Adv. Energy Mater.* **2021**, *11* (2), 2000982.

(59) Sun, J.; Klechikov, A.; Moise, C.; Prodana, M.; Enachescu, M.; Talyzin, A. V. A Molecular Pillar Approach To Grow Vertical Covalent Organic Framework Nanosheets on Graphene: Hybrid Materials for Energy Storage. *Angew. Chem. Int. Ed.* **2018**, *57* (4), 1034–1038.

(60) Rogers, J. A.; Someya, T.; Huang, Y. Materials and Mechanics for Stretchable Electronics. *Science.* **2010**, *327* (5973), 1603–1607.

(61) Koo, M.; Park, K. Il; Lee, S. H.; Suh, M.; Jeon, D. Y.; Choi, J. W.; Kang, K.; Lee, K. J.

Bendable Inorganic Thin-Film Battery for Fully Flexible Electronic Systems. *Nano Lett.* **2012**, *12* (9), 4810–4816.

(62) Tian, B.; Ning, G.-H.; Tang, W.; Peng, C.; Yu, D.; Chen, Z.; Xiao, Y.; Su, C.; Loh, K. P. Polyquinoneimines for Lithium Storage: More than the Sum of Its Parts. *Mater. Horiz.* **2016**, *3* (5), 429–433.

(63) Song, Z.; Zhan, H.; Zhou, Y. Anthraquinone Based Polymer as High-Performance Cathode Material for Rechargeable Lithium Batteries. *Chem. Commun.* **2009**, 4, 448–450.

(64) Sharma, P.; Damien, D.; Nagarajan, K.; Shaijumon, M. M.; Hariharan, M. Perylene-Polyimide-Based Organic Electrode Materials for Rechargeable Lithium Batteries. *J. Phys. Chem. Lett.* **2013**, *4* (19), 3192–3197.

(65) Ockwig, N. W.; Co, A. P.; Keeffe, M. O.; Matzger, A. J.; Yaghi, O. M. Porous, Crystalline, Covalent Organic Frameworks. *Science.* **2005**, *310*, 1166–1171.

(66) Wan, S.; Guo, J.; Kim, J.; Ihee, H.; Jiang, D. A Belt-Shaped, Blue Luminescent, and Semiconducting Covalent Organic Framework. *Angew. Chem. Int. Ed.* **2008**, *47* (46), 8826 –8830.

(67) Lohse, M. S.; Rotter, J. M.; Margraf, J. T.; Werner, V.; Becker, M.; Herbert, S.; Knochel, P.; Clark, T.; Bein, T.; Medina, D. D. From Benzodithiophene to Diethoxy-Benzodithiophene Covalent Organic Frameworks-Structural Investigations. *CrystEngComm* **2016**, *18* (23), 4295–4302.

(68) Hunt, J. R.; Doonan, C. J.; LeVangie, J. D.; Côté, A. P.; Yaghi, O. M. Reticular Synthesis of Covalent Organic Borosilicate Frameworks. *J. Am. Chem. Soc.* **2008**, *130* (36), 11872–11873.

(69) Kuhn, P.; Antonietti, M.; Thomas, A. Porous, Covalent Triazine-Based Frameworks Prepared by Ionothermal Synthesis. *Angew. Chem. Int. Ed.* **2008**, *47* (18), 3450–3453.

(70) Uribe-Romo, F. J.; Hunt, J. R.; Furukawa, H.; Klöck, C.; O'Keeffe, M.; Yaghi, O. M. A Crystalline Imine-Linked 3-D Porous Covalent Organic Framework. *J. Am. Chem. Soc.* **2009**, *131* (13), 4570–4571.

(71) Chen, X.; Addicoat, M.; Irle, S.; Nagai, A.; Jiang, D. Control of Crystallinity and Porosity of Covalent Organic Frameworks by Managing Interlayer Interactions Based on Self-Complementary π-Electronic Force. *J. Am. Chem. Soc.* **2013**, *135* (2), 546–549.

(72) Song, J. R.; Sun, J.; Liu, J.; Huang, Z. T.; Zheng, Q. Y. Thermally/Hydrolytically Stable Covalent Organic Frameworks from a Rigid Macrocyclic Host. *Chem. Commun.* **2014**, *50* (7), 788–791.

(73) Uribe-Romo, F. J.; Doonan, C. J.; Furukawa, H.; Oisaki, K.; Yaghi, O. M. Crystalline Covalent Organic Frameworks with Hydrazone Linkages. *J. Am. Chem. Soc.* **2011**, *133* (30), 11478–11481.

(74) Jackson, K. T.; Reich, T. E.; El-Kaderi, H. M. Targeted Synthesis of a Porous Borazine-Linked Covalent Organic Framework. *Chem. Commun* **2012**, *48*, 8823–8825.

(75) Nagai, A.; Chen, X.; Feng, X.; Ding, X.; Guo, Z.; Jiang, D. A Squaraine-Linked Mesoporous Covalent Organic Framework. *Angew. Chem. Int. Ed.* **2013**, *52* (13), 3770–3774.

(76) Dalapati, S.; Jin, S.; Gao, J.; Xu, Y.; Nagai, A.; Jiang, D. An Azine-Linked Covalent Organic Framework. *J. Am. Chem. Soc.* **2013**, *135* (46), 17310–17313.

(77) Guo, J.; Xu, Y.; Jin, S.; Chen, L.; Kaji, T.; Honsho, Y.; Addicoat, M. A.; Kim, J.; Saeki, A.; Ihee, H.; Seki, S.; Irle, S.; Hiramoto, M.; Gao, J.; Jiang, D. Conjugated Organic Framework with Three-Dimensionally Ordered Stable Structure and Delocalized π Clouds. *Nat. Commun.* **2013**, *4* (1), 2736.

(78) Fang, Q.; Zhuang, Z.; Gu, S.; Kaspar, R. B.; Zheng, J.; Wang, J.; Qiu, S.; Yan, Y. Designed Synthesis of Large-Pore Crystalline Polyimide Covalent Organic Frameworks. *Nat. Commun.* **2014**, *5*, 4503.

(79) Chen, X.; Addicoat, M.; Jin, E.; Xu, H.; Hayashi, T.; Xu, F.; Huang, N.; Irle, S.; Jiang, D. Designed Synthesis of Double-Stage Two-Dimensional Covalent Organic Frameworks. *Sci. Rep.* **2015**, *5*, 14650.

(80) Zeng, Y.; Zou, R.; Luo, Z.; Zhang, H.; Yao, X.; Ma, X.; Zou, R.; Zhao, Y. Covalent Organic Frameworks Formed with Two Types of Covalent Bonds Based on Orthogonal Reactions. *J. Am. Chem. Soc.* **2015**, *137* (3), 1020–1023.

(81) Du, Y.; Yang, H.; Whiteley, J. M.; Wan, S.; Jin, Y.; Lee, S. H.; Zhang, W. Ionic Covalent Organic Frameworks with Spiroborate Linkage. *Angew. Chem. Int. Ed.* **2016**, *55* (5), 1737–1741.

(82) Bi, S.; Yang, C.; Zhang, W.; Xu, J.; Liu, L.; Wu, D.; Wang, X.; Han, Y.; Liang, Q.; Zhang, F. Two-Dimensional Semiconducting Covalent Organic Frameworks via Condensation at Arylmethyl Carbon Atoms. *Nat. Commun.* **2019**, *10* (1), 2467.

(83) Jin, E.; Asada, M.; Xu, Q.; Dalapati, S.; Addicoat, M. A.; Brady, M. A.; Xu, H.; Nakamura, T.; Heine, T.; Chen, Q.; Jiang, D. Supplementary Materials for Two-Dimensional Sp^2 Carbon-Conjugated Covalent Organic Frameworks. *Science.* **2017**, *357* (6352), 673.

(84) Zhuang, X.; Zhao, W.; Zhang, F.; Cao, Y.; Liu, F.; Bi, S.; Feng, X. A Two-Dimensional

Conjugated Polymer Framework with Fully Sp^2-Bonded Carbon Skeleton. *Polym. Chem.* **2016**, *7* (25), 4176–4181.

(85) Lyu, H.; Diercks, C. S.; Zhu, C.; Yaghi, O. M. Porous Crystalline Olefin-Linked Covalent Organic Frameworks. *J. Am. Chem. Soc.* **2019**, *141* (17), 6848–6852.

(86) Waller, P. J.; Lyle, S. J.; Osborn Popp, T. M.; Diercks, C. S.; Reimer, J. A.; Yaghi, O. M. Chemical Conversion of Linkages in Covalent Organic Frameworks. *J. Am. Chem. Soc.* **2016**, *138* (48), 15519–15522.

(87) Das, G.; Skorjanc, T.; Sharma, S. K.; Gándara, F.; Lusi, M.; Shankar Rao, D. S.; Vimala, S.; Krishna Prasad, S.; Raya, J.; Han, D. S.; Jagannathan, R.; Olsen, J. C.; Trabolsi, A. Viologen-Based Conjugated Covalent Organic Networks via Zincke Reaction. *J. Am. Chem. Soc.* **2017**, *139* (28), 9558–9565.

(88) Yahiaoui, O.; Fitch, A. N.; Hoffmann, F.; Fröba, M.; Thomas, A.; Roeser, J. 3D Anionic Silicate Covalent Organic Framework with Srs Topology. *J. Am. Chem. Soc.* **2018**, *140* (16), 5330–5333.

(89) Zhao, C.; Diercks, C. S.; Zhu, C.; Hanikel, N.; Pei, X.; Yaghi, O. M. Urea-Linked Covalent Organic Frameworks. *J. Am. Chem. Soc.* **2018**, *140* (48), 16438–16441.

(90) Guan, X.; Li, H.; Ma, Y.; Xue, M.; Fang, Q.; Yan, Y.; Valtchev, V.; Qiu, S. Chemically Stable Polyarylether-Based Covalent Organic Frameworks. *Nat. Chem.* **2019**, *11* (6), 587–594.

(91) Zhang, B.; Wei, M.; Mao, H.; Pei, X.; Alshmimri, S. A.; Reimer, J. A.; Yaghi, O. M. Crystalline Dioxin-Linked Covalent Organic Frameworks from Irreversible Reactions. *J. Am. Chem. Soc.* **2018**, *140* (40), 12715–12719.

(92) Geng, K.; He, T.; Liu, R.; Dalapati, S.; Tan, K. T.; Li, Z.; Tao, S.; Gong, Y.; Jiang, Q.; Jiang, D. Covalent Organic Frameworks: Design, Synthesis, and Functions. *Chem. Rev.* **2020**, *120*(16), 8814-8933.

(93) El-Kaderi, H. M.; Hunt, J. R.; Mendoza-Cortés, J. L.; Côté, A. P.; Taylor, R. E.; O'Keeffe, M.; Yaghi, O. M. Designed Synthesis of 3D Covalent Organic Frameworks. *Science.* **2007**, *316* (5822), 268–272.

(94) Huang, N.; Zhai, L.; Coupry, D. E.; Addicoat, M. A.; Okushita, K.; Nishimura, K.; Heine, T.; Jiang, D. Multiple-Component Covalent Organic Frameworks. *Nat. Commun.* **2016**, *7*, 12325.

(95) Ding, S. Y.; Gao, J.; Wang, Q.; Zhang, Y.; Song, W. G.; Su, C. Y.; Wang, W. Construction of Covalent Organic Framework for Catalysis: Pd/COF-LZU1 in Suzuki-Miyaura Coupling Reaction. *J. Am. Chem. Soc.* **2011**, *133* (49), 19816–19822.

(96) Kandambeth, S.; Mallick, A.; Lukose, B.; Mane, M. V.; Heine, T.; Banerjee, R. Construction of Crystalline 2D Covalent Organic Frameworks with Remarkable Chemical (Acid/Base) Stability via a Combined Reversible and Irreversible Route. *J. Am. Chem. Soc.* **2012**, *134* (48), 19524–19527.

(97) Wang, Z.; Li, Y.; Liu, P.; Qi, Q.; Zhang, F.; Lu, G.; Zhao, X.; Huang, X. Few Layer Covalent Organic Frameworks with Graphene Sheets as Cathode Materials for Lithium-Ion Batteries. *Nanoscale* **2019**, *11* (12), 5330–5335.

(98) Xu, S.; Wang, G.; Biswal, B. P.; Addicoat, M.; Paasch, S.; Sheng, W.; Zhuang, X.; Brunner, E.; Heine, T.; Berger, R.; Feng, X. A Nitrogen-Rich 2D Sp^2 -Carbon-Linked Conjugated Polymer Framework as a High-Performance Cathode for Lithium-Ion Batteries. *Angew. Chem. Int. Ed.* **2019**, *58* (3), 849–853.

(99) Papageorgiou, D. G.; Kinloch, I. A.; Young, R. J. Graphene/Elastomer Nanocomposites. *Carbon.* **2015**, *95*, 460–484.

(100) Mohan, V. B.; Brown, R.; Jayaraman, K.; Bhattacharyya, D. Characterisation of Reduced Graphene Oxide: Effects of Reduction Variables on Electrical Conductivity. *Mater. Sci. Eng. B Solid-State Mater. Adv. Technol.* **2015**, *193* (C), 49–60.

(101) Holban, A. M.; Grumezescu, A. M.; Andronescu, E. *Inorganic Nanoarchitectonics Designed for Drug Delivery and Anti-Infective Surfaces*; Elsevier Inc., 2016.

(102) Meguid, S. A.; Weng, G. J. *Micromechanics and Nanomechanics of Composite Solids*; Springer, 2017.

(103) Wang, S.; Wang, Q.; Shao, P.; Han, Y.; Gao, X.; Ma, L.; Yuan, S.; Ma, X.; Zhou, J.; Feng, X.; Wang, B. Exfoliation of Covalent Organic Frameworks into Few-Layer Redox-Active Nanosheets as Cathode Materials for Lithium-Ion Batteries. *J. Am. Chem. Soc.* **2017**, *139* (12), 4258–4261.

(104) Carole A Coopera, Diana Ravicha, David Lipsb, Joerg Mayerb, H. D. W. Distribution and Alignment of Carbon Nanotubes and Nanofibrils. *Compos. Sci. Technol.* **2002**, *62*, 1105–1112.

(105) Yoo, H. J.; Jung, Y. C.; Sahoo, N. G.; Cho, J. W. Polyurethane-Carbon Nanotube Nanocomposites Prepared by in-Situ Polymerization with Electroactive Shape Memory. *J. Macromol. Sci. Part B Phys.* **2006**, *45 B* (4), 441–451.

(106) Ohzuku, T.; Wakamatsu, H.; Takehara, Z.; Yoshizawa, S. Nonaqueous Lithium/Pyromellitic Dianhydride Cell. *Electrochim. Acta* **1979**, *24* (6), 723–726.

(107) Boschi, T.; Pappa, R.; Pistoia, G.; Tocci, M. On the Use of Nonylbenzo-Hexaquinone as a Substitute for Monomeric Quinones in Non-Aqueous Cells. *J. Electroanal. Chem.*

1984, *176* (1–2), 235–242.

(108) Tobishima, S.; Yamaki, J.; Yamaji, A. Cathode Characteristics of Organic Electron Acceptors for Lithium Batteries. *J. Electrochem. Soc.* **1984**, *131* (1), 57–63.

(109) Pasquali, M.; Pistoia, G.; Boschi, T.; Tagliatesta, P. Redox Mechanism and Cycling Behaviour of Nonylbenzo-Hexaquinone Electrodes in Li Cells. *Solid State Ionics* **1987**, *23* (4), 261–266.

(110) Funt, B. L.; Hoang, P. M. Voltammetric Response of Solutions of Electroactive Polymers. *J. Electrochem. Soc.* **1984**, *131* (10), 2295.

(111) Foos, J. S.; Erker, S. M.; Rembetsy, L. M. Synthesis and Characterization of Semiconductive Poly-1,4-Dimethoxybenzene and Its Derived Polyquinone. *J. Electrochem. Soc.* **1986**, *133* (4), 836–841.

(112) Bailey, S. I.; Ritchie, I. M.; Searcy, N.; Singh, P. Preparation and Characterization of Surface Modified Electrodes from Hydroxyanthraquinones. *J. Appl. Electrochem.* **1988**, *18* (3), 368–373.

(113) Foos, J. S. Synthesis and Characterization of Semiconductive Poly-1,4-Dimethoxybenzene and Its Derived Polyquinone. *J. Electrochem. Soc.* **1986**, *133* (4), 836.

(114) Song, Z.; Zhan, H.; Zhou, Y. Anthraquinone Based Polymer as High Performance Cathode Material for Rechargeable Lithium Batteries. *Chem. Commun.* **2009**, 4, 448–450.

(115) Xu, W.; Read, A.; Koech, P. K.; Hu, D.; Wang, C.; Xiao, J.; Padmaperuma, A. B.; Graff, G. L.; Liu, J.; Zhang, J. G. Factors Affecting the Battery Performance of Anthraquinone-Based Organic Cathode Materials. *J. Mater. Chem.* **2012**, *22* (9), 4032–4039.

(116) Li, J.; Jing, X.; Li, Q.; Li, S.; Gao, X.; Feng, X.; Wang, B. Bulk COFs and COF Nanosheets for Electrochemical Energy Storage and Conversion. *Chem. Soc. Rev.* **2020**, *49* (11), 3565–3604.

(117) Sun, T.; Xie, J.; Guo, W.; Li, D. S.; Zhang, Q. Covalent–Organic Frameworks: Advanced Organic Electrode Materials for Rechargeable Batteries. *Adv. Energy Mater.* **2020**, *10* (19), 1904199.

(118) Wang, S.; Wang, Q.; Shao, P.; Han, Y.; Gao, X.; Ma, L.; Yuan, S.; Ma, X.; Zhou, J.; Feng, X.; Wang, B. Exfoliation of Covalent Organic Frameworks into Few-Layer Redox-Active Nanosheets as Cathode Materials for Lithium-Ion Batteries. *J. Am. Chem. Soc.* **2017**, *139* (12), 32.

(119) Li, Q.; Wang, H.; Wang, H. guo; Si, Z.; Li, C.; Bai, J. A Self-Polymerized Nitro-

Substituted Conjugated Carbonyl Compound as High-Performance Cathode for Lithium-Organic Batteries. *ChemSusChem* **2020**, *13* (9), 2449–2456.

(120) Yao, C. J.; Wu, Z.; Xie, J.; Yu, F.; Guo, W.; Xu, Z. J.; Li, D. S.; Zhang, S.; Zhang, Q. Two-Dimensional (2D) Covalent Organic Framework as Efficient Cathode for Binder-Free Lithium-Ion Battery. *ChemSusChem* **2020**, *13* (9), 2457–2463.

(121) Molina, A.; Patil, N.; Ventosa, E.; Liras, M.; Palma, J.; Marcilla, R. New Anthraquinone-Based Conjugated Microporous Polymer Cathode with Ultrahigh Specific Surface Area for High-Performance Lithium-Ion Batteries. *Adv. Funct. Mater.* **2020**, *30* (6), 1908074.

(122) Song, Z.; Zhan, H.; Zhou, Y. Polyimides: Promising Energy-Storage Materials. *Angew. Chem.* **2010**, *122* (45), 8622–8626.

(123) Xu, F.; Jin, S.; Zhong, H.; Wu, D.; Yang, X.; Chen, X.; Wei, H.; Fu, R.; Jiang, D. Electrochemically Active, Crystalline, Mesoporous Covalent Organic Frameworks on Carbon Nanotubes for Synergistic Lithium-Ion Battery Energy Storage. *Sci. Rep.* **2015**, *5* (1), 8225.

(124) Wang, G.; Chandrasekhar, N.; Biswal, B. P.; Becker, D.; Paasch, S.; Brunner, E.; Addicoat, M.; Yu, M.; Berger, R.; Feng, X. A Crystalline, 2D Polyarylimide Cathode for Ultrastable and Ultrafast Li Storage. *Adv. Mater.* **2019**, *31* (28), 1901478.

(125) Yang, D.; Yao, Z.; Wu, D.; Zhang, Y. Structure-Modulated Crystalline Covalent Organic Frameworks for High-Rate Li-Ion Batteries. *Journal Mater. Chem. A* **2016**, *4* (47), 18621–18627.

(126) Luo, Z.; Liu, L.; Ning, J.; Lei, K.; Lu, Y.; Li, F.; Chen, J. A Microporous Covalent-Organic Framework with Abundant Accessible Carbonyl Groups for Lithium-Ion Batteries. *Angew. Chem. Int. Ed.* **2018**, *57* (30), 9443–9446.

(127) Zu, Y.; Xu, Y.; Ma, L.; Kang, Q.; Yao, H.; Hou, J. Carbonyl Bridge-Based P−π Conjugated Polymers as High-Performance Electrodes of Organic Lithium-Ion Batteries. *ACS Appl. Mater. Interfaces* **2020**, *12* (16), 18457–18464.

(128) Mumyatov, A. V.; Shestakov, A. F.; Dremova, N. N.; Stevenson, K. J.; Troshin, P. A. New Naphthalene-Based Polyimide as an Environment-Friendly Organic Cathode Material for Lithium Batteries. *Energy Technol.* **2019**, *7* (5), 1801016.

(129) Xu, F.; Wang, H.; Wu, M.; Nan, J.; Li, T.; Cao, S. an. Electrochemical Properties of Poly(Anthraquinonyl Imide)s as High-Capacity Organic Cathode Materials for Li-Ion Batteries. *Mater. Chem. Phys.* **2018**, *214*, 120–125.

(130) Cariello, M.; Johnston, B.; Bhosale, M.; Amores, M.; Wilson, E.; McCarron, L. J.;

Wilson, C.; Corr, S. A.; Cooke, G. Benzo-Dipteridine Derivatives as Organic Cathodes for Li- And Na-Ion Batteries. *ACS Appl. Energy Mater.* **2020**, *3* (9), 8302–8308.

(131) Chen, S.; Jia, T.; Zhou, G.; Zhang, C.; Hou, Q.; Wang, Y.; Luo, S.; Shi, G.; Zeng, Y. A Cross-Linked Triphenylamine-Based Polymer Cathode Material with Dual Anion-Cation Reversible Insertion for Lithium Ion Battery. *J. Electrochem. Soc.* **2019**, *166* (12), A2543–A2548.

(132) Peng, H.; Wang, S.; Kim, M.; Kim, J.; Yamauchi, Y.; Yu, J.; Li, D. Highly Reversible Electrochemical Reaction of Insoluble 3D Nanoporous Polyquinoneimines with Stable Cycle and Rate Performance. *Energy Storage Mater.* **2020**, *25*, 313–323.

Chapter 2

Characterisation Methods

2.1 Introduction

In this chapter, the characterisation methods used to analyse the performance of the materials reported in this thesis are described, such as gas sorption, XRD, and TEM. Electrochemical measurements, including cyclic voltammetry (CV), galvanostatic charge/discharge, electrochemical impedance spectroscopy (EIS), are also introduced because of their importance in the characterisation of Li-ion batteries.

2.2 Electrochemical Measurements

2.2.1 Cyclic Voltammetry

A basic requirement of the electrodes in rechargeable Li-ion batteries is that must be able to undergo reversible electrochemical redox reactions. Cyclic voltammetry (CV) is the primary method used to study the redox properties of electrochemically active compounds[1] as it can investigate whether a compound is redox-active. CV can also be used to understand the reversibility of redox reactions, determine the redox potentials, which is a crucial value for the energy-storage systems, and probe reaction kinetics and diffusion properties. CV profiles are affected by a variety of parameters such as scan rate, temperature, electrolyte solutions, and materials utilised for the various electrode components. In a CV experiment, the applied potential (E) is swept at a fixed scan rate (v) and the resulting current (i) response is measured at the working electrode of interest (Figure 2-1a). The formal redox potential for a given simple process can usually be approximated, as $E_{1/2}$, from the average of the two peak potentials for the oxidation ($E_{p,a}$) and reduction ($E_{p,c}$) processes (where $E_{1/2} = (E_{p,a} + E_{p,c})/2$) (Figure 2-1).[2]

In the CV measurement, different kinds of behaviour can be observed from the current response, such as information about the chemical and electrochemical reversibility of redox processes. Chemical reversibility is used to denote whether or not the reduced species may undergo any subsequent reaction or it is completely returned to the reduced form on the reverse sweep. Generally, a chemically reversible reaction would have an oxidation and reduction peak in the CV (Figure 2-1b and 2-1c). For example, for a chemically irreversible oxidation reaction, the corresponding reduction reaction would not be observed in the CV (Figure 2-1d). For electrochemical reversibility (Figure 2-1b), it is featured with a 1:1 ratio of anodic and cathodic peak current ($i_{p,a}$ and $i_{p,c}$) and a defined peak split ΔE_p (the potential difference between the anodic and cathodic peak, $57/n$ mV (with n as the number of transferred electrons per reaction)).

This describes a relation to electron transfer kinetics such that a reversible system has fast kinetics with a low barrier to electron transfer (i.e. the rate constant for the electron transfer is greater than 0.020 cm/s).[2] A quasi-reversible electrochemical system (with good chemical reversibility) will return the reduced species to the oxidised species but requires a greater overpotential to do so (due to more sluggish kinetics). An electrochemically irreversible system describes a case with a large barrier so that large potentials are required (i.e. the rate constant for the electron transfer is less than 5.0×10^{-5} cm/s).

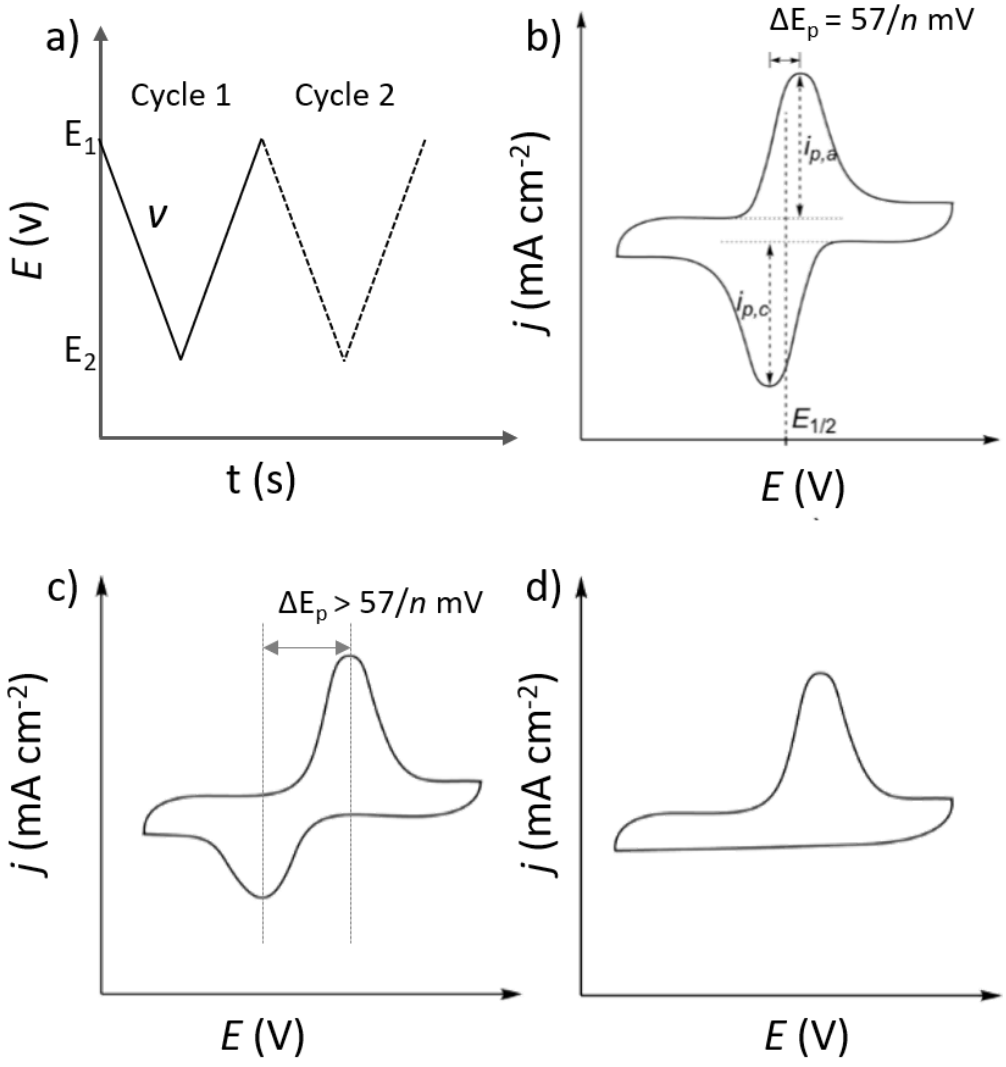

Figure 2-1. (a) CV waveform for the reduction of an electroactive species; Common types of CV curves: (b) electrochemically reversible, (c) quasi-reversible electrochemical system, and (d) chemical irreversible behaviour. Redrawn from reference [3].

Potential windows are chosen to enable the study of the electrochemical region of interest and selection of the upper and lower limits must be carefully considered to avoid irreversible oxidative and reductive decomposition reactions, respectively, of the various components including the electrode and electrolyte. Therefore, the requirements for the potential window should be large enough to allow the inclusion of most of the capacity of the device and be small enough to avoid undesirable irreversible redox processes to occur.

2.2.2 Electrochemical Kinetic Study

In CV measurements, the total current measured under a potential sweep rate can be expressed as the sum of the current related to the slow diffusion-controlled process (i_{diff}) and the current related to the fast surface-controlled process (i_{surf}) (Equation 2-1).[4] The current also obeys a power-law relationship with the sweep rate, which is given by Equation 2-2.

$$i = i_{surf} + i_{diff} = k_1 v + k_2 v^{1/2} \quad \text{(Equation 2-1)}$$

$$i = a v^b \quad \text{(Equation 2-2)}$$

$$lni = lna + blnv \quad \text{(Equation 2-3)}$$

where a and b are adjustable parameters, v is the scan rate, k_1 and k_2 are constants.[4–8] The b value can provide the kinetic information about the electrochemical reactions (Equation 2-2) and is determined from the slope of the linear plot of ln$i$ vs. ln$v$ (Equation 2-3). Generally, as shown in Figure 2-2, there are two well-defined conditions, b = 0.5 and b = 1. A b-value close to 0.5 indicates that the current is controlled by semi-infinite linear diffusion. By contrast, a b value close to 1 indicates that the current is surface-controlled. Therefore, the energy storage mechanism (surface-controlled or diffusion-controlled process) can be determined by establishing the relationship between the peak current response and the sweep rate to estimate the value of b.

The range of b values from 0.5 to 1.0 indicates a "transition" area; it means the electrochemical reaction contains a diffusion-controlled and surface-controlled process. Generally, the smaller the b value is, the larger the contribution from diffusion-controlled processes, while the surface-controlled process contribution increases with increasing the b value. It was found that the b value was strongly dependent on the potential, sweep rate, and charge storage mechanism, in addition to the material type. In Equation 2-1, the exact surface-controlled contribution ($k_1 v$)

and diffusion-controlled contribution ($k_2v^{1/2}$) can be further quantified, where k_1 and k_2 constants can be simulated by plotting $iv^{-1/2}$ *vs.* $v^{1/2}$, in which k_1 and k_2 are the slope and intercept of the linear fitting plot.

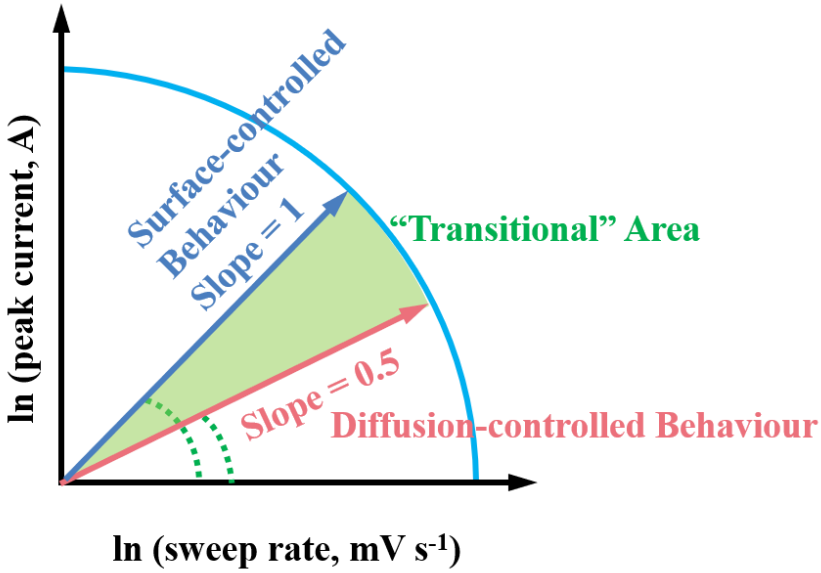

Figure 2-2. Power-law dependence of the peak current on sweep rate (from Equation 2-2 and Equation 2-3) for surface-controlled materials (b = 1.0) and typical diffusion-controlled materials (b = 0.5). The "transition" area between surface-controlled and diffusion-controlled materials area is located in the range of b = 0.5–1.0. Redrawn from reference [8].

2.2.3 Galvanostatic Charge/Discharge Cycling

Galvanostatic charge/discharge (GCD) is an essential measurement to evaluate the available specific capacity (mAh g^{-1}) of an electroactive material, as well as the cycling performance, rechargeability, and rate capability. In the GCD test, a constant current is applied to charge (positive current) or discharge (negative current) the cell to monitor the cell potential increasing (charging) or decreasing (discharging). The period of the measurement is determined by the applied current and the potential window that was chosen for the test. The GCD profile provides several types of useful information about the cell. First, the operational stability of the device can be implied by the shape of the GCD profile (Figure 2-3a). If the profile exhibits a single, distinct plateau, it implies a charge/discharge process that shows only negligible changes of the system until the redox-active material is almost fully reacted. Multiple plateaus indicate multiple redox reactions and lead to several operating voltages of the device. Furthermore, if

the charge/discharge profile is sloping, the respective redox system is significantly changing throughout the charge/discharge process impeding a constant operating voltage.[9,10]

On the GCD profile, the discharge potential of the cell (at a given applied current density) can be directly inferred from the plateau if there is a prominent plateau on the discharge profile. On the other hand, if the profile is a slope line, the discharge potential can be approximated from the average voltage value of the starting and finishing voltage of the slope. The theoretical voltage only depends on the redox systems used, the electrolyte, and the temperature, and it is usually close to the open-circuit voltage. However, the operating voltage can deviate from this due to internal-resistance losses and polarization effects, especially at high applied current, and this deviation is described as the overpotential required to drive the reaction in practical conditions (Figure 2-3b). Comparing the charge and discharge potential can provide further insight. Significant differences between the charge and discharge voltage can indicate strong polarization of the electrode during the charging/discharging process, or even result from different mechanisms (with differing energy barriers) for the charging and discharging steps.

From the applied current and the obtained loading time, the capacity of the cell (*i.e.*, the charge transferred during (dis)charge) can be determined, usually given in mAh. Considering the amount of active material leads to the specific capacity (in mAh g^{-1}), which is a key parameter for cell performance.[10] Comparison of the specific capacity to the theoretical specific capacity gives an evaluation of the electrochemical effectiveness of the compound (Figure 2-3d).

Temperature is also an important parameter in the GCD measurements. The internal resistance of the system increases at low temperatures, which leads to a decreased voltage resulting in a lower capacity and stored energy. At high temperatures, the chemical activities of the involved redox-active species increase, likely resulting in intensified self-discharge.[9,10] In this thesis, all the cell tests are carried out at 25 °C.

Cycle life is an important property of an energy-storage device. With the discussed experimental techniques available, the cycle life of a cell can be studied.[9] Cycle life is expressed by the development of the capacity and Coulombic efficiency over many charge/discharge cycles and is mainly determined by the reversibility of the electrochemical and related processes. The number of cycles is usually stated until 80% capacity retention of the initial capacity is achieved.[9] Apparently, this characteristic is important in the case of applications that involve lots of charging and discharging per time.

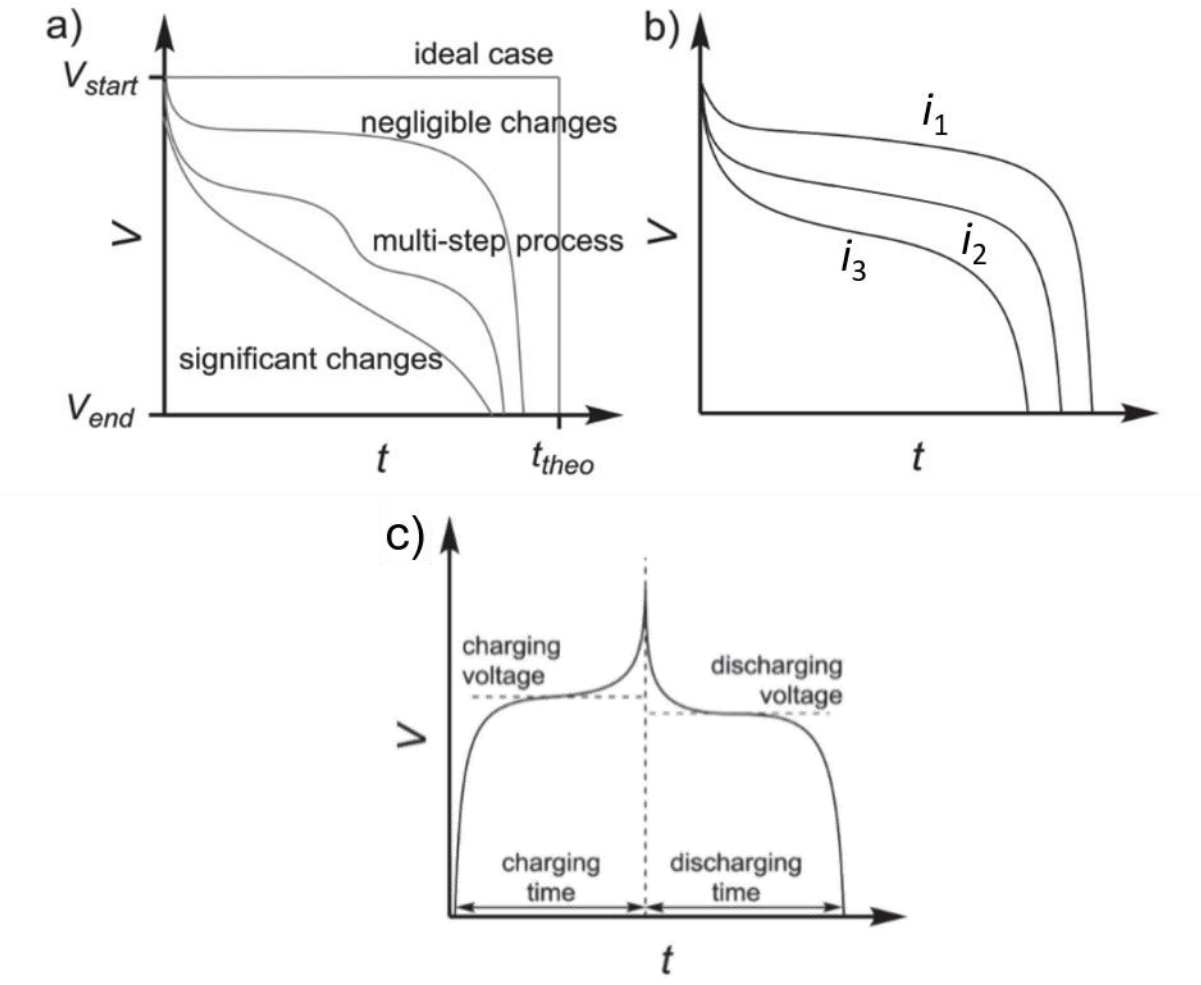

Figure 2-3. Typical voltage-time profile for a discharging process: (a) for different redox-system behaviour; (b) at different discharging currents ($i_3 > i_2 > i_1$), Typical charging/discharging curve. Reprinted with permission from reference 3. Copyright 2015 John Wiley & Sons.[3]

2.2.4 Electrochemical Impedance Spectroscopy

Electrochemical impedance spectroscopy (EIS) is a powerful tool to characterise the charge-transfer characteristics of an electrode and cell. EIS utilises a small amplitude, alternating signal (sinusoidal waveform) to probe the impedance characteristics of a cell, wherein the applied signal may be an alternating voltage or current with a fixed amplitude.[11] The signal is scanned over a wide range of frequencies to generate an impedance spectrum for the electrochemical cell under test. EIS measurements described in this thesis utilised the

application of a sinusoidal voltage perturbation, where the current response is measured to generate the frequency-dependent impedance characterisation.

The impedance spectrum is commonly displayed in the form of a Nyquist plot. A typical Nyquist profile is a plot of the imaginary part of impedance (*Im*(*Z*)) *vs.* the real part (Re(*Z*)) for different alternating current (AC) frequencies.

A resistor is the simplest electrical circuit. Resistors obey Ohm's law:

$$R = \frac{V}{I} \qquad \text{(Equation 2-4)}$$

Where R is the resistance, V is the voltage, I is the current. Therefore, for a resistor, the current is always proportional to the voltage. There is no reactive, like phase shift, so the resistance is not dependent on the frequency. Therefore, the impendence of a resistor (Z_R) can be written as:

$$Z_R = R \qquad \text{(Equation 2-5)}$$

The Nyquist plot for a resistor is a single point on the x-axis at any frequency (Figure 2-3a).

A capacitor has a purely reactive impedance and, ideally, zero resistance. The impedance of the capacitor (Z_C) is inversely proportional to the frequency when an alternating voltage is applied across a capacitor. It means the impedance increase with decreasing the frequency. The impedance of a capacitor can be described as:

$$Z_C = \frac{1}{j\omega C} \qquad \text{(Equation 2-6)}$$

Where j is the imaginary unit, ω equals $2\pi f$ and C is the capacitance. The Nyquist plot of a capacitor looks like a vertical line with the zero Re (Z) (Figure 2-4b).

In a series of resistors and capacitors, the impedance values are additive (Equation 2-7).

$$Z = \sum_n Z_n = Z_R + Z_C = R + \frac{1}{j\omega C} \qquad \text{(Equation 2-7)}$$

Figure 2-4c shows the Nyquist plot of this circuit. The Re(*Z*) is equal to the resistance of the resistor for all frequencies, and the Im(*Z*) follows the same behaviour as for the ideal capacitor.

In a parallel circuit of resistors and capacitors, the admittances (the reciprocals of the impedances) are additive:

$$Y = \frac{1}{Z} = \sum_n \frac{1}{Z_n} = \frac{1}{R} + j\omega C \qquad \text{(Equation 2-8)}$$

From rearranging Equation 2-8, we can get Equation 2-9

$$Z = \frac{R}{1+j\omega CR} \qquad \text{(Equation 2-9)}$$

Therefore, at high frequency, i.e., $\omega \rightarrow \infty$, the impedance tends towards zero. At low frequency, i.e., $\omega \rightarrow 0$, the total impedance of the circuit equals R. The Nyquist plot for this circuit is a semicircle, intercepting the Re(Z) axis at 0 and R (Figure 2-4d).

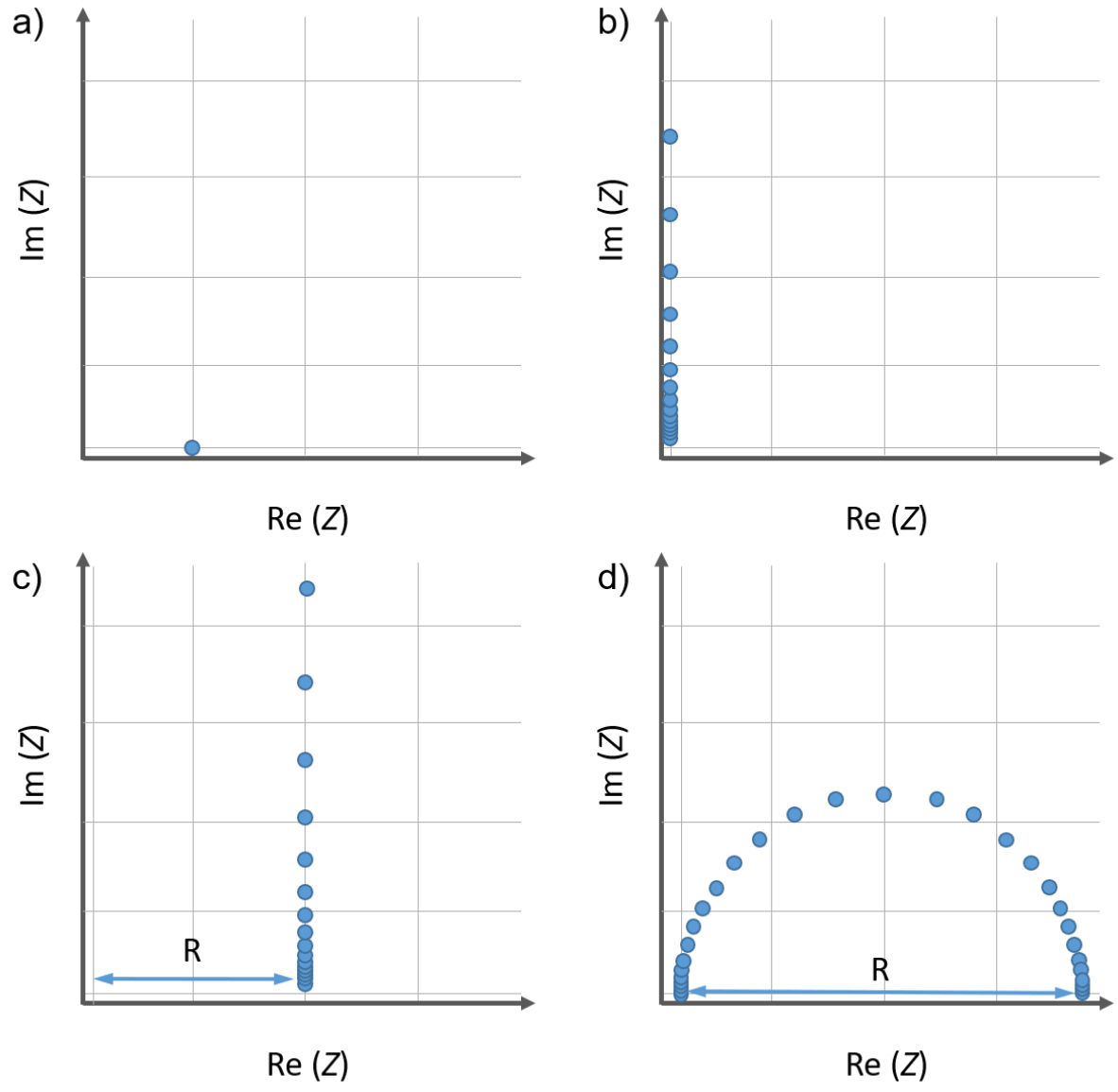

Figure 2-4. (a)The Nyquist plot for a resistor; (b) The Nyquist plot for a capacitor; (c) The Nyquist plot for a series of resistor and capacitor; (d) The Nyquist plot for a parallel of resistor and capacitor. Redrawn from reference [12].

The Nyquist plot obtained from an EIS measurement of a redox-active compound shows a kinetic- and a diffusion-controlled region. It displays as a semicircle in the high-frequency region and a straight line in the low-frequency region, which are both offset by the electrolyte's resistance R_E (Figure 2-5). The semicircles in high-frequency regions denote charge transfer resistance (Rc), which is related to reaction kinetics, can be readily analysed: The abscissa-based diameter represents the charge-transfer resistance R_{CT}, which can be expressed as the function of exchange current i_0:

$$R_{CT} = \frac{RT}{Fi_0} \qquad \text{(Equation 2-10)}$$

The double-layer capacitance, C_D, can be determined by the peak AC frequency (ω_p) of the semicircle:

$$\frac{1}{\omega_p} = R_{CT}C_D \qquad \text{(Equation 2-11)}$$

The straight line that appeared at the low AC frequencies is the Warburg impedance, which is corresponding to the diffusion control.

$$Im(Z) = Re(Z) - R_E - R_{CT} + R_{CT}^2 C_D(\frac{k_{Ox}}{\sqrt{D_{Ox}}} + \frac{k_{Re}}{\sqrt{D_{Re}}})^2 \qquad \text{(Equation 2-12)}$$

Therefore, for an ideal Warburg-type system, the line has a slope equal to 1 (*i.e.* 45 degrees)and intersects the abscissa at $R_E + R_{CT} - R_{CT}^2 C_D(\frac{k_{Ox}}{\sqrt{D_{Ox}}} + \frac{k_{Re}}{\sqrt{D_{Re}}})^2$, which reduces to $R_E + R_{CT} - R_{CT}^2 C_D \frac{k^2}{D}$ in case of equal rate constants and diffusion coefficients for the oxidation and reduction process.[13]

Figure 2-6 is the corresponding equivalent circuit including a redox-active species interacting with an electrode surface. In this circuit, the capacitor (C_D), the charge transfer resistance (R_{CT}), the resistance of the solution (R_E), and the mass transport resistance (Z_W) were considered. The C_D is in parallel to the resistance R_{CT} and Z_W, and they are connected in series to R_E. If the semicircle is imperfect, appearing with suppressed dimensions, the capacitor may be replaced by the constant phase element (CPE) in the equivalent circuit.

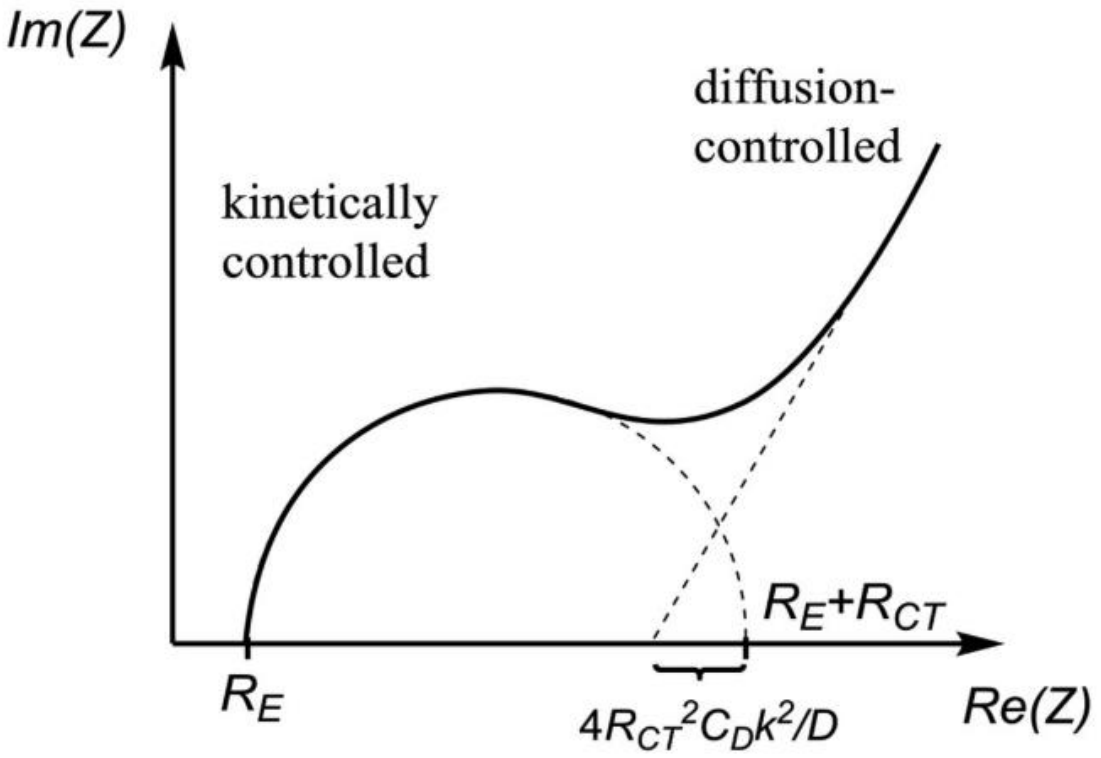

Figure 2-5. Typical Nyquist plot for an electrochemically active system. Reprinted with permission from reference 3. Copyright 2015 John Wiley & Sons.[3]

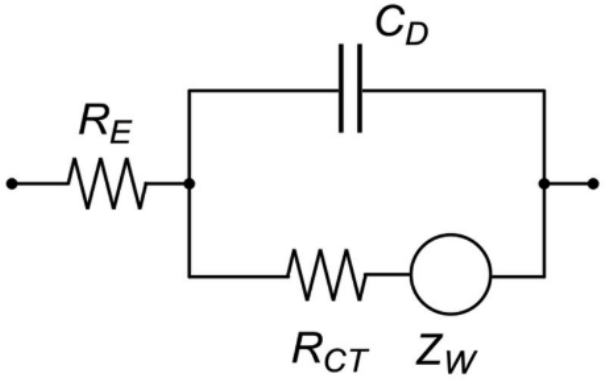

Figure 2-6. EIS equivalent circuit for the general case of a redox-active species interacting at an electrode surface. Z_W refers to the diffusion-based Warburg element. Reprinted with permission from reference 3. Copyright 2015 John Wiley & Sons.[3]

2.2.5 Preparation of Electrodes

The positive electrodes were prepared using the following procedure: The active material and carbon black (Super C65, IMERYS, particle size less than 50 nm) were ground by pestle and mortar for 30 minutes. The solid was transferred into a small vial that was equipped with a stirrer bar. Poly (vinylidene fluoride) solution (5 wt.% PVDF in NMP solution) was added to the vial. The mass ratio of active materials, carbon black, and PVDF was 6:3:1 or 7:2:1. Additional NMP was added to adjust the viscosity to form a slurry. After stirring the suspensions for 12 h, finely dispersed slurries were obtained and these were then coated onto aluminium foil substrates (thickness × width × height = 0.005 × 16 × 25 cm) using a doctor blade at a fixed thickness. The substrates were then dried at room temperature for 6 h followed by drying under vacuum pressure at 80 ℃ for 12 hours to afford dry films. The films were then punched into discs with diameters of 10 mm. The discs were dried overnight under vacuum at 80 ℃ and transferred directly into a glovebox kept under an Ar atmosphere with H_2O and O_2 concentrations ≤ 0.1 ppm. The resulting electrode loadings were in the range of 0.3-0.6 mg cm^{-2}.

Coin cells (CR2025) were assembled inside the Ar-filled glovebox (Figure 2-7). Lithium foil with a diameter of 12 mm and a thickness of 0.38 mm was used as the counter electrode, and glass microfiber (Whatman GF/F) was used as the separator. A mixture of 1,3-dioxolane and 1,2-dimethoxyethane (1:1 vol/vol) containing 1 M lithium bis(trifluoromethanesulfonyl)imide (LiTFSI) was used as the primary electrolyte formulation (Duoduo Chemicals). After preparation, the coin cells were taken out of the glovebox and tested.

In this thesis**,** CV (using a Biologic mpg2 potentionstat) was recorded starting from open circuit potential to the cathodic scan (discharge) direction. Electrochemical impedance spectroscopy (Biologic) was carried out over a frequency range from 1 MHz to 100 mHz, with an applied sinusoidal voltage amplitude of ±10 mV. Galvanostatic discharge-charge cycling of the cells was measured using a Maccor Series 4000 battery cycler. All potentials are given versus Li/Li^+. All electrochemical measurements were performed on the coin cells at 25 °C.

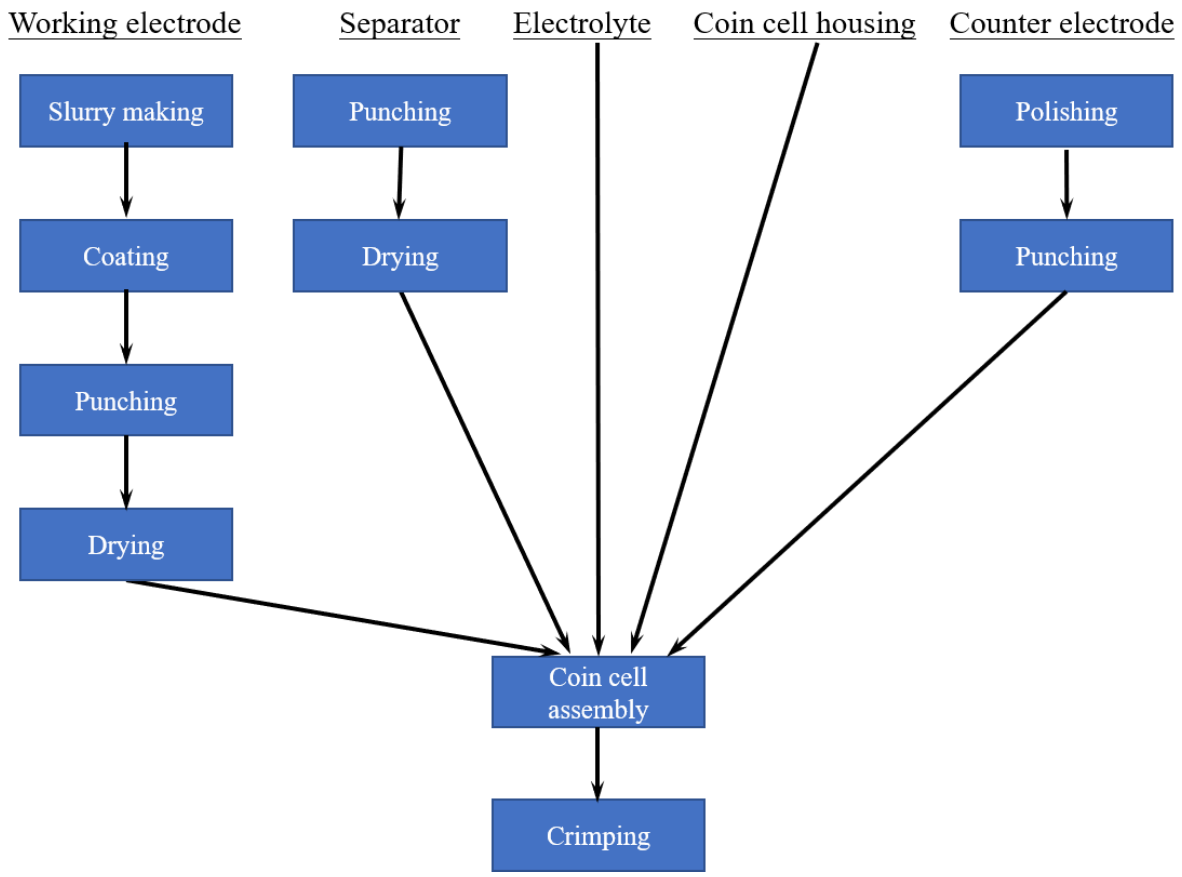

Figure 2-7. Flow chart of the coin cell construction procedure. Coin cell housing includes spacer, spring, lower case, and upper case. First, a working electrode is prepared from the powder of the active material. Then, a counter electrode is prepared from a clean lithium foil and the separators are punched out. Finally, a cell is assembled inside an argon-filled glovebox.

2.3 Gas sorption

Gas adsorption is a well-established technique for the characterisation of the texture of porous solids and fine powders. Adsorption is defined as the enrichment of molecules, atoms, or ions in the vicinity of an interface.[14] The material that is adsorbed is called the adsorbate, while the material that can adsorb other components is known as adsorbent. In general, adsorption can be classified as physical (physisorption) and chemical (chemisorption). Physisorption is a general phenomenon and describes the interaction between the gas molecules (absorbate) and the surface of the solid (absorbent) via intermolecular forces (*e.g.*, van der Waals). The interactions, such as polarisation, can be affected by the geometric and electronic properties of the gas and the surface. Chemisorption is noted when forming chemical bonds between the gas and the surface of a solid via intermolecular forces.

The surface of the adsorbent contains three levels (Figure 2-8), (1) the van der Waals surface formed by the outer surface of the solid, (2) the gas probe-accessible surface (known as the Connolly surface in simulation studies) denoted by the gas probe rolling over the van der Waals surface, (3) the r-distance surface located at distance r from the probe-accessible surface. Smaller gases can be beneficial for obtaining more accurate information of solid pore size. The pore size can be classified as macropore (pores with widths exceeding 50 nm), mesopore (pores of widths between 2 and 50 nm), and micropore (pores with widths less than 2 nm). Physical filling of micropores usually starts at low relative pressures and vary with the shape and dimensions of pores, gas probe, and their interaction. For mesopores, filling occurs in multiple stages, as monolayer adsorption firstly occurs where all the gas molecules are in contact with the surface, followed by the multilayer adsorption when the gas accommodates more than one layer. The gas then condenses to a liquid-like phase in the pore at a pressure less than the saturation pressure of the bulk liquid, generally at a partial pressure (P/P_0) of around 0.5.

The complete analysis of mesopore and micropore requires the relative pressure range $10^{-7} \leq P/P_0 \leq 1$ with special instruments to ensure the sample cell and manifold can be evacuated to very low pressures, as well as the ≥99.999% purity of the absorptive gas and the amount of remaining un-adsorbed gas in the effective void volume (dead space). In general, the dead space under operational conditions is measured using a non-adsorbing gas such as helium. It should be noted that before the measurements, the sample should be degassed at an elevated temperature to remove all physisorbed species from the surface to avoid incorrect results.

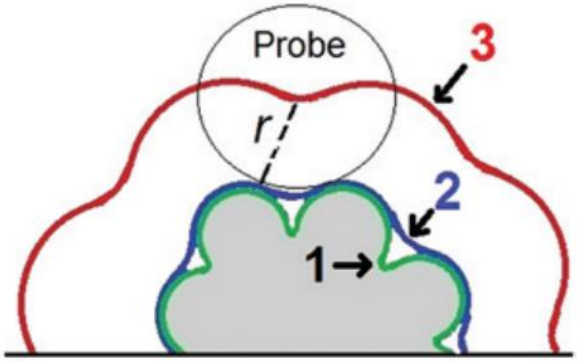

Figure 2-8. Schematic illustration of several possible surfaces of an adsorbent. 1: van der Waals; 2: Probe-accessible; 3: Accessible, r-distance. Reprinted from reference 14. Copyright 2015 IUPAC & De Gruyter.[14]

In practical experiments, the gas probes include various subcritical fluids (*e.g.*, N_2 at 77 K, CO_2 at 298 K, H_2 at 77 K), organic vapours, and supercritical gases. Gas adsorption measurements usually monitor the adsorption of these gas probes and give the relationship between the amount of gas adsorbed and the equilibrium pressure of the gas at constant temperature (known as adsorption isotherm). According to the 2015 IUPAC document, the physisorption isotherms are displayed in Figure 2-9.[14]

Generally, uptakes at very low pressures represent abundant micropores, at around $P/P_0 = 0.5$ are associated with mesopores, and at high pressures mean rich macropores. The steepness of isotherms implies the distribution of pore sizes, for example, a steep Type Ia isotherm at very low pressures indicates enhanced adsorbent-adsorptive interactions in the narrow micropores while the broad Type I(b) isotherm indicates a broader pore size distribution in the micropore range. For Type I isotherms, the internal surface areas within the material are larger than the external surface areas, resulting in the bulging isotherm shape. By contrast, macropores and non-pores lead to the concave Type II isotherm. Adsorption at high P/P_0 is a result of unrestricted monolayer-multilayer absorption. Point B indicates the completion of monolayer coverage and the onset of multilayer adsorption in the isotherm. For the Type III isotherm, the relatively weak interaction between the gas and the surface cannot generate the identifiable monolayer formation, and thus point B disappears, meanwhile the absorbed gas molecules occupy more favoured sites on the surface of the macroporous or non-porous solid. Type IV isotherms arise from hierarchical structures with both micropores and mesopores. Besides the gas-surface interaction, mesopore absorption behaviour also depends on the interaction between the molecules in the condensed state. The hysteresis loop in Type IV(a) isotherms is caused by the capillary condensation in the mesopores. This happens when the pore width exceeds a certain critical width dependent on the absorption system and temperature (under N_2 for pores wider than ~4 nm).[14] Thus, Type IV(b) isotherms are observed with smaller mesopores. The Type V isotherm represents no adsorption at low pressure due to weak absorbent-absorbate interactions but a rise at higher pressure attributed to molecular clustering followed by pore filling. The stepwise shape of Type VI isotherm is attributed to layer-by-layer adsorption on a highly uniform non-porous surface. The step height represents the capacity of the absorbed layer whilst the sharpness is dependent on the system and temperature.

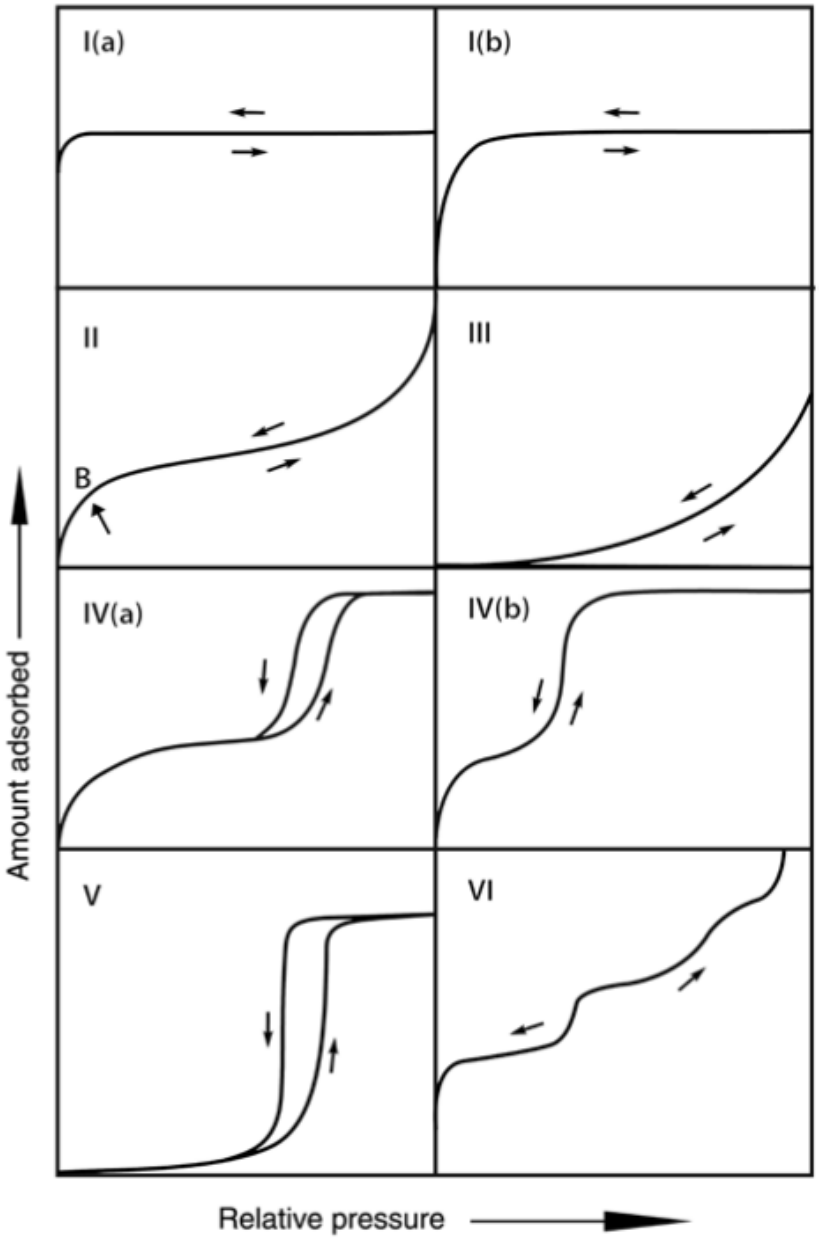

Figure 2-9. Classification of physisorption isotherms. Figure reprinted from literature source.[14] Type I isotherms with a steep increase of adsorption at relatively low pressures are given by microporous materials. Type II isotherms are normally associated with macroporous or non-porous materials. Type III isotherms are not common. They only occurred when adsorbent and adsorbate show weak interactions between each other. Type IV isotherms are associated with mesoporous materials. The hysteresis loop is from capillary condensation in mesopores. This is a commonly observed isotherm type for COFs. Type V isotherms are similar to type III which adsorbent shows weak interaction with an adsorbate. Type VI isotherms can be observed in non-porous materials which shows stepwise multilayer adsorption. Reprinted from reference 14. Copyright 2015 IUPAC & De Gruyter.[14]

2.3.1 Brunauer-Emmett-Teller Model

The Brunauer-Emmett-Teller (BET) model assumes the adsorbate behaves as an ideal gas under isothermal conditions and considers multilayer adsorption. The following assumptions are made in the model: (1) The gas molecules can adsorb onto the surface in infinite layers; (2) The gas molecules only interact with adjacent layers; (3) Langmuir theory can be applied to each layer.[14] The BET equation in linear form is:[14]

$$\frac{P/P_0}{n_a(1-P/P_0)} = \frac{1}{n_m c} + \frac{c-1}{n_m c} \times (P/P_0) \qquad \text{(Equation 2-13)}$$

Where P is the equilibrium pressure, P_0 is the saturation pressure, n_a is the amount adsorbed at the relative pressure P/P_0 and n_m is the monolayer adsorbed gas quantity c is the BET constant, defined as:

$$c = \exp(\frac{E_1 - E_L}{RT}) \qquad \text{(Equation 2-14)}$$

Where E_1 is the heat of adsorption for the first layer and E_L is the heat of adsorption for the second layer and beyond. n_m can thus be derived from the intercept of the BET equation by plotting $\frac{P/P_0}{n_a(1-P/P_0)}$ vs. P/P_0. Using n_m derived from the BET model, SA_{BET} can thus be derived:

$$SA_{BET} = n_m N_A a_m \qquad \text{(Equation 2-15)}$$

Where N_A is the Avogadro constant and a_m is the cross-sectional area of the adsorbate molecule.

The BET method is the most widely used procedure for evaluating the surface areas of solids, but it has some drawbacks. For example, the assumption of the homogeneous surface leads to ignorance of the differences between the surface and lateral adsorbate-adsorbate interactions.[15] This will result in the nonlinearity of BET plots at $P/P_0 < 0.5$, as high energy sites are occupied at lower relative pressures. Besides, the differentiating mono-multilayer adsorption from pore filling just reflects an "apparent" BET surface area instead of a real internal surface, which may be an overestimation.

2.3.2 Micropore Size Analysis

To understand the micropore size distribution, many methods have been developed. An empirical method is the application of several molecular probes of progressively increasing molecular diameter. The method is based on the measurement of both adsorption rates and

capacities. However, this method does not consider the complexity of the most microporous materials. Various semi-empirical methods include those proposed by Horvath and Kawazoe, Saito and Foley, and Cheng and Yang for the study of the pore size distribution of slit, cylindrical and spherical pores, respectively.[15–17] Despite the drawback of these semi-empirical methods is they tend to underestimate the pore size, these methods may be in some cases useful for the comparison of microporous materials. Microscopic treatments such as density functional theory (DFT) and molecular simulation are considered to be superior and to provide a more reliable approach to pore size analysis over the complete nanopore range because they can describe the configuration of the adsorbed phase at the molecular level. Different pore shape models, such as a slit, cylinder, and spherical geometries and hybrid shapes, have been developed for various material classes for instance carbons, silicas, zeolites. Non-local density functional theory (NL-DFT) based methods for pore size/volume analysis of nanoporous materials are now available for many adsorption systems.[15,17] They are included in commercial software and are also featured in international standards.

2.3.3 Mesopore Size Analysis

The methods for mesopore size analysis, including those developed by Barrett, Joyner, and Halenda (BJH) and Broeckhoff and de Boer, make use of the modified Kelvin equation.[15,16] Considering the preadsorbed multilayer film, the Kelvin equation is combined with a standard isotherm (the *t*-curve), which is determined on certain well-defined nonporous solids. However, the standard *t*-curve is not entirely satisfactory for the analysis of narrow mesopores because the curvature and enhanced surface forces are not properly considered. The Kelvin equation-based procedures, such as the BJH method, significantly underestimate the pore size for narrow mesopores (for pore diameter less than 10 nm, the pore size will be underestimated by ~ 20–30 %).[15,17] The limitations of the Kelvin equation can be avoided by applying microscopic methods based on molecular simulation or DFT (e.g., NLDFT). They get the essential features of both micropore and mesopore filling and hysteresis.[18,19] Therefore, a more reliable assessment of the pore size distribution over the complete range can be obtained through microscopic methods based on molecular simulation or DFT.[17,19] It is important to ensure that the chosen DFT and molecular simulation-based methods are compatible with the experimental nanoporous system.

In this thesis, N_2 adsorption isotherms of samples were obtained using a Micromeritics ASAP 2020 or ASAP 2420 volumetric adsorption analyser with approximately 100 mg samples at 77.3 K with an equilibration interval of 30 s. Samples were degassed at 120 ℃ for 12 hours under vacuum (10^{-5} bar) before analysis. The surface areas were calculated in the relative pressure range (P/P_0) from 0.05 to 0.12 using Brunauer-Emmet-Teller (SA_{BET}) method. Pore size distributions of the samples derived from fitting the NL-DFT model to the adsorption data.

2.4 Nuclear Magnetic Resonance

Nuclear magnetic resonance (NMR) spectroscopy is a spectroscopic technique used to observe local magnetic fields around atomic nuclei. During a measurement, the sample is placed in a magnetic field and the NMR signal is produced by excitation of the nuclei sample with radio waves into nuclear magnetic resonance, which is detected with sensitive radio receivers. The intramolecular magnetic field around an atom in a molecule changes the resonance frequency, therefore, giving access to details of the electronic structure of a molecule and its functional groups. NMR spectroscopy is often a definitive method to confirm the chemical structure of monomolecular organic compounds because the fields are unique or highly characteristic to individual compounds. In this thesis, ^{1}H and $^{13}C\{^{1}H\}$ NMR spectra were collected in solution on a Bruker Avance 400 NMR spectrometer at 400 MHz and 100 MHz, respectively. The samples were dissolved in DMSO-d_6 and the NMRs were referenced against the ^{1}H or ^{13}C signal of this solvent.

For insoluble samples, the chemical structural information can be obtained by solid-state NMR spectroscopy. The anisotropic part of many spin interactions is present in solid-state NMR, unlike in solution-state NMR where rapid tumbling motion averages out many of the spin interactions. As a result, solid-state NMR spectra are characterised by larger linewidths than in solution-state NMR, which can be utilised to give quantitative information on the molecular structure, conformation and dynamics of the material. Solid-state NMR is often combined with magic angle spinning to remove anisotropic interactions and improve the resolution as well as the sensitivity of the technique. In this thesis, C^{13} magic-angle spinning measurements were carried out at 100 MHz using a Bruker Avance III HD spectrometer and a 4 mm (rotor o.d.) probe. Spectra were acquired at a spin rate of 10 kHz. Cross-polarisation spectra were recorded with total suppression of spinning sidebands, 1 ms contact time and with a recycle delay of

4 s. Carbon spectral referencing is relative to neat tetramethylsilane, carried out by setting the high-frequency signal from an external sample of adamantane to 38.5 ppm.

2.5 Fourier-transform Infrared Spectroscopy

Infrared (IR) spectroscopy is a technique for the analysis of the interactions between infrared radiation with materials by measuring absorption, emission, or reflection. Absorption of IR radiation corresponds to vibrational frequencies within molecules and, therefore, IR spectroscopy can be used to determine the functional groups and overall structures. Fourier transform infrared (FT-IR) spectroscopy is a measurement technique that allows one to extract frequency peaks from the raw data by a data-processing technique called Fourier transform.[20] During the FT-IR measurement, infrared light is guided through an interferometer and then through the sample. A moving mirror inside the apparatus alters the distribution of infrared light that passes through the interferometer. The signal directly recorded, called an "interferogram", represents light output as a function of mirror position. In this thesis, FT-IR spectra of the samples were recorded on a Bruker alpha spectrometer or Nicolet iS50 FT-IR by attenuated total reflectance. *Ex situ* FT-IR spectra were measured on a Thermo Scientific Nicolet iS50 FT-IR spectrometer by attenuated total reflectance inside a glovebox under a dry N_2 atmosphere.

2.6 Powder X-Ray Diffraction

Powder X-Ray diffraction (PXRD) is a commonly used technique to study the crystalline structure of materials. During the measurement, the sample is irradiated with X-rays. The interaction of the incident rays with the sample electron cloud produces constructive interference (and a diffracted ray) when conditions satisfy Bragg's Law [21] (Equation 2-16 and Figure 2-10)

$$2d\ sin\theta\ = n\lambda \qquad \text{(Equation 2-16)}$$

Where d is the spacing of the crystal lattice plane, θ is the angle of incident X-rays, n is an integer and λ is the wavelength of X-rays.

In this thesis, PXRD diffraction patterns were collected at room temperature in vertical transmission mode from loose powder samples held on Mylar film in aluminium well plates,

using a Panalytical Empyrean diffractometer equipped with a high throughput screening XYZ stage, X-ray focusing mirror, and PIXcel detector with Cu Kα (λ = 1.541 Å) radiation. Data were measured over the 2θ range of 1-56° over 30 minutes.

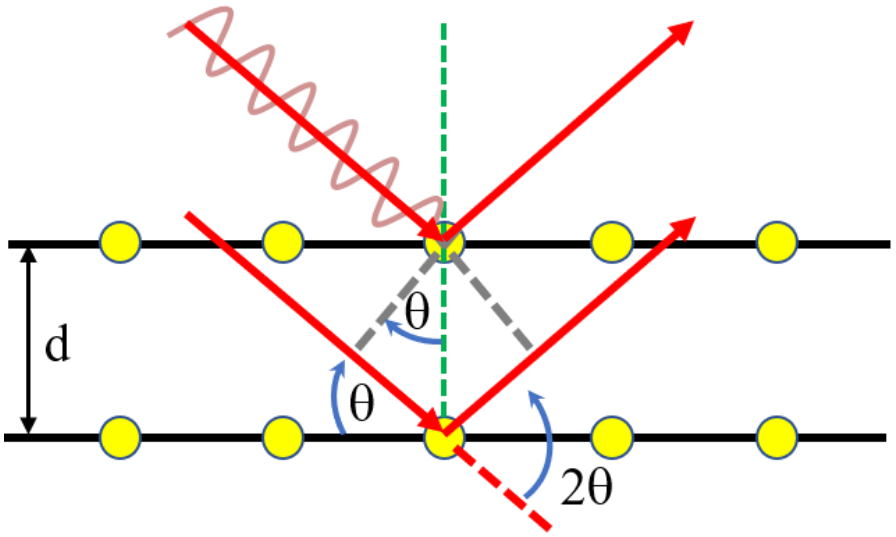

Figure 2-10. Schematic representation of the Bragg model of diffraction. Redrawn from reference [22].

2.7 Element Analysis

Element analysis (EA) is a well-understood technique to determine the elemental composition of a sample quantitively. In general, the % of carbon, hydrogen, and nitrogen, amongst other elements, can be measured by EA through combustion analysis. The principles of EA rely on the tendency that all atoms prefer to be in their highest oxidation states during combustion. In pure oxygen, at high temperatures, all available carbon, hydrogen, and nitrogen will burn to become CO_2, H_2O, and NO_X. The mass of these oxides can be used to calculate the composition of the sample. In this thesis, EA was measured on a Thermo EA1112 Flash CHNS-O analyser.

2.8 Field Emission Scanning Electron Microscope

Field emission scanning electron microscope (FE-SEM) is used to investigate the surface morphology of materials. The FE-SEM is one microscope that works with electrons rather than light.[23] The electrons are accelerated in a high electrical field gradient. Within the high vacuum column, these so-called primary electrons are focused and deflected by electronic lenses to

produce a narrow scan beam that bombards the sample. Secondary electrons, as a result, are emitted from each spot on the sample. The angle and velocity of these secondary electrons, collected by a detector, relate to the surface structure of the object. Therefore, the surface topology of the sample can be constructed. To be observed with an SEM, samples should be made conducive for currents (at least on the surface) otherwise the non-conductive sample collects charge from the electron beam which causes image artifacts to appear. This can be done by coating the sample with an ultrathin layer (1.5–3.0 nm) of an electrically conductive metal (gold or gold-palladium) by a low-vacuum sputter coating. In this thesis, the morphology of the samples was studied on a Hitachi S-4800 cold field emission scanning electron microscope. Samples were prepared by depositing the dry powders on 15 mm Hitachi M4 aluminium stubs using an adhesive high-purity carbon tab before coating with a 2 nm layer of gold using an Emitech K550X automated sputter coater. Imaging was conducted at a working voltage of 10 kV and a working distance of 4 mm using a combination of upper and lower secondary electron detectors.

2.9 Transmission Electron Microscopy

Transmission electron microscopy (TEM) is a microscopy technique to investigate the structure of materials, in which a beam of electrons passes through a sample. An image is generated from the interaction of the electrons with the sample as the beam is transmitted through the specimen. The image is then magnified by other lenses before being detected. In this thesis, TEM images were obtained using a JEOL 2100+ microscope operating at 200KV equipped with a Gatan Rio Camera. The samples were prepared by drop-casting sonicated ethanol suspensions of the materials onto a copper grid.

2.10 Ultraviolet-visible spectroscopy

Ultraviolet-visible (UV-Vis) spectroscopy refers to absorption or reflectance spectroscopy with observed reflectance or absorption in the ultraviolet region or the adjacent visible region. UV–Vis spectroscopy uses light in the visible and adjacent ranges. In the visible region, the absorption or reflectance observed directly affects the perceived colour of the chemical involved. In this region of the spectrum, atoms and molecules undergo electronic

transitions.[24,25] In this thesis, UV-visible absorption spectra of the solution were measured on a Cary 5000 UV-vis-NIR spectrometer.

2.11 Raman Microscopy

Raman microscopy is a spectroscopic technique typically used to determine vibrational, rotational and other low-frequency modes of molecules, which provide the structural information of the materials.[26] Raman is a light scattering effect. The Raman signal is produced by photons being inelastically scattered after colliding with molecules in the gas phase, solution, or on a substrate surface. When an intense source of light is used to excite molecules to a virtually excited state, elastic scattering (Rayleigh scattering) happens at the same time as the inelastic scattering (Figure 2-11). There is no change in energy in the Rayleigh scattering and photos are scattered with the same frequency at which collide with the surface therefore the light of the same wavelength. Rayleigh scattering accounts for the majority of light scattered from the surface.[27] Raman scattering includes Stokes and anti-Stokes scattering. Upon collision, the Stokes scattering happens when energy is transferred from photon to molecule (*i.e.* $h\nu_0 - h\nu_m$), and the Anti-Stokes scattering happens if energy is transferred from a vibrationally excited state to the ground state (*i.e.* $h\nu_0 + h\nu_m$). Its presence is a result of the Raman effect. The resulting Raman spectrum is calculated by the difference in energy between the incident photons and the scattered light. For a vibrational mode of a molecule to be Raman active, a change in the polarisability of the molecule must occur. Polarisation and a dipole moment are created when the molecule is present in an electric field, pushing the electrons in the molecule away from the nuclei. In the measurement, the sample is illuminated with a laser beam visible, near infrared, or near ultraviolet range. The laser light interacts with the molecular vibrations, phonons or other excitations in the system, resulting in the energy of the laser photons being shifted up or down. This shift in energy gives information about the vibrational modes in the system. In this thesis, Raman spectra were recorded with a Raman spectrometer (Renishaw inVia) equipped with a microscope to facilitate the focal point of the excitation laser directly on the material being studied. A 532 nm wavelength excitation laser was used for all Raman measurements. For the measurement, loose powders were mounted onto a Pyrex glass slide and measured in air.

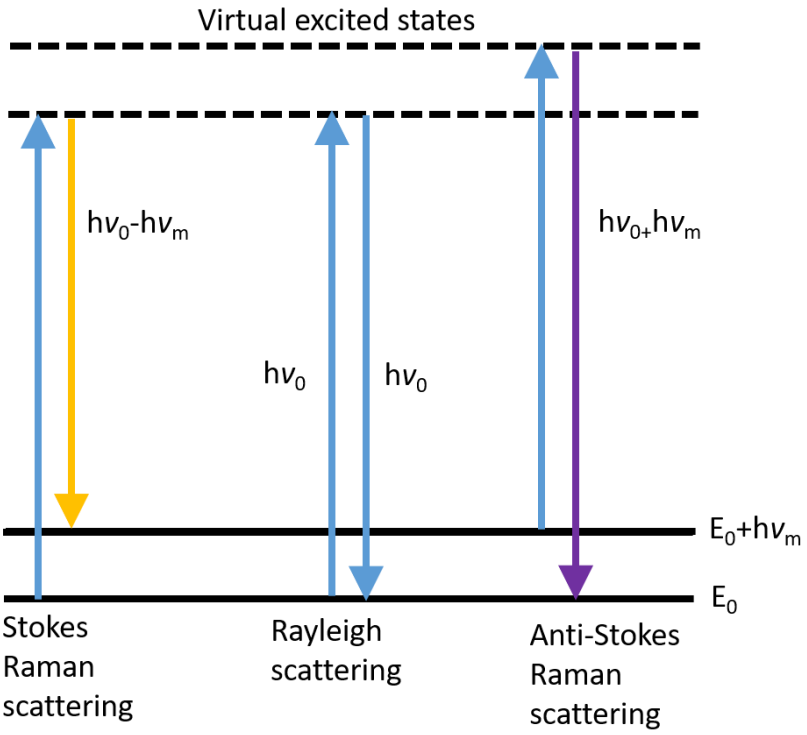

Figure 2-11. Schematic representation of Rayleigh and Raman scattering. ν_0 indicates laser frequency (blue: no energy difference), Stokes scattering (yellow: incident photon loss energy), and anti-Stokes scattering (purple: incident photon gains energy). Redrawn from reference [28].

2.12 Thermogravimetric Analysis

Thermogravimetric analysis (TGA) measures the mass of a sample over time as the temperature changes.[29] This measurement provides information like phase transitions, absorption, and desorption, thermal decomposition, and so on. In this thesis, TGA was performed in platinum pans using a Q5000IR analyser (TA instruments) with an automated vertical overhead thermobalance. The samples were heated at 10 °C min^{-1} to 800 °C under N_2.

2.13 Reference

(1) Elgrishi, N.; Rountree, K. J.; McCarthy, B. D.; Rountree, E. S.; Eisenhart, T. T.; Dempsey, J. L. A Practical Beginner's Guide to Cyclic Voltammetry. *J. Chem. Educ.* **2017**, *95* (2), 197–206.

(2) Lord, H. L.; Zhan, W.; Pawliszyn, J. *Electrochemical Methods Fundamentals and Applications*; John Wiley & Sons, 2001.

(3) Friebe, C.; Schubert, U. S. Development of Active Organic and Polymeric Materials for Batteries and Solar Cells: Introduction to Essential Characterization Techniques. *Adv. Energy Mater.* **2015**, *5* (24), 1–14.

(4) Wang, J.; Polleux, J.; Lim, J.; Dunn, B. Pseudocapacitive Contributions to Electrochemical Energy Storage in TiO_2 (Anatase) Nanoparticles. *J. Phys. Chem. C* **2007**, *111* (40), 14925–14931.

(5) Come, J.; Taberna, P.-L.; Hamelet, S.; Masquelier, C.; Simon, P. Electrochemical Kinetic Study of $LiFePO_4$ Using Cavity Microelectrode. *J. Electrochem. Soc.* **2011**, *158* (10), A1090–A1093.

(6) Sathiya, M.; Prakash, A. S.; Ramesha, K.; Tarascon, J. M.; Shukla, A. K. V_2O_5-Anchored Carbon Nanotubes for Enhanced Electrochemical Energy Storage. *J. Am. Chem. Soc.* **2011**, *133* (40), 16291–16299.

(7) Augustyn, V.; Come, J.; Lowe, M. A.; Kim, J. W.; Taberna, P. L.; Tolbert, S. H.; Abruña, H. D.; Simon, P.; Dunn, B. High-Rate Electrochemical Energy Storage through Li^+ Intercalation Pseudocapacitance. *Nat. Mater.* **2013**, *12* (6), 518–522.

(8) Liu, J.; Wang, J.; Xu, C.; Jiang, H.; Li, C.; Zhang, L.; Lin, J.; Shen, Z. X. Advanced Energy Storage Devices: Basic Principles, Analytical Methods, and Rational Materials Design. *Adv. Sci.* **2017**, *5* (1), 1700322.

(9) Reddy, T. B. *Handbook of Batteries*; McGraw-Hill Education, 2011.

(10) Kiehne, H. A. *Battery Technology Handbook*; CRC Press, 2003.

(11) Negroiu, R.; Svasta, P.; Pirvu, C.; Vasile, A.; Marghescu, C. Electrochemical Impedance Spectroscopy for Different Types of Supercapacitors. *Proc. Int. Spring Semin. Electron. Technol.* **2017**, 1–4.

(12) Rubinson, J. F.; Kayinamura, Y. P. Charge Transport in Conducting Polymers: Insights from Impedance Spectroscopy. *Chem. Soc. Rev.* **2009**, *38* (12), 3339–3347.

(13) Lvovich, V. F. *Impedance Spectroscopy: Applications to Electrochemical and Dielectric Phenomena*; John Wiley & Sons, 2012.

(14) Thommes, M.; Kaneko, K.; Neimark, A. V.; Olivier, J. P.; Rodriguez-Reinoso, F.; Rouquerol, J.; Sing, K. S. W. Physisorption of Gases, with Special Reference to the Evaluation of Surface Area and Pore Size Distribution. *Pure Appl. Chem.* **2015**, *87* (9–10), 1051–1069.

(15) S. Lowell, Joan E. Shields, Martin A. Thomas, M. T. *Characterization of Porous Solids and Powders: Surface Area, Pore Size and Density*; Springer, Dordrecht, 2004.

(16) Jean Rouquerol, Françoise Rouquerol, Philip Llewellyn, Guillaume Maurin, K. S. W. S. *Adsorption by Powders and Porous Solids: Principles, Methodology and and Applications*; Academic Press, 2014.

(17) Thommes, M.; Cychosz, K. A. Physical Adsorption Characterization of Nanoporous Materials: Progress and Challenges. *Adsorption* **2014**, *20* (2–3), 233–250.

(18) Monson, P. A. Understanding Adsorption/Desorption Hysteresis for Fluids in Mesoporous Materials Using Simple Molecular Models and Classical Density Functional Theory. *Microporous Mesoporous Mater.* **2012**, *160*, 47–66.

(19) Landers, J.; Gor, G. Y.; Neimark, A. V. Density Functional Theory Methods for Characterization of Porous Materials. *Colloids Surfaces A Physicochem. Eng. Asp.* **2013**, *437*, 3–32.

(20) Mohamed Shameer, P.; Mohamed Nishath, P. Exploration and Enhancement on Fuel Stability of Biodiesel: A Step Forward in the Track of Global Commercialization. In *Advanced Biofuels: Applications, Technologies and Environmental Sustainability*; Elsevier Ltd, 2019; pp 181–213.

(21) H.P. Meyers, H. P. M. *Introductory Solid State Physics*; CRC Press, 2014.

(22) Epp, J. *X-Ray Diffraction (XRD) Techniques for Materials Characterization*; Elsevier Ltd, 2016.

(23) Semnani, D. *Geometrical Characterization of Electrospun Nanofibers*; Elsevier Ltd., 2017.

(24) Douglas A. Skoog, F. James Holler, S. R. C. *Principles of Instrumental Analysis*; Brooks Cole, 2007.

(25) Sarfraz, A.; Raza, A. H.; Mirzaeian, M.; Abbas, Q.; Raza, R. Electrode Materials for Fuel Cells. In *Reference Module in Materials Science and Materials Engineering*; Elsevier, 2020.

(26) Vandenabeele, P. *Practical Raman Spectroscopy - An Introduction*; John Wiley & Sons, Ltd, 2013.

(27) Lohumi, S.; Kim, M. S.; Qin, J.; Cho, B. K. Raman Imaging from Microscopy to

Macroscopy: Quality and Safety Control of Biological Materials. **2017**, *93*, 183–198.

(28) Baker, M. Raman Spectroscopy. *Biophotonics Vib. Spectrosc. Diagnostics* **2016**.

(29) Bottom, R. Thermogravimetric Analysis. *Princ. Appl. Therm. Anal.* **2008**, *1* (906), 87–118.

Chapter 3

Long Cycle Life of Positive Electrode Enhanced by Composites of Crosslinked Polyimide and Reduced Graphene Oxide

Some of the results presented in Chapter 3 are taken from Paper I.

Crosslinked Polyimide and Reduced Graphene Oxide Composites as Long Cycle Life Positive Electrode for Lithium-Ion Cells, Hui Gao, Bingbing Tian, Haofan Yang, Alex R. Neale, Marc A. Little, Reiner Sebastian Sprick, Laurence J. Hardwick, * and Andrew I. Cooper*

3.1 Author Contributions

All the polyimide and polyimide on reduced graphene oxide (rGO) composites were synthesised by the thesis author. All the electrochemical experiments, including CV, galvanostatic charge/discharge measurement, rate performance, EIS, were carried out by the thesis author. All the electrochemical experiments were measurement completed using coin cells assembled by the thesis author. Mr. Haofan Yang recorded SEM images. Dr. Yundong Zhou carried out Raman spectrum measurement of rGO.

3.2 Abstract

A 3D redox-active polyimide was designed and hybridised with rGO using an in situ polycondensation reaction of pyromellitic dianhydride (PMDA) and tetra-(4-aminophenyl) methane (TAPM). By itself, the polyimide (**PI)** has a low specific capacity of 3 mAh g^{-1} in a lithium-ion half-cell resulting from the deficient utilisation of the redox-active groups on 3D structures. By contrast, the integration of reduced graphene oxide (rGO) with **PI** significantly enhances the utilisation of the redox-active sites to 86% and results in a specific capacity as high as 172 mAh g^{-1} at 500 mA g^{-1} (50 wt.% of rGO). The performance improvement results from the larger surface area and the faster charge transport within the composites.

3.3 Introduction

Functionalised organic materials have the potential to be candidate electrodes for the next-generation lithium-ion batteries,[1,2] due to the easy tailoring and the high theoretical capacity resulted from the lightweight of active sites. Among the organic positive electrode materials, such as conductive polymers,[3,4] organosulfur compounds,[5–7] nitroxyl radical-bearing compounds,[8,9] conjugated carbonyls-containing compounds,[10–13] imine-functionalised compounds,[14,15] and azo-functionalised molecules,[16,17] conjugated carbonyl compounds are particularly promising. An ideal electrode material should have a high capacity, voltage, and conductivity, fast kinetics, low self-discharge, low solubility, good thermal stability and be easy to synthesis. Among the organic cathode materials, however, conductive polymers show poor capacity because of their low doping level. Organosulfur compounds suffer from sluggish reaction kinetics. The self-discharge impedes the practical application of organic radicals. Carbonyl compounds are the most widely studied because of their high capacity and fast kinetics.[18] The conjugated carbonyl groups can react reversibly with lithium ions forming an intermediate with a delocalized charge at potentials around 2.5 V *vs*. Li^+/Li.[19] For example, pyrene-4,5,9,10-tetraone undergoes a four-electron reduction process at an average potential of 2.59 V *vs*. Li^+/Li and reaches a high reversible capacity of 360 mAh g^{-1}.[10] However, small-molecular compounds always suffer from fast capacity fading due to severe dissolution into aprotic electrolytes. The dissolution of the small organic active material in the electrolyte can be suppressed by various strategies, including grafting the electroactive molecule into a conductive backbone (*e.g.* glassy-carbon and Ketjenblack),[20] forming a salt,[21] and synthesising insoluble polymeric materials.[22] Polymeric materials are advantageous because their molecular

structures can be chemically tuned based on the employment of different monomers to improve their performance.[23] Recent reports have shown that polymers containing conjugated carbonyl groups show better capacity retention over hundreds of cycles than the corresponding monomers.[24,25] However, it remains challenging for the polymeric organic electrode material due to the inefficient utilisation of the redox-active carbonyl site, particularly at high current rates and during long-term operation. The inefficient utilisation of the carbonyl sites in the polymers is because the accessibility of the carbonyl functional groups is hindered by the polymeric chain.

Conductive coatings and the incorporation of conductive additives have been demonstrated to enhance charge transport in organic electroactive materials for higher rate capability.[26–28] For example, a microporous polyimide covalent-organic framework and carbon nanotube composite that was prepared by *in situ* polycondensation was reported to exhibit a near 100% capacity retention after 8000 cycles, 95 mAh g^{-1} at 2000 mA g^{-1} (19.2 C), and 104 mAh g^{-1} at 200 mA g^{-1} (1.9 C). What is more, the utilisation of the redox-active sites in the COFs was enhanced from 22.6% to 82.9% by the adding of CNT into the COFs. Because the thickness of the COFs became thinner with the presence of CNT, so more electrochemical redox-active sites are accessible.[29] Inspired by this concept, in this chapter, a polyimide (PI) was designed and combined with the conductive rGO for the stable structure and fast redox reactions. In this project, rGO is chosen to be the conductive additive as it has good conductivity and the heteroatom in the structure is a benefit for the reactive monomers to be adsorbed on the surface of rGO, so the polymerisation occurs on the surface of rGO.

3.4 Experimental Section

3.4.1 Materials

Pyromellitic dianhydride (PMDA), *N*-methyl-2-pyrrolidone (NMP), polyvinylidene fluoride (PVDF), and isoquinoline were purchased from Sigma Aldrich. Tetra-(4-aminophenyl) methane (TAPM) was purchased from Manchester Organics, and mesitylene was obtained from Acros Organics. *N*,*N*-Dimethylformamide and tetrahydrofuran were obtained from Fisher. Reduced graphene oxide (rGO) was obtained from Ossila (U. K.; see Figure 3-1 for Raman spectra of CNTs and Table 3-1 for the fitted data). The top panel in Figure 3-1 is the Raman spectrum of rGO and the bottom panels are the zoomed-in and fitted spectra. The fitting and

assignment information can be found in Table 3-1. The D band at 1330 cm^{-1} corresponds to scattering from local defects or disorders present in carbon, and the G bands at 1586 cm^{-1} are from the in-plane tangential stretching of the C−C bonds in the graphitic structure.[30–32] All reagents were used as received without further purification.

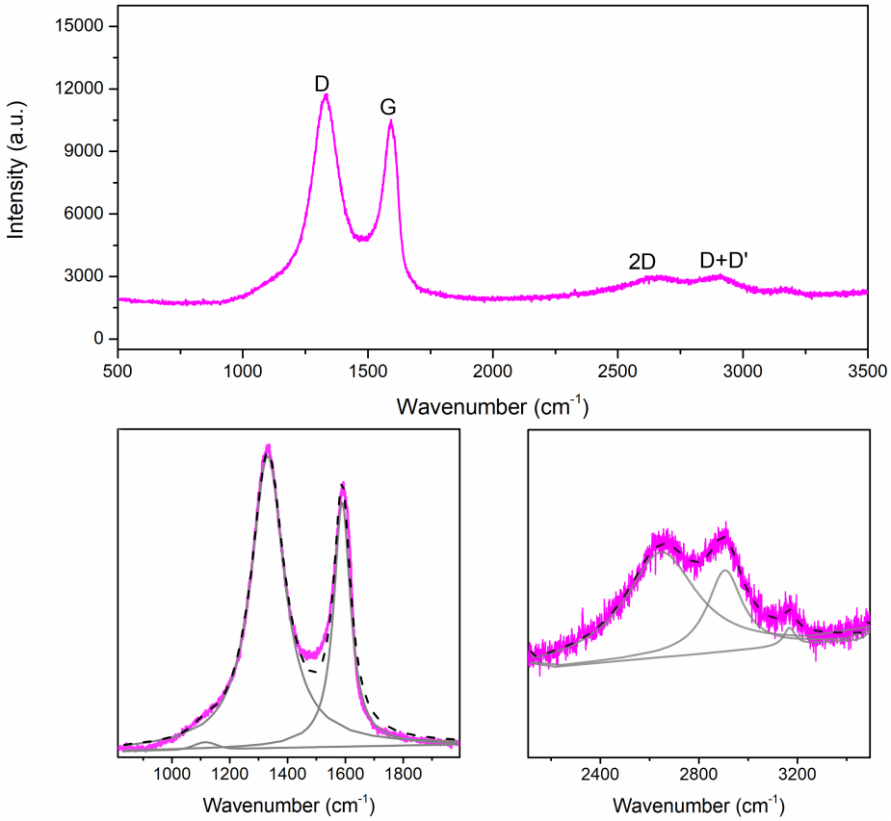

Figure 3-1. Raman spectra of reduced graphene oxide (top) and the corresponding fitted spectral regions (bottom), where the grey lines are the individual fitted peaks and the black dashed lines show the cumulative fit.

Table 3-1. Fitting and assignment information for Raman spectrum of rGO.

Peak Position / cm^{-1}	Amplitude intensity	Integral intensity	FWHM / cm^{-1}	Assignment
1116	231	22289 [a]	90.39743[a]	
1330	9624	1945050	139.56747	D
1586	8046	850249	70.28838	G
2651	891	410018	351.56153	G’ (2D)
2907	690	171420	171.97613	D+G (or D”)
3169	153	13067	56.37192	

[a]Peak fitting was attained using a Gaussian function; fitting of all other peaks was attained using a Lorentzian function. FWHM = full-width at half-maximum. RBM = radial breathing mode. The spectrum is in agreement with previous studies on the Raman spectroscopy of rGO, and all assignments of Raman peaks adapted from previous literature.[30–32]

3.4.2 Preparation of Mechanically Combined PI/rGO Composite

PI/rGO composite was made by the mechanical ball milling method. PI (50 mg) and rGO (50 mg) were placed in a ball mill grinding jar together with seven steel balls (Φ = 3 mm). The mixture was then ball milled at 30 Hz for 30 minutes. The product was recovered for the jar to give the physical mixture PI/rGO. Ball milling was processed on Retsch MM400 with the Grinding jar sizes of 25 ml.

3.4.3 Theoretical Specific Capacity Calculation

The molecular weight of the repeating A unit (M_A = PMDA) and B unit (M_B = TAPM) in the **PI** are 214.15 and 316.44 g mol^{-1}, respectively (Figure 3-2). The contribution of the pyromellitic diimide and tetraphenylmethane to the repeating unit of the polymer is ½ and ¼, respectively. Therefore, the molecular weight of the polyimide repeating unit M_w = 214.15/2+316.44/4= 186.18 g mol^{-1}. And there is only one electrochemical redox site in one repeating unit of the polyimide. The theoretical capacity is 144 mAh g^{-1} calculated using Equation 1-2.

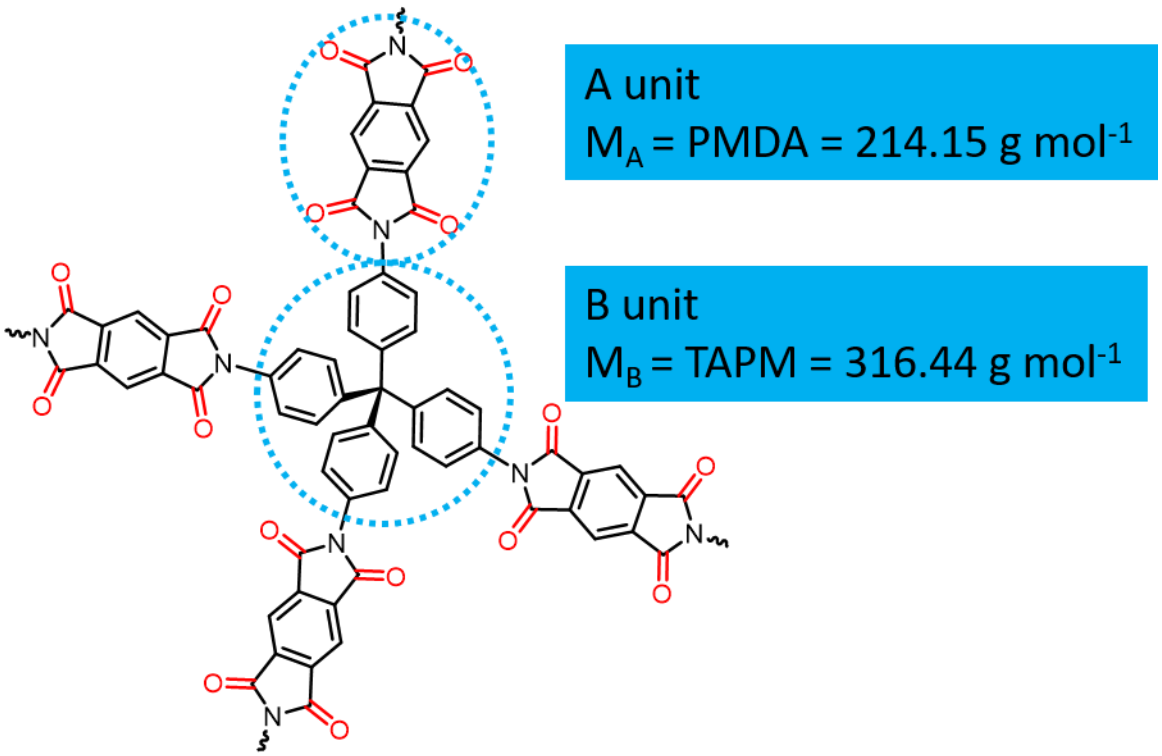

Figure 3-2. Chemical structure of **PI**.

3.4.4 Electrochemical Test Protocol

In the electrode, the mass ratio of active materials (**PI/PIX** (where x = 10, 30 or 50 wt% of rGO)): carbon black: PVDF is 6: 3: 1. In the coin cells, **PI/PIX** was used as the working positive electrode, lithium as the counter electrode, and 1 M LiTFSI in DOL and DME (1:1 v/v) as an electrolyte solution. Here, LiTFSI-DME/DOL-based electrolyte was used to avoid the rapid reduction of organic electrodes capacity in the carbonate electrolyte.[24,33]

Please see Chapter 2 (Section 2.2 Electrochemical Measurements) for the electrochemical test protocol.

3.5 Polyimide Synthesis and Characterisation

The redox-active polyimide **PI** was synthesised according to a reported polycondensation procedure (Scheme 3-1).[34] A 10 mL Pyrex tube was charged with pyromellitic dianhydride (43.6 mg, 0.2 mmol) and tetra-(4-aminophenyl)methane (38.1 mg, 0.1 mmol) in solution of *N*-methyl-2-pyrrolidone (NMP) (0.2 mL), 1,3,5-mesitylene (1.0 mL), and isoquinoline (0.02 mL).

This reaction mixture was homogenized by ultrasonication (VWR, Ultrasonic cleanser, USC-1200TH, output: HF 45 kHz, 180 W) for 10 minutes and the tube was flash-frozen at 77 K (liquid N_2 bath), degassed by three freeze-pump-thaw cycles, and evacuated to an internal pressure of 100 mTorr. The tube was sealed off and heated at 160 °C for 5 days to afford a yellow precipitate, which was isolated by filtration over a medium glass frit and washed with *N*,*N*-dimethylformamide (50.0 mL) and tetrahydrofuran (50.0 mL). The product was dried under reduced pressure at 85 °C to give **PI** as a yellow powder (67 mg, 90%). Anal. calcd. for $(C_{45}H_{20}N_4O_8)_n$: C 72.5, H 2.68, N 7.52%; found: C 65.85, H 3.53, N 8.03%. **PI** is insoluble in water and common organic solvents, such as acetone, ethanol, *n*-hexane, tetrahydrofuran, *N,N'*-dimethylformamide.

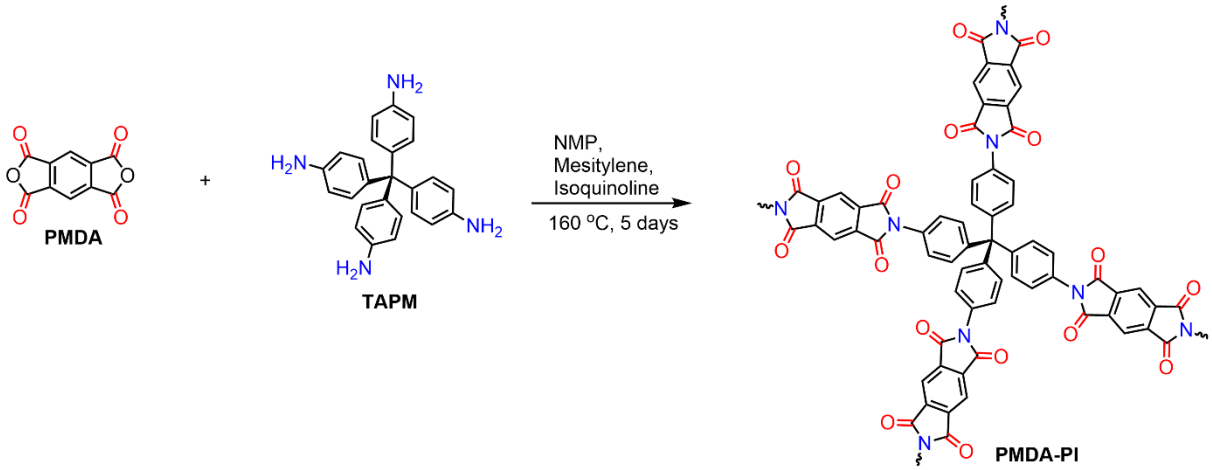

Scheme 3-1. Synthesis of the PMDA-based polyimide polymer network.

The chemical structure of the polyimide was characterised by Fourier-transform infrared spectroscopy (FT-IR). It shows that the stretching vibrations of the $-NH_2$ groups in **TAPM**, at around 3300 cm^{-1}, disappear in the IR spectra of the **PI**, indicating that **TAPM** underwent polycondensation with **PMDA** (Figure 3-3). Bands at 1772 and 1719 cm^{-1}, attributed to asymmetric and symmetric stretching vibrations of the C=O groups of the five-membered imide rings, were observed in the IR spectra of the **PI**, as was the band at 1356 cm^{-1}, assigned to C–N–C moiety. In addition, in the IR spectrum for **PI** there were no IR bands at 1763 cm^{-1}, corresponding to unreacted anhydride starting material, or at around 1650 cm^{-1}, corresponding to amic acid intermediates. Therein, amic acid describes the group containing carboxylic acid and an amide linker as the intermediate product of the reaction between the anhydride of **PMDA** and primary amines of **TAPM**. These results demonstrate the successful reaction of the **PMDA** and **TAPM**.

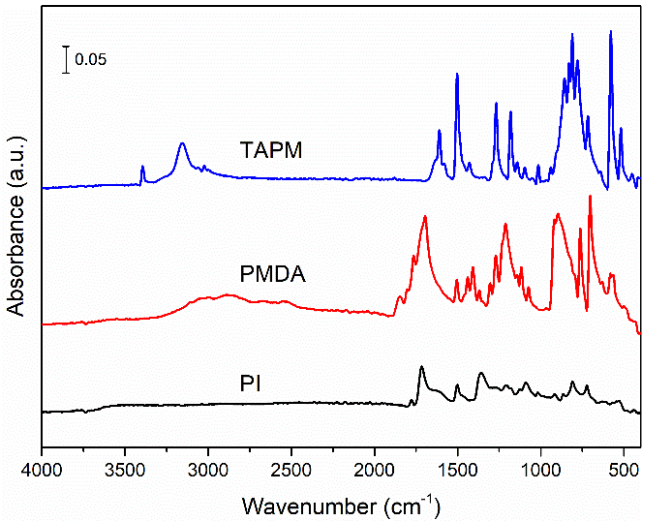

Figure 3-3. FT-IR Spectra of **PI**, **PMDA**, **TAPM**.

SEM was used to determine the morphology of the **PI**. The SEM images of the pristine **PI** show that has a spherical particle morphology and the diameters of the particles range from 1.0 to 7.0 μm (Figure 3-4). In the SEM images, it was also observed that the spherical particles tended to aggregate. Powder X-ray diffraction (PXRD) patterns show that **PI** was amorphous (Figure 3-5). Thermogravimetric analysis (TGA) demonstrated that the **PI** has high thermal stability and did not appear to decompose up to 500 °C under an N_2 atmosphere. The mass loss below 100 °C was attributed to a loss of water that was adsorbed by the polyimide sample. The adsorption behaviour of **PI** was also investigated using N_2 sorption isotherms recorded at 77.3 K. Before recording the adsorption isotherm, the **PI** sample was degassed under 120 °C for 12 hours to remove any water from the sample. The N_2 sorption isotherm indicated that **PI** is non-porous, which indicates the polymer networks are interpenetrated, which is often observed for crosslinked porous polymers.[35,36]

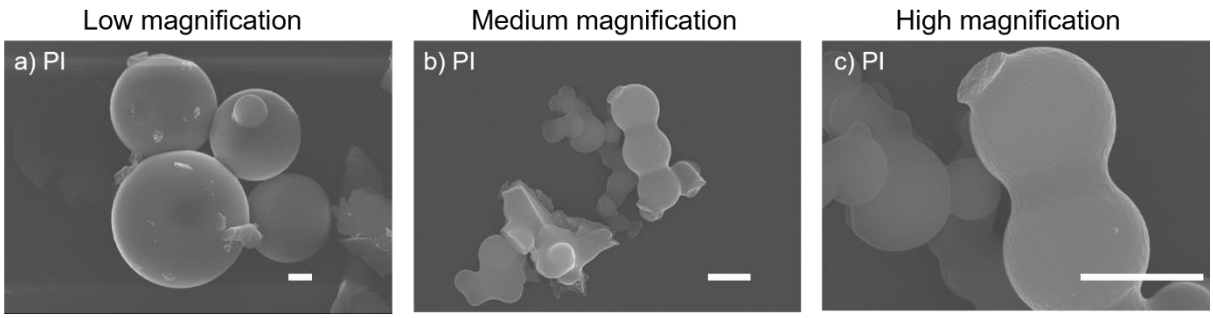

Figure 3-4. SEM images of **PI** (Scale bar: 1 μm).

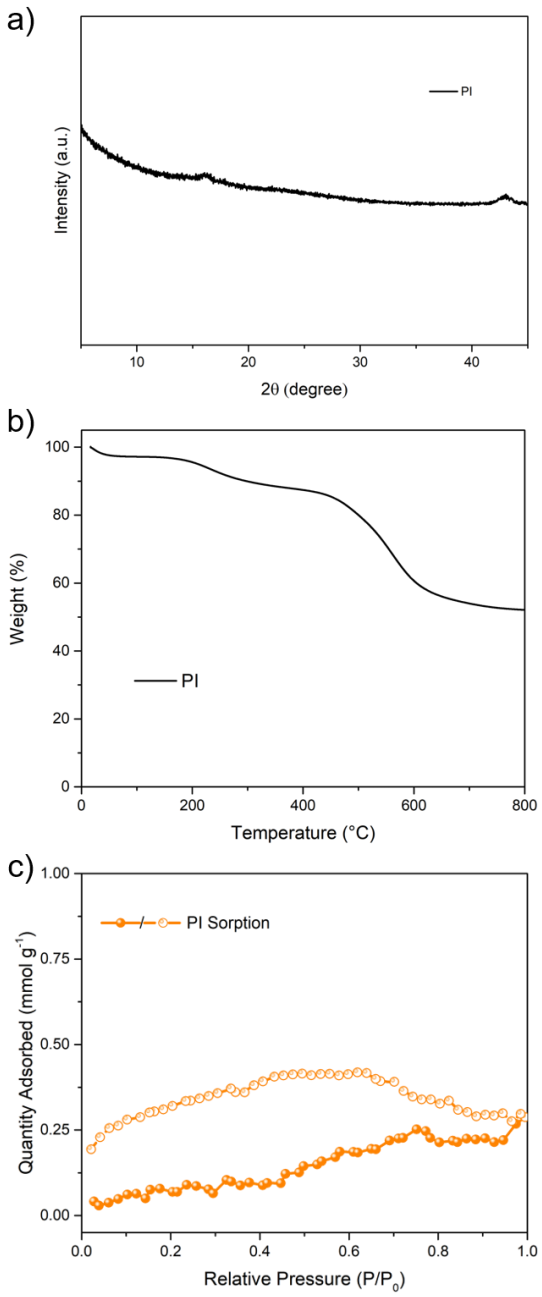

Figure 3-5. (a) Amorphous PXRD patterns of **PI**; (b) TGA plot of **PI**; (c) N_2 sorption isotherms of **PI** (77.3 K, solid symbols = adsorption; open symbols = desorption).

3.6 Polyimide Composite Synthesis and Characterisation

After synthesising **PI**, it was decided that a series of **PI** composites would be synthesised using the same synthetic procedure, but with rGO added into the reaction mixture (Scheme 3-2). Typically, a 10 mL Pyrex tube was charged with pyromellitic dianhydride (43.6 mg, 0.2 mmol),

tetra-(4-aminophenyl)methane (38.1 mg, 0.1 mmol) and reduced graphene oxide (10, 30, 50 wt.% of the composite based on the yield of the **PI**) in solution of *N*-methyl-2-pyrrolidone (NMP) (0.2 mL), 1,3,5-mesitylene (1.0 mL), and isoquinoline (0.02 mL). This reaction mixture was homogenized by ultrasonication for 10 minutes and the tube was flash-frozen at 77 K (liquid N_2 bath), degassed by three freeze-pump-thaw cycles, and evacuated to an internal pressure of 100 mTorr. The tube was sealed off and heated at 160 °C for 5 days to afford a yellow precipitate, which was isolated by filtration over a medium glass frit and washed with *N*,*N*-dimethylformamide (50.0 mL) and tetrahydrofuran (50.0 mL). The product was dried under reduced pressure at 85 °C to give a black powder. In total, four samples were synthesised using the same method: **PI** and rGO composite with 10, 30, and 50 wt. % rGO. The composites are named **PIX**, where **X** = 10, 30, and 50 wt.% of rGO. The yields calculated for **PI10**, **PI30**, and **PI50** were 89.4%, 88.7%, and 87.5%, respectively. Anal. calcd. for **PI10**: C 70.48, H 2.64, N, 8.18%; found: C 64.45, H 3.01, N 7.00%; Anal. calcd. for **PI30**: C 77.04, H 2.05, N 6.36%; found: C 67.42, H 2.43, N 6.74%; Anal. calcd. for **PI50**: C 83.60, H 1.47, N 4.50%; found: C 68.91, H 1.96, N 6.70%).

In the composite, the interaction between the rGO and polyimide is based on the non-covalent bonding, including physical adsorption and the π-stacking interaction which is from the rGO and the conjugated parts in the polymers as well as the heteroatoms with free electron pair.

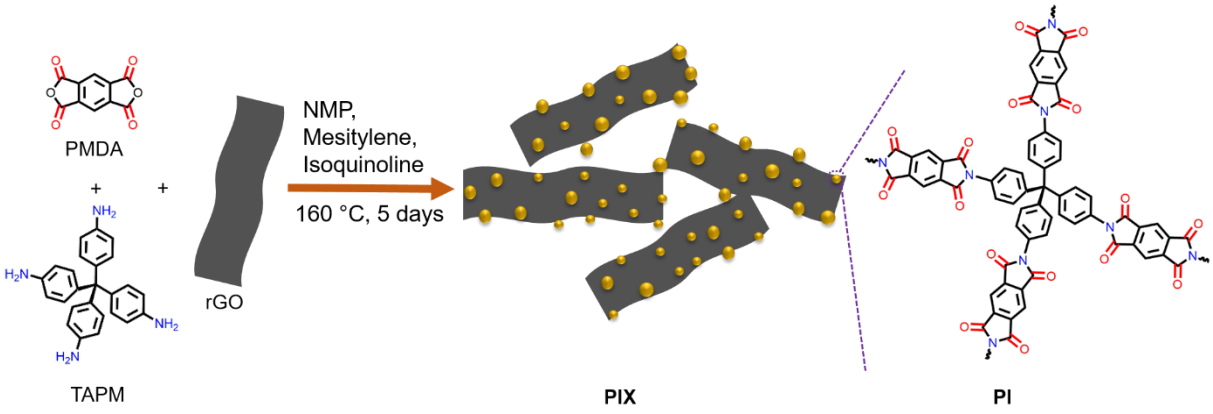

Scheme 3-2. Synthesis of the PMDA-based polyimide and rGO composite.

The **PIX** composites were first characterised by FT-IR (Figure 3-6). The characteristic NH_2 peaks were not observed in the **PIX** IR spectra. A new peak at 1356 cm^{-1} assigned to C–N–C moiety was observed. Peaks at 1772 and 1719 cm^{-1}, attributed to C=O groups of the five-membered imide rings, were observed. This indicates that PMDA reacted with TAPM.

Furthermore, the bands at 1566 and 1191 cm^{-1}, the stretching vibrations of the C=C and C-O-C increased with the rGO content. XRD pattern shows that all the composites samples are amorphous. The TGA profile exhibits that all the composites samples have good thermal stability up to 500 °C under N_2 atmosphere. The mass loss at low temperatures may result from water loss. Compared to the **PI** sample, the **PIX** composites were observed to lose more mass under 100 °C, indicating that the samples adsorb more water when hybridised with rGO. All the PIX composites were found to retain 50% of their mass at 800 °C (Figure 3-4c). The mass loss is from the decomposition of the polyimide. The mass loss observed for the PIX composite materials was comparable to that of the PI.

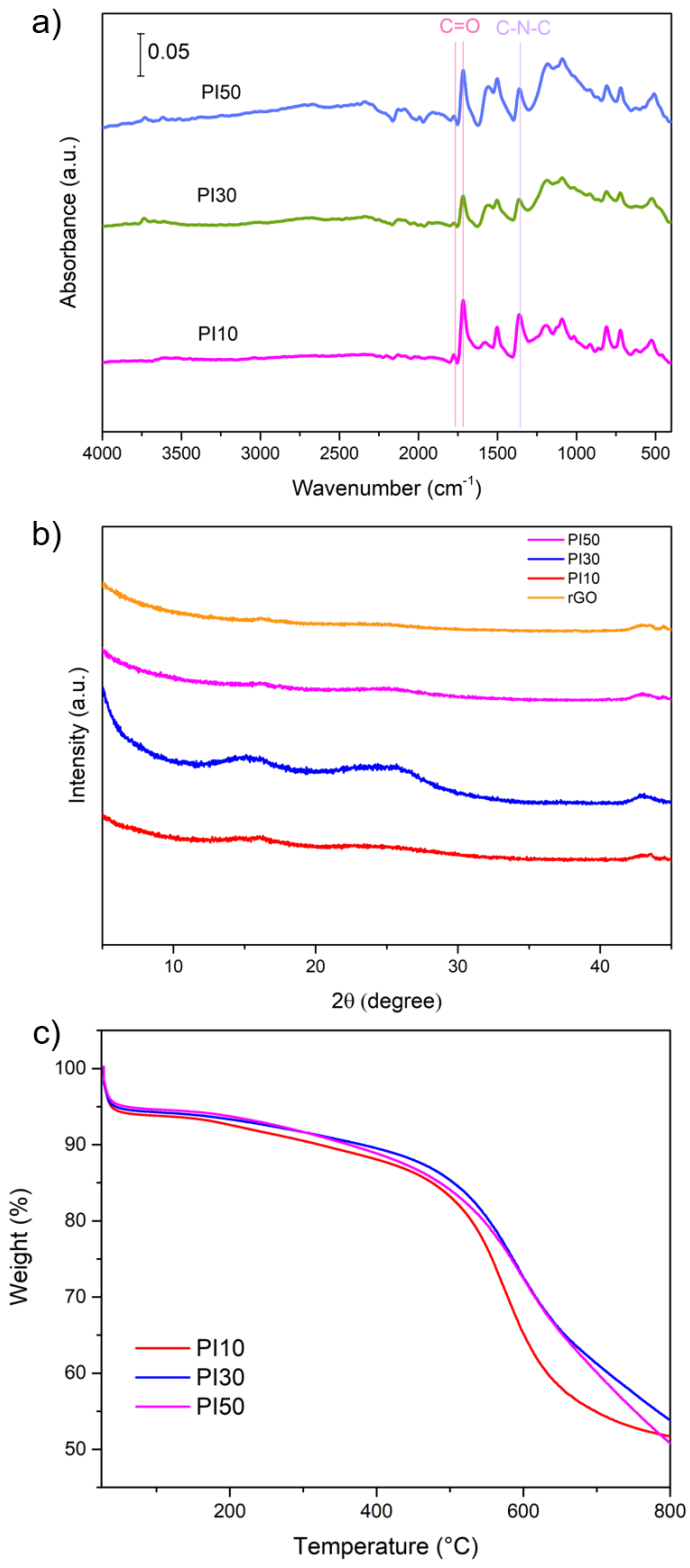

Figure 3-6. (a) FT-IR spectra of PIX; (b) Amorphous PXRD patterns of the **PIX** composites, and rGO; (c) TGA of **PIX.**

The morphology of the **PIX** composites and rGO were characterised by the SEM (Figure 3-7). The rGO powder exhibits a sheet-like morphology as shown in the SEM images. In the composite, we can see that the particle size becomes smaller when adding the rGO in the PIXs because of less aggregation, and further decreases with more rGO. **PI10**, **PI30**, and **PI50** have diameter ranges of 0.2–1.4, 0.2–1.2 and 0.1–0.8 μm, respectively. What is more, the **PI** spheres become less aggregated with the increase of rGO.

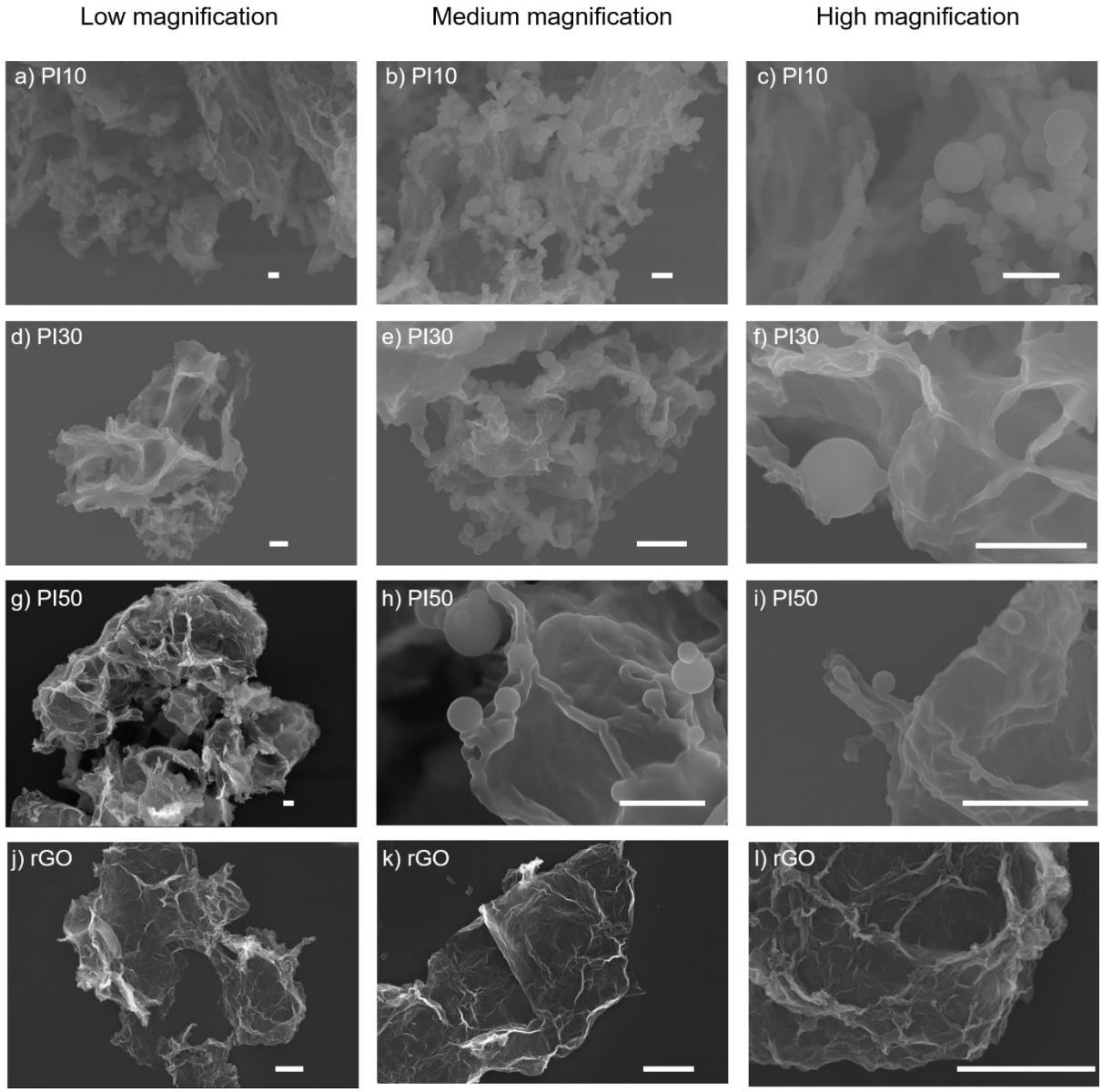

Figure 3-7. SEM Images of (a, b, c) **PI10**; (d, e, f) **PI30**; (g, h, i) **PI50** and (j, k, l) rGO (scale bar: 1μm).

N_2 sorption measurements at 77.3 K were carried out to assess the porosity of **PIX** composite and rGO. **PI10** shows low absorption of N_2 at $P/P_0 = 1.0$, which means **PI10** has a low surface area with a SA_{BET} of 6 m^2 g^{-1}. PI30 and PI50 have Type II gas sorption profiles. The increase of N_2 uptake at a very low relative pressure ($P/P^0 < 0.01$) indicates the presence of micropores in the **PI30** and **PI50**. The adsorption isotherms of **PI30** and **PI50** show an evident hysteresis loop in the medium-pressure region (P/P^0 =0.4–0.7), reflecting that mesopores exist in the composites. Additionally, an increase in the high-pressure region (P/P^0 =0.8–1.0) is also observed in the adsorption and desorption isotherms of the **PI30** and **PI50**, revealing the presence of macropores in these materials. The N_2 isotherm shows that rGO could improve the porosity of **PIX**, as the N_2 sorption capacity of all the **PIXs** composites is higher than that of PI at P/P^0 = 1.0. Pore size distributions of **PIXs** were determined by non-local density functional theory (NL-DFT; Figure 3-8) and indicated the presence of micropores and to a lesser extent of meso- and macropores. SA_{BET} also demonstrates the conclusion.[37] The SA_{BET} of **PIXs** increased with the wt.% of rGO content from 52 m^2 g^{-1} for **PI10** up to 563 m^2 g^{-1} for **PI50** (Table 3-2), even higher than the value of rGO (439 m^2 g^{-1}). Therefore, it appears that the introduction of rGO in the **PIX** composites increases both the SA_{BET} and *t*-plot micropore area of the composite, which has previously been observed by others.[37] Both **PI30** and **PI50** have pores with an average width of 15 Å, which is larger than the diameter of Li^+ cation (1.52 Å) and could, therefore, be beneficial for Li^+ ion transport within the material.

Table 3-2. Surface areas and pore properties of **PI** and the **PIX** composites.

Sample	**SA_{BET}[a] (m^2 g^{-1})**	***t*-plot micropore area[b] (m^2 g^{-1})**	**Total pore volume[c] (cm^3 g^{-1})**
PI	6	-	-
PI10	52	18	0.032
PI30	233	129	0.143
PI50	563	246	0.36

[a]Surface area calculated from the N_2 adsorption isotherms at 77.3 K using the BET equation; [b]Micropore surface area calculated from the nitrogen adsorption isotherms at 77.3 K using the *t*-plot equation with the carbon black model; [c]Pore volume calculated from the nitrogen isotherm at $P/P_0 = 0.99$, 77.3 K.

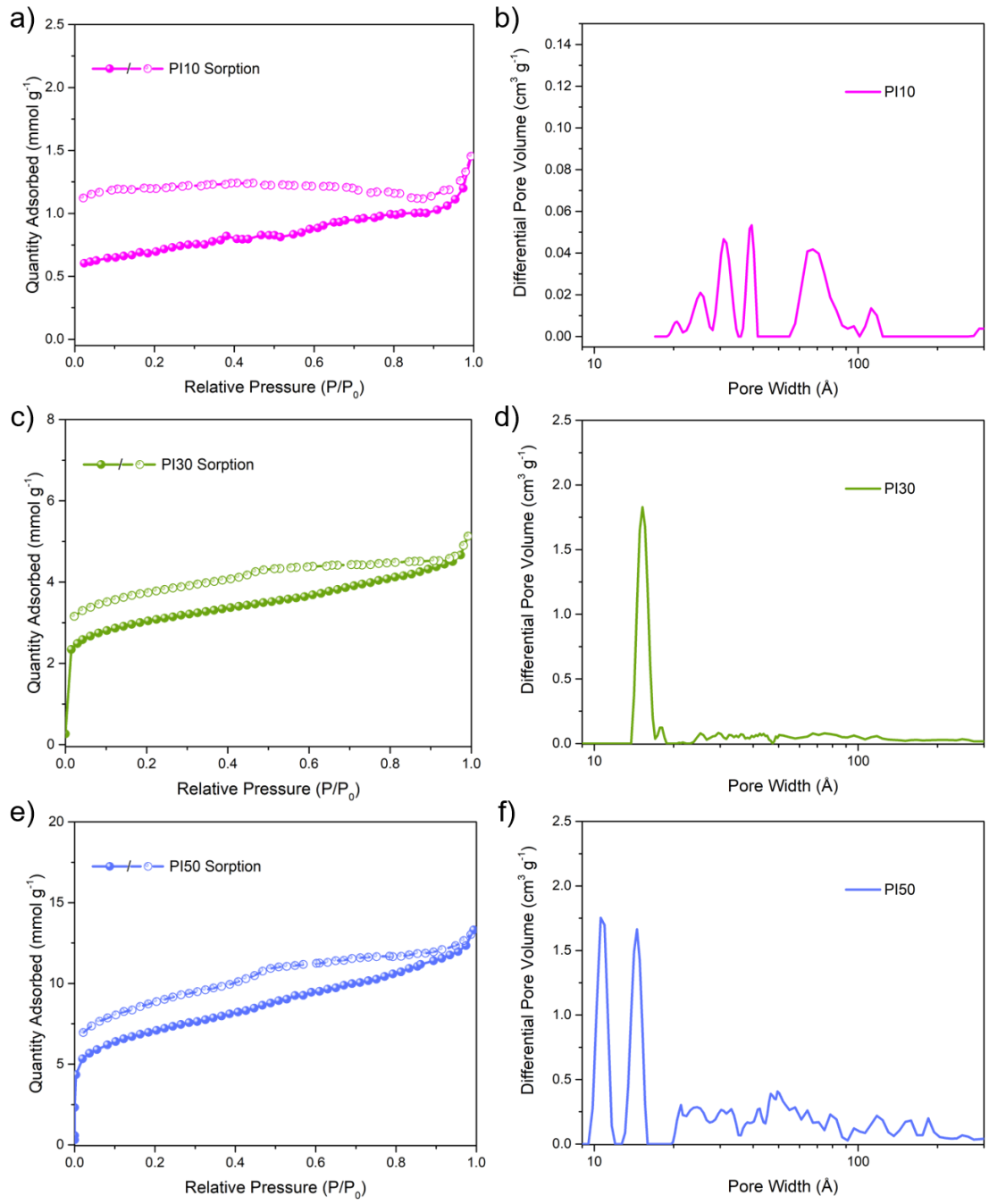

Figure 3-8. (a,c,e) N_2 sorption isotherms of **PIX** composites (77.3 K, solid symbols = adsorption; open symbols = desorption); (b,d,f) Pore size distribution plots of the **PIX** composites (calculated by NL-DFT for pillared clay).

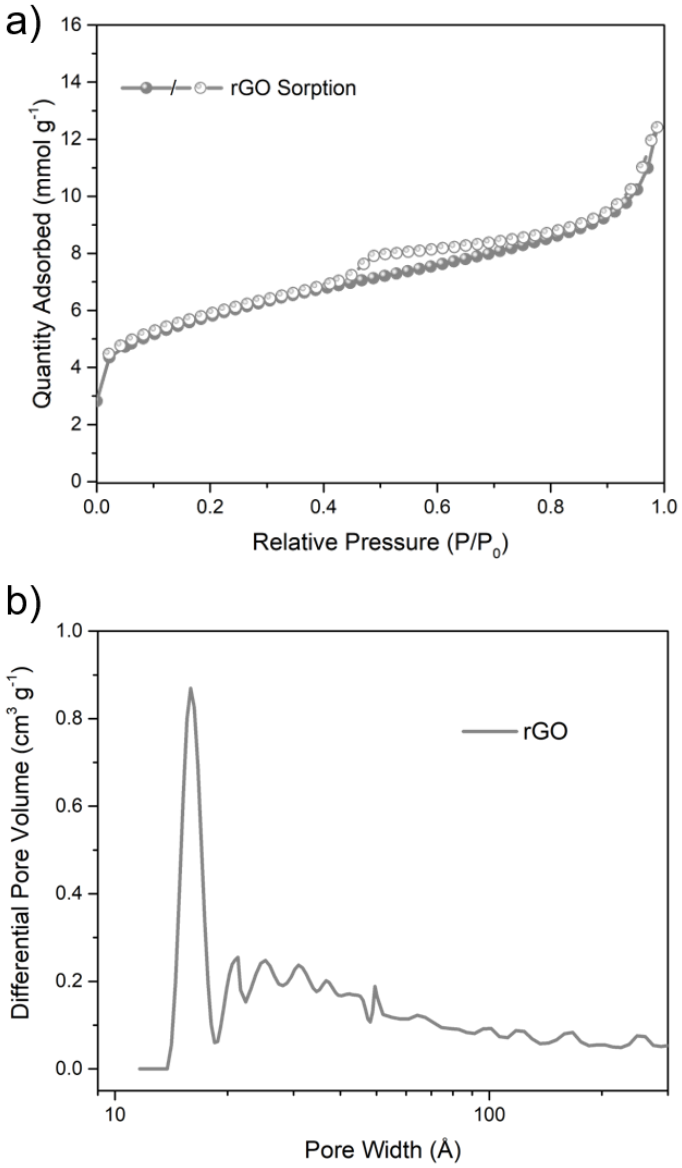

Figure 3-9. (a) N_2 sorption isotherms of rGO (77.3 K, solid symbols = adsorption; open symbols = desorption); (b) Pore size distribution plots of the rGO (calculated by NL-DFT for pillared clay).

3.7 Electrochemical Performance of PI and PIX

Next, we evaluated the electrochemical performance of **PI** and the **PIX** composites as the positive electrode. CV was performed using the **PI** and **PIX** coin cells at 0.1 mV s^{-1} (Figure 3-10) from open circuit potential (2.7 V), with all the samples exhibiting similar shaped CV characteristics. Two pairs of redox peaks corresponding to the two-electron reaction of the carbonyl groups in one PMDA unit were centred at approximately 2.3 and 2.0 V.[24] Furthermore, the peak current densities and integral charge (as normalized to the mass unit of **PI** active material) increased as the mass ratio of rGO in the **PIX** composite was increased. **PI** has the smallest integral charge area, when compared with the **PIX** composites, showing low utilisation of redox-active sites on **PI**. The smaller particle sizes of **PI** in the **PIX** composites mean that they have a larger surface area/volume ratio, which might enhance the number of exposed redox sites on **PI** and thus increases their utilisation. It is also possible that rGO in the composites enhances charge transport within these materials, which is also beneficial.

Galvanostatic charge/discharge experiments were performed in a voltage window of 1.5 to 3.4 V for all positive electrodes (Figure 3-10). In the charge/discharge profile, all the electrode material shows a slope rather than a plateau. Take **PI50** for example, when the cell is discharged from 3.4 to 1.5V, the discharge profile has a slope from about 2.3 to 2.0 V. Therefore, the average discharge potential is approximately 2.15 V. At a current density of 500 mA g^{-1}, **PI** has a limited capacity of 3 mAh g^{-1}, which is only 2.2% of the maximum theoretical specific capacity for **PI** (144 mAh g^{-1}, see Figure 3-2 for calculation details). This low utilisation of its electrochemical redox-active sites is likely due to the poor electrical conductivity of **PI**, and non-accessible redox sites due to the inherent non-porosity of the polymer. Indeed, it was found that the composites (containing rGO) show higher capacities of 14, 53, and 172 mAh g^{-1} at 500 mA g^{-1} for **PI10**, **PI30**, and **PI50**, respectively. While rGO can contribute to the capacity of the **PIX** composites (*vide infra*), rGO can only contribute up to 5, 21, and 48 mAh g^{-1} to the specific capacities of **PI10**, **PI30**, and **PI50**, respectively. Hence, the utilisation of redox-active sites, compared to the theoretical specific capacity, increases significantly to 6.2, 22, and 86% for **PI10**, **PI30**, and **PI50**, respectively. Moreover, **PIX** materials exhibited good cycle life performance, and capacity retentions after 200 cycles are 93, 96, and 98% for **PI10**, **PI30**, and **PI50** (Figure 3-10).

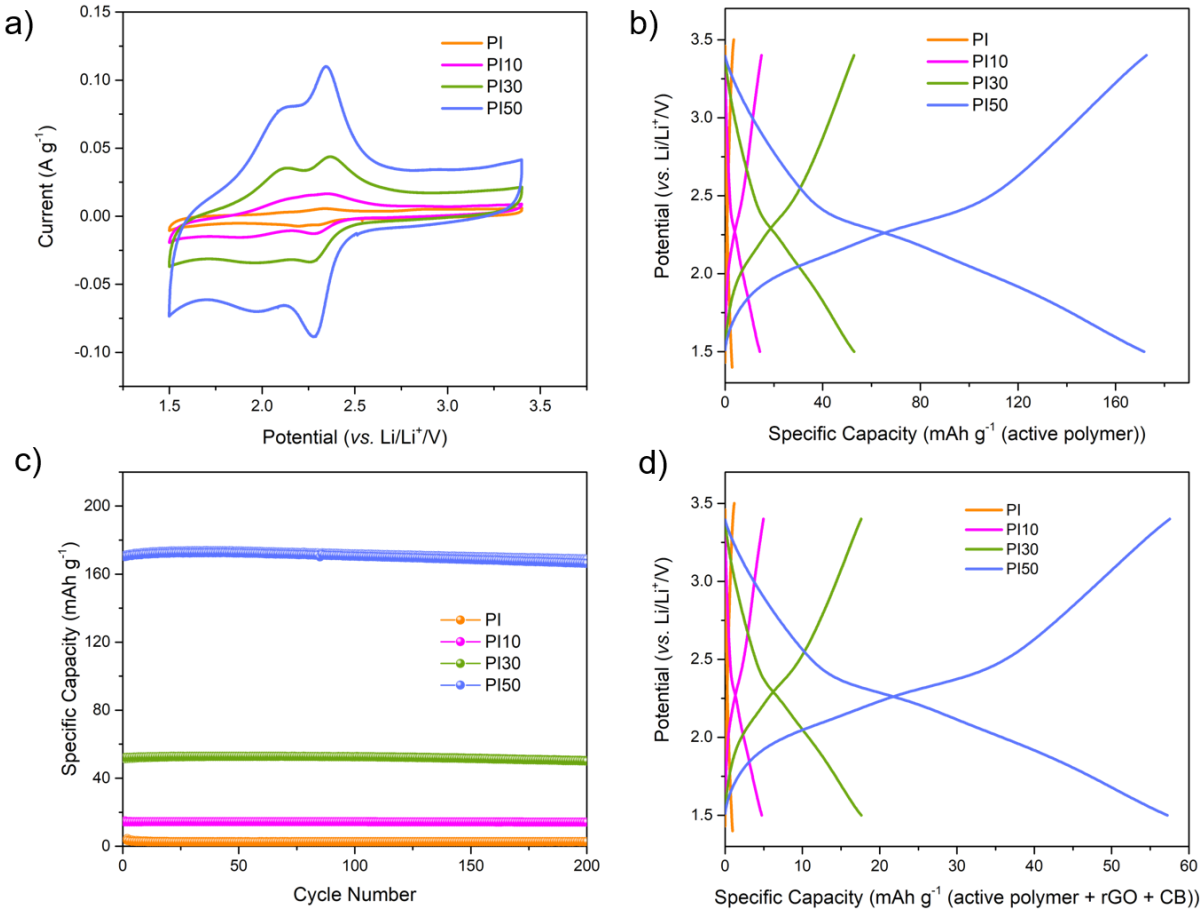

Figure 3-10. (a) Cyclic voltammetry profiles at a scan rate of 0.1 mV s^{-1}; (b) Charge-discharge profiles at 500 mA g^{-1}; (c) Cycling performances over 200 cycles at 500 mA g^{-1}; (d) Charge-discharge profiles (based on active polymer, rGO, and carbon black (CB)) at 500 mA g^{-1} for **PI**, **PI10**, **PI30**, and **PI50**.

The capacity of **PI50** is comparable to typical positive electrode materials used in commercial cells, such as $LiCoO_2$ which has a capacity of 145 mAh g^{-1} and a cycle life of 1000, when considering the active material.[38] However, the capacity of the **PI50** cell was only 52 mAh g^{-1} (Figure 3-10) when calculated based on the total mass of the active material and conductive additives. Here, all gravimetric capacities and currents are normalized to the mass of the active material (**PI**), with the exception of Figure 3-10d, wherein the galvanostatic charge/discharge profiles are based on the mass of the whole electrode in the cell.

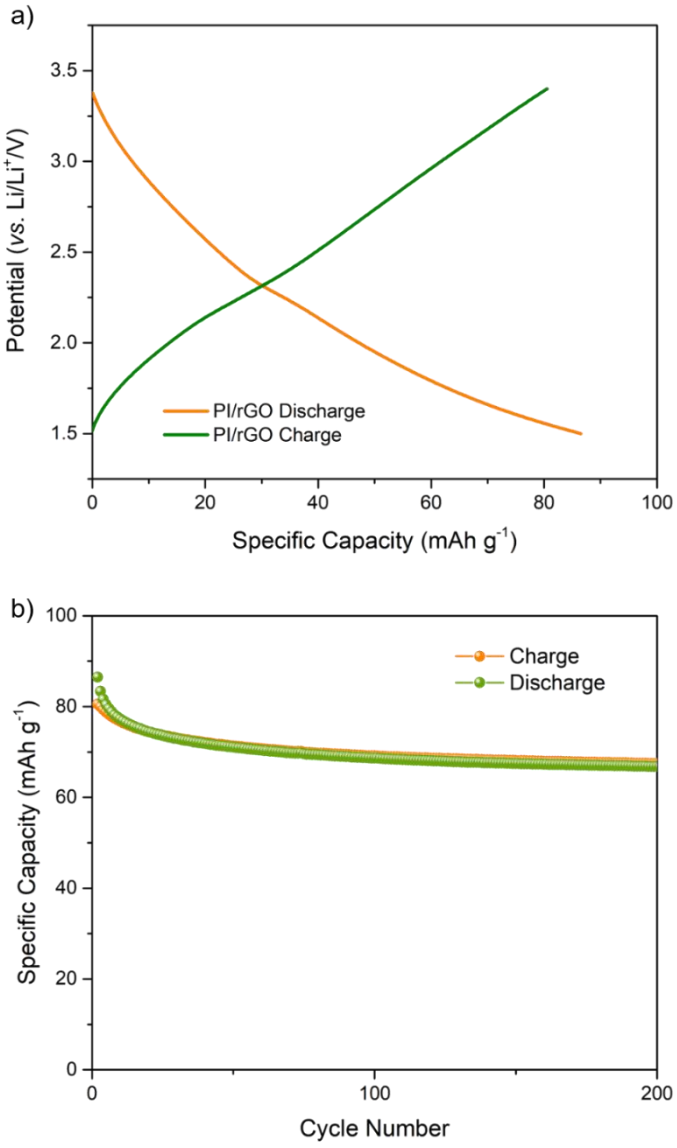

Figure 3-11. (a) Galvanostatic charge/discharge curve of PI/rGO at 500 mA g^{-1}; (b) Cycling performance over 200 cycles for at PI/rGO at 500 mA g^{-1}.

The intricate mixture of the **PIX** composites was further explored to obtain an increase in performance. For this, a physical mixture of **PI** with rGO (PI/rGO) was prepared by ball milling a 1:1 mass ratio of **PI** and rGO. When this composition was used as the active component the resulting cell had a capacity of 86 mAh g^{-1} (Figure 3-11) at 500 mA g^{-1}, which is 70% lower than **PI50**, which was synthesised by *in situ* polycondensation. The physical mixture also has lower capacity retention of 78% after 200 cycles (Figure 3-11). The additives used in the cells—that is, rGO and carbon black—were also tested for their electrochemical performance,

to evaluate their respective contributions towards the overall performance of the cells. When tested under the same conditions rGO: PVDF (9: 1 by mass) and carbon black: PVDF (9:1 by mass), these materials exhibited specific capacities of 48 and 1 mAh g^{-1}, respectively, originating primarily from capacitive charging of the electrochemical double layer (Figure 3-12).

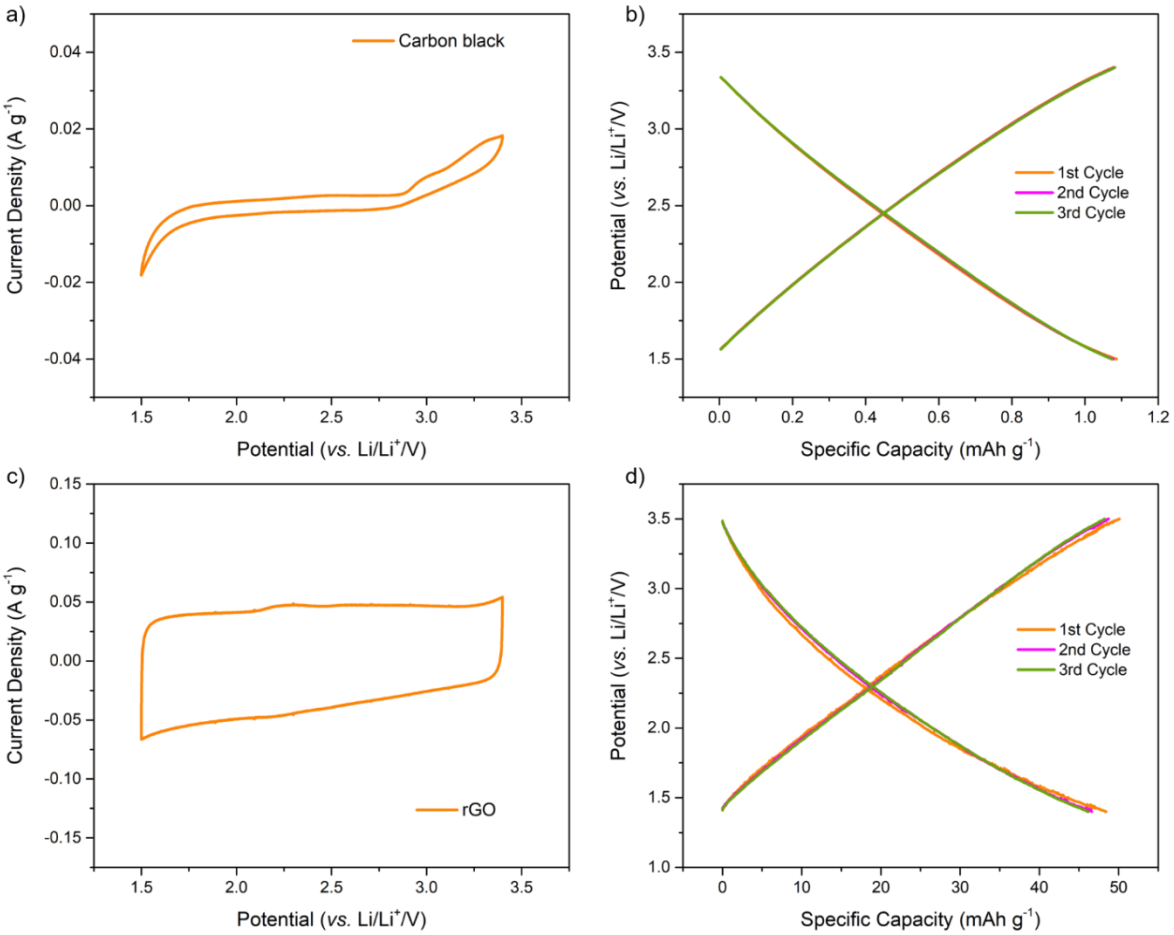

Figure 3-12. (a) Cyclic voltammetry profile of carbon black (Super C65) at a scan rate of 0.5 mV s^{-1}; (b) Galvanostatic charge/discharge curve of carbon black (Super C65) at 500 mA g^{-1}; (c) Cyclic voltammetry profile of rGO at a scan rate of 0.5 mV s^{-1}; (d) Galvanostatic charge/discharge curve of rGO at 500 mA g^{-1}.

Cycle life is another important factor for the performance of a rechargeable battery, in addition to the specific capacity of the material. The long-term cycling performance of **PI50** was studied at 2000 mA g^{-1} (Figure 3-13a). A capacity of over 125 mAh g^{-1} was observed, and minor capacity loss was observed corresponding to 80% retention of the highest recorded capacity after 9000 charge-discharge cycles (equating to a capacity loss of *ca.* 0.0027% per cycle,),

demonstrating stable active site utilisation and excellent rate performance. The Coulombic efficiency was also maintained at close to 100%, at a current density of 2000 mA g^{-1} (about 13.8 C). The capacity fading during long cycling may be because there are trace amounts of Li ions trapped in the polymer. The cycling performance of **PI50** outperforms a series of organic hybrid materials, prepared using graphene, rGO, and carbon nanotubes (Figure 3-13 and Table 3-3). For example, a polyimide COF (PI-ECOF-1/rGO50) was reported to have a 76% capacity retention after 300 charge-discharge cycles under 1 C,[24] a poly(imide-benzoquinone) COF (PIBN-G) exhibited 88% of the initial capacity after 300 charge-discharge cycles under 5 C,[11] and a polyarylimide COF (2D-PAI@CNT) showing the highest cycling performance reported (at 100% retention after 8000 charge-discharge cycles at 20 C).[29] In this context, it is important to note that long-term testing is required to make fair conclusions regarding materials performances, which is unfortunately often not reported.

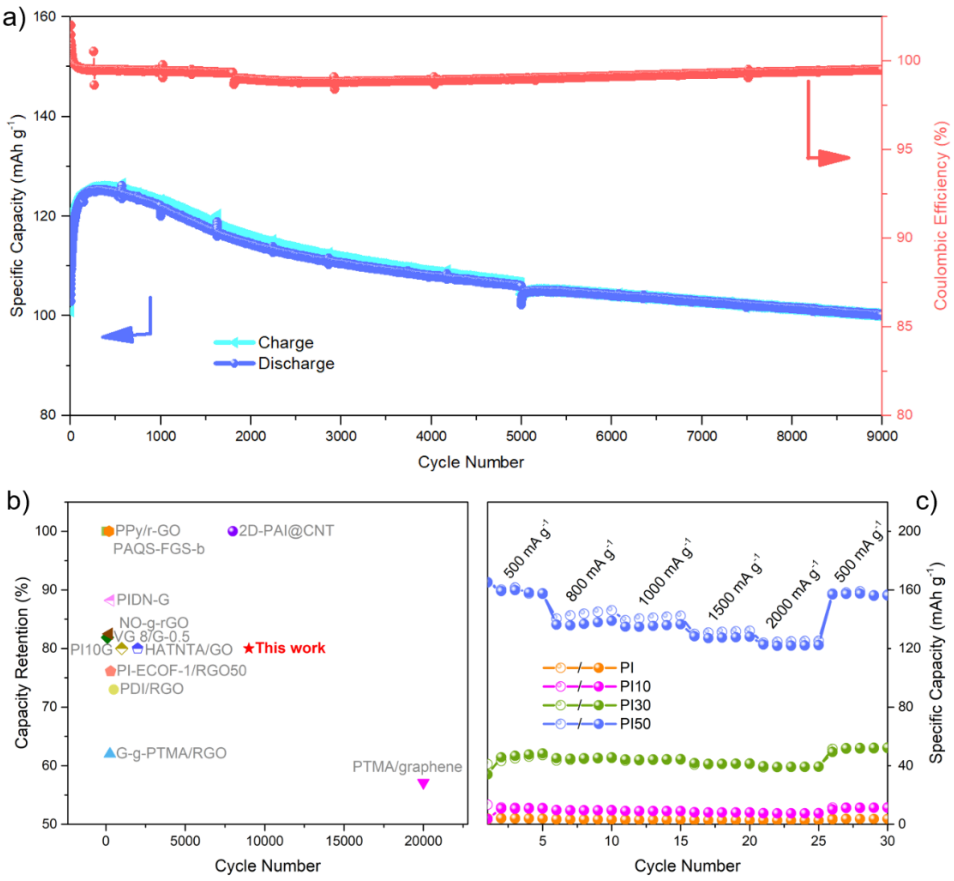

Figure 3-13. (a) Long-term cycling stability of **PI50** at 2000 mA g^{-1}; (b) Comparison of the cycling performance to other polyimide cathodes (reference information for comparative data shown in Table 3-3); (c) Rate performance of **PI**, **PI10**, **PI30**, and **PI50**. Please note that the break in the Coulombic efficiency plot is due to a break in the cycling measurement.

Table 3-3. Battery performance comparison of **PIX50** with other reported PI cathodes (Chemical structures displayed in Figure 3-14).

Sample	**Key Functional Group**	**Capacity Max (mAh g^{-1})**	**Capacity Retention (%)**	**Symbol and Colour used in Figure 3-13b**	**Ref.**
2D-PAI@CNT	Naphthimide	104 at 0.96 C	100 after 8000 cycles (20 C)	Purple sphere	[29]
PIBN-G	Imide-benzoquinone	270 at 0.1 C	88.2 after 300 cycles (5 C)	Pink triangle	[11]
PI-ECOF-1/rGO50	Imide	167 at 0.1 C	76.1 after 300 cycles (1 C)	Orange pentagon	[24]
PAQS-FGS-b	Anthraquinone	165 at 0.1 C	100 after 20 cycles (10 C)	Green square	[39]
G-g-PTMA/RGO	Nitroxide radical	466 at 200 mA g^{-1}	62 after 250 cycles (400 mA g^{-1})	Cayno triangle	[40]
PTMA/graphene	Nitroxide radical	222 at 1 C	57.1 after 20000 cycles (100 C)	Magnet triangle	[41]
VG 8/G-0.5	Anthraquinone	330 at 50 mA g^{-1}	81.9 after 100 cycles (100 mA g^{-1})	Green diamond	[42]
PI10G	Imide	232.6 at 0.1 C	80 after 1000 cycles (50 C)	Khaki diamond	[43]
HATN/GO	Hexaazatrinaphthalene	410 at 50 mA g^{-1}	80 after 2000 cycles (500 mA g^{-1})	Blue Pentagon	[44]
PDI/RGO	Imide	81.5 at 25 mA g^{-1}	73 after 500 cycles (25 mA g^{-1})	Yellow circle	[45]
NO-g-rGO	Nitroxide radical	310 at 0.5 C	82.5 after 200 cycles (0.5 C)	Brown triangle	[46]
PI50	Imide	172 at 500 mA g^{-1}	80 after 9000 cycles (2000 mA g^{-1} =13.8 C)	Red star	**This work**

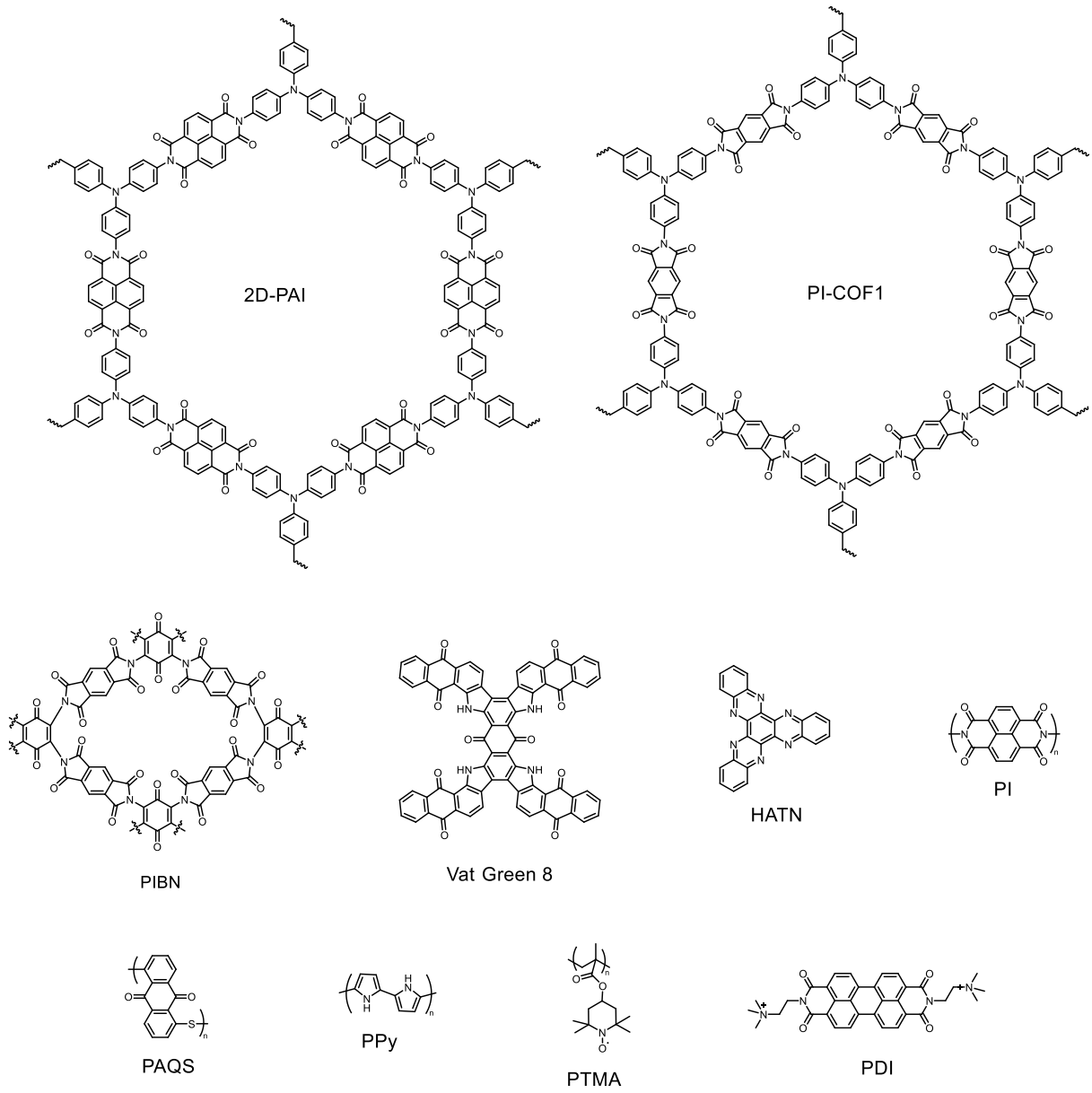

Figure 3-14. Chemical structures of the molecule are mentioned in Table 3-3.

To understand the potential structural/chemical changes of **PI50** after the long-term cycling test, FT-IR spectra were measured for the as-made material and for electrode material that was recovered from a cell of 500 charge-discharge cycles at 500 mA g^{-1}. For the cycled material, the coin cell was disassembled inside a glovebox and the electrode was washed with DOL before being dried under reduced pressure at room temperature to remove residual electrolyte salt. The FT-IR measurements were then performed under a dry N_2 atmosphere. The FT-IR spectra of the **PI50** electrodes before and after 500 cycles showed that the characteristic carbonyl (1772 and 1718 cm^{-1}) and C-N-C (1356 cm^{-1}) bands were retained after cycling (Figure 3-15). The FT-IR spectra of the electrode before and after cycling are taken from

different coin cells, so the intensity of the peaks at the same wavenumber is different. SEM images taken after the cycling experiment showed no obvious changes to the morphology of **PI50** after 500 cycles (Figure 3-16).

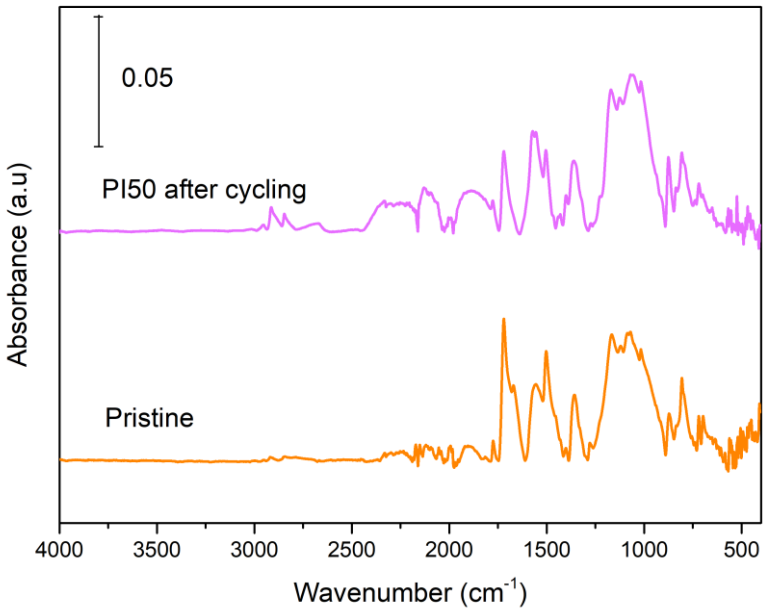

Figure 3-15. FT-IR spectra of **PI50** electrode before and after 500 cycles. The scale bar is the intensity of the absorbed signal.

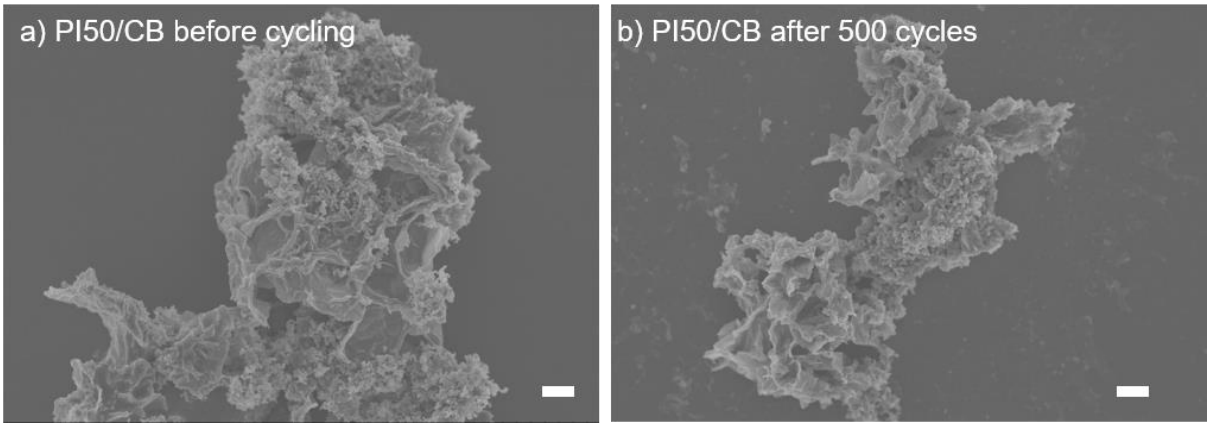

Figure 3-16. SEM Images of **PI50** electrode before and after 500 cycles at 500 mA g^{-1} (scale bar: 1µm)

The rate performance of **PI** and the **PIX** composites were investigated at different current densities (Figure 3-13c) and found the capacity decreases over the current rate range from 500–2000 mA g^{-1} (3.5 C to 13.9 C). Reversible capacities for **PI50** of 165, 145, 142, 132, and 125

mAh g^{-1} were determined at 500, 800, 1000 1500, and 2000 mA g^{-1}, respectively. In addition, the capacity of 165 mAh g^{-1} for **PI50** recovered to 159 mAh g^{-1} after 20 cycles at different currents, corresponding to 96% of the initial capacity at 500 mAh g^{-1}, implying good rate performance. **PI50** has the best rate performance in the **PI** and **PIX** electrodes because the reduced particle size of polyimide in **PI50** improved the contact between the polyimide and the conductive carbon and the increased amount of rGO in the composite leading to a better conductivity of the electrode. It is proved by the EIS test, in which **PI50** shows the smallest charge transfer resistance (Figure 3-18 and Table 3-4). The rate performance of **PI50** is better than many other reported polyimide electrode materials; for example, PI-ECOF-1/rGO30 and PI-ECOF-1/rGO50 discharged at 10 C still retain capacities of 60 mAh g^{-1} and 90 mAh g^{-1},[24] while DAAQ-ECOF has a capacity of 87 mAh g^{-1} at a current density of 2000 mA g^{-1}, which is equivalent to 13.2 C.[47]

To further understand the rate capability, the electrochemical reaction kinetics of **PI50** were investigated by scanning the CV at different sweep rates (Figure 3-17). The current response (i) of **PI50** to the applied sweep rate (v, 0.1–1.0 mV s^{-1}) was measured (Figure 3-17b). According to the power law, $i = av^b$, b-values close to 0.5 indicate that the current is controlled by semi-infinite linear diffusion, by contrast, b-values close to 1 indicate that the current is surface-controlled. The b-values of four redox peaks R1, R2, O1 and O2 (0.90, 0.90, 0.86, and 0.89) are all close to 1 (Figure 3-17b), indicating that the charge storage in **PI50** is a fast surface-controlled process, which is expected as storage is through reversible redox-active functional groups. To account for some of the dominant capacitive contributions from the rGO, the equivalent peak analysis was performed following baseline subtractions from linear back extrapolation of the positive and negative currents baselines in the region of ca. 2.8 - 3.2 V *vs*. Li^+/Li. Consequently, the derived b-values for R1, R2, O1, and O2 reduced only slightly (0.8, 0.74, 0.84, 0.85, respectively, Figure 3-17c), further supporting the nature of the surface-controlled processes on the active polymer. Further analysis of the voltammetric sweep rate dependence enables the surface-controlled contribution to the current response to be quantitatively distinguished.[29,48] We can express the current response at a fixed potential as being the combination of two separate mechanisms, surface-controlled contribution and diffusion-controlled insertion processes; $i = k_1v + k_2v^{1/2}$. The exact surface-controlled contribution (k_1v) can be further quantified, where k_1 and k_2 constants can be simulated by plotting $iv^{-1/2}$ vs $v^{1/2}$, in which $k_1$and k_2 are the slope and intercept of the linear fitting plot. At

0.1 mV s^{-1}, the surface contribution was determined to be 68%, which is further enhanced to 87% at 1 mV s^{-1}.

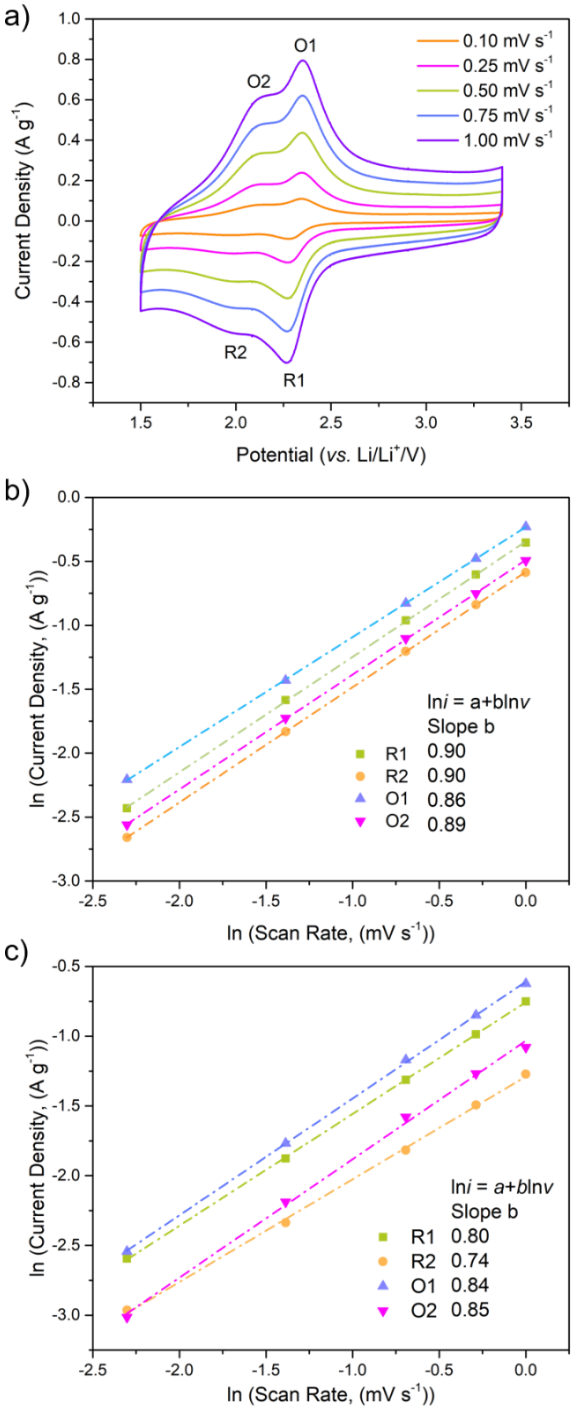

Figure 3-17. (a) Cyclic voltammograms of **PI50** collected at different scan rates; (b) ln *i vs.* ln V plots to determine the b values of different peaks; **(c)** ln*i* vs. ln*v* plots to determine the b values of different peaks based on the subtracted data.

EIS was employed to further characterise the electrochemical and transport behaviour of **PI** and the **PIX** composites (Figure 3-18a). A charge transfer resistance value R_c was obtained by fitting Nyquist plots using an equivalent circuit model (Figure 3-18b). In this circuit, the constant phase element (CPE), the charge transfer resistance (R_c), the resistance of the solution (R_s), and the mass transport resistance (W) were considered. The CPE is in parallel to the resistance R_c and W, and they are connected in series to Rs (see the equivalent circuit diagram in Figure 3-18b). The semicircles in high-frequency regions denote charge transfer resistance (R_c), which is related to reaction kinetics, and the linear increase in the low-frequency regions represents Li^+ diffusion resistance in the electrolyte. Fitted values for the individual elements in the equivalent circuit of the EIS data of **PI** and the **PIX** composite electrodes are summarised in Table 3-4. It was found that that the R_c of **PI50** (22.1 Ω) is smaller than that of **PI** (47.4 Ω), **PI10** (38.1 Ω), **PI30** (35.4 Ω), supporting the assertion of improved charge transfer in **PI50** due to optimisation of contact between the **PI** and conductive carbon network.

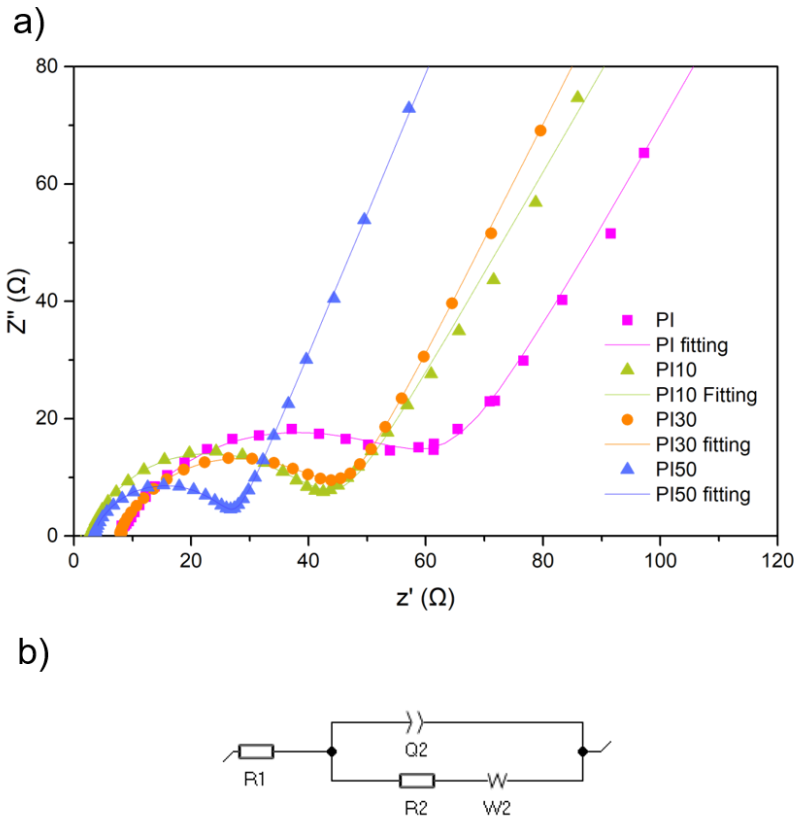

Figure 3-18. (a) EIS spectra of **PI** and the **PIX** composite electrodes; (b) Equivalent circuit used for fitting the electrochemical impedance data. The R_s (R1), R_c (R2), CPE (Q2) and W (W2) represent cell solution resistance, charge-transfer resistance, constant phase element and Warburg impedance.

Table 3-4. Fitted values of elements in the equivalent circuit for EIS data of **PI** and the **PIX** composite electrodes.

	R_s (Ω)	CPE (F)	R_c (Ω)	W(Ω)
PI	8.1	22.9×10^{-6}	47.7	26.3
PI10	2.7	24.1×10^{-6}	38.1	4.3
PI30	7.7	37.8×10^{-6}	35.4	10.3
PI50	3.3	17.7×10^{-6}	22.1	4.2

3.8 Investigation of the Redox Intermediates

It is important to gain insight into the mechanism of the lithiation and delithiation of conjugated carbonyl-containing compounds for further material discovery. Here *ex situ* FT-IR spectroscopy was used to understand the redox processes. The underlying redox processes of the polyimide in the presence of lithium ions were investigated using *ex situ* FT-IR spectroscopy (Figure 3-19a). Cells with **PI50** as the active material were disassembled at the end of the lithiation and delithiation stages, washed by DOL and dried under reduced pressure at room temperature, and FT-IR spectra were then recorded. It was found that for the pristine electrode materials, the IR band at 1497 and 1579 cm^{-1} can be assigned to the vibration of C=C bonds, and peaks at 1718 and 1772 cm^{-1} are assigned to the vibration of the C=O bonds in **PI50**. When the sample was discharged to 1.5 V (lithiation), a new band at 1450 cm^{-1} became visible and this band is attributed to the vibration of C=C bonds. A new band at 1313 cm^{-1} can be assigned to the vibration of C–O bonds, indicating the formation of new C=C bonds and C–O–Li bonds in lithiated **PI50**. The signal at 1718 and 1772 cm^{-1} relating to C=O bonds is weaker after discharge to 1.5 V. When charged back to 3.4 V, the band at 1450 and 1313 cm^{-1} disappeared and the signal at 1718 and 1772 cm^{-1} returned to a state similar to that of the pristine sample, implying that the lithiation/delithiation process is reversible under these conditions. The IR signal intensity of carbonyl groups on the polyimide is reduced, but still, a low-intensity band remains visible indicates that not full, but rather a partial lithiation of the polyimide C=O bonds occurs during the discharging process. This is in line with the observed electrochemical performance. The reversible changes of the C=O and C=C bonds vibrational modes in the electrode agree with the lithiation/delithiation of carbonyls in **PI50**, which is evidence for participation of C=O double bonds in the redox reaction.

Based on these results we suggest a mechanism as outlined in Figure 3-19b that involves redox reactions of carbonyl units in **PI**. This is in line with previous reports that have also suggested

that only two carbonyl groups of dianhydride PMDA moieties participate in the redox reactions due to the electrostatic repulsion between injected negative charges.[12,49]

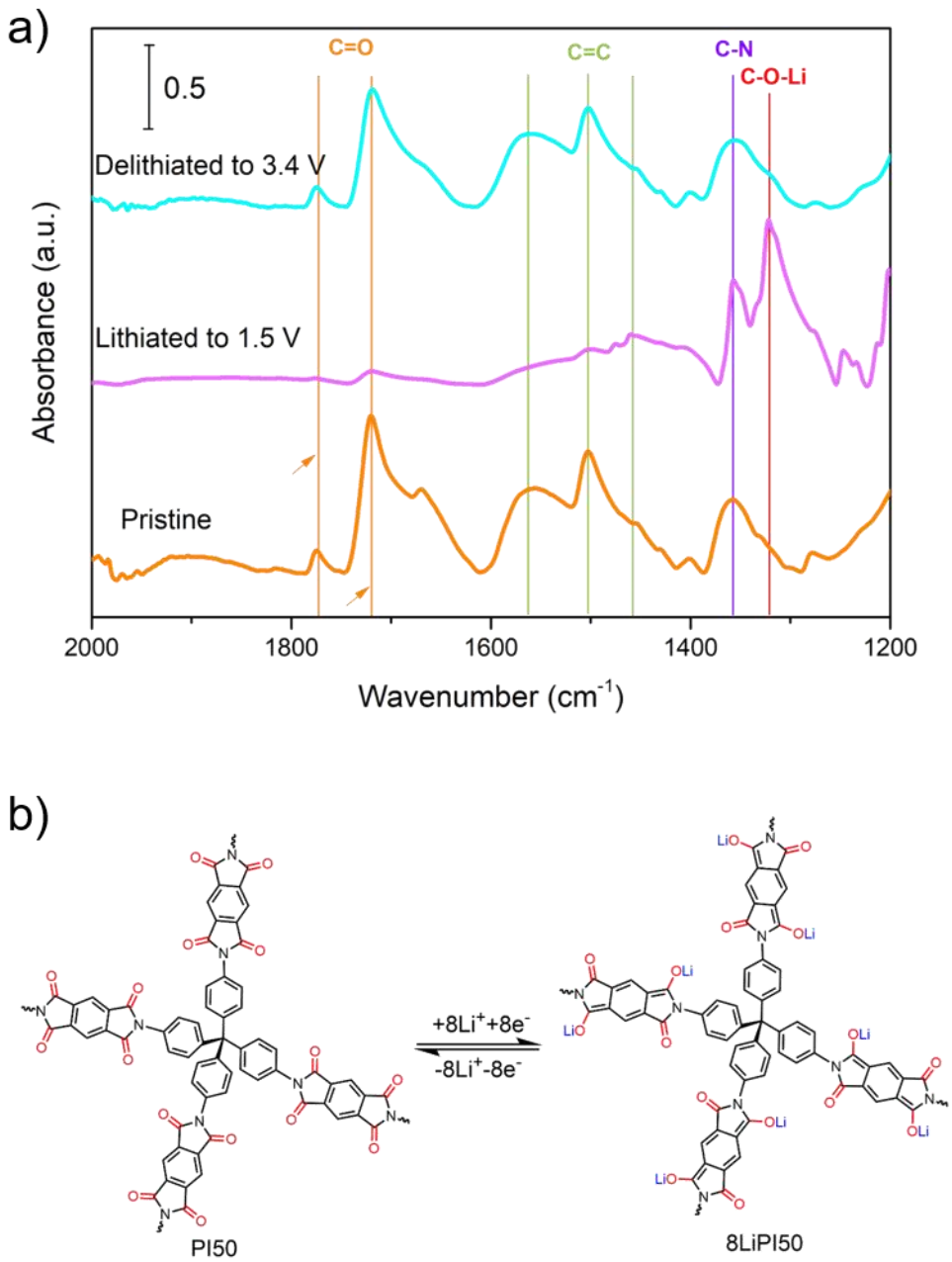

Figure 3-19. (a) FT-IR spectra of **PI50** electrode materials at different states of lithiation/delithiation (pristine, lithiated to 1.5 V and delithiated to 3.4 V); (b) Proposed reversible electrochemical redox mechanism of **PI50** during the lithiation/delithiation process.

3.9 Conclusions

PIX composites were synthesised by *in situ* polycondensation on rGO and used as redox-active positive electrode material in a lithium-ion cell. The reduced particle size of the polyimide polymer in the composites from this synthesis route resulted in the dramatic enhancement of the accessible electrochemically active surface area and, in turn, improved both electron transfer and Li^+ ion transport to the redox-active carbonyl groups. As a consequence, the electrochemical performance of **PI** was improved and the composite materials were found to have much greater specific capacities, with **PI50** having the largest of 172 mAh g^{-1} at 500 mA g^{-1}. This corresponded to high utilisation of the redox-active sites of 86%, and a retention of 80% of the capacity of 125 mAh g^{-1} after 9000 cycles at 2000 mA g^{-1}. Detailed FT-IR investigations showed conclusively the mechanism of storage on the **PI** resulted from the participation of C=O double bonds in the redox reaction.

The use of redox-active functional groups in polymers as a high-rate, long-life energy storage mechanism shows promise. However, the relative amount of redox-active material needs to be considered, which is thus far too low for practical applications. This is because of the significant ratio of conductive additives that are used. Looking forward, there is a need to optimise these materials in terms of their accessible redox-active sites while lowering the carbon loadings.

3.10 References

(1) Wang, S.; Wang, L.; Zhang, K.; Zhu, Z.; Tao, Z.; Chen, J. Organic $Li_4C_8H_2O_6$ Nanosheets for Lithium-Ion Batteries. *Nano Lett.* **2013**, *13* (9), 4404–4409.

(2) Bhosale, M. E.; Chae, S.; Kim, J. M.; Choi, J. Y. Organic Small Molecules and Polymers as an Electrode Material for Rechargeable Lithium Ion Batteries. *J. Mater. Chem. A* **2018**, *6* (41), 19885–19911.

(3) Zhu, L. M.; Lei, A. W.; Cao, Y. L.; Ai, X. P.; Yang, H. X. An All-Organic Rechargeable Battery Using Bipolar Polyparaphenylene as a Redox-Active Cathode and Anode. *Chem. Commun* **2013**, *49*, 567.

(4) Nigrey, P. J.; MacInnes, D.; Nairns, D. P.; MacDiarmid, A. G.; Heeger, A. J. Lightweight Rechargeable Storage Batteries Using Polyacetylene, $(CH)_x$ as the Cathode-Active Material. *J. Electrochem. Soc.* **1981**, *128* (8), 1651.

(5) Visco, S. J.; DeJonghe, L. C. Ionic Conductivity of Organosulfur Melts for Advanced Storage Electrodes. *J. Electrochem. Soc.* **1988**, *135* (12), 2905.

(6) Deng, S.-R.; Kong, L.-B.; Hu, G.-Q.; Wu, T.; Li, D.; Zhou, Y.-H.; Li, Z.-Y. Benzene-Based Polyorganodisulfide Cathode Materials for Secondary Lithium Batteries. *Electrochim. Acta* **2006**, *51* (13), 2589–2593.

(7) Wang, D. Y.; Guo, W.; Fu, Y. Organosulfides: An Emerging Class of Cathode Materials for Rechargeable Lithium Batteries. *Acc. Chem. Res.* **2019**, *52* (8), 2290–2300.

(8) Oyaizu, K.; Nishide, H. Radical Polymers for Organic Electronic Devices: A Radical Departure from Conjugated Polymers? *Adv. Mater.* **2009**, *21* (22), 2339–2344.

(9) Janoschka, T.; Hager, M. D.; Schubert, U. S. Powering up the Future: Radical Polymers for Battery Applications. *Adv. Mater.* **2012**, *24* (48), 6397–6409.

(10) Liang, Y.; Zhang, P.; Chen, J. Function-Oriented Design of Conjugated Carbonyl Compound Electrodes for High Energy Lithium Batteries. *Chem. Sci.* **2013**, *4* (3), 1330–1337.

(11) Luo, Z.; Liu, L.; Ning, J.; Lei, K.; Lu, Y.; Li, F.; Chen, J. A Microporous Covalent–Organic Framework with Abundant Accessible Carbonyl Groups for Lithium-Ion Batteries. *Angew. Chem. Int. Ed.* **2018**, *57* (30), 9443–9446.

(12) Song, Z.; Zhan, H.; Zhou, Y. Polyimides: Promising Energy-Storage Materials. *Angew. Chemie - Int. Ed.* **2010**, *49* (45), 8444–8448.

(13) Lu, Y.; Hou, X.; Miao, L.; Li, L.; Shi, R.; Liu, L.; Chen, J. Cyclohexanehexone with Ultrahigh Capacity as Cathode Materials for Lithium-Ion Batteries. *Angew. Chem. Int.*

Ed. **2019**, *58* (21), 7020–7024.

(14) Matsunaga, T.; Kubota, T.; Sugimoto, T.; Satoh, M. High-Performance Lithium Secondary Batteries Using Cathode Active Materials of Triquinoxalinylenes Exhibiting Six Electron Migration. *Chem. Lett.* **2011**, *40* (7), 750–752.

(15) Peng, C.; Ning, G. H.; Su, J.; Zhong, G.; Tang, W.; Tian, B.; Su, C.; Yu, Di.; Zu, L.; Yang, J.; Ng, M. F.; Hu, Y. S.; Yang, Y.; Armand, M.; Loh, K. P. Reversible Multi-Electron Redox Chemistry of π-Conjugated N-Containing Heteroaromatic Molecule-Based Organic Cathodes. *Nat. Energy* **2017**, *2* (7), 17074.

(16) Luo, C.; Ji, X.; Hou, S.; Eidson, N.; Fan, X.; Liang, Y.; Deng, T.; Jiang, J.; Wang, C. Azo Compounds Derived from Electrochemical Reduction of Nitro Compounds for High Performance Li-Ion Batteries. *Adv. Mater.* **2018**, *30* (23), 1706498.

(17) Luo, C.; Borodin, O.; Ji, X.; Hou, S.; Gaskell, K. J.; Fan, X.; Chen, J.; Deng, T.; Wang, R.; Jiang, J.; Wang, C. Azo Compounds as a Family of Organic Electrode Materials for Alkali-Ion Batteries. *Proc. Natl. Acad. Sci.* **2018**, *115* (9), 2004–2009.

(18) Lu, Y.; Zhang, Q.; Li, L.; Niu, Z.; Chen, J. Design Strategies toward Enhancing the Performance of Organic Electrode Materials in Metal-Ion Batteries. *Chem* **2018**, *4* (12), 2786–2813.

(19) Häupler, B.; Wild, A.; Schubert, U. S. Carbonyls: Powerful Organic Materials for Secondary Batteries. *Adv. Energy Mater.* **2015**, *5* (11), 1402034.

(20) Jaffe, A.; Saldivar Valdes, A.; Karunadasa, H. I. Quinone-Functionalized Carbon Black Cathodes for Lithium Batteries with High Power Densities. *Chem. Mater.* **2015**, *27* (10), 3568–3571.

(21) Chen, H.; Armand, M.; Courty, M.; Jiang, M.; Grey, C. P.; Dolhem, F.; Tarascon, J. M.; Poizot, P. Lithium Salt of Tetrahydroxybenzoquinone: Toward the Development of a Sustainable Li-Ion Battery. *J. Am. Chem. Soc.* **2009**, *131* (25), 8984–8988.

(22) Tian, B.; Ning, G.-H.; Tang, W.; Peng, C.; Yu, D.; Chen, Z.; Xiao, Y.; Su, C.; Loh, K. P. Polyquinoneimines for Lithium Storage: More than the Sum of Its Parts. *Mater. Horiz.* **2016**, *3* (5), 429–433.

(23) Muench, S.; Wild, A.; Friebe, C.; Häupler, B.; Janoschka, T.; Schubert, U. S. Polymer-Based Organic Batteries. *Chem. Rev.* **2016**, *116* (16), 9438–9484.

(24) Wang, Z.; Li, Y.; Liu, P.; Qi, Q.; Zhang, F.; Lu, G.; Zhao, X.; Huang, X. Few Layer Covalent Organic Frameworks with Graphene Sheets as Cathode Materials for Lithium-Ion Batteries. *Nanoscale* **2019**, *11* (12), 5330–5335.

(25) Molina, A.; Patil, N.; Ventosa, E.; Liras, M.; Palma, J.; Marcilla, R. New

Anthraquinone-Based Conjugated Microporous Polymer Cathode with Ultrahigh Specific Surface Area for High-Performance Lithium-Ion Batteries. *Adv. Funct. Mater.* **2020**, *30* (6), 1908074.

(26) Huang, Y.; Li, K.; Liu, J.; Zhong, X.; Duan, X.; Shakir, I.; Xu, Y. Three-Dimensional Graphene/Polyimide Composite-Derived Flexible High-Performance Organic Cathode for Rechargeable Lithium and Sodium Batteries. *J. Mater. Chem. A* **2017**, *5* (6), 2710–2716.

(27) Sui, D.; Xu, L.; Zhang, H.; Sun, Z.; Kan, B.; Ma, Y.; Chen, Y. A 3D Cross-Linked Graphene-Based Honeycomb Carbon Composite with Excellent Confinement Effect of Organic Cathode Material for Lithium-Ion Batteries. *Carbon N. Y.* **2020**, *157*, 656–662.

(28) Zhu, Z.; Chen, J. Review—Advanced Carbon-Supported Organic Electrode Materials for Lithium (Sodium)-Ion Batteries. *J. Electrochem. Soc.* **2015**, *162* (14), A2393–A2405.

(29) Wang, G.; Chandrasekhar, N.; Biswal, B. P.; Becker, D.; Paasch, S.; Brunner, E.; Addicoat, M.; Yu, M.; Berger, R.; Feng, X. A Crystalline, 2D Polyarylimide Cathode for Ultrastable and Ultrafast Li Storage. *Adv. Mater.* **2019**, *31* (28), 1901478.

(30) Rahaman, A. Bin; Sarkar, A.; Chakraborty, K.; Mukherjee, J.; Pal, T.; Ghosh, S.; Banerjee, D. Observation of Different Charge Transport Processes and Origin of Magnetism in RGO and RGO-ZnSe Composite. *J. Phys. Chem. C* **2019**, *123* (25), 15441–15450.

(31) Puthen Peediyakkal, H.; Yu, J.; Munakata, H.; Kanamura, K. Highly Durable Non-Platinum Catalyst for Protic Ionic Liquid Based Intermediate Temperature PEFCs. *Electrochemistry* **2019**, *87* (1), 35–46.

(32) Sharma, P.; Bhalla, V.; Dravid, V.; Shekhawat, G.; Jinsong-Wu; Senthil Prasad, E.; Raman Suri, C. Enhancing Electrochemical Detection on Graphene Oxide-CNT Nanostructured Electrodes Using Magneto-Nanobioprobes. *Sci. Rep.* **2012**, *2*, 1–7.

(33) Xu, W.; Read, A.; Koech, P. K.; Hu, D.; Wang, C.; Xiao, J.; Padmaperuma, A. B.; Graff, G. L.; Liu, J.; Zhang, J. G. Factors Affecting the Battery Performance of Anthraquinone-Based Organic Cathode Materials. *J. Mater. Chem.* **2012**, *22* (9), 4032–4039.

(34) Fang, Q.; Wang, J.; Gu, S.; Kaspar, R. B.; Zhuang, Z.; Zheng, J.; Guo, H.; Qiu, S.; Yan, Y. 3D Porous Crystalline Polyimide Covalent Organic Frameworks for Drug Delivery. *J. Am. Chem. Soc.* **2015**, *137* (26), 8352–8355.

(35) Cooper, A. I. Conjugated Microporous Polymers. *Adv. Mater.* **2009**, *21* (12), 1291–1295.

(36) Thomas, J. M. H.; Trewin, A. Amorphous PAF-1: Guiding the Rational Design of Ultraporous Materials. *J. Phys. Chem. C* **2014**, *118* (34), 19712–19722.

(37) Khattak, A. M.; Sin, H.; Ghazi, Z. A.; He, X.; Liang, B.; Khan, N. A.; Alanagh, H. R.; Iqbal, A.; Li, L.; Tang, Z. Controllable Fabrication of Redox-Active Conjugated Microporous Polymers on Reduced Graphene Oxide for High Performance Faradaic Energy Storage. *J. Mater. Chem. A* **2018**, *6* (39), 18827–18832.

(38) Nitta, N.; Wu, F.; Lee, J. T.; Yushin, G. Li-Ion Battery Materials: Present and Future. *Mater. Today* **2015**, *18* (5), 252–264.

(39) Song, Z.; Xu, T.; Gordin, M. L.; Jiang, Y. B.; Bae, I. T.; Xiao, Q.; Zhan, H.; Liu, J.; Wang, D. Polymer-Graphene Nanocomposites as Ultrafast-Charge and -Discharge Cathodes for Rechargeable Lithium Batteries. *Nano Lett.* **2012**, *12* (5), 2205–2211.

(40) Li, Y.; Jian, Z.; Lang, M.; Zhang, C.; Huang, X. Covalently Functionalized Graphene by Radical Polymers for Graphene-Based High-Performance Cathode Materials. *ACS Appl. Mater. Interfaces* **2016**, *8* (27), 17352–17359.

(41) Guo, W.; Yin, Y. X.; Xin, S.; Guo, Y. G.; Wan, L. J. Superior Radical Polymer Cathode Material with a Two-Electron Process Redox Reaction Promoted by Graphene. *Energy Environ. Sci.* **2012**, *5* (1), 5221–5225.

(42) Ai, W.; Zhou, W.; Du, Z.; Sun, C.; Yang, J.; Chen, Y.; Sun, Z.; Feng, S.; Zhao, J.; Dong, X.; Huang, W.; Yu, T. Toward High Energy Organic Cathodes for Li-Ion Batteries: A Case Study of Vat Dye/Graphene Composites. *Adv. Funct. Mater.* **2017**, *27* (19), 1603603.

(43) Lyu, H.; Li, P.; Liu, J.; Mahurin, S.; Chen, J.; Hensley, D. K.; Veith, G. M.; Guo, Z.; Dai, S.; Sun, X. G. Aromatic Polyimide/Graphene Composite Organic Cathodes for Fast and Sustainable Lithium-Ion Batteries. *ChemSusChem* **2018**, *11* (4), 763–772.

(44) Wang, J.; Tee, K.; Lee, Y.; Riduan, S. N.; Zhang, Y. Hexaazatriphenylene Derivatives/GO Composites as Organic Cathodes for Lithium Ion Batteries. *J. Mater. Chem. A* **2018**, *6* (6), 2752–2757.

(45) Deng, W.; Yu, J.; Qian, Y.; Wang, R.; Ullah, Z.; Zhu, S.; Chen, M.; Li, W.; Guo, Y.; Li, Q.; Liu, L. Strongly Coupled Perylene Bisimide/Reduced Graphene Oxide as Organic Cathode Materials for Lithium Ion Batteries. *Electrochim. Acta* **2018**, *282*, 24–29.

(46) Lu, C.; Pan, G.; Huang, Q.; Wu, H.; Sun, W.; Wang, Z.; Sun, K. Polynitroxide-Grafted-Graphene: A Superior Cathode for Lithium Ion Batteries with Enhanced Charge Hopping Transportation. *J. Mater. Chem. A* **2019**, *7* (9), 4438–4445.

(47) Wang, S.; Wang, Q.; Shao, P.; Han, Y.; Gao, X.; Ma, L.; Yuan, S.; Ma, X.; Zhou, J.; Feng, X.; Wang, B. Exfoliation of Covalent Organic Frameworks into Few-Layer Redox-Active Nanosheets as Cathode Materials for Lithium-Ion Batteries. *J. Am. Chem.*

Soc. **2017**, *139* (12), 4258–4261.

(48) Wang, J.; Polleux, J.; Lim, J.; Dunn, B. Pseudocapacitive Contributions to Electrochemical Energy Storage in TiO_2 (Anatase) Nanoparticles. *J. Phys. Chem. C* **2007**, *111* (40), 14925–14931.

(49) Kim, K. C.; Liu, T.; Lee, S. W.; Jang, S. S. First-Principles Density Functional Theory Modeling of Li Binding: Thermodynamics and Redox Properties of Quinone Derivatives for Lithium-Ion Batteries. *J. Am. Chem. Soc.* **2016**, *138* (7), 2374–2382.

Chapter 4

Integrated Covalent Organic Framework/Carbon Nanotube Composite as Li-ion Positive Electrode with Ultra-high Rate Performance

Some of the results presented in Chapter 4 are taken from Paper II.

Integrated Covalent Organic Framework/Carbon Nanotube Composite as Li-ion Positive Electrode with Ultra-high Rate Performance, Hui Gao, Qiang Zhu, Alex R. Neale, Mounib Bahri, Xue Wang, Haofan Yang, Lunjie Liu, Rob Clowes, Nigel D. Browning, Reiner Sebastian Sprick, Marc A. Little, Laurence J. Hardwick* and Andrew I. Cooper*

4.1 Author Contributions

All COFs and the COF on CNT composites were synthesised by the thesis author. All the electrochemical experiments were carried out by the thesis author. FT-IR spectra were recorded by the thesis author. Modeling calculations were performed by Mr. Qiang Zhu and Ms. Xue Wang. Dr. Marc Little carried out PXRD analyses. Mr. Haofan Yang carried out SEM. Mr. Lunjie Liu carried out UV-vis measurements. Mr. Rob Clows performed N_2 gas sorption measurements. Dr. Mounib Bahri recorded TEM images. Dr. David Costa recorded Raman spectra of carbon nanotube. Dr. Alex Neale fitted Raman data for the carbon nanotube.

4.2 Abstract

COFs are promising electrode materials for Li-ion batteries owing to their modularity, porosity, and robust crystalline networks. However, the utilisation of redox-active sites embedded in their networks is often suppressed by the low intrinsic conductivities of bulk-grown COFs, which results in poor electrochemical performance. Herein, a general strategy to improve the energy storage capability of COFs-based electrode materials through integrating COF with carbon nanotubes (CNT) is demonstrated. The COF composites feature an abundance of π-conjugated redox-active phenanthrenequinone units, a robust β-ketoenamine linkage, and well-defined mesopores. The COF and CNT composite material (2,7-diamino-9,10-phenanthrenequinone (DAPQ)-COFX – where X = 10, 30, and 50 wt.% of CNT) was prepared by *in situ* polycondensation, resulting in the formation of tube-type core-shell structures with intimately grown COF layers on the CNT surface in the optimised composites. The synergistic structural design enables superior electrochemical performance, providing DAPQ-COF50 with 95% utilisation of redox-active sites, long cycling stability (76% after 3000 cycles at 2000 mA g^{-1}), and ultra-high rate performance, with 58% capacity retention at 50 A g^{-1}. This rate translates to charging times of *ca.* 11 seconds (320 C), implying that DAPQ-COFX has great capability in the application of high-power cells. Indeed, this power density and the rapid charge/discharge time are competitive with electrochemical capacitors.

4.3 Introduction

Rechargeable Li-ion batteries are widely used in daily life with the ever-growing application in the powering of portable devices, like smartphones and laptops, and the drive to shift towards electric vehicles. In addition to enlarging practical energy densities, the development of new materials and technologies is required to address the demand for higher power applications, enabling high current rates and rapid (dis)charge times without sacrificing cycling stability or lifetime. In this regard, the electrochemical processes based on the simple, reversible redox reactions of organic electrode materials commonly lead to higher rate performances, compared to inorganic electrode materials based on conventional intercalation reactions.[1,2] As such, organic electrode materials are promising candidates for the next generation sustainable Li-ion batteries with faster charging function.[3,4] However, electrodes based on small organic molecules suffer from the drawback of dissolution in organic electrolytes leading to poor

cycling stabilities. Great efforts, including grafting the electroactive molecule into a conductive backbone,[5] forming a salt,[6] and synthesising insoluble polymeric materials,[7] have been devoted to solving the dissolution of the small organic active material in the electrolyte. Polymeric materials are advantageous because, in addition to the targeted insolubility, their molecular structures can be chemically tuned based on the employment of different monomers to improve their performance.[8,9]

Covalent organic frameworks (COFs) are a class of materials that form 2 or 3D structures through reversible reactions between organic precursors resulting in strong, covalent bonds to afford porous, stable, and crystalline materials. With the advantage of high porosity, adjustable and periodic pores, well-defined structures, and functional skeletons, COFs have great potential applications in batteries. In contrast to traditional polymers, COFs enable precise integration of the redox-active building blocks into two- or three-dimensional topologies with long-range ordered skeletons and nanopores. The modular synthesis is facile to tailor the redox properties of COFs because of the diversity of building blocks and atomically controllable arrangement. Therefore, the battery performance could be adjusted by the design of different building blocks of the COFs. In addition, the ordered one-dimensional nanopores in the COFs is a benefit for the diffusion and access of electrolytes to the electroactive sites. For example, Dichtel *et al.* compared a naphthalene diimide COF (TAPB-NDI COF) to an amorphous analogue (TAPB-NDI Amp) and a chemically similar linear polymer to determine how structural properties affected the battery performance relationship.[10] The TAPB-NDI COF, which had a SA_{BET} surface area of 490 $m^2\ g^{-1}$, delivered 60 mAh g^{-1} (95% of its theoretical capacity) under C/20. By contrast, the TAPB-NDI Amp, which had a much lower BET surface area of 20 $m^2\ g^{-1}$, only delivered 16 mAh g^{-1} at the same scan rate, corresponding to only 25% of its theoretical capacity. Compared to the small molecule in isolation or a linear polymer with a relatively low molecular weight, the COFs exhibited good stability in organic solvents, leading to the COF having stable cycling performance in battery applications. Feng *et al.* reported a 2-D polyimide COF (2D-PAI COF) that delivered a capacity of 104.4 mAh g^{-1} and kept 100% capacity retention after 50 cycles at 0.1 A g^{-1}, implying remarkable chemical stability of 2D-PAI.[11] The cycling stability of 2D-PAI is superior to the fast capacity-fading of the 2D-PAI electroactive monomer in isolation. Furthermore, the π-π stacking interlayer structure and the π-conjugated intralayer skeletons in the COFs allow charges to move fast through preorganised pathways.[12] Recently, several pioneering works have been reported that utilise COFs as active material in Li-ion batteries.[13–16] However, close packing of 2D COF has been shown to make it difficult

to reach the interior active sites which are deeply buried inside the 1D channels, especially at a high current density. Inevitably, this leads to insufficient utilisation of the redox-active sites and thus lowering the capacity and rate performance. Wang *et al.*[17] reported a strategy to accelerate the diffusion-controlled redox reactions of COFs through delamination of COFs into few-layer nanosheets, which enhanced the electrochemical performance significantly.

Conductive coating and incorporation of conductive additives have been used to improve the electron transportation of organic cathode materials, which has resulted in higher rate performances being achieved.[18–23] Graphene, reduced graphene oxide (rGO) and carbon nanotubes (CNT) have been used as conductive additives because of their extraordinary electronic conductivity, and it has been reported that graphene, rGO and CNT based composites can enhance the electrochemical performance of batteries.[24–26] For example, Feng *et al.*[16] reported a 2D microporous COF and CNT composite (2D CCP-HATN@CNT), which was synthesised by in situ polymerisation on graphene, as cathode materials for Li-ion batteries. 2D CCP-HATN@CNT high capacity of 116 mAh g^{-1} with 99% utilisation of its redox-active sites and good cycling stability (91% after 1000 cycles) and rate capability (82%, 1.0 A g^{-1} *vs.*0.1 A g^{-1}). While the pure 2D CCP-HATN only delivered a limited capacity of 62.5 mAh g^{-1}. Taken together, these results suggest that covalent-organic framework composites can be made to be highly stable and undergo fast redox reactions.

Chemical components, including the type of linkages and the number of redox-active sites, are essential factors for determining the stability and maximum theoretical capacities of organic-based electrodes in Li-ion batteries. For example, the β-ketoenamine-linkage has been used to synthesise COFs with high stability and crystallinity.[27] While 2,7-diamino-9,10-phenanthrenequinone (DAPQ) is a good electrochemical motif because it has two conjugated carbonyl groups that are redox-active, which, unlike imides, can simultaneously react with Li^+. The phenanthrenequinone motif also has a high discharge potential because of the presence of a three-fold charge-stabilisation mechanism.[28] In addition, the π-conjugated structure of DAPQ can stabilise charge and can form intermolecular π-π stacking interactions that could stabilise the packing of 2D layers in a COF structure. In this chapter, composites of a 2D COF (DAPQ-COF, Scheme 4-2) and CNTs were synthesised using *in situ* Schiff-base condensation reaction of 1,3,5-triformylphloroglucinol (TFG) with 2,7-diamino-9,10-phenanthrenequinone (DAPQ) and studies at Li-ion batteries. By itself, DAPQ-COF was found to have a low specific capacity of 73 mAh g^{-1} as the active material in a Li-ion half-cell, corresponding to 46% utilisation of the redox-active groups in DAPQ-COF. However, a significant performance improvement was

observed with the addition of CNT during *in situ* polymerisations of DAPQ-COF. A DAPQ-COF composite containing 50 wt.% of CNT has a 95% utilisation of the redox-active sites and a specific capacity of 162 mAh g^{-1} at 500 mA g^{-1}. In this chapter, CNT was chosen as the conductive additive because the CNT has better conductivity compared to rGO which was used in Chapter 3.

4.4 Experimental section

4.4.1 Materials

9,10-Phenanthrenequinone (PQ) and 1,3,5-triformylphloroglucinol (TFG, see Figure 4-1 for the ^{13}C NMR spectrum of TFG) were obtained from TCI LTD. Acetic acid, palladium on carbon, catalyst-free, multi-walled carbon nanotubes with outer diameter and length ranges of 7-15 nm and 0.5-10 µm (CNTs, see Figure 4-2 for Raman spectra of CNTs and Table 4-1 for the fitted data), anhydrous NMP, PVDF, and isoquinoline were purchased from Sigma Aldrich. 1,4-dioxane, n-Butanol, and 1,2-Dichlorobenzene (*o*-DCB) were obtained from Alfa-Aesar. Fuming nitric acid, sodium carbonate, dimethylacetamide (DMAc), and mesitylene were obtained from Acros Organics. Concentrated sulfuric acid, DMF, dimethyl sulfoxide (DMSO), acetone, and methanol were obtained from Fisher. All chemicals were used as received without further purification.

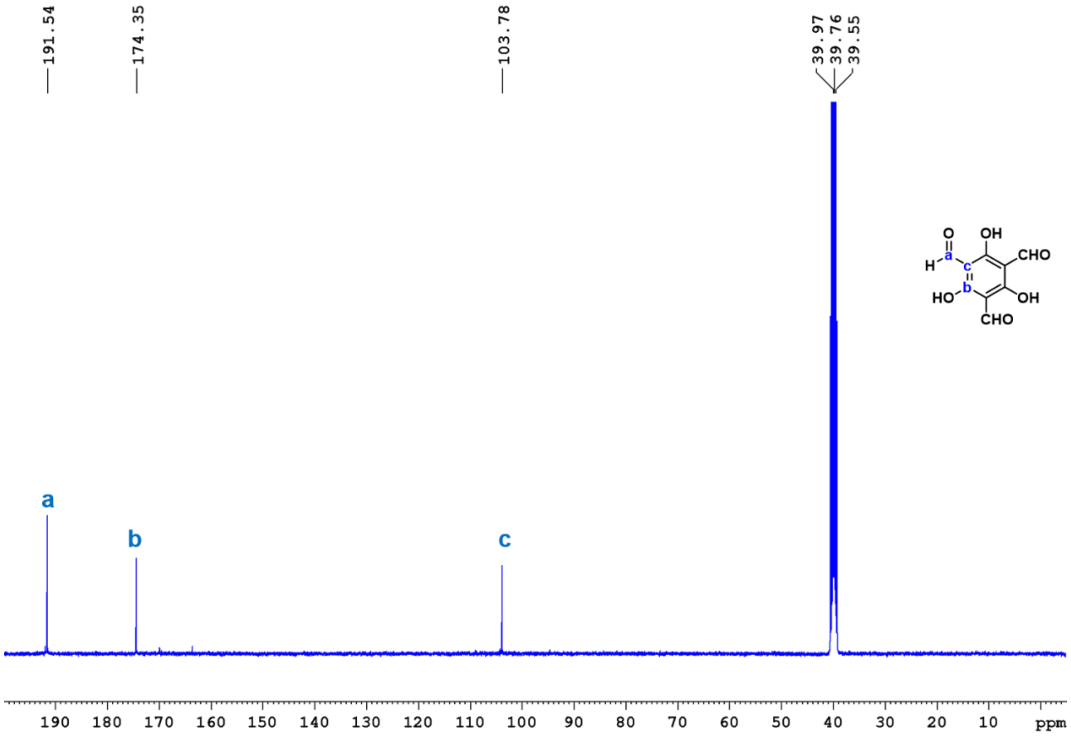

Figure 4-1. ^{13}C NMR (100 MHz, DMSO-d_6) spectrum of TFG.

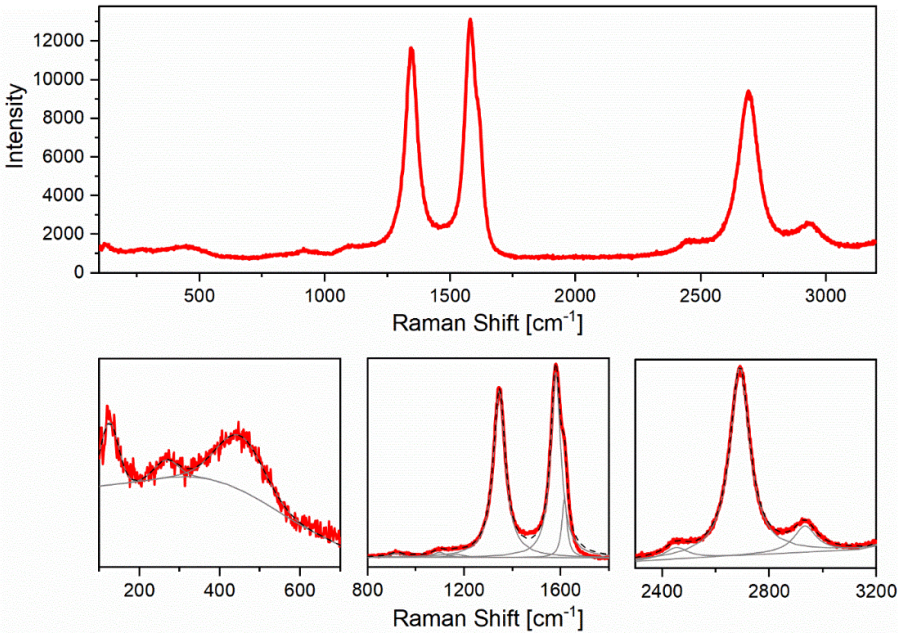

Figure 4-2. Raman spectra of multi-walled CNTs (top) and the corresponding fitted spectral regions (bottom), where the grey lines are the individual fitted peaks and the black dashed lines show the cumulative fit.

Table 4-1. Fitting and assignment information for Raman spectra of CNTs.

Peak Position / cm^{-1}	Amplitude intensity	Integral intensity	FWHM / cm^{-1}	Assignment
125		20099 [a]	52.7 [a]	RBM
266		7467 [a]	68.6 [a]	RBM
450		45567 [a]	137.5 [a]	
919	253	26234	66.1	
1098	321	34029	67.4	
1168	192	25566	84.8	
1345	10608	1008698	60.5	D
1579	11784	934322	50.5	G
1615	3702	152824	26.3	D’
2452	520	86274	105.7	
2689	8385	1188159	90.2	G’ (2D)
2932	1175	185082	100.2	D+G (or D”)

[a]Peak fitting was attained using a Gaussian function; all other peak fitting was attained using a Lorentzian function. FWHM = full-width at half-maximum. RBM = radial breathing mode. The spectrum is in agreement with previous studies on the Raman spectroscopy of carbon nanotubes, and all assignments of Raman peaks adapted from previous literature.[29–31]

4.4.2 Synthetic Procedures

4.4.2.1 Synthesis of DAPQ Monomer

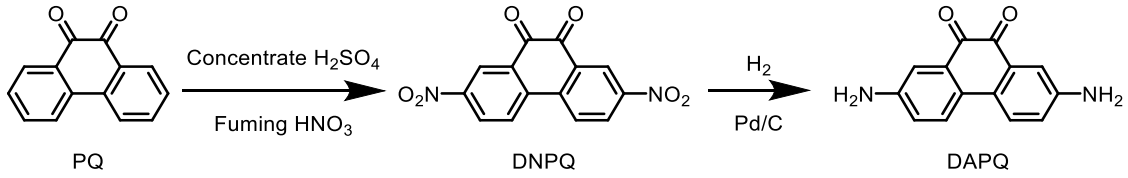

Scheme 4-1. Synthetic route from PQ to DAPQ monomer.

2,7-dinitro-9,10-phenanthrenequinone (DNPQ) was synthesised according to a literature procedure.[32] In a two-necked flask, PQ (2.0 g, 9.6 mmol) was added to a solution of fuming nitric acid (>90%) (28.0 mL) and concentrated sulfuric acid (95%) (2.8 mL). The reaction was heated under reflux for 2 hours and then poured onto 500 mL of ice water. After cooling the reaction mixture to room temperature, the pH was adjusted to a neutral value by adding saturated sodium carbonate solution. The suspension was then filtered to obtain the solid product, which was washed with deionized water. The product was finally recrystallized from acetic acid to afford DNPQ as a yellow solid in a yield of 38%: 1.1 g. ^{1}H NMR (400 MHz, DMSO-d_6, δ [ppm]): 8.75-8.70 (m, 4H), 8.62-8.56 (dd, J_{HH} = 8.5, 2.5 Hz, 2H). ^{13}C NMR (100 MHz, DMSO-d_6, δ [ppm]): 176.2, 148.8, 138.9, 134.0, 129.0, 128.1, 123.2. HRMS (EIS): calcd. for $([C_{14}H_6N_2O_6]+Na)^+$: m/z = 321.0118; found: 321.0123. Elemental analysis (EA): calcd. for $C_{14}H_6N_2O_6$: C, 56.39; H, 2.03; N, 9.39; found: C, 56.11; H, 1.99; N, 9.27.

DAPQ was synthesised according to a patent procedure.[33] Palladium on carbon (10 wt.% palladium) (100.0 mg) was added to a mixture of DNPQ (1.0 g, 3.35 mmol) in N_2 degassed methanol (100 mL). The reaction mixture was degassed with N_2 for 10 minutes and then purged with H_2 for 15 minutes. The reaction mixture was stirred at room temperature overnight under a positive pressure of H_2. Afterward, the suspension was filtered through the Celite, which was washed with methanol. The solvent was then removed from the dark blue filtrate by rotary evaporation to afford DAPQ as a black coloured solid in a yield of 88%: 0.7 g. ^{1}H NMR (400 MHz, DMSO-d_6): 7.71-7.50 (d, J_{HH}= 8.6 Hz, 2H), 7.16-7.02 (d, J=2.5 Hz, 2H), 6.92-6.80 (dd, J_{HH}=8.5, 2.5 Hz, 2H), 5.52 (s, 4H). ^{13}C NMR (100 MHz, DMSO-d_6, δ [ppm]): 181.1, 148.5, 130.6, 125.9, 124.7, 122.0, 113.3. HRMS (EIS): calcd. for $([C_{14}H_{10}N_2O_2]+Na)^+$: m/z =

261.0634; found: 261.0623. EA: Calcd. for $C_{14}H_{10}N_2O_2$: C, 70.58; H, 4.23; N, 11.76; found: C, 67.19; H, 4.26; N, 11.11.

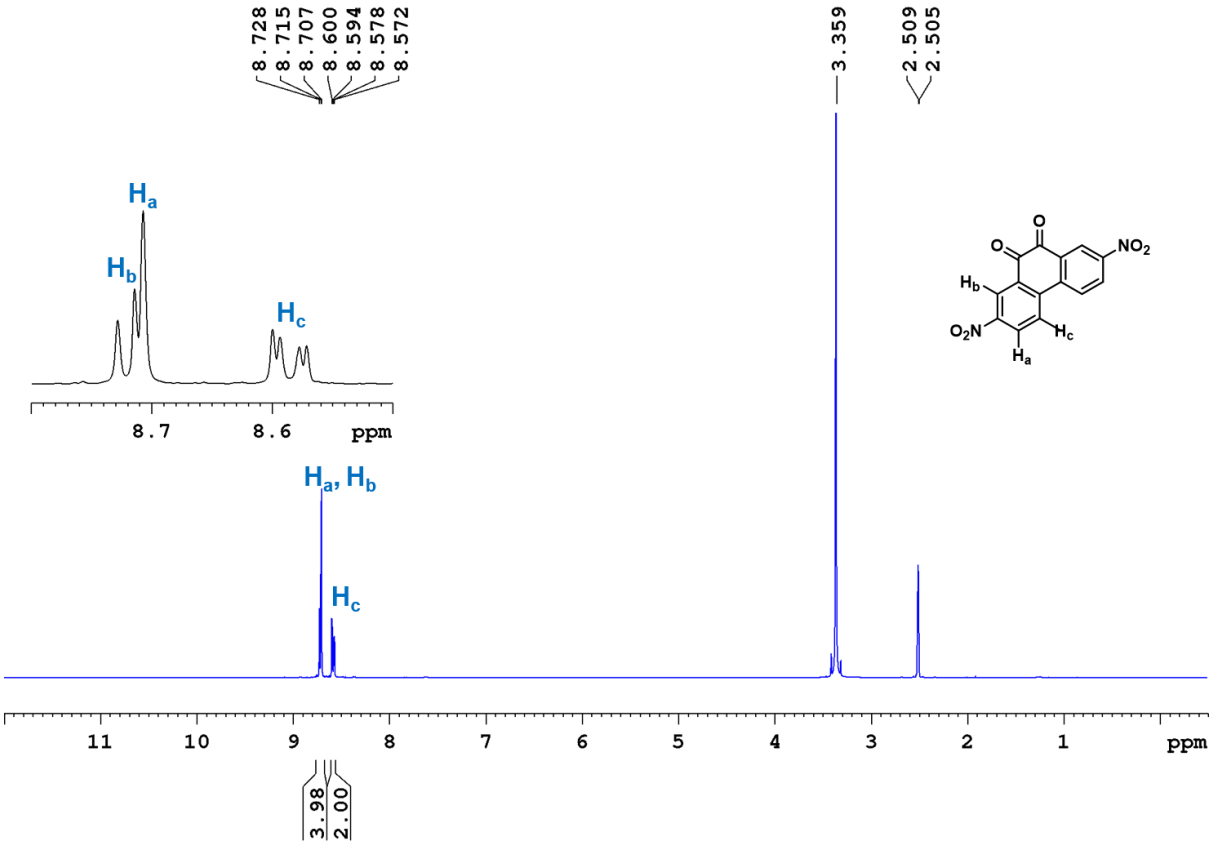

Figure 4-3. ^{1}H NMR (400 MHz, DMSO-d_6) spectrum of DNPQ.

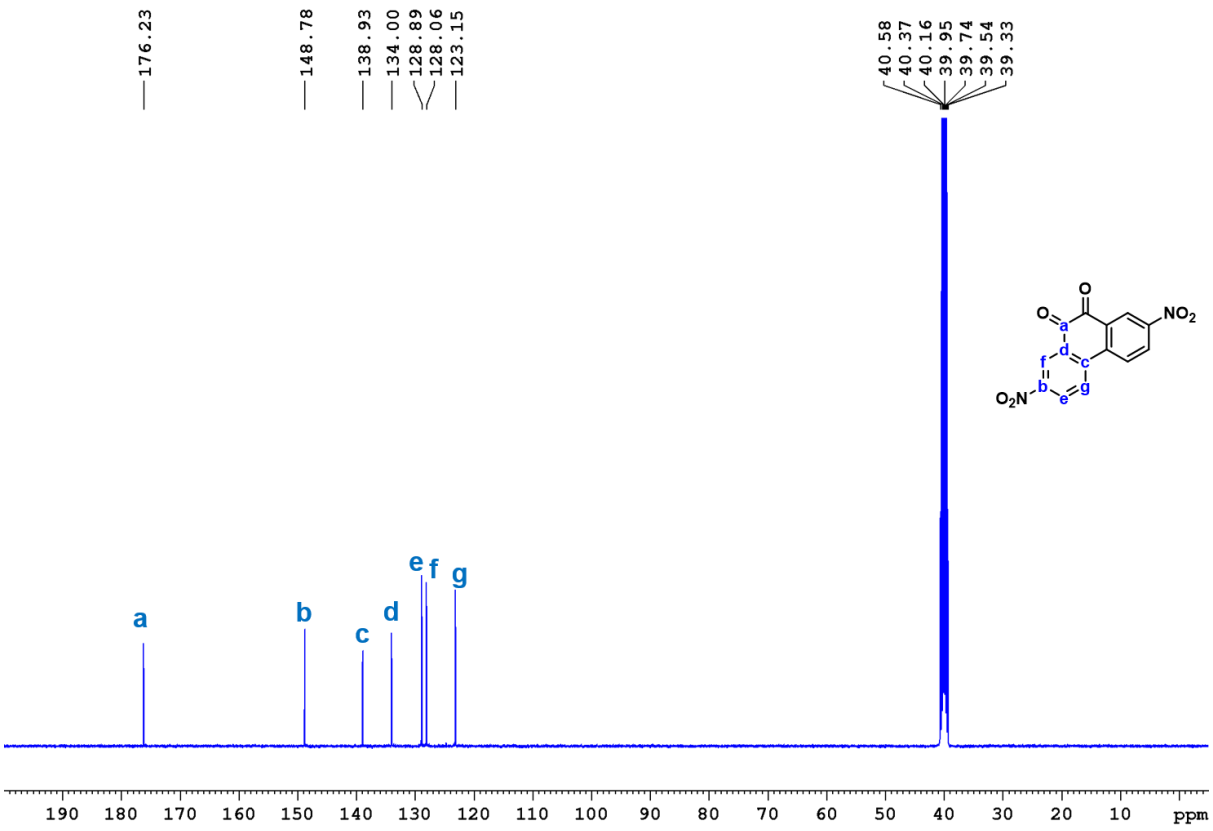

Figure 4-4. ^{13}C NMR (100 MHz, DMSO-d_6) spectrum of DNPQ.

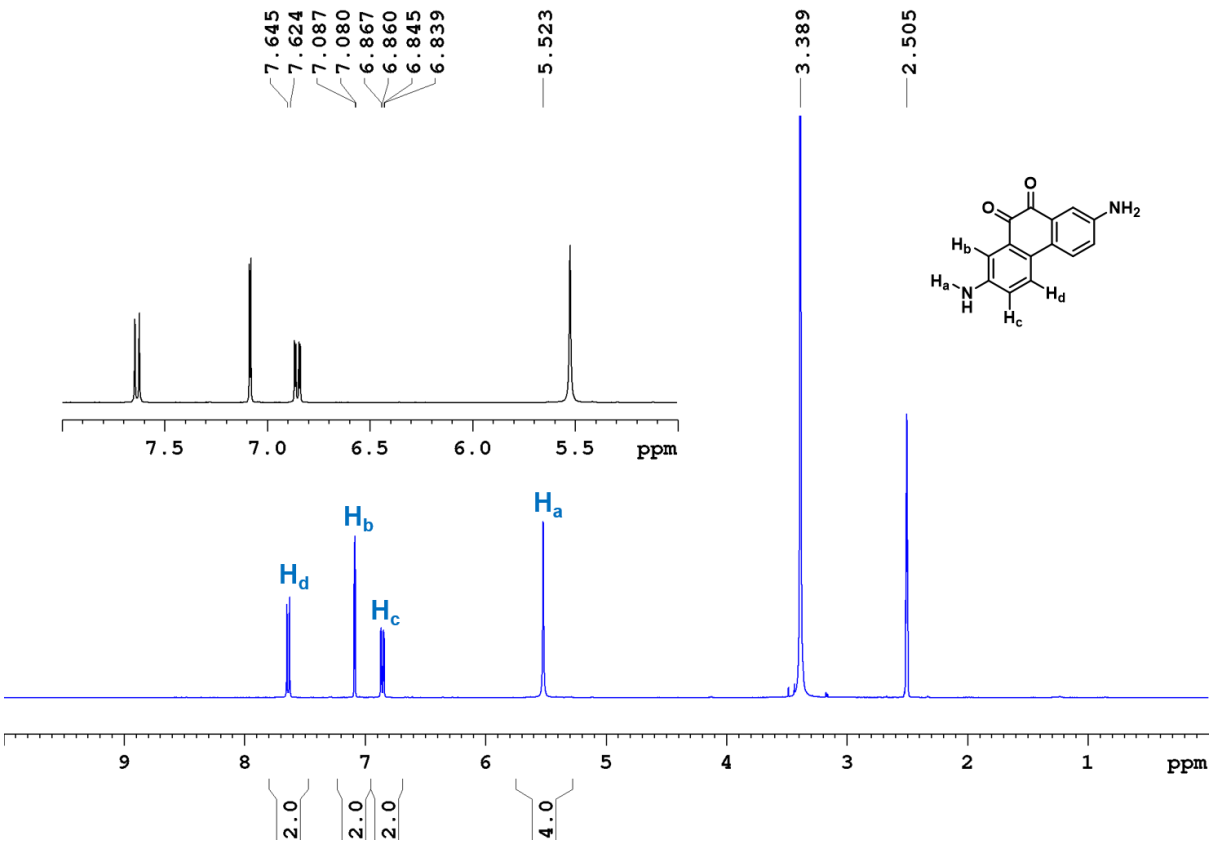

Figure 4-5. ^{1}H NMR (400 MHz, DMSO-d_6) spectrum of DAPQ.

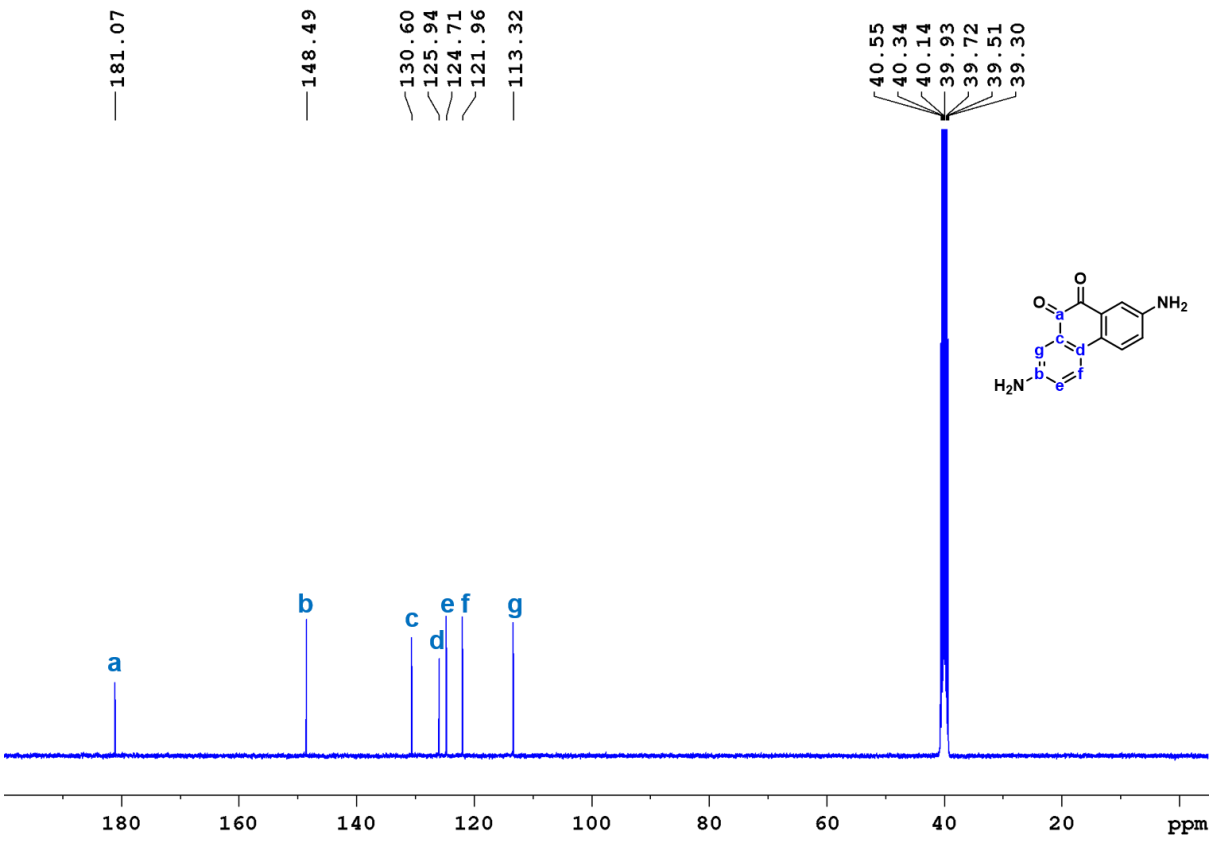

Figure 4-6. ^{13}C NMR (100 MHz, DMSO-d_6) spectrum of DAPQ.

4.4.2.2 Synthesis of COFs Powders

Synthesis of DAPQ-COF: A 10 mL Pyrex tube (outer × inner diameter = 1.3 × 1.0 cm with a length 15 cm) was charged with TFG (10.5 mg, 0.05 mmol), DAPQ (17.9 mg, 0.075 mmol), mesitylene (0.9 mL), 1,4-dioxane (0.3 mL), and aqueous acetic acid (0.1 mL, 3 M). This mixture was homogenized by sonication for 10 minutes and the Pyrex glass tube was subjected to three freeze-pump-thaw cycles and evacuated to an internal pressure of 100 mTorr. The tube was sealed and then placed in an oven at 120 °C for 3 days. The black precipitate was collected by filtration and washed with DMF (3 × 5 mL), DMSO (3 × 5 mL), and acetone (3 × 5 mL). The resulting solid was dried and then subjected to washing by Soxhlet extraction with methanol for 24 hours. The powder was collected and dried under reduced pressure at 85°C to afford DAPQ-COF as a black powder in a yield of 91%: 22.6 mg. EA: Calcd for $(C_{10}H_5NO_2)n$: C, 70.18; H, 2.94; N, 8.18; found: C, 62.41; H, 3.42; N, 8.20.

Synthesis of DAPQ-COFX: A 10 mL Pyrex tube (outer × inner diameter = 1.3 × 1.0 cm with a length 15 cm) was charged with TFG (10.5 mg, 0.05 mmol), DAPQ (17.9 mg, 0.075 mmol), CNT (2.6, 10.0, and 23.4 mg, which corresponds to 10, 30, 50 wt.% of CNT in the composites, respectively, assuming the DAPQ-COF yield from the composite reaction was also 91%), mesitylene (0.9 mL), 1,4-dioxane (0.3 mL), and aqueous acetic acid (0.1 mL, 3 M). This mixture was homogenized by sonication for 10 minutes and the Pyrex glass tube was subjected to three freeze-pump-thaw cycles and evacuated to an internal pressure of 100 mTorr. The tube was sealed and then placed in an oven at 120 °C for 3 days. The black precipitate was collected by filtration and washed with DMF (3 × 5 mL), DMSO (3 × 5 mL), and acetone (3 × 5 mL). The resulting solid was dried and then subjected to washing by Soxhlet extraction with methanol as the solvent for 24 hours. The powder was collected and dried under reduced pressure at 85°C to afford DAPQ-COFX as black powders. The yields calculated for DAPQ-COF10, DAPQ-COF30, and DAPQ-COF50 were 95, 92, and 89%, respectively. EA: Calcd for DAPQ-COF10: C, 73.16; H, 2.61; N, 7.36; found: C, 65.90; H, 3.37; N, 6.59. Calcd for DAPQ-COF30: C, 79.13; H, 2.05; N, 5.73; found: C, 69.91; H, 2.63; N, 5.09. Calcd for DAPQ-COF50: C, 85.09; H, 1.47; N, 4.09; found: C, 77.34; H, 2.43; N, 3.94.

Optimisation of experimental conditions: To optimise the synthesis of DAPQ-COF, DMAc/mesitylene, DMAc/*o*-DCB, DMAc/1,4-dioxane, mesitylene/1,4-dioxane, and o-DCB/*n*-butanol, solvent mixtures, the reaction temperature, and the concentrations of acetic acid were all screened (Table 4-2). From these reactions, it was found that a mesitylene/1,4-dioxane (0.9: 0.3 ml) solvent system, a reaction temperature of 150 °C, and 0.3 mL of 6 M acetic acids afforded a DAPQ-COF sample with the highest crystallinity (Table 4-2). The same reaction conditions were used to produce the DAPQ-COFX composites.

4.4.3 Simulation X-ray Diffraction Patterns for COF structures

Structural models of DAPQ-COF were generated using the Accelrys3 Materials Studio (version 5.5) program suite.[34] Initially, an A-A stacked model was generated with hexagonal *P*6/*m* space group symmetry in which the *a* and *b* unit cell parameters were based on the distance between the centre of the trisubstituted rings in a structural model. The *c*-axis was based on a stacking distance between the COF layers of 3.4 Å. The A-A stacked model was

then optimised using the Geometry Optimization routine, which includes energy minimization and cell parameter optimisation using a Universal Force Field. An A-B stacked model was generated using the same approach but to have hexagonal $P6_3$ symmetry and a *c* unit cell axis of 6.8 Å. Simulated PXRD patterns were calculated using the Reflex Plus module. The predicted PXRD pattern of the A-A stacked model is more closely matched to the experimental PXRD data of DAPQ-COF (Figure 4-9) and the experimental data was refined with Pawley refinement in TOPAS Academic (Figure 4-8a).[35]

Table 4-2. Synthesis of DAPQ-COF under different reaction conditions.

Entry[a]	Solvent (mL)	Acetic acid	Reaction temperature (°C)	Yield (%)	Form
1	DMAc/mesitylene (0.5:0.5)	0.05 mL, 6 M	120	83	Amorphous
2	DMAc/mesitylene (0.9:0.3)	0.05 mL, 6 M	120	82	Amorphous
3	DMAc/mesitylene (0.3:0.9)	0.05 mL, 6 M	120	80	Amorphous
4	DMAc/*o*-DCB (0.5:0.5)	0.05 mL, 6 M	120	90	Amorphous
5	DMAc/*o*-DCB (0.9:0.3)	0.05 mL, 6 M	120	85	Amorphous
6	DMAc/*o*-DCB (0.3:0.9)	0.05 mL, 6 M	120	90	Amorphous
7	DMAc/1,4-dioxane (0.5:0.5)	0.05 mL, 6 M	120	98	Amorphous
8	DMAc/1,4-dioxane (0.9:0.3)	0.05 mL, 6 M	120	92	Amorphous
9	DMAc/1,4-dioxane (0.3:0.9)	0.05 mL, 6 M	120	91	Amorphous
10	DMAc/1,4-dioxane (0.5:0.5)	0.05 mL, 6 M	150	92	Amorphous
11	DMAc/1,4-dioxane (0.9:0.3)	0.05 mL, 6 M	150	90	Amorphous
12	DMAc/1,4-dioxane (0.3:0.9)	0.05 mL, 6 M	150	91	Amorphous
13	Mesitylene/1,4-dioxane (0.5:0.5)	0.05 mL, 6 M	120	93	Crystalline
14	Mesitylene/1,4-dioxane (0.9:0.3)	0.05 mL, 6 M	120	95	Crystalline
15	Mesitylene/1,4-dioxane (0.3:0.9)	0.05 mL, 6 M	120	90	Semicrystalline
16	Mesitylene/1,4-dioxane (0.9:0.3)	0.10 mL, 3 M	120	91	Crystalline(high)
17	Mesitylene/1,4-dioxane (0.96:0.24)	0.05 mL, 6 M	120	89	Crystalline
18	Mesitylene/1,4-dioxane (1.0:0.2)	0.05 mL, 6 M	120	88	Crystalline
19	*o*-DCB/*n*-butanol (0.5:0.5)	0.05 mL, 6 M	120	98	Amorphous
20	*o*-DCB/*n*-butanol (0.9:0.3)	0.05 mL, 6 M	120	91	Amorphous
21	*o*-DCB/*n*-butanol (0.3:0.9)	0.05 mL, 6 M	120	73	Amorphous

[a] TFG (0.05 mmol), DAPQ (0.075 mmol), 3 days.

4.4.4 Theoretical Specific Capacity Calculation

The repeating unit in DAPQ-COF consists of 1/2 of an A unit (M_A) and 1/3 of a B unit (M_B) (Figure 4-7). Hence, the molecular weight of the repeating unit cell in DAPQ-COF is 171.13 g mol^{-1} ($C_{10}H_5NO_2$). The number of electrons (*n*) involved in the repeating unit is equal to 1, assuming 2 electrons are involved in each phenanthrenequinone unit. Therefore, using Equation 1-2, the theoretical capacity of DAPQ-COF is calculated to be 157 mAh g^{-1}.

The specific capacities of the DAPQ-COFX composites were calculated based on the mass of the DAPQ-COF in the composite. However, both DAPQ-COF and CNT contribute to the overall capacity of the electrode, so the total specific capacity of the DAPQ-COFX composites was calculated using Equation 4-1:

$$C_{\mathrm{DAPQ-COFX}} = \frac{a\times m\times C_{\mathrm{DAPQ-COF}}+\mathrm{b}\times m\times C_{\mathrm{CNT}}}{a\times m} \qquad \text{(Equation 4-1)}$$

Where, $C_{\mathbf{DAPQ\text{-}COFX}}$ and $C_{\mathbf{DAPQ\text{-}COF}}$ are the specific capacities of DAPQ-COFX and DAPQ-COF**,** respectively, in the composite electrodes. C_{CNT} is the specific capacity of pure CNT (13 mAh g^{-1}) without DAPQ-COF and *m* is the mass of the DAPQ-COFX**.** *a* and *b* are the contents of DAPQ-COF and CNT in the DAPQ-COFX**,** such that *a*+*b*=1. Therefore, the capacity contribution of CNT in the DAPQ-COFX is

$$C_{\text{DAPQ-COFX}}\text{-}C_{\text{DAPQ-COF}} = (b\times C_{\text{CNT}})/a \qquad \text{(Equation 4-2)}$$

Using Equation 4-2, the contribution of CNT in the composite is calculated and listed in Table 4-3. The capacity contribution of CNT in DAPQ-COF10, DAPQ-COF30 and DAPQ-COF50 is 1, 6 and 13 mAh g^{-1}, respectively.

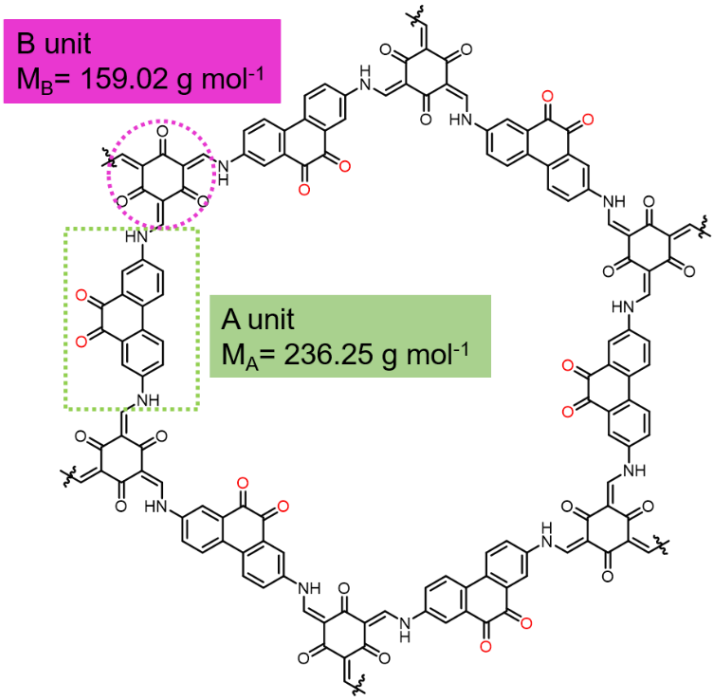

Figure 4-7. Chemical structure of DAPQ-COF.

Table 4-3. Capacity contribution of CNT in DAPQ-COFX.

Sample	Calculation of capacity contribution of CNT in DAPQ-COFX (mAh g^{-1})
DAPQ-COF10	0.1×13/0.9 = 1
DAPQ-COF30	0.3×13/0.7 = 6
DAPQ-COF50	0.5×13/0.5 = 13

4.4.5 Electrochemical Test Protocol

In DAPQ-COF electrode, the mass ratio of active materials (DAPQ-COF): carbon black: PVDF is 6: 3: 1. In the DAPQ-COFX electrode, the mass ratio of active materials (DAPQ-COF): carbon black: PVDF is 7: 2: 1. In the coin cells, DAPQ-COF/DAPQ-COFX was used as the working positive electrode, lithium as the counter electrode, and 1 M LiTFSI in DOL and DME (1:1 v/v) as an electrolyte solution.

Please see Chapter 2 (Section 2.2 Electrochemical Measurements) for the electrochemical test protocol.

4.5 DAPQ-COF Design, Synthesis, and Characterisation

DAPQ-COF was synthesised via a Schiff-base condensation reaction. Typically, a 2:3 stoichiometric molar ratio of TFG and DAPQ were dispersed in a mixture of mesitylene and 1,4-dioxane, and the reagents were heated to 120 °C for 3 days to afford the crystalline 2-D COF. After isolation, the product was washed with DMF, THF, and then by Soxhlet using methanol. Finally, the product was dried at 80 °C under vacuum to afford the product in a yield of 91% (Scheme 4-2, see section 4.9.3 for detailed reaction conditions). The condensation reaction is followed by an irreversible keto-enol tautomerization, which enhances the chemical stability of the COF.[36]

Powder X-ray diffraction (PXRD) was used to confirm the structure of DAPQ-COF (Figure 4-8a). The experimental PXRD pattern of DAPQ-COF closely matched the simulated PXRD pattern of the aligned A-A stacked model (Figure 4-2). A Pawley refinement also confirmed that the PXRD data was consistent with DAPQ-COF having the same hexagonal *P*6/*m* symmetry (a=b=29.42 Å, c = 3.62 Å, V = 2717.5 Å^3) and comparable dimensions to the eclipsed A-A stacked model. The diffraction peaks at 2θ (Cu-Kα) = 3.37, 5.84, 6.74, and 8.90° assigned to the [100]. [2$\bar{1}$0], [200], [3$\bar{1}$0] reflections of DAPQ-COF, respectively (Figure 4-8a). The PXRD confirmed DAPQ-COF was crystalline closely matched the predicted model and multiple reflections indicate that DAPQ-COF has high periodicity in 3D.

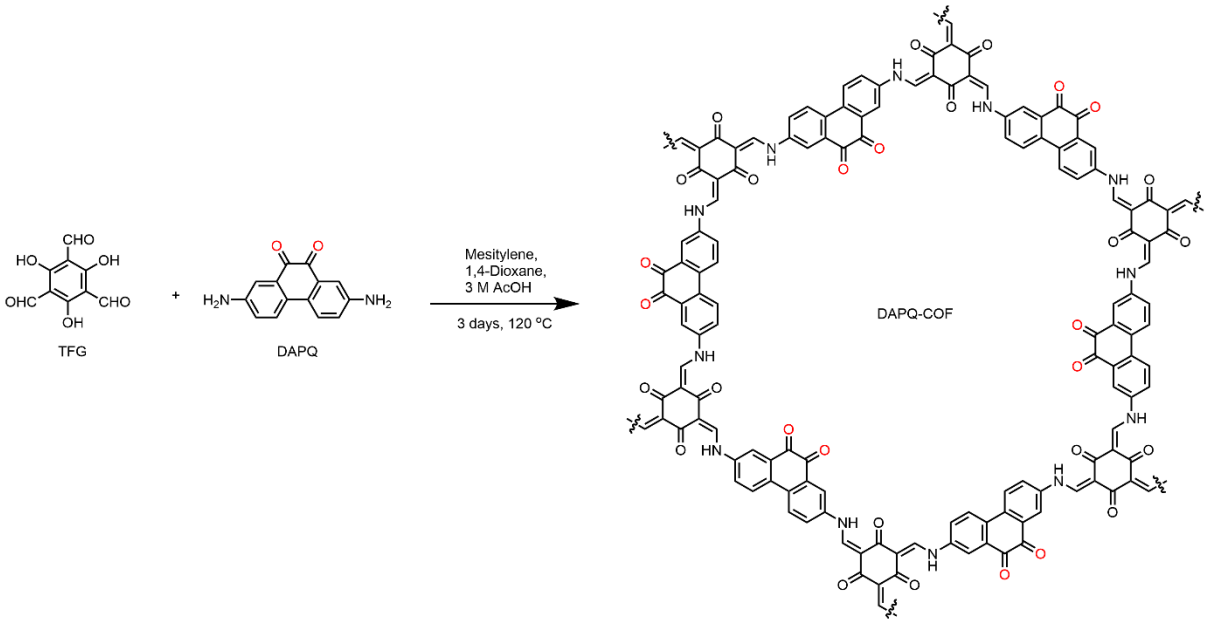

Scheme 4-2. Synthesis of DAPQ-COF.

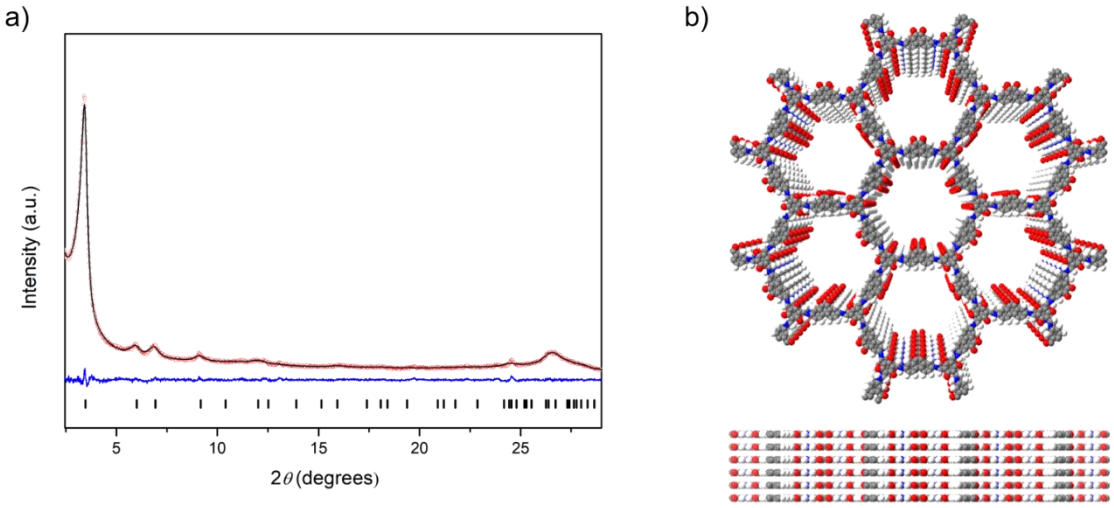

Figure 4-8. (a) PXRD pattern fitting of DAPQ-COF with Pawley refinement (Cu-Kα). Red circles: experimental PXRD pattern, black line: fitting pattern, blue curve: difference between experimental and refinement, black bars: reflection positions, R_p = 2.21%, R_{wp} = 3.17% (*P*6/*m*, $a = b = 29.42$ Å, $c = 3.62$ Å, $V = 2717.5$ Å^3). (b) Structural models for DAPQ-COF with perfectly eclipsed AA stacking patterns, shown parallel to the pore channel along the crystallographic *c* axis (top) and parallel to the hexagonal layers (bottom). Grey, white, red, and blue atoms represent carbon, hydrogen, oxygen, and nitrogen, respectively.

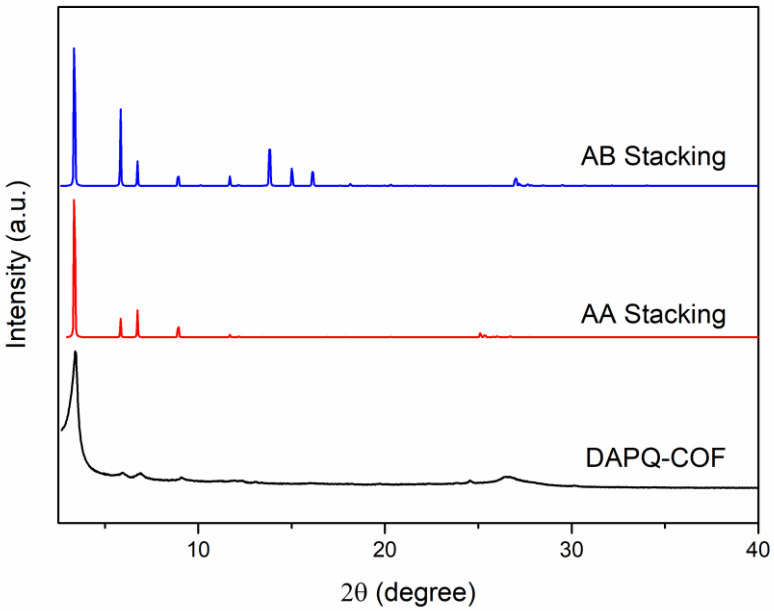

Figure 4-9. Experimental PXRD pattern of DAPQ-COF and the simulated PXRD pattern for A-A and A-B stacking model.

The chemical structure of as-prepared DAPQ-COF was characterised by Fourier-transform infrared spectroscopy (FTIR) and ^{13}C cross-polarization magic angle spinning (CP-MAS) solid-state NMR spectroscopy (Figure 4-10). N-H stretching vibrations at 3436, 3340, and 3220 cm^{-1} in the IR spectra of the DAPQ precursor were not observed in DAPQ-COF, indicating complete consumption of DAPQ in the reactions. Strong absorption bands at 1250 and 1572 cm^{-1} in the spectra of DAPQ-COF and the DAPQ-COFX composites were assigned to β-ketoenamine C−N moieties and C=C stretching vibrations, respectively, indicating the COF was in its keto form,[36] as shown in Scheme 4-2. In the ^{13}C solid-state NMR spectrum, peaks at 146 and 108 ppm were assigned to the enamine carbon (=CNH) and α-enamine carbon, respectively, and likewise confirmed the formation of β-ketoenamine-linked COF.[37] Furthermore, the aldehyde carbon signal of TFG at 192 ppm was not found in the CP-MAS spectrum of DAPQ-COF.

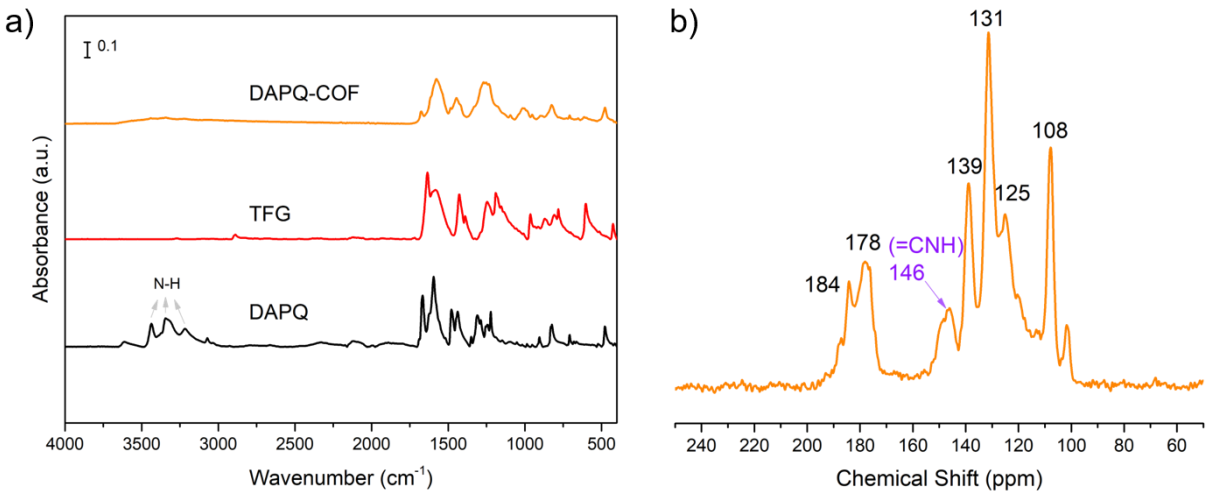

Figure 4-10. (a) FT-IR spectra of TFG, DAPQ, DAPQ-COF; (b) ^{13}C solid-state NMR CP/MAS spectrum of DAPQ-COF.

N_2 sorption experiments were performed at 77 K to measure the porosity of DAPQ-COF. The N_2 gas sorption profile of DAPQ-COF is a Type II plot (Figure 4-11). The isotherms of the DAPQ-COF exhibit a rise of nitrogen uptake at a very low relative pressure ($P/P_0 < 0.01$), indicating the existence of permanent micropores. In addition, the nitrogen uptakes continuously increased over the P/P_0 range from 0.1 to 0.8 in the isotherms, implying the presence of mesopores in DAPQ-COF. Besides, the N_2 uptake increase at the P/P_0 exceeds 0.9,

reflecting the presence of macropores in the COF. From sorption results, the SA_{BET} was calculated to be 245 m^2 g^{-1}, uptake of 5.8 mmol g^{-1} at 1 bar. Pore diameters of COFs were calculated based on nonlocal density functional theory models. The pore diameters of DAPQ-COF were calculated to be 22 Å, which is comparable to the pore size in the A-A stacked model (~25 Å).

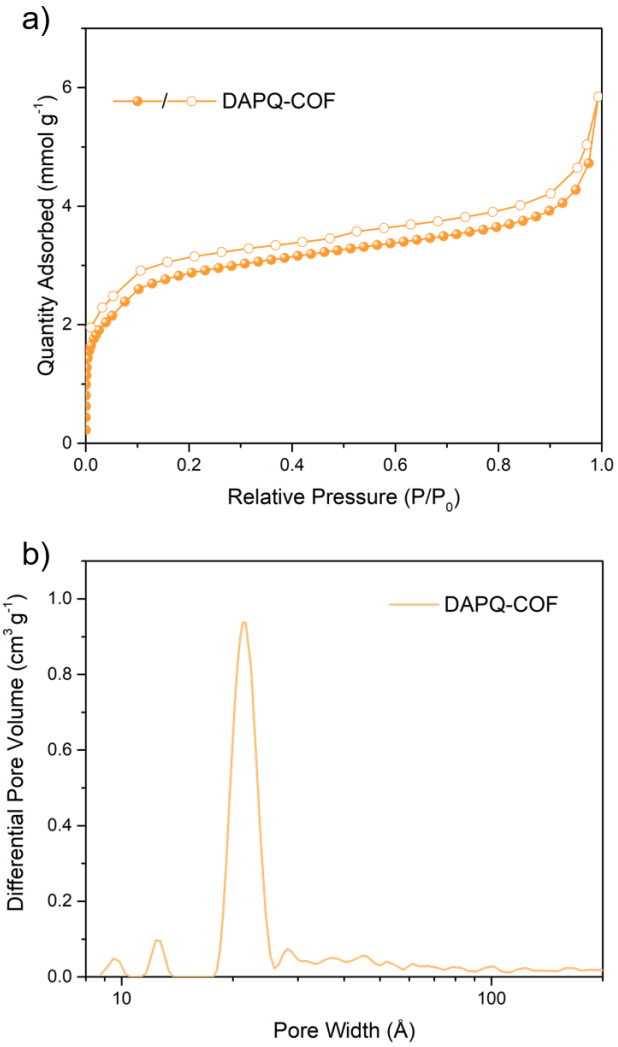

Figure 4-11. (a) N_2 sorption isotherms of DAPQ-COF (77.3 K, solid symbols = adsorption; open symbols = desorption); (b) Pore size distribution plots of DAPQ-COF (calculated by NL-DFT for pillared clay).

The crystalline structure of DAPQ-COF was further confirmed by high-resolution transmission electron microscopy (HR-TEM). The HR-TEM images revealed that DAPQ-COF has an ordered structure with hexagonal pores oriented along its crystallographic *c* axis (area outlined in yellow, Figure 4-12f). Both HR-TEM images and corresponding fast-Fourier transformation

(FFT) of the DAPQ-COF confirmed its crystallinity, and the calculated lattice distance of 1.29 nm corresponds to the (2,-2,0) plane of the eclipsed model and matched the refined PXRD pattern well (Figure 4-9). The morphologies of DAPQ-COF were recorded by scanning electron microscope (SEM). DAPQ-COF displays a rod-like morphology in the SEM images, (Figure 4-13).

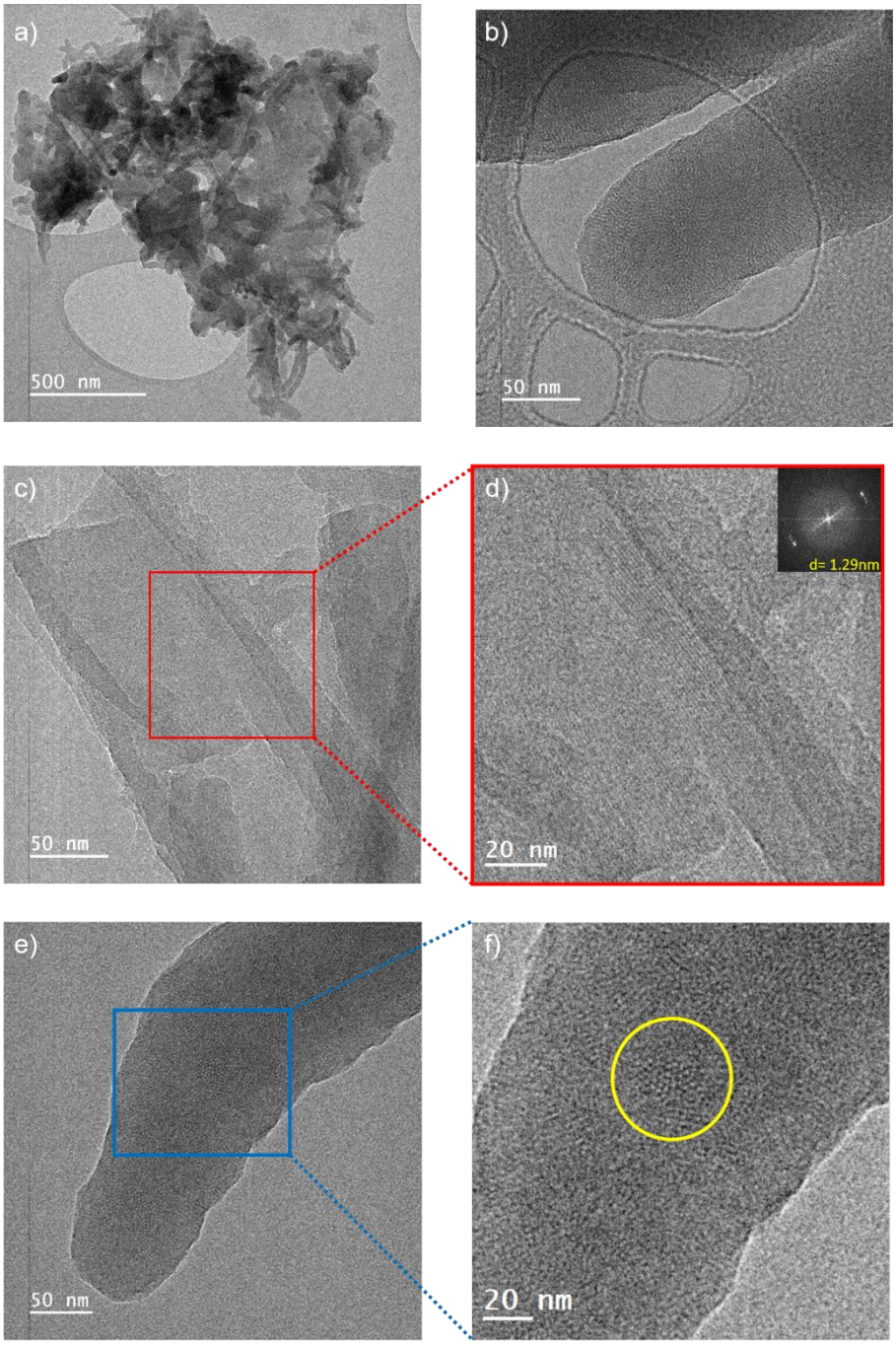

Figure 4-12. TEM images of DAPQ-COF (insert shows FFT image of the crystalline COF structure with a *d*-spacing of 1.29).

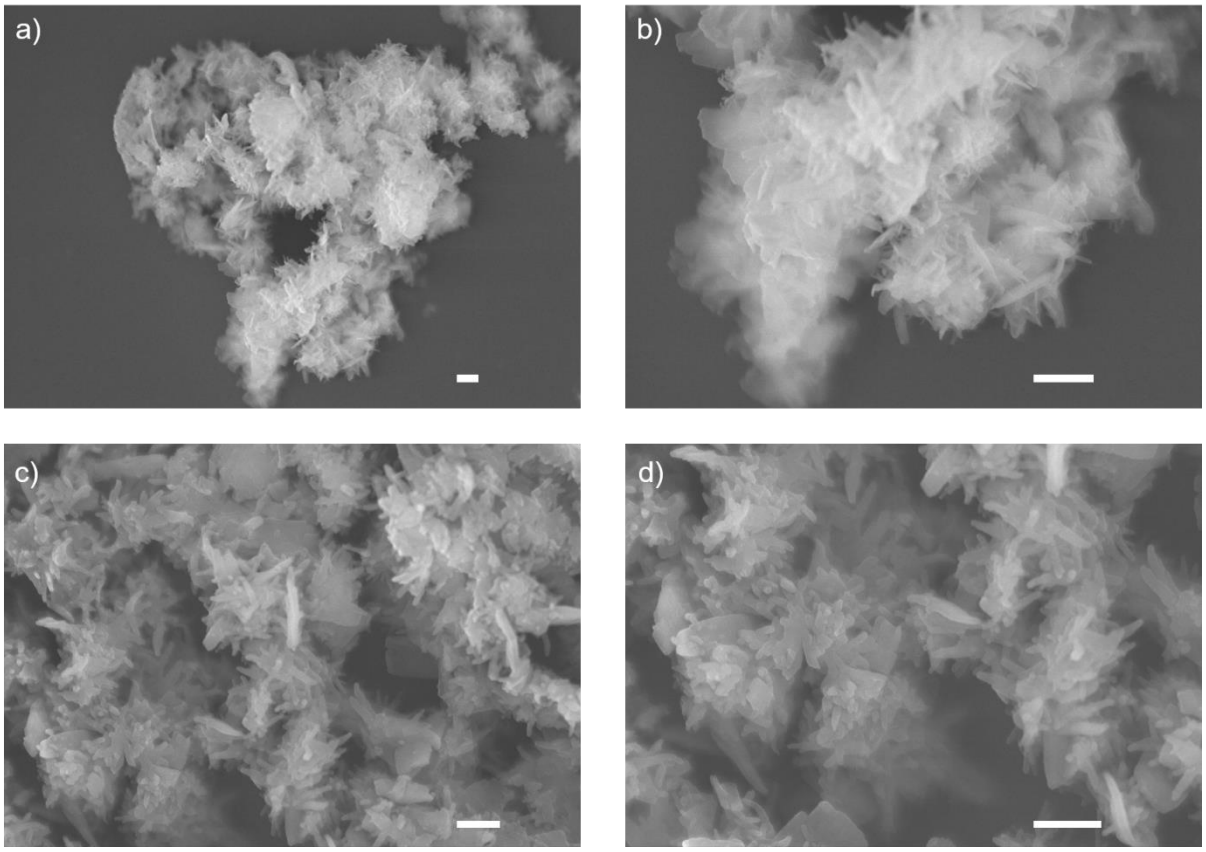

Figure 4-13. SEM images of DAPQ-COF (scale bar: 1 μm).

DAPQ-COF was found to have good chemical stability in organic solvents, water, and aqueous acid, which is beneficial for its utilisation in battery applications. PXRD patterns and FT-IR spectra (Figure 4-14) of DAPQ-COF recorded before and after exposure the sample to *N*,*N*-dimethylformamide, *N*-methyl-2-pyrrolidone, water, and up to 12 M HCl (aq.) for 24 hours were comparable, demonstrating that DAPQ-COF maintained its crystallinity and did not appear to decompose after being immersed in these liquids.

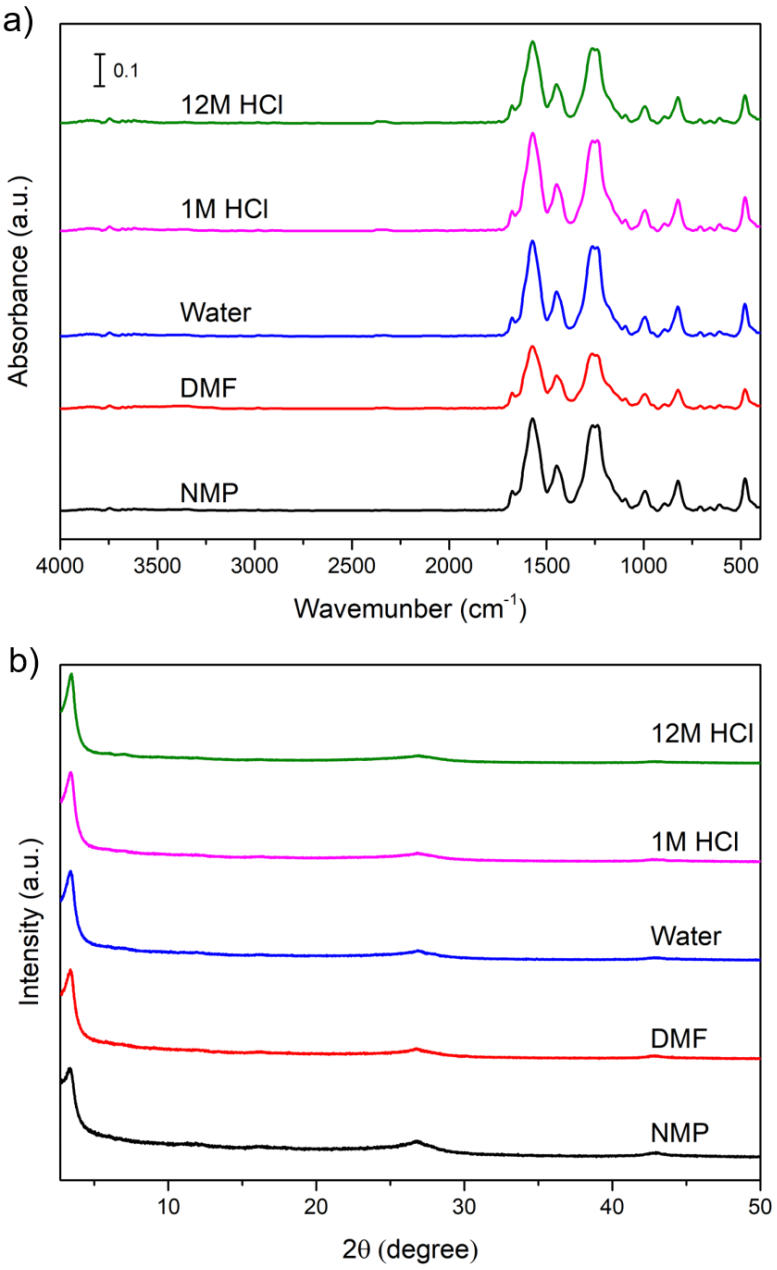

Figure 4-14. (a) FT-IR and (b) PXRD spectra of DAPQ-COF after exposure to water, aqueous acid, *N*-dimethylformamide, and *N*-methyl-2-pyrrolidone for 24 hours.

4.6 DAPQ-COF and CNT Composite Design, Synthesis and Characterisation

After successfully synthesising DAPQ-COF, it was decided that a series of DAPQ-COF composites would be synthesised using the same synthetic procedure, but with CNT added into the reaction mixture. In the composite reactions, a 2:3 stoichiometric molar ration of TFG with DAPQ was dispersed in a mixture of mesitylene and 1,4-dioxane. CNT was added to the reaction mixture and the suspension was sonicated for 30 min to ensure the reaction precursors were well mixed. Finally, the reagents were heated to 120 °C for 3 days to afford the composites. The product was washed with DMF, THF, and then by Soxhlet with methanol. Finally, the product was dried at 80 °C under vacuum and got yield above 90%. In total, four samples were synthesised using the same method: DAPQ-COF and CNT composite with 10, 30, and 50 wt.% CNT (assuming the DAPQ-COF yield from the composite reaction was also 91%). The composites are named DAPQ-COFX, where X = 10, 30, and 50 wt.% of CNT. (Scheme 4-3, see section 4.4.3 for detailed reaction conditions). In the composite, the interaction between the CNT and COF is based on the non-covalent bonding, such as physical adsorption and the π-stacking interaction. The graphitic sidewalls of CNTs provide the possibility for π-stacking interactions with the conjugated structure of COFs and heteroatoms with free electron pair. Also, there is a chance that the COF formed inside the CNT channels as well. For this study, catalyst-free CNT with outer diameter and length ranges of 7-15 nm and 0.5-10 µm, respectively, were used. For brevity, these are simply abbreviated to CNT, and all available properties and further characterisations, including Raman spectra and electron micrographs, are provided in Section 4.9.

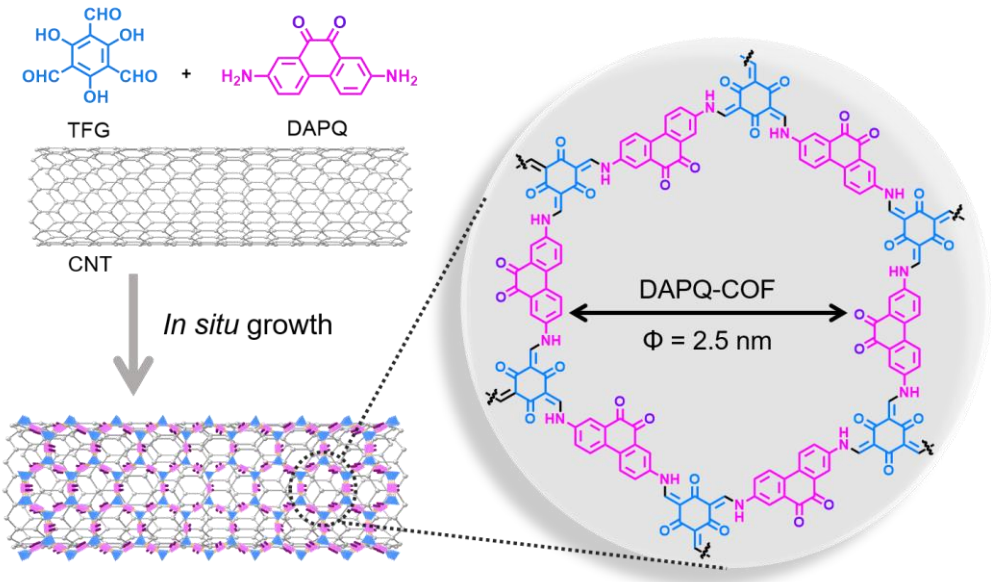

Scheme 4-3. Scheme showing the synthesis of DAPQ-COF and CNT composite.

PXRD was used to confirm the crystallinity in the DAPQ-COFX composites. As shown in Figure 4-15a, the PXRD patterns of DAPQ-COF10 display good crystallinity with an intense peak at 3.37°, which corresponds to (110) reflection. The addition of CNT decreases the crystallinity of DAPQ-COFX. DAPQ-COF30 and DAPQ-COF50 show poor crystallinity. However, the PXRD patterns indicated that DAPQ-COF adopted the same structure in the DAPQ-COFX composites. The chemical structure of DAPQ-COFX composites was characterised by FT-IR (Figure 4-15). The characteristic N-H peaks, stretching vibrations at 3436, 3340, and 3220 cm^{-1}, were not observed in the IR spectra of the composites. New peaks at 1250 and 1572 cm^{-1} belong to the β-ketoenamine C−N moieties and C=C stretching vibrations appeared. The IR spectra imply that the reaction happened successfully and the COF was in its keto form.

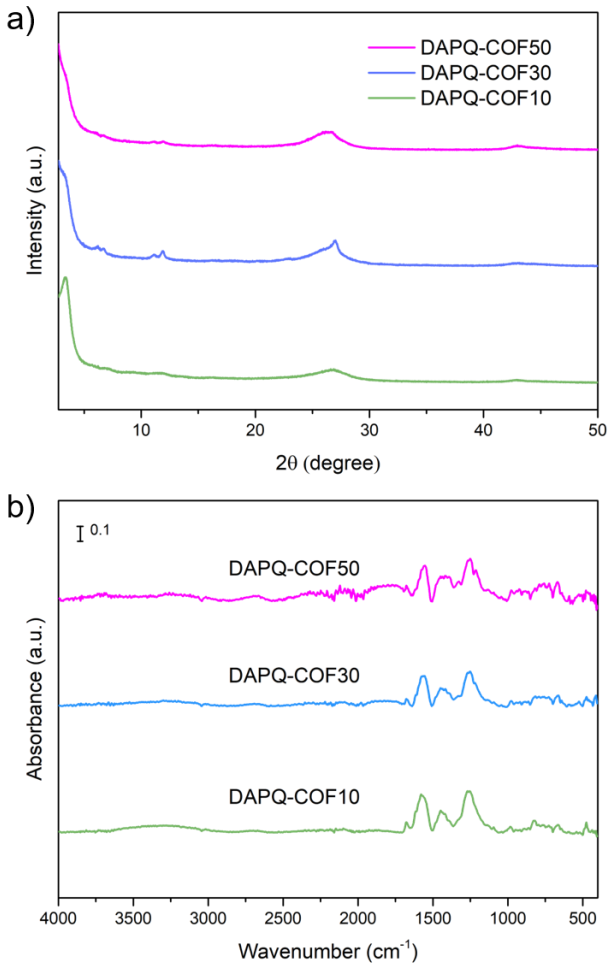

Figure 4-15. (a) PXRD pattern and (b) FTIR spectra of DAPQ-COF10, DAPQ-COF30, and DAPQ-COF50.

The porosity of the DAPQ-COFX composites and CNT were studied by N_2 adsorption. Figure 4-16 presents the nitrogen sorption isotherms and pore distribution curves of CNT and the three composites prepared with different masses of CNT. As shown in Figure 4-16, all the DAPQ-COFX composites and CNT exhibit type II isotherms. The N_2 uptake at low pressures ($P/P_0 \approx 0.01$) indicates that these composites possess micropores. The hysteresis loop at the medium pressure region ($P/P_0 = 0.4-0.7$) reveals that mesopores exist in the materials. A large number of macropores are detectable by the N_2 adsorption method in the higher pressure range ($P/P^0 > 0.8$). Compared to the nitrogen sorption isotherm of DAPQ-COF, it is clear that there are more macropores in the composites. This may be because of the introduction of CNT in the composite. With the addition of more CNT, the N_2 uptake at high pressure increased. The nitrogen sorption isotherm of CNT shows a Type II profile and a large uptake at high pressure. The SA_{BET} of DAPQ-COFXs increased as the wt.% of CNT was increased from 130 $m^2 g^{-1}$ for DAPQ-COF10 up to 197 $m^2 g^{-1}$ for DAPQ-COF50 (Table 4-4). The DAPQ-COFX composites exhibited reduced surface areas (DAPQ-COF10 < DAPQ-COF30 < DAPQ-COF50) relative to both pure COF and CNT components. The pore size distribution (Figure 4-16b, calculated by NL-DFT for pillared clay) also confirms the presence of micropores and mesopores. All the DAPQ-COFX composites have pores with an average width of 14 Å, which is larger than the diameter of Li-ion (1.52 Å) and could, therefore, be beneficial for Li-ion transport within the composites. The detailed BET surface areas, pore volumes, and pore sizes of the DAPQ-COF, DAPQ-COFX, and CNT are listed in Table 4-4.

Table 4-4. Surface areas and pore volumes of DAPQ-COF and the DAPQ-COF composites.

Sample	SA_{BET}[a] ($m^2 g^{-1}$)	Total pore volume[b] ($cm^3 g^{-1}$)
DAPQCOF	245	0.131
DAPQCOF10%CNT	130	0.086
DAPQCOF30%CNT	143	0.069
DAPQCOF50%CNT	197	0.115
CNT	247	0.322

[a]Surface area calculated from the N_2 adsorption isotherms at 77.3 K using the BET equation;
[b]Pore volume calculated from the nitrogen isotherm at $P/P_0 = 0.99$, 77.3 K.

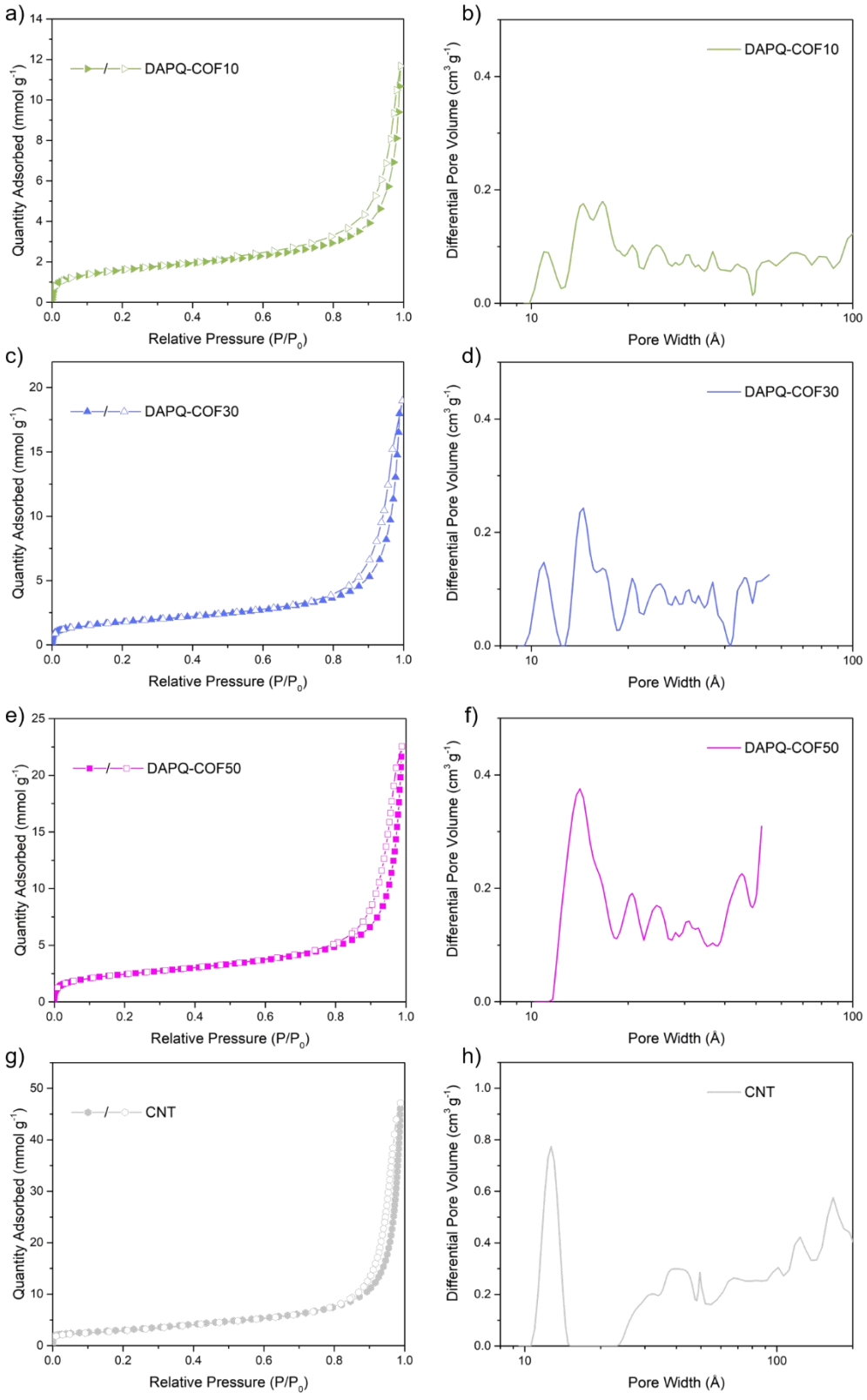

Figure 4-16. (a,c,e,g) N_2 sorption isotherms of DAPQ-COFX composites, and CNT (77.3 K, solid symbols = adsorption; open symbols = desorption); (b,d,f,h) Pore size distribution plots of the DAPQ-COFX composites, and CNT (calculated by NL-DFT for pillared clay).

TEM was used to confirm the structure of the DAPQ-COFX composites. Tube-type core-shell structures of DAPQ-COFX with the COF structure grown around the external surface of the CNT were observed in the TEM images (Figure 4-17). The COF layers grown on the surface of the CNTs retain their crystallinity and thicker COF layers were observed in DAPQ-COF10, compared to DAPQ-COF30 and DAPQ-COF50. The HR-TEM image of the pure CNTs used in this work is provided in Figure 4-17d. The morphologies of DAPQ-COF and the DAPQ-COFX composites were recorded by SEM (Figure 4-18). DAPQ-COF was found to have a rod-like morphology in the SEM images. By contrast, DAPQ-COF10, DAPQ-COF30, and DAPQ-COF50 appear to retain bulk CNT morphology, supporting a uniform COF layer on the surface. Whereas for DAPQ-COF10, we only observed rod-shaped particles, implying the CNTs were completely covered in a thicker layer of COF. In the *in situ* synthesis, the COFs tend to grow on the surface of the CNT because of the non-covalent interaction between the reactive monomers and the CNT. With more CNT in the composite, there is more surface for the COFs to grow on. So, the thickness of COF layers decreases with the increase of CNT mass weight. Thinner COF layers shorten the ion transport pathway and make more electrochemical active sites accessible. Therefore, Thinner COF layers are good for electrochemical performance.

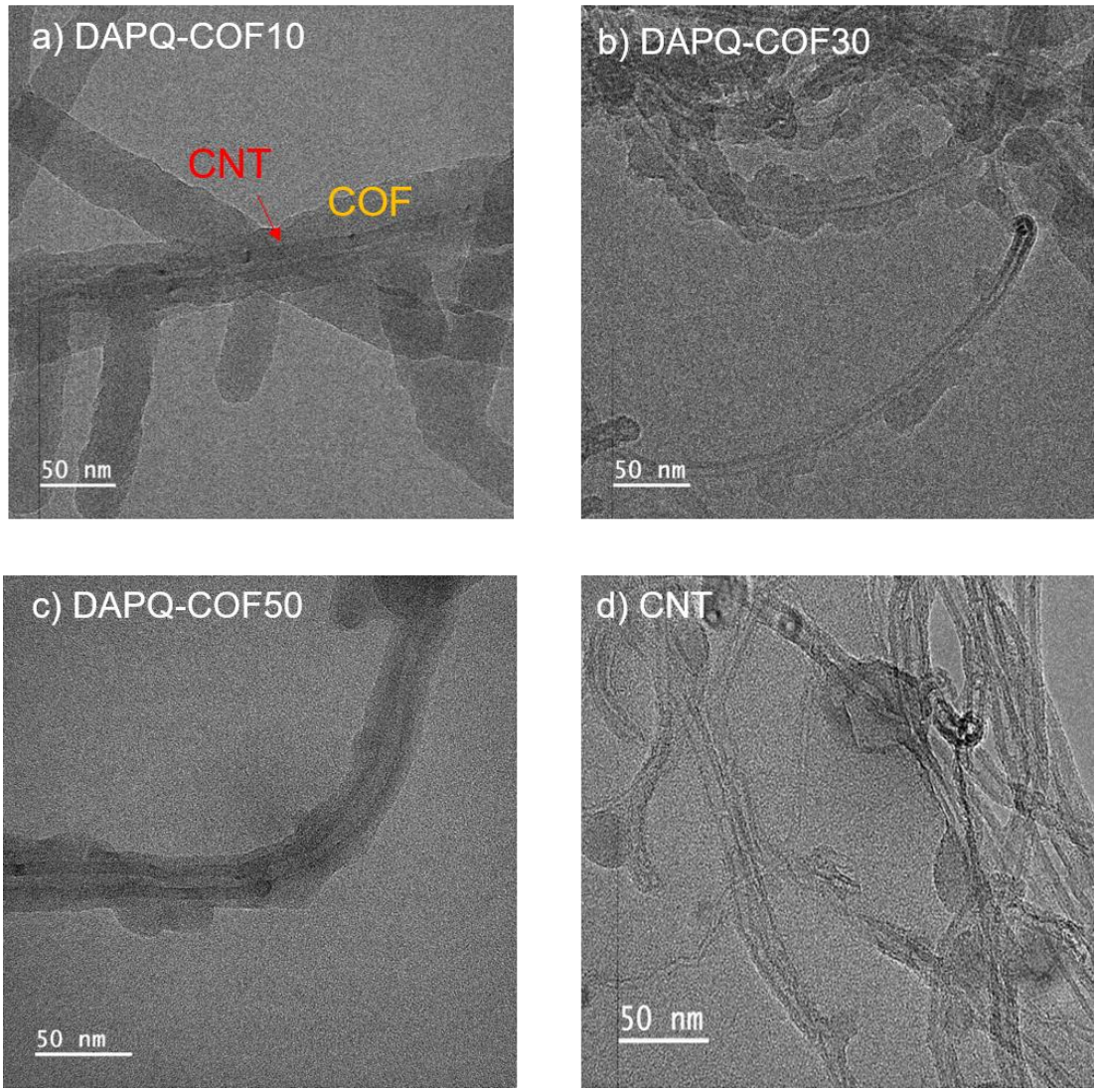

Figure 4-17. TEM images of (a) DAPQ-COF10; (b) DAPQ-COF30; (c) DAPQ-COF50; and (d) CNT.

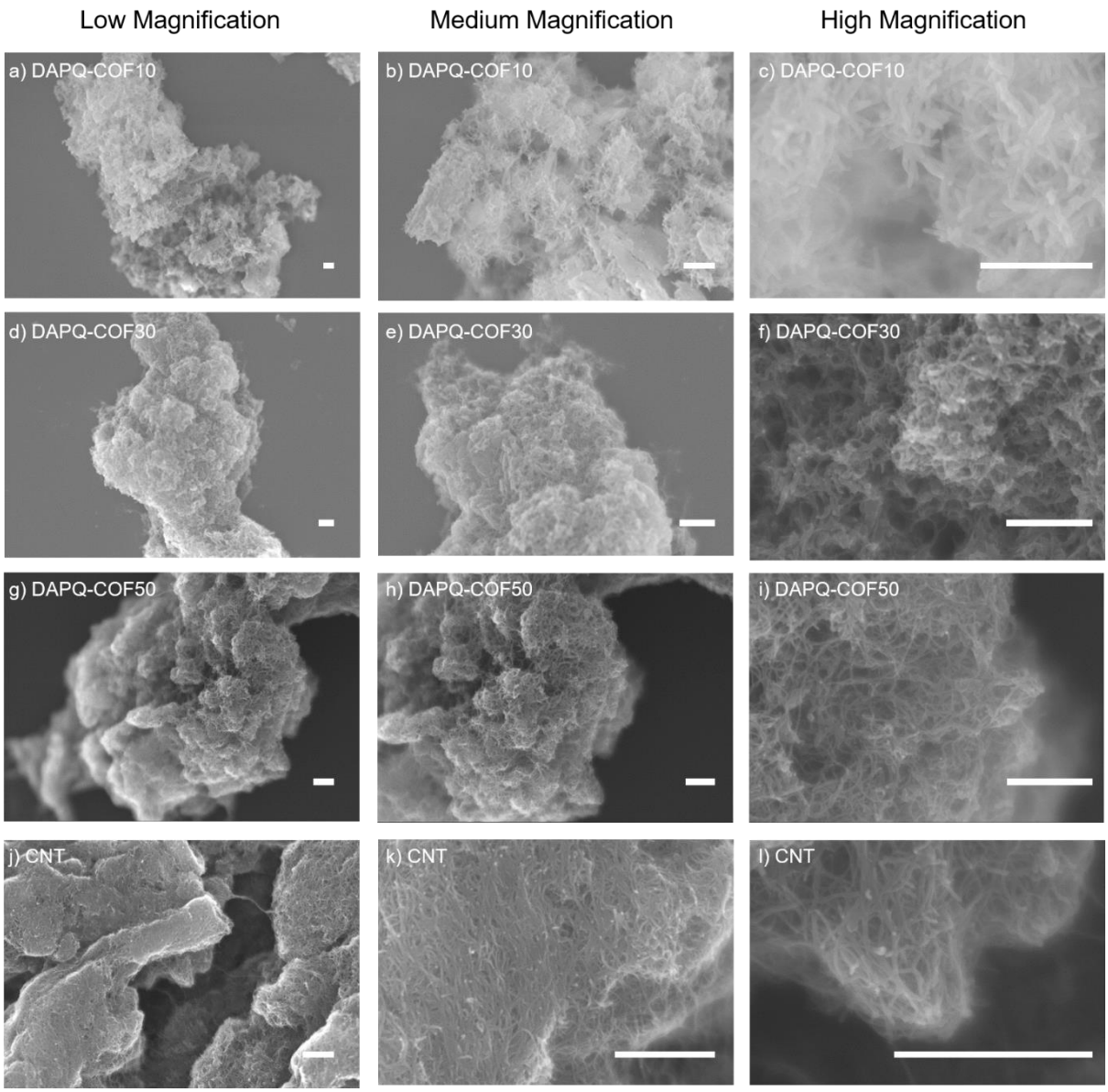

Figure 4-18. SEM images of DAPQ-COF10 (a-c), DAPQ-COF30 (d-f), DAPQ-COF50 (g-i), CNT (j-l); scale bar: 1 μm.

4.7 Electrochemical Characterisation

The electrochemical performance of DAPQ-COF and the DAPQ-COFX composites as positive electrodes for Li-ion coin cells was then investigated. Coin cells were assembled with DAPQ-COF or the DAPQ-COFX composites as the positive electrode and Li as the counter electrode. 1 M LiTFSI in DOL and DME (1:1 v/v) was used as the electrolyte formulation because it supports good performance in organic cathode materials.[14,23,38] By contrast, Li-ion battery electrolytes based on lithium hexafluorophosphate salt in organic carbonates showed poor cycling performance for the DAPQ-COF-based materials investigated here (Figure 4-19). This might be caused by the undesired side reaction of the active site with the carbonated-based electrolyte.[38,39] Therefore, LiTFSI based electrolyte was chosen for the rest of the tests.

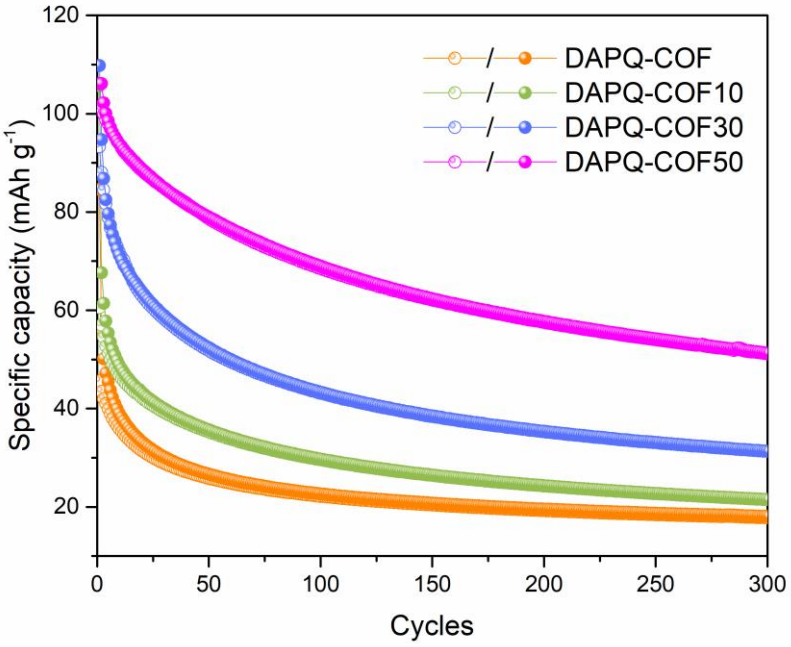

Figure 4-19. Cycling performance of DAPQ-COF and DAPQ-COFX in a conventional Li-ion battery electrolyte (1 M $LiPF_6$ in ethylene carbonate/dimethyl carbonate (1:1 v/v) over 300 cycles at 500 mA g^{-1} operated in the voltage range of 1.5-3.2 V.

CV of DAPQ-COF and DAPQ-COFX was performed on the coin cells at 0.1 mV s^{-1} in a potential window of 1.5 -3.2 V, starting from open circuit potential (2.8 V) to the cathodic scan (discharge) direction. (Figure 4-20a). All the samples had similarly shaped CV curves with two

pairs of redox peaks at 2.3 and 2.8 V, corresponding to the two-electron reaction of the carbonyl groups in one DAPQ unit.[40] Further, the peak current densities and integral charge (based on the mass of DAPQ-COF active material) increased as the mass ratio of CNT in the DAPQ-COFX composite was increased. DAPQ-COF50 has the highest integral charge area, indicating more efficient utilisation of redox-active sites in DAPQ-COF50 than in DAPQ-COF. This may be because the CNT in the composites enhances charge transport, but it is important to note that all electrode composites (DAPQ-COF and the DAPQ-COFX composites) contained conductive carbon black (30% by weight for DAPQ-COF and 20% by weight for the DAPQ-COFX composites).

Galvanostatic charge/discharge tests were carried out over a voltage window of 1.5 to 3.2 V on all the positive electrodes (Figure 4-20b). The sloping plateaus in the voltage profiles agree well with the corresponding CV curves, which were attributed to the reversible reduction/oxidation of the carbonyl groups in the DAPQ units. The average discharge potential of DAPQ-COFs and DAPQ-COFX composite is about 2.56 V, which is higher than most of the reported COF-based positive electrodes (Table 4-5).[41–43] In Table 4-5, the average discharge potential of the COFs based cathode materials. Most of them have an average discharge potential around 2.3 V. TEMPO-COF exhibited the highest discharge potential of 3.15 V because of the high redox potential of the nitroxyl radical.[17] DAPQ-COF contains an abundance of electron-withdrawing groups (C=O), which could decrease the lowest unoccupied molecular orbital level and, in turn, raise the reduction potential.[44] At the current density of 500 mA g^{-1}, DAPQ-COF has a specific capacity of 73 mAh g^{-1}, corresponding to only 46% of its theoretical capacity (based on its theoretical specific capacity of 157 mAh g^{-1}, see Figure 4-7 for full details). However, in DAPQ-COF10, DAPQ-COF30, and DAPQ-COF50 the specific capacity at 500 mA g^{-1} improved to 92, 116, and 162 mAh g^{-1}, respectively. Considering that CNT can contribute 1, 6, and 13 mAh g^{-1} to the specific capacities of DAPQ-COF10, DAPQ-COF30 (see Table 4-3 for full details), the utilisation of redox-active sites increased to 58, 70, and 95% in DAPQ-COF10, DAPQ-COF30, and DAPQ-COF50, respectively. Moreover, DAPQ-COF and DAPQ-COFX retained a near-constant capacity after 400 cycles and their Coulombic efficiencies were nearly 100%, highlighting their excellent electrochemical stability (Figure 4-20).

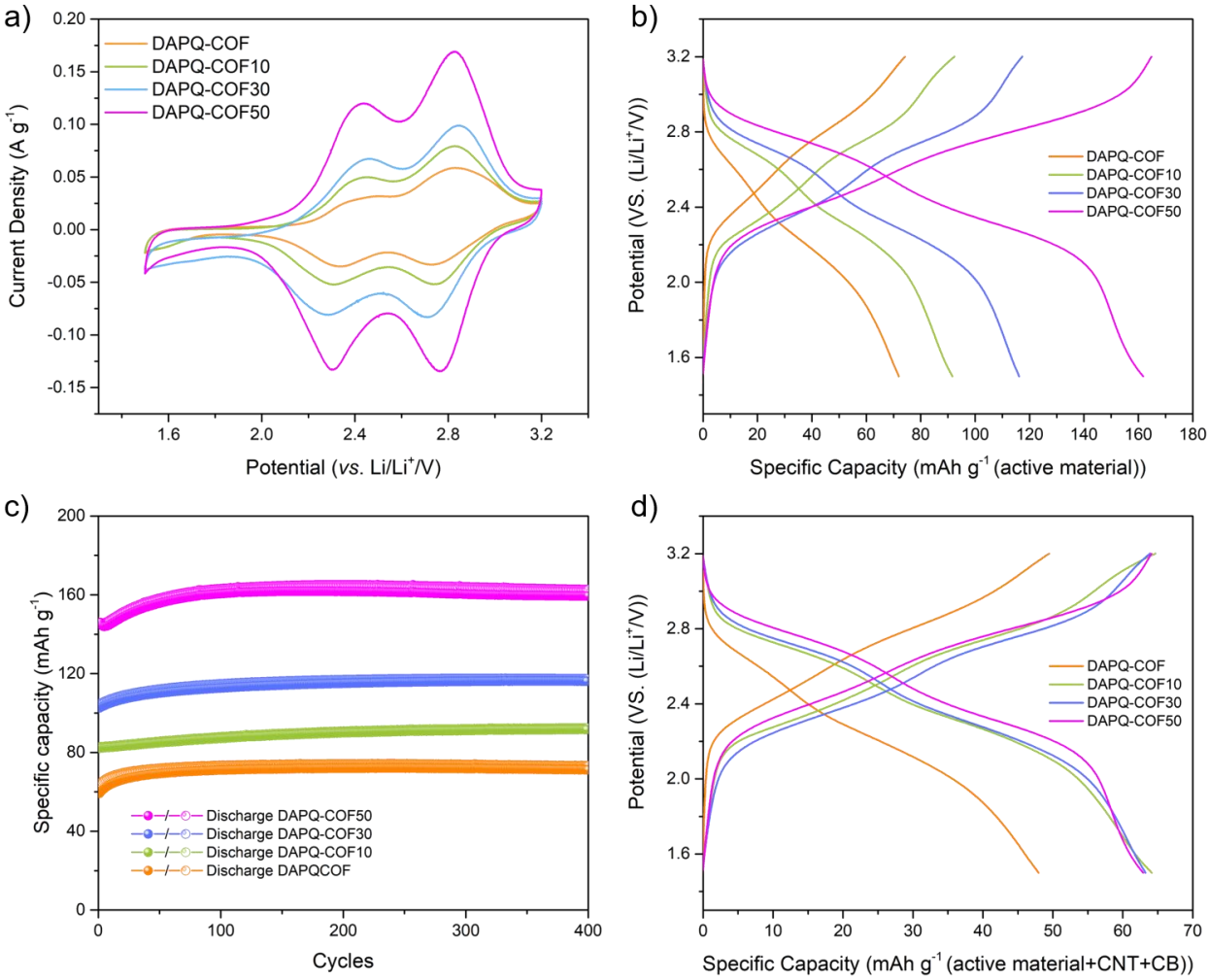

Figure 4-20. (a) Cyclic voltammetry profiles at a scan rate of 0.1 mV s^{-1}; (b) Charge-discharge profiles at 500 mA g^{-1}; (c) Cycling performances over 400 cycles at 500 mA g^{-1} for DAPQ-COF, DAPQ-COF 10, DAPQ-COF30, and DAPQ-COF50; (d) Charge-discharge profiles (based on active material, CNT, and carbon black (CB)) at 500 mA g^{-1} for DAPQ-COF, DAPQ-COF 10, DAPQ-COF30, and DAPQ-COF50. In panel (c) the charge and discharge capacities are represented by open and solid symbols.

Table 4-5. Average discharge potential and cycling performance comparison of DAPQ-COFX with other COFs based electrodes reported in the literature.

Active compound	Key functional group	Discharge capacity (mAh g^{-1})/Current density (mA g^{-1})	Cycling performance (Current density)	Average discharge Voltage (vs. Li^+/Li /V)	Specific Energy (Wh/kg)	Ref.
PIBN-G	Imide-benzoquinone	271 / 28	88% after 300 cycles (1400 mA g^{-1})	2.3	621	[25]
2D CCP-HATN@CNT	Hexaaza-trinaphthalene	116 / 11.7	91% after 1000 cycles (500 mA g^{-1})	2.02	234	[45]
PI-ECOF-1	Imide	112 / 14.2	77% after 300 cycles (142 mA g^{-1})	2.02	226	[14]
PI-ECOF-1/rGO50	Imide	167 / 14.2	70% after 300 cycles (142 mA g^{-1})	2.02	337	[14]
2D-PAI@CNT	Naphthimide	104.4 / 100	100% after 8000 cycles (500 mA g^{-1})	2.42	251	[15]
2D-PAI	Naphthimide	28.5 / 100	100% after 50 cycles (100 mA g^{-1})	2.42	68.9	[15]
DAAQ-ECOF	Anthraquinone	145 / 20	92% after 1800 cycles (500 mA g^{-1})	2.3	333.5	[17]
DABQ-ECOF	Benzoquinone	210 / 20	—/—/—	2.8	588	[17]
TEMPO-ECOF	Nitroxide radical	115 / 20	—/—/—	3.15	362	[17]
D_{TP}-A_{NDI}-COF@CNTs	Naphthimide	74 / 200	100% after 700 cycles (200 mA g^{-1})	2.4	177	[22]
Tp-DANT-COF	Naphthimide	93.4 / 200	85% after 600 cycles (1000 mA g^{-1})	2.4	224	[46]
Tb-DANT-COF	Naphthimide	144.4 / 50	75% after 300 cycles (500 mA g^{-1})	2.5	360	[46]

PPTODB	Pyrene-4,5,9,10-tetraone	198 / 20	68% after 150 cycles (20 mA g^{-1})	2.5	495	[47]
DAAQ-TFP	Anthraquinone	50 / 78.5	19% after 500 cycles (157 mA g^{-1})	2.2	161	[41]
DAPH-TFP	Phenazine	82 / 85.5	43% after 500 cycles (171 mA g^{-1})	2.3	221.26	[41]
PEDOT@DAAQ-TFP	Anthraquinone	52 / 78.5	28% after 500 cycles (157 mA g^{-1})	2.2	137	[41]
PEDOT@DAPH-TFP	Phenazine	94 / 85.5	31% after 500 cycles (171 mA g^{-1})	2.3	228	[41]
DAPQ-COF	Phenanthrenequinone	73 / 500	100% after 400 cycles (500 mA g^{-1})	2.56	184	**This work**
DAPQ-COF10	Phenanthrenequinone	92 / 500	100% after 400 cycles (500 mA g^{-1})	2.56	236	**This work**
DAPQ-COF30	Phenanthrenequinone	116 / 500	100% after 400 cycles (500 mA g^{-1})	2.56	297	**This work**
DAPQ-COF50	Phenanthrenequinone	161 / 500	76% after 3000 cycles (2000 mA g^{-1})	2.56	412	**This work**

When the DAPQ monomer was used as the positive electrode it delivered an initial capacity of 204 mAh g^{-1} at 500 mA g^{-1} (91% of its theoretical specific capacity) (Figure 4-21), which is higher than DAPQ-COF and the DAPQ-COFX composites, but its capacity rapidly decreased to 21 mAh g^{-1} after only 10 cycles. The rapid reduction in performance of the DAPQ monomer is attributed to its dissolving in the electrolyte, which then caused the electrolyte to turn blue (Figure 4-21c). Conversely, DAPQ-COF and the DAPQ-COFX composites had low solubility in the electrolyte, and only a trace amount of the DAPQ monomer was found in the UV-Vis spectra of the electrode-soaked solvents (Figure 4-21b). The negligible solubility of DAPQ-COF and the DAPQ-COFX composites in the electrolyte greatly improved their cycling performance. We also prepared an amorphous polymer sample by reacting the DAPQ and TFG monomers in DMAc and mesitylene solvent. By comparison to DAPQ-COF by itself, the amorphous sample had a much lower SA_{BET} of 52 m^2 g^{-1} (Figure 4-22b) and a capacity of 19

mAh g^{-1} at 500 mA g^{-1} (Figure 4-22). For the amorphous sample, 19 mAh g^{-1} corresponds to 12% utilisation of the active sites and highlights how the poor uniform porosity hinders diffusion of the electrolyte.[10] We next explored whether the intricate tube-type core-shell structure of the DAPQ-COFX composites was required to obtain the higher rate performances. A sample of DAPQ-COF and CNT was prepared by ball milling dry samples of DAPQ-COF and CNT in a 1:1 mass ratio (DAPQ-COF/CNT). When DAPQ-COF/CNT was used as the active material, the resulting coin cell had a capacity of 129 mAh g^{-1} (Figure 4-23) at 500 mA g^{-1}, which is 32 mAh g^{-1} lower than DAPQ-COF50 under the same conditions. Hence, the *in situ* grown DAPQ-COF50 composite, with its tube-type core-shell structure with DAPQ-COF grown as a thin crystalline outer layer on the CNTs had better electrochemical accessibility of active sites.

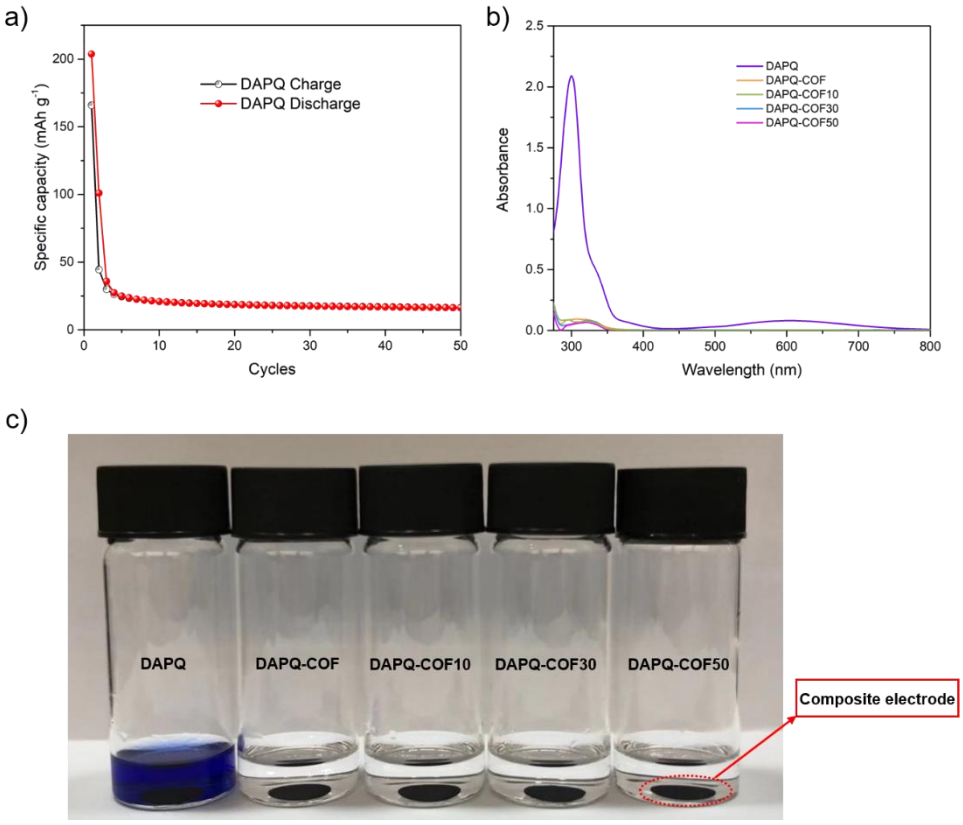

Figure 4-21. (a) Cycling performance of the DAPQ monomer over 50 cycles at 500 mA g^{-1} operated in the voltage range of 1.5-3.2 V; (b) UV/Vis spectra of DOL/DME (1/1 v/v, total 2 mL) solutions that were used to immerse the DAPQ, DAPQ-COF, and the DAPQ-COFX composite electrodes for two days; (c) Solubility of the DAPQ, DAPQ-COF, and the DAPQ-COFX composite electrodes in the electrolyte. In each vial, the electrode was immersed in 2 mL of the DOL and DME mixture (1/1 v/v) for two days.

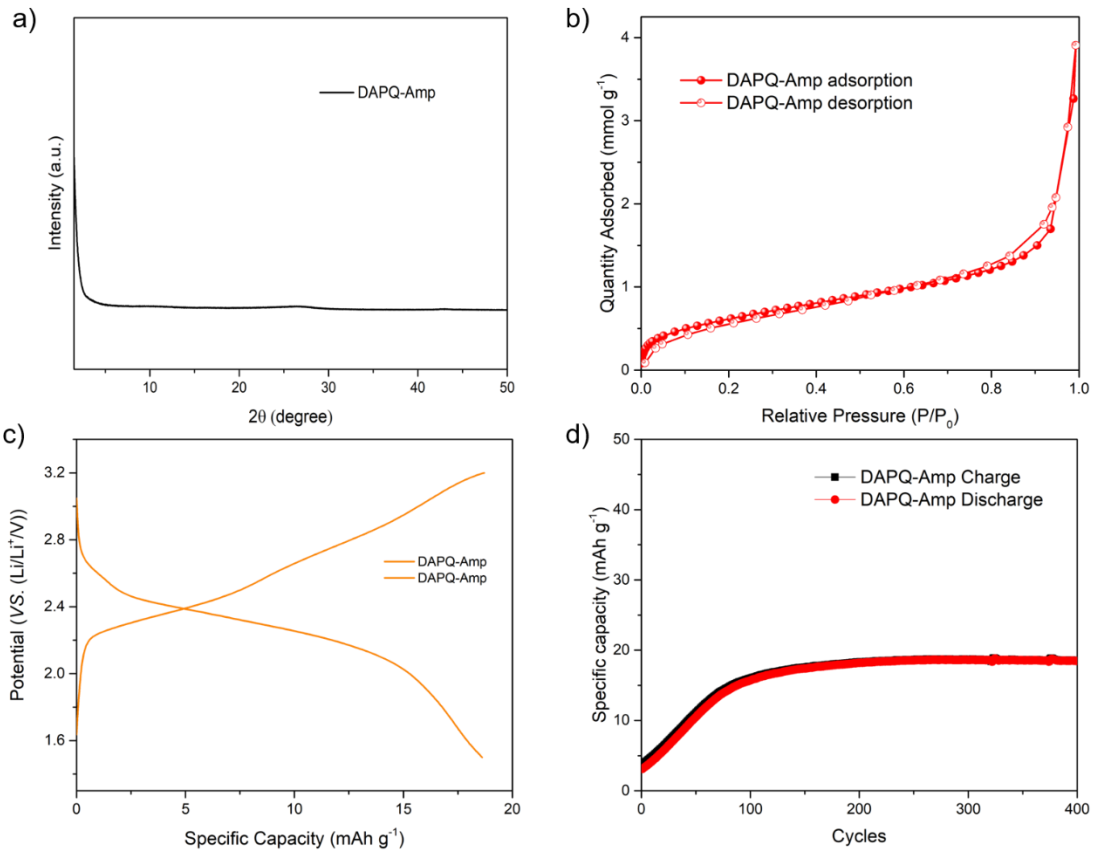

Figure 4-22. (a) PXRD pattern of the amorphous DAPQ-based polymer sample (DAPQ-Amp). DAPQ-Amp was prepared by reacting the DAPQ and TFG monomers in DMAc and mesitylene solvent mixture, as described in the experimental section; (b) N_2 gas sorption of DAPQ-Amp at 77.3 K (solid symbols = adsorption; open symbols = desorption). The calculated SA_{BET} is 51 m^2 g^{-1}; (c) Galvanostatic charge/discharge curve of amorphous DAPQ-COF electrode at 500 mA g^{-1}; (d) Cycling performance over 400 cycles for amorphous DAPQ-COF electrode at 500 mA g^{-1} operated in the voltage range of 1.5-3.2 V.

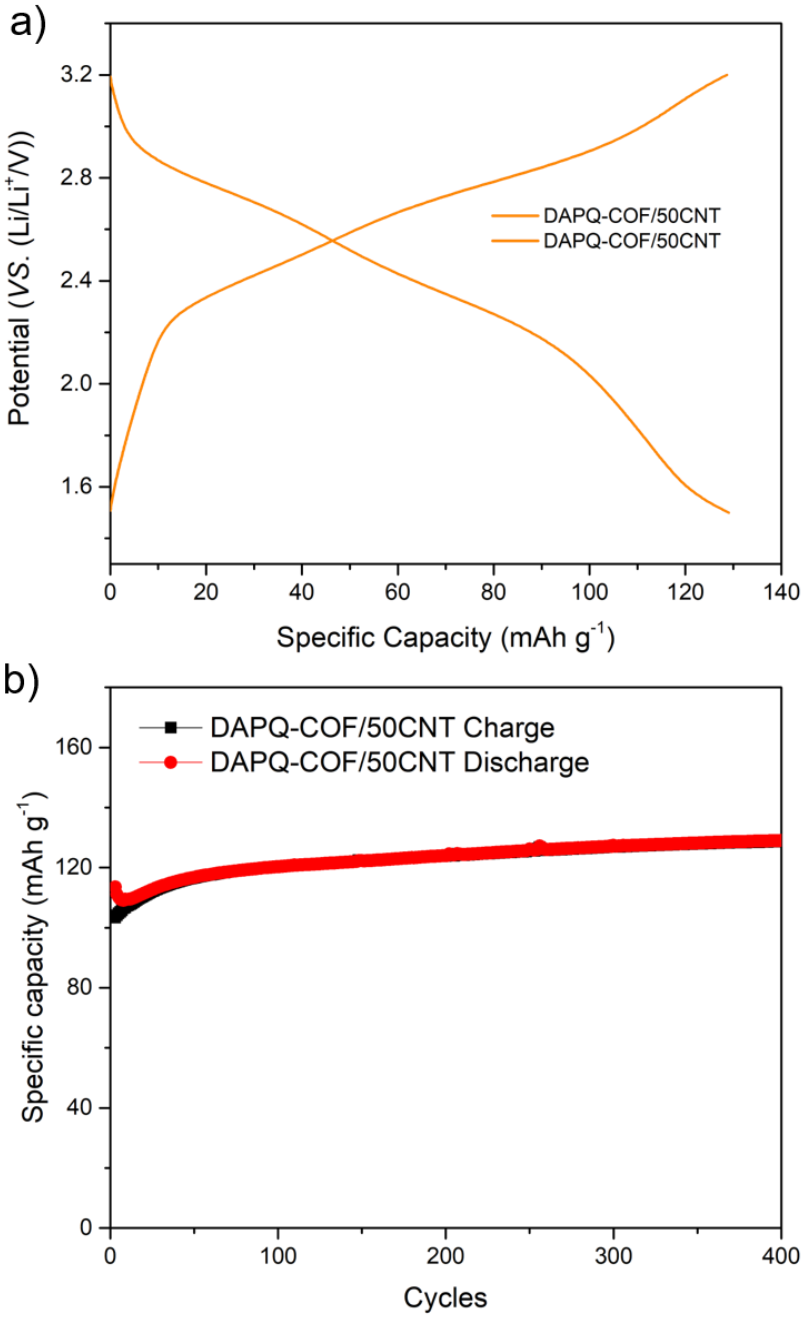

Figure 4-23. (a) Galvanostatic charge/discharge curve of DAPQ-COF/50CNT (physically mixed composite) at 500 mA g^{-1}; (b) Cycling performance over 400 cycles for DAPQ-COF/50CNT at 500 mA g^{-1} operated in the voltage range of 1.5-3.2 V.

To calculate the capacity contributions of CNT and carbon black towards the overall capacities of the composites, their electrochemical performances in isolation were also investigated. CNT delivered a capacity of 13 mAh g^{-1} under 500 mA g^{-1} when its electrode was made from CNT: PVDF (9:1 by mass), while carbon black delivered a capacity of 1 mAh g^{-1} under 500 mA g^{-1} when its electrode was made from carbon black: PVDF (9:1 by mass) (Figure 4-24).

The capacity of the DAPQ-COF50 active material is comparable to positive electrode materials used in commercial cells, such as $LiFePO_4$ that has a capacity of 162 mAh g^{-1}.[48] However, when the capacities of the composites are calculated based on the total mass of the active material plus the conductive additives, the DAPQ-COFX electrodes with different amounts of CNT exhibit similar specific capacities at around 63 mAh g^{-1} (Figure 4-20d). Therein, the voltage profiles indicate the higher quantity of CNT within the DAPQ-COFX composites results in reduced overpotentials on charge and discharge within the studied ranges. However, given the similar specific capacities of all DAPQ-COFX electrodes when considering the total electrode mass, adding too much conductive additive was not an ideal strategy for maximising energy densities for practical cells. As we are focusing on the electrochemical properties of DAPQ-COF active material in this research, all gravimetric capacities and currents are normalized to the mass of the active material (DAPQ-COF), with the exception of Figure 4-20d.

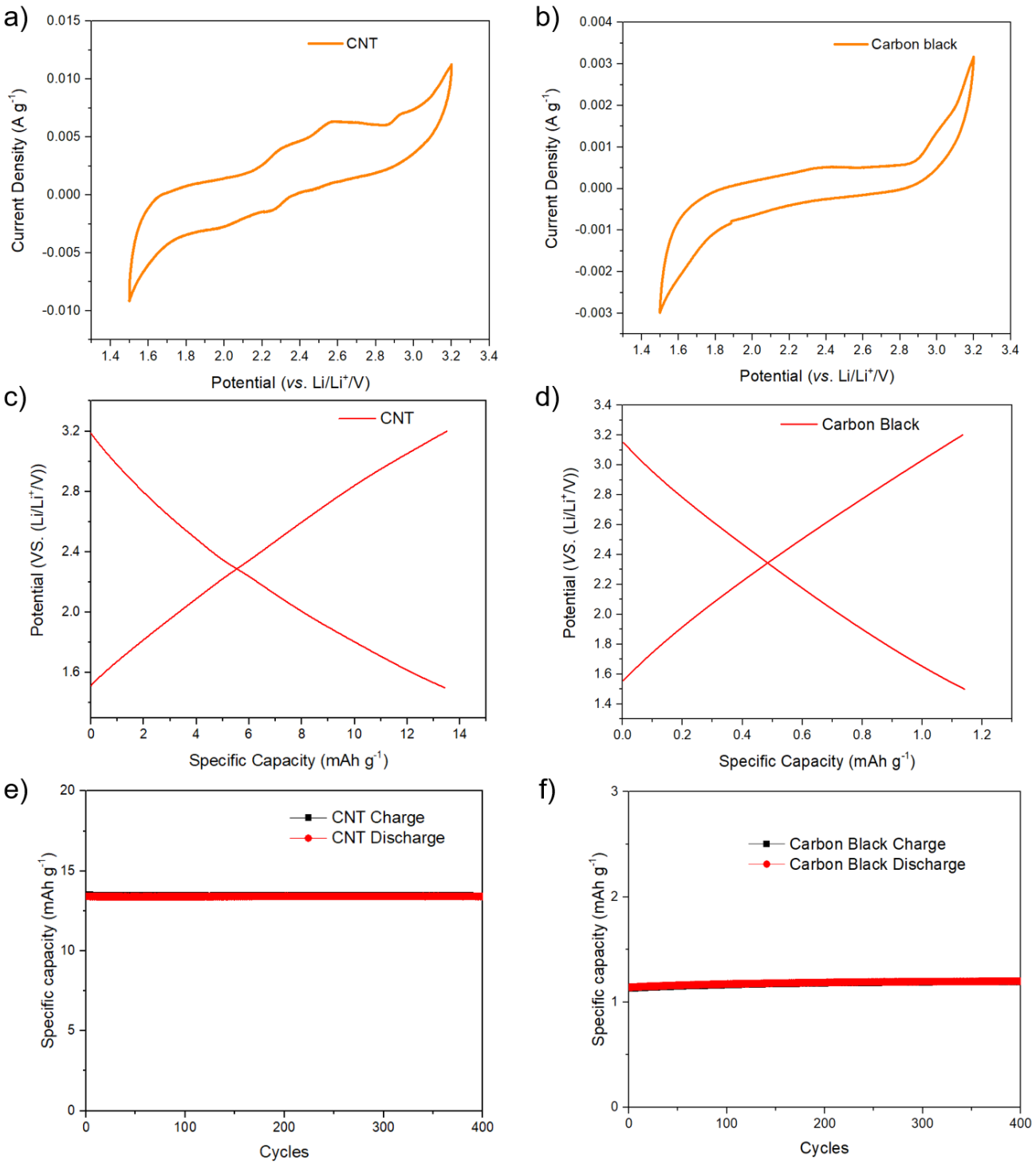

Figure 4-24. (a) Cyclic voltammetry profile of CNT electrode at a scan rate of 0.1 mV s^{-1}; (b) Cyclic voltammetry profile of carbon black electrode at a scan rate of 0.1 mV s^{-1}; (c) Galvanostatic charge/discharge curve of CNT electrode at 500 mA g^{-1}; (d) Galvanostatic charge/discharge curve of carbon black electrode at 500 mA g^{-1}; (e) Cycling performance over 400 cycles for CNT electrode at 500 mA g^{-1} operated in the voltage range of 1.5-3.2 V; (f) Cycling performance over 400 cycles for carbon black electrode at 400 mA g^{-1} operated in the voltage range of 1.5-3.2 V.

Cyclic stability is another important criterion to estimate the performance of a battery. In this study, the long-term cycling performance of DAPQ-COF50 was studied by repeated charge/discharge experiments at a current density of 2000 mA g^{-1} (about 12.7 C) (Figure 4-25). DAPQ-COF50 reached a capacity of 146 mAh g^{-1} during cycling, and a small capacity loss was observed for DAPQ-COF50 during 3000 charge/discharge cycles. After 3000 cycles, DAPQ-COF50 retained 76% of its highest recorded capacity (a capacity loss of ca. 0.008% per cycle), indicating stable active site utilisation and good cycling stability. The Coulombic efficiency for DAPQ-COF50 was also maintained at close to 100%, at a current density of 2000 mA g^{-1}. The cycling performance of DAPQ-COF50 is better than many other reported COFs active materials (Table 4-5). For example, a polyimide-based COF (Tb-DANT-COF) exhibited a 75% capacity retention after 300 charges/discharge cycles at 500 mA g^{-1},[46] a 2-D boroxine-linked chemically-active pyrene-4,5,9,10-tetraone COF (PPTODB) delivered 88% of the initial capacity after 150 charge-discharge cycles under 20 mA g^{-1},[47] and 2D polyarylimide-based COF (2D-PAI@CNT) has the highest cycling performance reported (100% capacity retention after 8000 charge-discharge cycles at 500 mA g^{-1}).

FT-IR spectroscopy was used to characterise the potential structural/chemical changes of DAPQ-COF after the charge/discharge cycling test. FT-IR spectra were recorded for the as-prepared electrode material and electrode material that was recovered from a cell after undergoing 400 charge-discharge cycles at 500 mA g^{-1}. For the cycled material, the coin cell was disassembled inside a glovebox and the electrode was washed with DOL before being dried under reduced pressure at room temperature. The FT-IR (ATR) measurements were then performed under a nitrogen atmosphere. The FT-IR spectrum of the DAPQ-COF50 electrodes after 400 cycles keeps the same as the spectrum of the fresh DAPQ-COF50 electrode (Figure 4-26). The characteristic carbonyl (1647 cm^{-1}) and C-N (1250 cm^{-1}) bands were retained after cycling. No obvious changes to the morphology of the DAPQ-COF50 electrode were observed from the SEM images taken before and after the 400 cycling charge/discharge experiment (Figure 4-27).

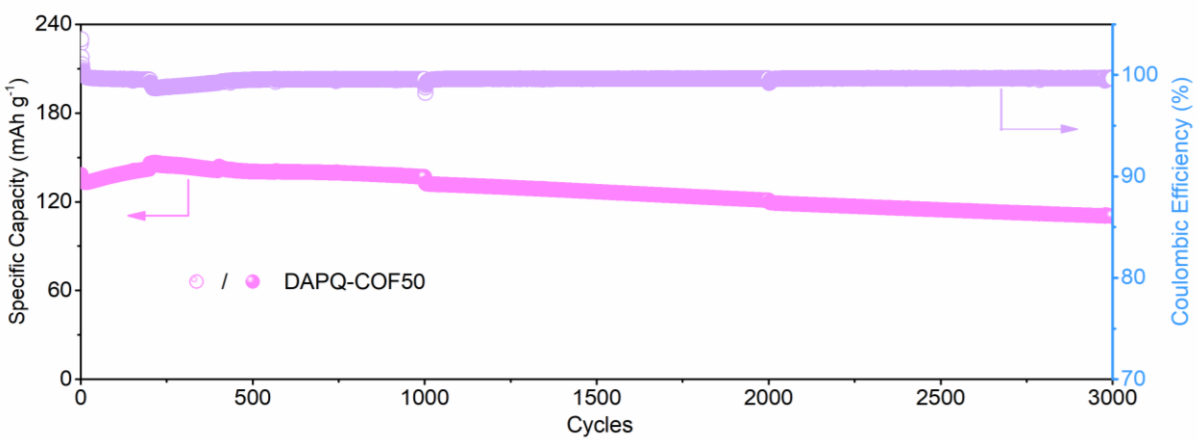

Figure 4-25. Long-term cycling stability of DAPQ-COF50 at 2000 mA g^{-1}, charge and discharge capacities are represented by open and solid symbols, respectively.

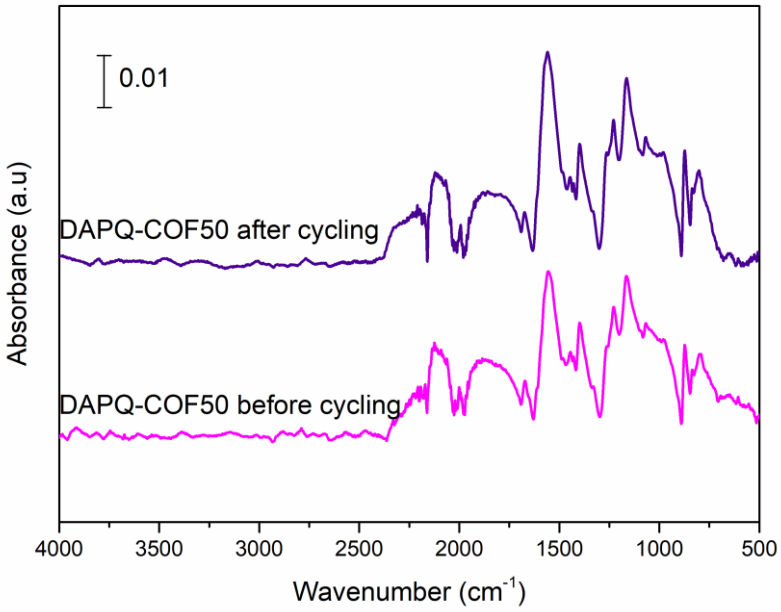

Figure 4-26. FT-IR spectra of DAPQ-COF50 electrode before and after 400 cycles.

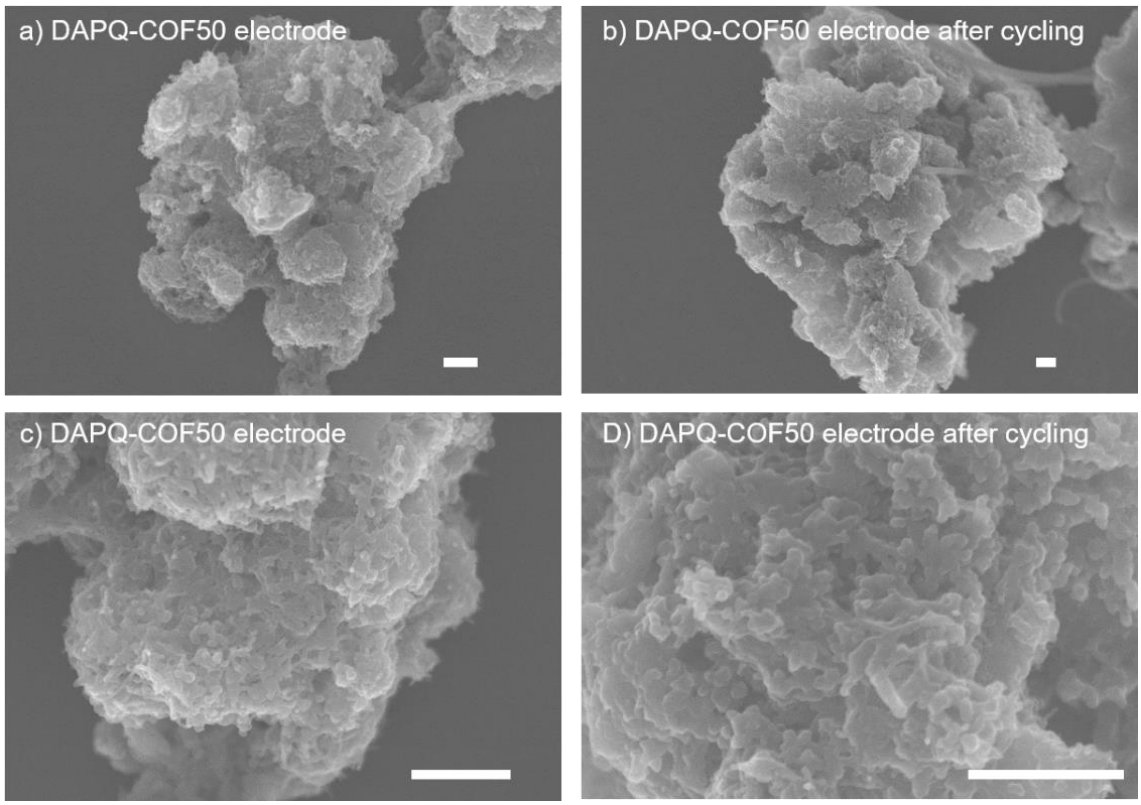

Figure 4-27. SEM images of DAPQ-COF50 electrode before and after 400 cycles at 500 mA g^{-1} (scale bar: 1µm).

The rate capability of DAPQ-COF and the DAPQ-COFX composites were then investigated over the range 500 – 2000 mA g^{-1} (Figure 4-28a). The capacity retention at 2000 mA g^{-1} for DAPQ-COF, DAPQ-COF10, DAPQ-COF30, and DAQ-COF50 were 64%, 77%, 90%, and 92%, respectively, as a result of the *in situ* growth of COF on the surface of the CNT improving the overall conductivity of the composite. The relatively thinner and intimately contacting layers in DAPQ-COF50 (and to some extent DAPQ-COF30) improve overall electrochemical accessibility that is unhindered even at high rates of (dis)charge. In addition, the capacity of all composites recovered to the initial values once the current was reduced back to 500 mA g^{-1} and Coulombic efficiency remained at approximately 100% for all cycles, indicating the higher rates of charge/discharge did not impact upon material stability in this measurement range.

Subsequently, we looked more in-depth at our best performing COF-composite, DAPQ-COF50, to demonstrate how the preparation of this material allows the boundaries of rate performance to be expanded. Therein, the rate performance of DAPQ-COF50 was tested up to 50000 mA g^{-1}. Despite some reasonable overpotential increases at the highest currents, the voltage profiles

consistently feature the same sloped plateaus associated with faradaic discharge and charge reactions, signifying the excellent transport properties of both Li^+ ions and electrons within the DAPQCOF-50 electrodes (Figure 4-28b). The rate performance for DAPQ-COF50 from 500 to 50000 mA g^{-1} shows excellent capacity retention, and no loss of Coulombic efficiency at ultra-high current densities (Figure 4-28c). DAPQ-COF50 delivers 129 mAh g^{-1} at 10000 mA g^{-1}, equating to a retention of 80% of the capacity attained at 500 mA g^{-1}. When the current density is pushed further to ultra-fast discharge/charge rates at 50000 mA g^{-1}, DAPQ-COFX still provides excellent rate performance and delivers 94 mAh g^{-1} discharge capacities (54% retention). For context, this upper testing limit of current density equates to an approximate C-rate of 320 C and, therefore, corresponds to a full charge or discharge in *ca*. 11 seconds. Therein, the C-rate is defined as the current required to completely (dis)charge the electrode in 1 h, based on the theoretical capacity of the active material. Furthermore, the ultra-high current cycling steps did not appear to affect the material stability since the capacity at 500 mA g^{-1} recovered to the initial values.

The rate capability of DAPQ-COF50 is superior to those of the recently reported COF cathodes, wherein the upper current density limit achieved here exceeds these earlier works by an order of magnitude (Figure 4-29 and Table 4-6). For example, a poly(imide-benzoquinone) COF on graphene (PIBN-G) showed 73% of the capacity at 10 C, compared with the capacity at 1 C.[25] A COF containing redox-active naphthalene diimide walls on CNT (D_{TP}-A_{NDI}-COF@CNTs) retained 85% capacity under 1000 mA g^{-1} (12 C) vs the capacity at 200 mA g^{-1} (2.4 C).[22] A polyarylimide hybrid (2D-PAI@CNT) has 92% of the capacity when discharged at 19.2 C.[15] However, in the reported COF cathodes materials, there have yet been no tests beyond 5000 mA g^{-1}. Comparable current densities have previously been reported for a non-COF organic electrode material, wherein a linear polymer (PNDI-T2) was reportedly measured up to 500 C, corresponding to the absolute current density of 27100 mA g^{-1}, but this material for comparison only exhibited a capacity of 23.3 mAh g^{-1}.[49] In our case, we tested the DAPQ-COF50 based cathode up to 50000 mA g^{-1}, and it delivered a capacity of 94 mAh g^{-1}, corresponding to a high power density of *ca.* 110 kW kg^{-1}. This magnitude of power density, and the rapid charge/discharge times, would be competitive with electrochemical capacitors.[50] For further comparison of the rate performance of our material with prior literature, we plot the comparison data as functions of absolute capacities and in terms of C-rates in the supporting information (Figure 4-29). Furthermore, Figure 4-30 shows the analogous non-log scaling of Figure 4-29b

to highlight the dramatic scale of capacity retention achieved at the ultra-high current densities used here.

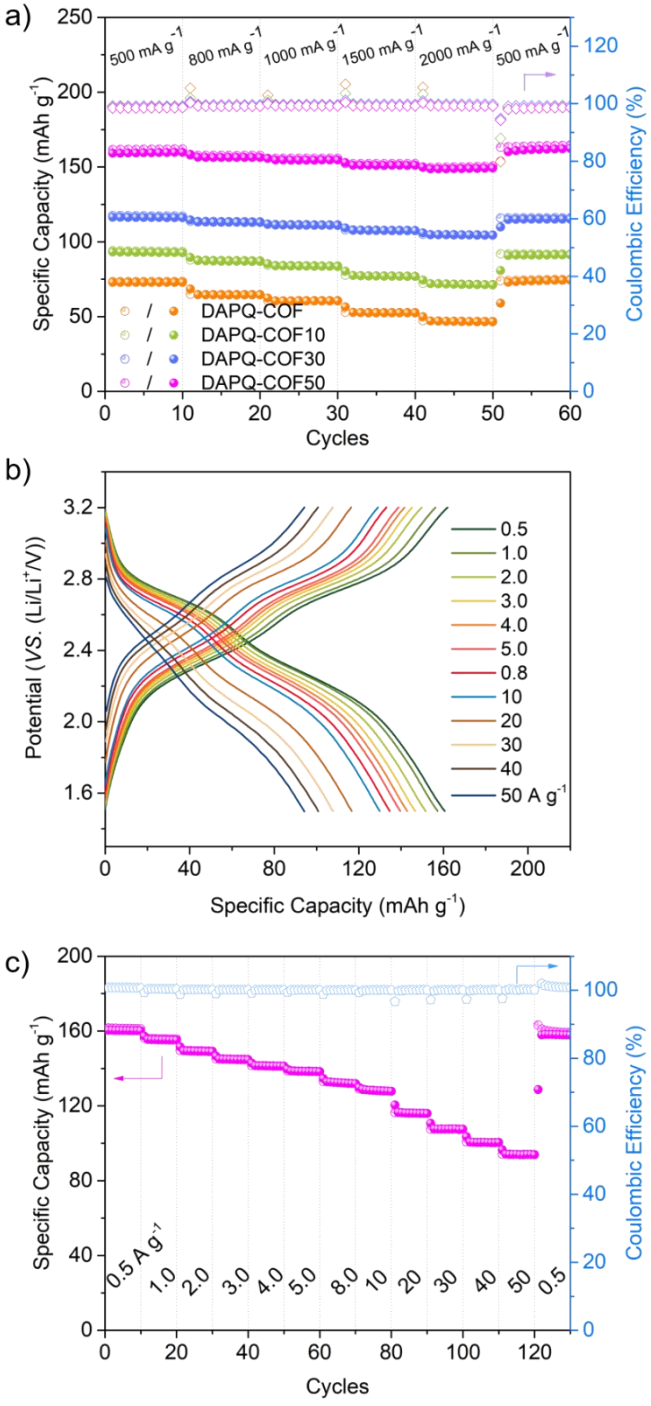

Figure 4-28. (a) Rate performances of DAPQ-COF, DAPQ-COF10, DAPQ-COF30, and DAPQ-COF50; (b) Charge-discharge profile of DAPQ-COF50 at different current density; (c) High rate performance of DAPQ-COF50. For panel (a) and (c) charge and discharge capacities are represented by open and solid symbols, respectively.

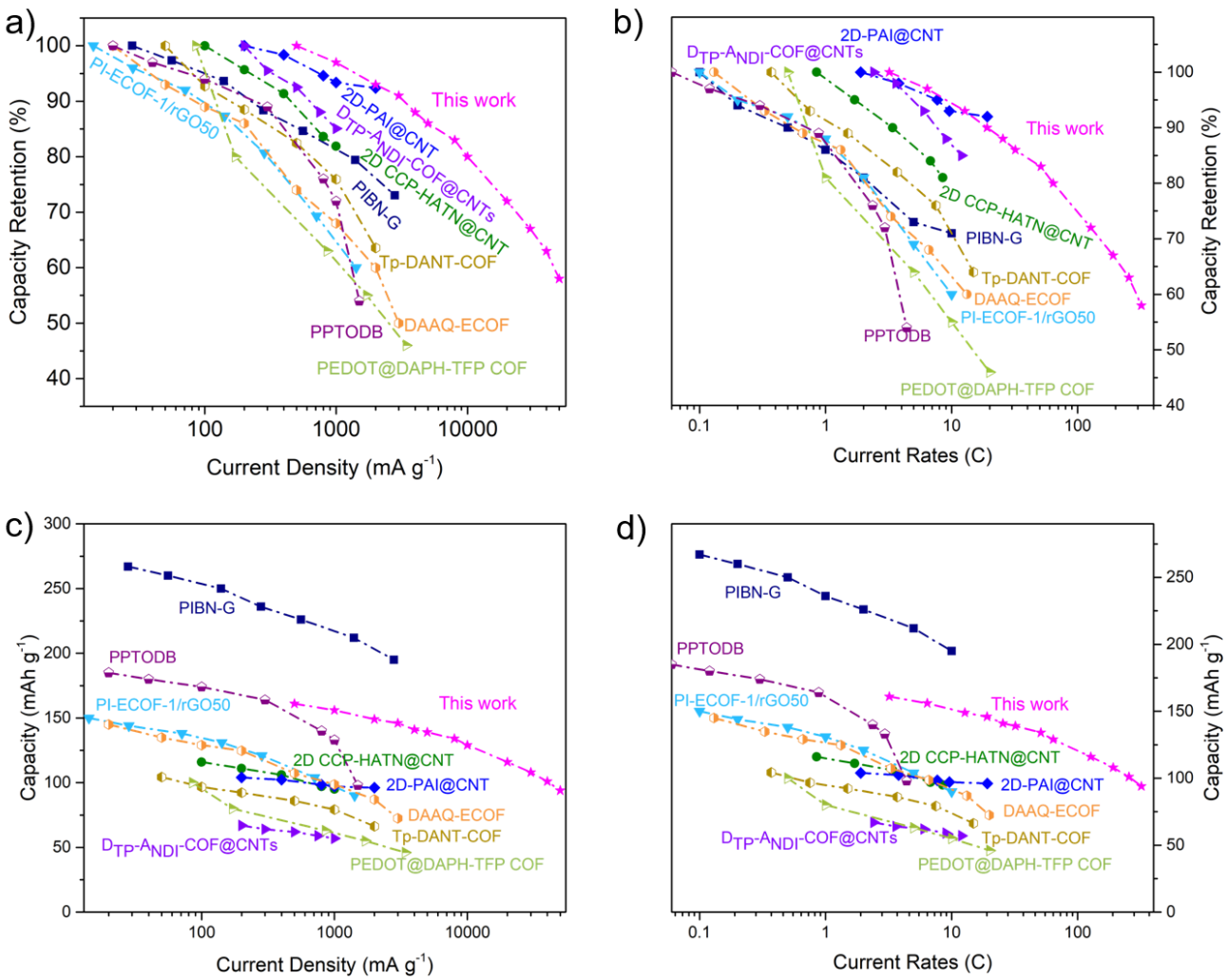

Figure 4-29. (a) Comparison of capacity retention of the COFs electrode as a function of gravimetric current densities; (b) Comparison of capacity retention of the COFs electrode as a function of C-rate based on the theoretical capacity of each material; (c) Comparison of the absolute specific capacity of the COFs electrode as a function of gravimetric current densities; (d) Comparison of the absolute capacity of the COFs electrode as a function of C-rate based on the theoretical capacity of each material.

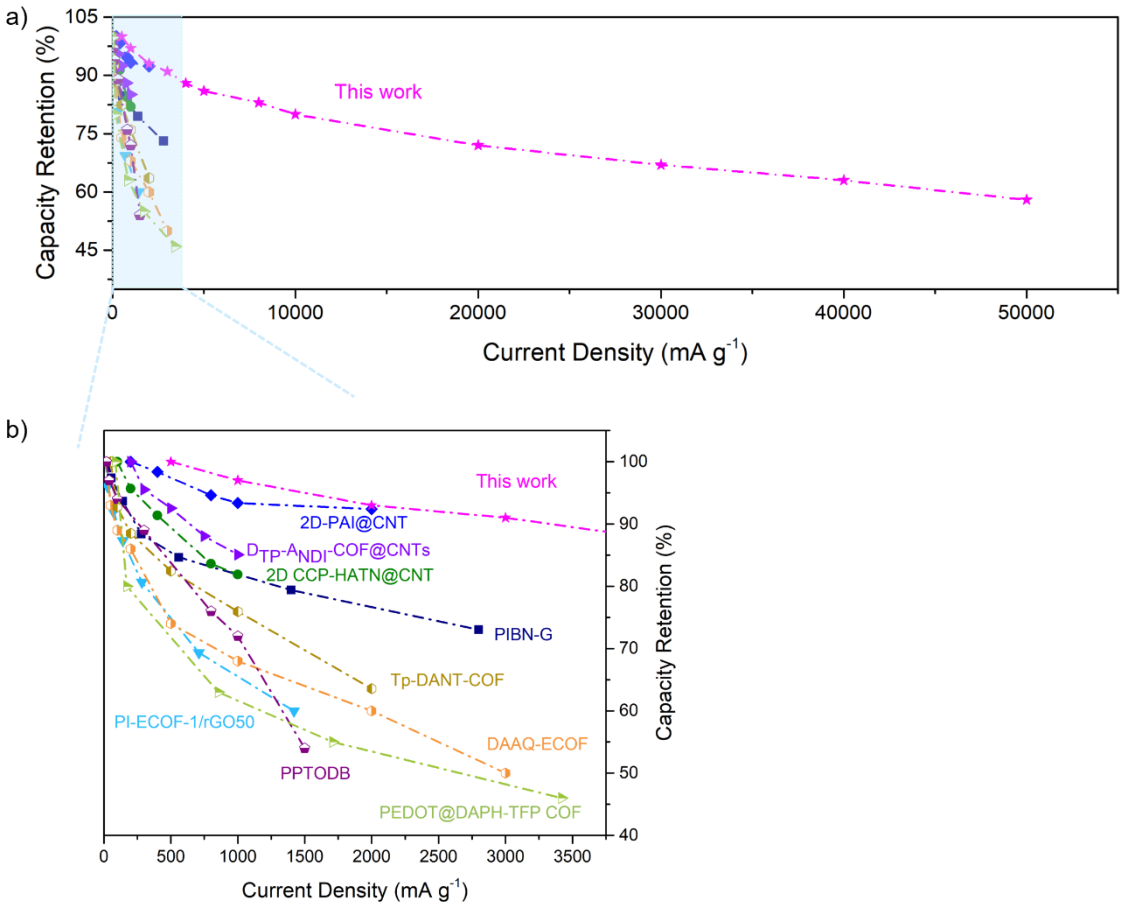

Figure 4-30. Comparison of capacity retention of the COFs electrodes as a function of gravimetric current density present in a non-logarithmic form.

Table 4-6. C-rate performance comparison of DAPQ-COFX with other reported COFs compounds electrode for data shown in Figures 4-29 and 4-30.

Active Material	Key functional group	Rate performance Current density (mA g^{-1}) Capacity retention (%)	Ref.
PIBN-G	Imide-benzoquinone	28, 56, 140, 280, 560, 1400, 2800, 56 100%, 94%, 90%, 86%, 81%, 73%, 94%	[25]
2D CCP-HATN@CNT	Hexaaza-trinaphthalene	100, 200, 400, 800, 1000, 100 100%, 95%, 90%, 84%, 81%, 100%	[45]
PI-ECOF-1	Imide	14.2, 28.4, 71, 142, 284, 710, 1420, 14.2 100%, 94%, 86%, 75%, 56%, 0.2%, 0.2%, 95%	[14]
PI-ECOF-1/rGO50	Imide	14.2, 28.4, 71, 142, 284, 710, 1420, 14.2 100%, 95%, 92%, 88%, 81%, 69%, 60%, 86%	[14]
2D-PAI@CNT	Naphthimide	28.6, 57.2, 114.4, 143, 286, 28.6 100%, 98%, 95%, 93%, 92%, 100%	[15]
DAAQ-ECOF	Anthraquinone	20, 50, 100, 200, 500, 1000, 2000, 3000, 20 100%, 93%, 89%, 86%, 74%, 68%, 60%, 50%, 100%	[17]
D_{TP}-A_{NDI}-COF@CNTs	Naphthimide	200, 300, 500, 750, 1000, 200 100%, 98%, 93%, 88%, 85%, 100%	[22]
Tp-DANT-COF	Naphthimide	50, 100, 200, 500, 1000, 2000 100%, 93%, 89%, 82%, 76%, 64%,	[46]
Tb-DANT-COF	Naphthimide	50, 100, 200, 500, 1000, 2000 100%, 86%, 80%, 72%, 65%, 56%	[46]
PPTODB	Pyrene-4,5,9,10-tetraone	20, 40, 100, 300, 800, 1000, 1500 100%, 97%, 94%, 89%, 76%, 72%, 54%	[47]
DAAQ-TFP	Anthraquinone	78.5, 157, 785, 1570, 3140 100%, 795, 54%, 41%, 30%	[41]
DAPH-TFP	Phenazine	85.5, 171, 855, 1710, 3420 100%, 76%, 63%, 56%, 51%	[41]
PEDOT@DAAQ-TFP	Anthraquinone	78.5, 157, 785, 1570, 3140 100%, 83%, 66%, 58% ,52%	[41]
PEDOT@DAPH-TFP	Phenazine	85.5, 171, 855, 1710, 3420 100%, 81%, 64%, 55%, 46%	[41]

DAPQ-COF	Phenanthrenequinone	500, 800, 1000, 1500, 2000, 500 100%, 89%, 83%, 72%, 64%, 100%	**This work**
DAPQ-COF10	Phenanthrenequinone	500, 800, 1000, 1500, 2000, 500 100%, 95%, 90%, 83%, 77%, 99%	**This work**
DAPQ-COF30	Phenanthrenequinone	500, 800, 1000, 1500, 2000, 500 100%, 97%, 96%, 92%, 90%, 99%	**This work**
DAPQ-COF50	Phenanthrenequinone	500, 1000, 2000, 3000, 4000, 5000, 8000, 10000, 20000, 30000, 40000, 50000 100%, 97%, 93%, 91%, 88%, 86%, 83%, 80%, 72%, 67%, 63%, 58%	**This work**

4.8 Charge Storage Mechanism of DAPQ-COF

To identify the Li^+ storage sites during discharging process, *ex situ* FT-IR spectra of cycled DAPQ-COF50 electrodes were recorded. As depicted in Figure 4-31, the bands at 1670 cm^{-1}, ascribed to the C=O groups in DAPQ structure, disappeared after discharging to 1.5 V. While a new signal at 1396 cm^{-1}, corresponding to the lithium enolate groups (C−O−Li), appeared when the electrode was fully discharged.[7,8,51] The infrared spectra of the initial and fully recharged samples are identical, indicating the reversible and stable electrochemical reactions based on the C=O bonds during the charge−discharge process. Based on these results we proposed a mechanism as outlined in Figure 4-31b that involves redox reactions of both carbonyl groups in DAPQ, in agreement with previous reports.[40,52]

To follow the nature of charge storage, the electrochemical reaction kinetics of DAPQ-COF50 were investigated by scanning the CV at various sweep rates (Figure 4-31c). The current response (i) of DAPQ-COF50 to the applied sweep rate (v, 0.1–1.0 mV s^{-1}) was recorded. According to the power law, $i = av^b$, b-values close to 0.5 indicate that the current is controlled by semi-infinite linear diffusion, by contrast, b-values close to 1 indicate that the current is surface-controlled.[53] It is found that the b-values of four redox peaks R1, R2, O1, and O2 (1.00, 0.99, 0.96, and 0.98) are all close to 1 (Figure 4-31d), indicating that the charge storage in DAPQ-COF50 is a fast surface-controlled process, which results from the high reactivity of carbonyl redox-active groups in DAPQ-COF50 not limited by ion diffusion within the studied sweep range. Further analysis of the voltammetric sweep rate dependence enables the surface-controlled contribution to the current response to be quantitatively distinguished.[54] The current response at a fixed potential can be expressed as the combination of two separate mechanisms,

namely surface-controlled contribution and diffusion-controlled insertion processes. In the equation of $i = k_1v + k_2v^{1/2}$, the exact surface-controlled contribution (k_1v) can be further quantified, where k_1 and k_2 constants can be simulated by plotting $iv^{-1/2}$ vs $v^{1/2}$, in which k_1 and k_2 are the slope and intercept of the linear fitting plot. At 0.1 mV s^{-1}, the surface contribution is determined to be 90%, which is further enhanced to 97% at 1 mV s^{-1}.

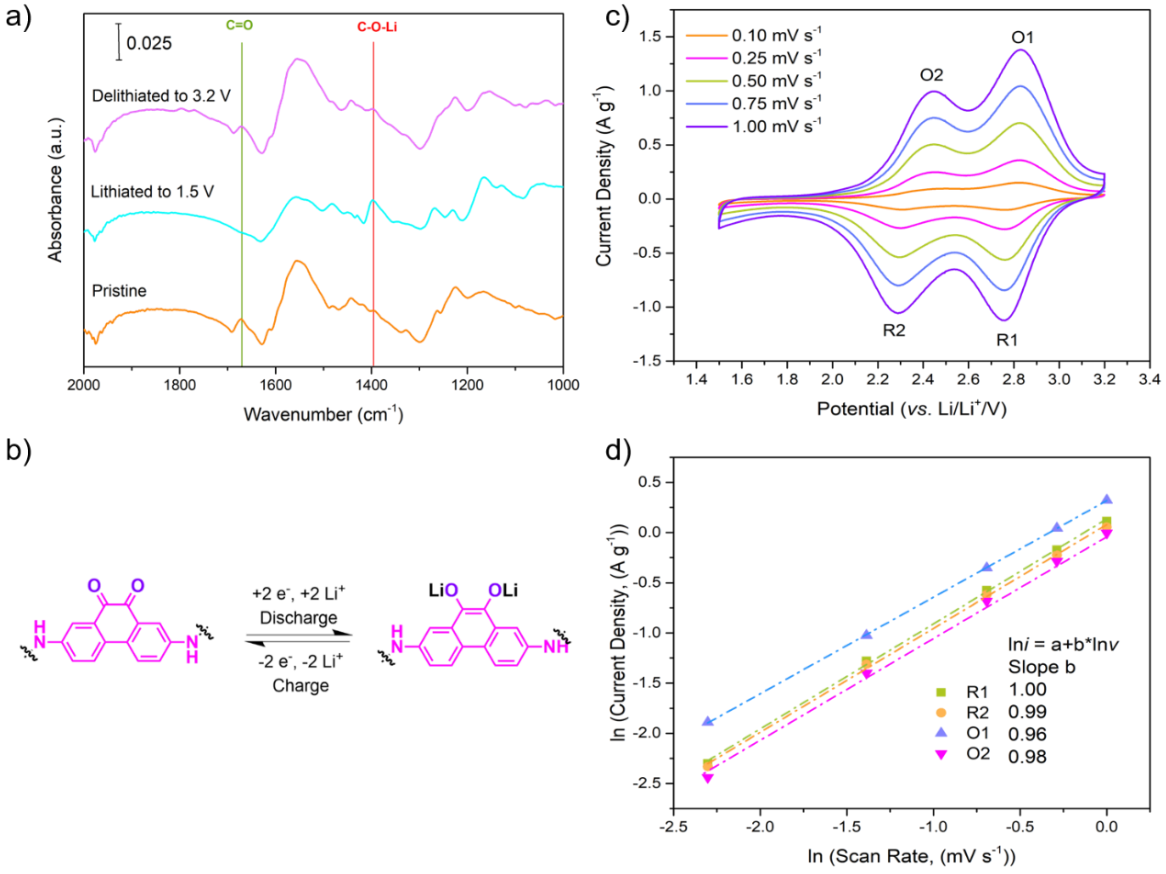

Figure 4-31. (a) FT-IR spectra of DAPQ-COF50 electrode materials at different states of lithiation/delithiation (pristine, lithiated to 1.5 V and delithiated to 3.2 V); (b) Proposed reversible electrochemical redox mechanism of DAPQ-COF50 during the lithiation/delithiation process; (c) Cyclic voltammograms of DAPQ-COF50 that were collected at different scan rates; (d) ln*i* vs. ln*v* plots to determine the b values of different peaks.

The electrochemical and transport behaviour of DAPQ-COF and the DAPQ-COFX composites were further characterised by EIS (Figure 4-32a). The Nyquist plots consist of a semicircle in high frequencies and a sloping line in low frequencies. The semicircle reflects the charge-transfer resistance R_{ct}, which is related to reaction kinetics, and the sloping line reflects the diffusion process of lithium ions in the electrode (Warburg impedance). The charge transfer

resistance value R_{ct} was acquired by fitting Nyquist plots with an equivalent circuit model (Figure 4-32b). In this circuit, the constant phase element (CPE), the charge transfer resistance (R_{ct}), the resistance of the solution (R_s), and the mass transport resistance (W) were considered. Fitted values for the individual elements in the equivalent circuit are summarised in Table 4-7. DAPQ-COF50 has the smallest R_{ct} (48.8 Ω) in the DAPQ-COF and DAPQ-COFX electrodes. This supports the assertion of improved charge transfer in DAPQ-COF50 due to optimisation of contact between the DAPQ-COF and conductive carbon network.

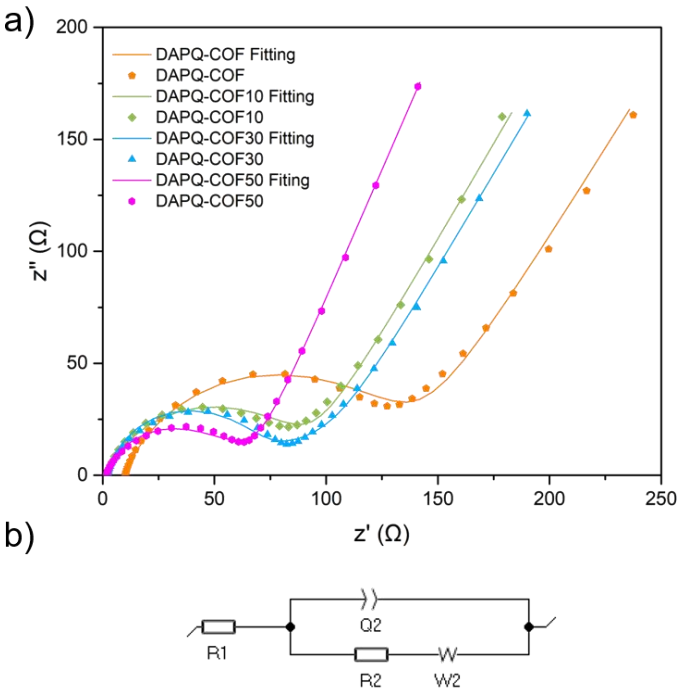

Figure 4-32. (a) EIS spectra of DAPQ-COF and the DAPQ-COFX composite electrodes, tested in coin cells in the pristine charged state at OCP from 1 MHz to 100 mHz at 25 °C; (b) Equivalent circuit used for fitting the electrochemical impedance data. The R_s (R1), R_{ct} (R2), CPE (Q2), and W (W2) represent cell solution resistance, charge-transfer resistance, constant phase element, and Warburg impedance.

Table 4-7. Fitted values of elements in the equivalent circuit for EIS data of DAPQ-COF and the DAPQ-COFX composite electrodes.

	R_s (Ω)	**CPE (F)**	**R_{ct} (Ω)**	**W(Ω)**
DAPQ-COF	9.7	21.8×10^{-6}	114.4	49.7
DAPQ-COF10	1.6	33.6×10^{-6}	80.2	34.1
DAPQ-COF30	2.2	22.7×10^{-6}	73.8	39.4
DAPQ-COF50	1.7	18.9×10^{-6}	48.8	52.7

4.9 Conclusion

A COF composite electrode was prepared by *in situ* polycondensation on CNTs. The cooperation of CNT, with the ability to grow thin COF layers on the external surfaces of the tube structures, increased the charge transfer and electrochemical accessibility of active sites of the DAPQ-COFX (where X = 10, 30, and 50 wt.% of CNT). DAPQ-COF50 had the largest capacity of 162 mAh g^{-1} at 500 mA g^{-1}, corresponding to 95% utilisation of its redox-active sites. In addition, the optimised DAPQ-COF50 composite retained 76% of the capacity after 3000 cycles at 2000 mA g^{-1} and exhibited excellent ultra-high rate performance, retaining 58% of its capacity at 50000 mA g^{-1}. For DAPQ-COF50, this translated to a rate of 320 C at 50000 mA g^{-1}, with resulted in charging times of 11 seconds. DAPQ-COF50 exceeds the rate capability of all other previously reported carbonyl-contained organic electrodes by an order of magnitude. DAPQ-COF50 also exhibits a power density of 110 kW kg^{-1}, which is comparable to electrochemical capacitor materials. The superior performance of DAPQ-COF50 is possibly due to synergistic effects between DAPQ-COF and CNTs, for example, the improved conductivity of DAPQ-COF in the DAPQ-COFX composites. The synthetic route by which the DAPQ-COFX composites are prepared enables the intimate growth of COFs on CNTs and yields a tube-type core-shell structure, which may also be beneficial. The open porous structures of the CNTs also facilitate the transport of ions to the reaction sites. Optimising the proportions of COF and CNT in the composite reaction mixtures enabled the thickness of the crystalline COF on the CNT to be tuned. It was shown that thinner COF surfaces dramatically promoted electrochemical accessibility required to drive these redox reactions through ultrafast charge/discharge cycles with a small drop in performance. Considering the reticular tunability of COFs and their pores, along with the wide diversity of redox-active organic blocks available, these results highlight the strong potential of COFs supported on conducting carbons to provide a distinctive platform for high-performance organic electrodes.

4.10 Reference

(1) Kim, J.; Kim, J. H.; Ariga, K. Redox-Active Polymers for Energy Storage Nanoarchitectonics. *Joule* **2017**, *1* (4), 739–768.

(2) Muench, S.; Wild, A.; Friebe, C.; Häupler, B.; Janoschka, T.; Schubert, U. S. Polymer-Based Organic Batteries. *Chem. Rev.* **2016**, *116* (16), 9438–9484.

(3) Song, Z.; Zhou, H. Towards Sustainable and Versatile Energy Storage Devices: An Overview of Organic Electrode Materials. *Energy Environ. Sci.* **2013**, *6* (8), 2280–2301.

(4) Armand, M.; Tarascon, J.-M. Building Better Batteries. *Nature* **2008**, *451* (7179), 652–657.

(5) Jaffe, A.; Saldivar Valdes, A.; Karunadasa, H. I. Quinone-Functionalized Carbon Black Cathodes for Lithium Batteries with High Power Densities. *Chem. Mater.* **2015**, *27* (10), 3568–3571.

(6) Chen, H.; Armand, M.; Courty, M.; Jiang, M.; Grey, C. P.; Dolhem, F.; Tarascon, J. M.; Poizot, P. Lithium Salt of Tetrahydroxybenzoquinone: Toward the Development of a Sustainable Li-Ion Battery. *J. Am. Chem. Soc.* **2009**, *131* (25), 8984–8988.

(7) Tian, B.; Ning, G.-H.; Tang, W.; Peng, C.; Yu, D.; Chen, Z.; Xiao, Y.; Su, C.; Loh, K. P. Polyquinoneimines for Lithium Storage: More than the Sum of Its Parts. *Mater. Horiz.* **2016**, *3* (5), 429–433.

(8) Ba, Z.; Wang, Z.; Luo, M.; Li, H. B.; Li, Y.; Huang, T.; Dong, J.; Zhang, Q.; Zhao, X. Benzoquinone-Based Polyimide Derivatives as High-Capacity and Stable Organic Cathodes for Lithium-Ion Batteries. *ACS Appl. Mater. Interfaces* **2020**, *12* (1), 807–817.

(9) Ouyang, Z.; Tranca, D.; Zhao, Y.; Chen, Z.; Fu, X.; Zhu, J.; Zhai, G.; Ke, C.; Kymakis, E.; Zhuang, X. Quinone-Enriched Conjugated Microporous Polymer as an Organic Cathode for Li-Ion Batteries. *ACS Appl. Mater. Interfaces* **2021**, *13* (7), 9064–9073.

(10) Jhulki, S.; Feriante, C. H.; Mysyk, R.; Evans, A. M.; Magasinski, A.; Raman, A. S.; Turcheniuk, K.; Barlow, S.; Dichtel, W. R.; Yushin, G.; Marder, S. R. A Naphthalene Diimide Covalent Organic Framework: Comparison of Cathode Performance in Lithium-Ion Batteries with Amorphous Cross-Linked and Linear Analogues, and Its Use in Aqueous Lithium-Ion Batteries. *ACS Appl. Energy Mater.* **2021**, *4*, 350–356.

(11) Wang, G.; Chandrasekhar, N.; Biswal, B. P.; Becker, D.; Paasch, S.; Brunner, E.; Addicoat, M.; Yu, M.; Berger, R.; Feng, X. A Crystalline, 2D Polyarylimide Cathode for Ultrastable and Ultrafast Li Storage. *Adv. Mater.* **2019**, *31* (28), 1901478.

(12) Feng, X.; Liu, L.; Honsho, Y.; Saeki, A.; Seki, S.; Irle, S.; Dong, Y.; Nagai, A.; Jiang,

D. High-Rate Charge-Carrier Transport in Porphyrin Covalent Organic Frameworks: Switching from Hole to Electron to Ambipolar Conduction. *Angew. Chem. Int. Ed.* ***2012***, *51*, 2618 –2622.

(13) Lei, Z.; Yang, Q.; Xu, Y.; Guo, S.; Sun, W.; Liu, H.; Lv, L. P.; Zhang, Y.; Wang, Y. Boosting Lithium Storage in Covalent Organic Framework via Activation of 14-Electron Redox Chemistry. *Nat. Commun.* **2018**, *9* (1), 576.

(14) Wang, Z.; Li, Y.; Liu, P.; Qi, Q.; Zhang, F.; Lu, G.; Zhao, X.; Huang, X. Few Layer Covalent Organic Frameworks with Graphene Sheets as Cathode Materials for Lithium-Ion Batteries. *Nanoscale* **2019**, *11* (12), 5330–5335.

(15) Wang, G.; Chandrasekhar, N.; Biswal, B. P.; Becker, D.; Paasch, S.; Brunner, E.; Addicoat, M.; Yu, M.; Berger, R.; Feng, X. A Crystalline, 2D Polyarylimide Cathode for Ultrastable and Ultrafast Li Storage. *Adv. Mater.* **2019**, *31* (28), 1901478.

(16) Xu, S.; Wang, G.; Biswal, B. P.; Addicoat, M.; Paasch, S.; Sheng, W.; Zhuang, X.; Brunner, E.; Heine, T.; Berger, R.; Feng, X. A Nitrogen-Rich 2D Sp^2-Carbon-Linked Conjugated Polymer Framework as a High-Performance Cathode for Lithium-Ion Batteries. *Angew. Chem. Int. Ed.* **2019**, *58* (3), 849–853.

(17) Wang, S.; Wang, Q.; Shao, P.; Han, Y.; Gao, X.; Ma, L.; Yuan, S.; Ma, X.; Zhou, J.; Feng, X.; Wang, B. Exfoliation of Covalent Organic Frameworks into Few-Layer Redox-Active Nanosheets as Cathode Materials for Lithium-Ion Batteries. *J. Am. Chem. Soc.* **2017**, *139* (12), 4258–4261.

(18) Huang, Y.; Li, K.; Liu, J.; Zhong, X.; Duan, X.; Shakir, I.; Xu, Y. Three-Dimensional Graphene/Polyimide Composite-Derived Flexible High-Performance Organic Cathode for Rechargeable Lithium and Sodium Batteries. *J. Mater. Chem. A* **2017**, *5* (6), 2710–2716.

(19) Sui, D.; Xu, L.; Zhang, H.; Sun, Z.; Kan, B.; Ma, Y.; Chen, Y. A 3D Cross-Linked Graphene-Based Honeycomb Carbon Composite with Excellent Confinement Effect of Organic Cathode Material for Lithium-Ion Batteries. *Carbon* **2020**, *157*, 656–662.

(20) Zhu, Z.; Chen, J. Review—Advanced Carbon-Supported Organic Electrode Materials for Lithium (Sodium)-Ion Batteries. *J. Electrochem. Soc.* **2015**, *162* (14), A2393–A2405.

(21) Song, Z.; Xu, T.; Gordin, M. L.; Jiang, Y. B.; Bae, I. T.; Xiao, Q.; Zhan, H.; Liu, J.; Wang, D. Polymer-Graphene Nanocomposites as Ultrafast-Charge and -Discharge Cathodes for Rechargeable Lithium Batteries. *Nano Lett.* **2012**, *12* (5), 2205–2211.

(22) Xu, F.; Jin, S.; Zhong, H.; Wu, D.; Yang, X.; Chen, X.; Wei, H.; Fu, R.; Jiang, D. Electrochemically Active, Crystalline, Mesoporous Covalent Organic Frameworks on

Carbon Nanotubes for Synergistic Lithium-Ion Battery Energy Storage. *Sci. Rep.* **2015**, *5* (1), 8225.

(23) Gao, H.; Tian, B.; Yang, H.; Neale, A. R.; Little, M. A.; Sprick, R. S.; Hardwick, L. J.; Cooper, A. I. Crosslinked Polyimide and Reduced Graphene Oxide Composites as Long Cycle Life Positive Electrode for Lithium-Ion Cells. *ChemSusChem* **2020**, *13* (20), 5571–5579.

(24) Yang, Y.; Wang, C.; Yue, B.; Gambhir, S.; Too, C. O.; Wallace, G. G. Electrochemically Synthesized Polypyrrole/Graphene Composite Film for Lithium Batteries. *Adv. Energy Mater.* **2012**, *2* (2), 266–272.

(25) Luo, Z.; Liu, L.; Ning, J.; Lei, K.; Lu, Y.; Li, F.; Chen, J. A Microporous Covalent-Organic Framework with Abundant Accessible Carbonyl Groups for Lithium-Ion Batteries. *Angew. Chem. Int. Ed.* **2018**, *57* (30), 9443–9446.

(26) Li, Y.; Jian, Z.; Lang, M.; Zhang, C.; Huang, X. Covalently Functionalized Graphene by Radical Polymers for Graphene-Based High-Performance Cathode Materials. *ACS Appl. Mater. Interfaces* **2016**, *8* (27), 17352–17359.

(27) Xu, F.; Jin, S.; Zhong, H.; Wu, D.; Yang, X.; Chen, X.; Wei, H.; Fu, R.; Jiang, D. Electrochemically Active, Crystalline, Mesoporous Covalent Organic Frameworks on Carbon Nanotubes for Synergistic Lithium-Ion Battery Energy Storage. *Sci. Rep.* **2015**, *5* (1), 8225.

(28) Liang, Y.; Zhang, P.; Chen, J. Function-Oriented Design of Conjugated Carbonyl Compound Electrodes for High Energy Lithium Batteries. *Chem. Sci.* **2013**, *4* (3), 1330–1337.

(29) Vollebregt, S.; Ishihara, R.; Tichelaar, F. D.; Hou, Y.; Beenakker, C. I. M. Influence of the Growth Temperature on the First and Second-Order Raman Band Ratios and Widths of Carbon Nanotubes and Fibers. *Carbon N. Y.* **2012**, *50* (10), 3542–3554.

(30) Lehman, J. H.; Terrones, M.; Mansfield, E.; Hurst, K. E.; Meunier, V. Evaluating the Characteristics of Multiwall Carbon Nanotubes. *Carbon N. Y.* **2011**, *49* (8), 2581–2602.

(31) Ruch, P. W.; Hardwick, L. J.; Hahn, M.; Foelske, A.; Kötz, R.; Wokaun, A. Electrochemical Doping of Single-Walled Carbon Nanotubes in Double Layer Capacitors Studied by in Situ Raman Spectroscopy. *Carbon.* **2009**, *47* (1), 38–52.

(32) Bravo, V.; Gil, S.; Costero, A. M.; Kneeteman, M. N.; Llaosa, U.; Mancini, P. M. E.; Ochando, L. E.; Parra, M. A New Phenanthrene-Based Bis-Oxime Chemosensor for Fe(III) and Cr(III) Discrimination. *Tetrahedron* **2012**, *68* (24), 4882–4887.

(33) Property, W. I.; Date, I. P.; Number, I. P. Compositions and Methods of Making

Expanded Hematopoietic Stem Cells Using Pten in Hibitors. WO2018/217567Al

(34) Accelrys., I. BIOVIA Materials Studio.

(35) Coelho, A. TOPAS-Academic. Coelho Software: Brisbane, Australia 2012.

(36) Kandambeth, S.; Mallick, A.; Lukose, B.; Mane, M. V.; Heine, T.; Banerjee, R. Construction of Crystalline 2D Covalent Organic Frameworks with Remarkable Chemical (Acid/Base) Stability via a Combined Reversible and Irreversible Route. *J. Am. Chem. Soc.* **2012**, *134* (48), 19524–19527.

(37) Deblase, C. R.; Silberstein, K. E.; Truong, T.-T.; Abruñ, H. D.; Dichtel, W. R. β-Ketoenamine-Linked Covalent Organic Frameworks Capable of Pseudocapacitive Energy Storage. *J. Am. Chem. Soc* **2013**, *135*, 16821–16824.

(38) Xu, W.; Read, A.; Koech, P. K.; Hu, D.; Wang, C.; Xiao, J.; Padmaperuma, A. B.; Graff, G. L.; Liu, J.; Zhang, J. G. Factors Affecting the Battery Performance of Anthraquinone-Based Organic Cathode Materials. *J. Mater. Chem.* **2012**, *22* (9), 4032–4039.

(39) Shi, Y.; Tang, H.; Jiang, S.; Kayser, L. V; Li, M.; Liu, F.; Ji, F.; Lipomi, D. J.; Ong, S. P.; Chen, Z. Understanding the Electrochemical Properties of Naphthalene Diimide: Implication for Stable and High-Rate Lithium-Ion Battery Electrodes. *Chem. Mater.* **2018**, *30* (10), 3508–3517.

(40) Liang, Y.; Zhang, P.; Chen, J. Function-Oriented Design of Conjugated Carbonyl Compound Electrodes for High Energy Lithium Batteries. *Chem. Sci.* **2013**, *4* (3), 1330–1337.

(41) Vitaku, E.; Gannett, C. N.; Carpenter, K. L.; Shen, L.; Abruña, H. D.; Dichtel, W. R. Phenazine-Based Covalent Organic Framework Cathode Materials with High Energy and Power Densities. *J. Am. Chem. Soc.* **2020**, *142* (1), 16–20.

(42) Lv, J.; Tan, Y. X.; Xie, J.; Yang, R.; Yu, M.; Sun, S.; Li, M. De; Yuan, D.; Wang, Y. Direct Solar-to-Electrochemical Energy Storage in a Functionalized Covalent Organic Framework. *Angew. Chem. Int. Ed.* **2018**, *57* (39), 12716–12720.

(43) Luo, Z.; Liu, L.; Ning, J.; Lei, K.; Lu, Y.; Li, F.; Chen, J. A Microporous Covalent-Organic Framework with Abundant Accessible Carbonyl Groups for Lithium-Ion Batteries. *Angew. Chem. Int. Ed.* **2018**, *57* (30), 9443–9446.

(44) Lee, S.; Kwon, J. E.; Hong, J.; Park, S. Y.; Kang, K. The Role of Substituents in Determining the Redox Potential of Organic Electrode Materials in Li and Na Rechargeable Batteries: Electronic Effects: Vs. Substituent-Li/Na Ionic Interaction. *J. Mater. Chem. A* **2019**, *7* (18), 11438–11443.

(45) Xu, S.; Wang, G.; Biswal, B. P.; Addicoat, M.; Paasch, S.; Sheng, W.; Zhuang, X.;

Brunner, E.; Heine, T.; Berger, R.; Feng, X. A Nitrogen-Rich 2D Sp 2 -Carbon-Linked Conjugated Polymer Framework as a High-Performance Cathode for Lithium-Ion Batteries. *Angew. Chem.Int. Ed.* **2019**, *58* (3), 849–853.

(46) Yang, D. H.; Yao, Z. Q.; Wu, D.; Zhang, Y. H.; Zhou, Z.; Bu, X. H. Structure-Modulated Crystalline Covalent Organic Frameworks as High-Rate Cathodes for Li-Ion Batteries. *J. Mater. Chem. A* **2016**, *4* (47), 18621–18627.

(47) Yao, C. J.; Wu, Z.; Xie, J.; Yu, F.; Guo, W.; Xu, Z. J.; Li, D. S.; Zhang, S.; Zhang, Q. Two-Dimensional (2D) Covalent Organic Framework as Efficient Cathode for Binder-Free Lithium-Ion Battery. *ChemSusChem* **2020**, *13* (9), 2457–2463.

(48) Yamada, A.; Chung, S. C.; Hinokuma, K. Optimized $LiFePO_4$ for Lithium Battery Cathodes. *J. Electrochem. Soc.* **2001**, *148* (3), A224.

(49) Li, X.; Li, Y.; Sarang, K.; Lutkenhaus, J.; Verduzco, R. Side-Chain Engineering for High-Performance Conjugated Polymer Batteries. *Adv. Funct. Mater.* **2021**, *31* (14), 2009263.

(50) Béguin, F.; Presser, V.; Balducci, A.; Frackowiak, E. Carbons and Electrolytes for Advanced Supercapacitors. *Adv. Mater.* **2014**, *26* (14), 2219–2251.

(51) Song, Z.; Qian, Y.; Gordin, M. L.; Tang, D.; Xu, T.; Otani, M.; Zhan, H.; Zhou, H.; Wang, D. Polyanthraquinone as a Reliable Organic Electrode for Stable and Fast Lithium Storage. *Angew. Chem. Int. Ed.* **2015**, *54* (47), 13947–13951.

(52) Wang, H.; Yao, C.-J.; Nie, H.-J.; Wang, K.-Z.; Zhong, Y.-W.; Chen, P.; Mei, S.; Zhang, Q. Recent Progress in Carbonyl-Based Organic Polymers as Promising Electrode Materials for Lithium-Ion Batteries (LIBs). *J. Mater. Chem. A* **2020**, *8* (24), 11906–11922.

(53) Augustyn, V.; Come, J.; Lowe, M. A.; Kim, J. W.; Taberna, P. L.; Tolbert, S. H.; Abruña, H. D.; Simon, P.; Dunn, B. High-Rate Electrochemical Energy Storage through Li^+ Intercalation Pseudocapacitance. *Nat. Mater.* **2013**, *12* (6), 518–522.

(54) Wang, J.; Polleux, J.; Lim, J.; Dunn, B. Pseudocapacitive Contributions to Electrochemical Energy Storage in TiO_2 (Anatase) Nanoparticles. *J. Phys. Chem. C* **2007**, *111* (40), 14925–14931.

Chapter 5

A Pyrene-4,5,9,10-tetraone-based Covalent Organic Framework as Positive Electrode for Li-ion Batteries with High Specific Capacity

Some of the results presented in Chapter 5 are taken from Paper III.

A Pyrene-4,5,9,10-tetraone-based Covalent Organic Framework as Positive Electrode for Li-ion Batteries with High Specific Capacity, Hui Gao, Qiang Zhu, Alex R. Neale, Mounib Bahri, Xue Wang, Haofan Yang, Yongjie Xu, Rob Clowes, Nigel D. Browning, Marc A. Little, Laurence J. Hardwick* and Andrew I. Cooper*

5.1 Author Contributions

All COFs and the COF on carbon nanotube (CNT) composites were prepared by the thesis author. All the electrochemical experiments were performed by the thesis author. Modeling calculations were carried out by Mr. Qiang Zhu and Ms. Xue Wang. Dr. Marc Little performed PXRD analyses. Mr. Haofan Yang carried out SEM. Mr. Rob Clowes performed N_2 gas sorption measurements. Dr. Mounib Bahri recorded TEM images.

5.2 Abstract

To follow on from Chapter 4, we aim to obtain a positive electrode material with a specific capacity larger than 200 mAh g^{-1} for Li-ion cells. Herein, a COF structure was designed, which has four functional carbonyl groups per repeat unit to increase the specific capacity, and the utilisation of the redox-active sites was improved by synthesising COF composites (PT-COFX) with carbon nanotubes (CNT) using an *in situ* polycondensation reaction to increasing charge transfer as developed in Chapter 4. The optimised composites had tube-type core-shell structures with intimately grown COF layers on the CNT surface. This synergistic structural design enables superior electrochemical performance: PT-COF50 exhibited 98% utilisation of redox-active sites, corresponding to the capacity of 280 mAh g^{-1}.

5.3 Introduction

Based on our research and the recent reports, to get a material with a greater specific capacity, 2,7-diaminopyrene-4,5,9,10-tetraone (DAPT) was targeted as the starting material. DAPT contains four redox-active carbonyl groups that can undergo reversible reactions with Li^+ ions. It has two more redox-active sites compared to the DAPQ molecule used in Chapter 4, and only a small increase in the molecular weight. DAPT was found to deliver a high initial capacity of 345 mAh g^{-1} at 100 mA g^{-1} in Li-ion cells, but its capacity rapidly faded to 40 mAh g^{-1} after 50 cycles as DAPT dissolves into the electrolyte, and similar behaviour being reported for structurally related organic molecules.[1] To avoid such a problem, a carbonyl functionalised 2D COF (PT-COF) was designed which is made from 1,3,5-triformylphloroglucinol (TFG) and 2,7-diaminopyrene-4,5,9,10-tetraone (DAPT) by Schiff base polycondensation reaction. During our exploration of the battery application of PT-COF, the structure of the as-synthesised PT-COF was independently reported for supercapacitor.[2] Here, PT-COF was found to have a specific capacity of 193 mAh g^{-1} at 200 mA g^{-1} in a Li-ion cell. This capacity is higher than the majority of the carbonyl-containing polymeric electrodes.[3] However, the capacity is only 71% utilisation of the redox-active sites in the PT-COF. Adopting the strategies used in Chapter 4, a composite of PT-COF thinly coated around CNT was synthesised. Through forming the tubular core-shell structure of the composites (PT-COFX) the electrochemical performance was greatly enhanced and we achieved specific capacities of up to 280 mAh g^{-1} at 200 mA g^{-1}.

5.4 Experimental Section

5.4.1 Materials

Dichlorodicyanobenzoquinone (DDQ) and 1,3,5-triformylphloroglucinol (TFG) were obtained from Tokyo Chemical Industry UK Ltd. Pyrene, sodium periodate, ruthenium (III) chloride hydrate, sodium dithionite, ammonium chloride, acetic acid, multi-walled carbon nanotubes with outer diameter and length ranges of 7-15 nm and 0.5-10 μm (CNTs), anhydrous NMP and PVDF were purchased from Sigma Aldrich. 1,4-dioxane was obtained from Alfa-Aesar. Fuming nitric acid and mesitylene were obtained from Acros Organics. Concentrated sulfuric acid, DMF, dimethyl sulfoxide (DMSO), dichloromethane (DCE), acetonitrile, Chloroform, acetone, sodium hydroxide, sodium hydrogen carbonate, ethyl acetate, and methanol were obtained from Fisher. All chemicals were used as received without further purification.

5.4.2 Synthesis of Monomer

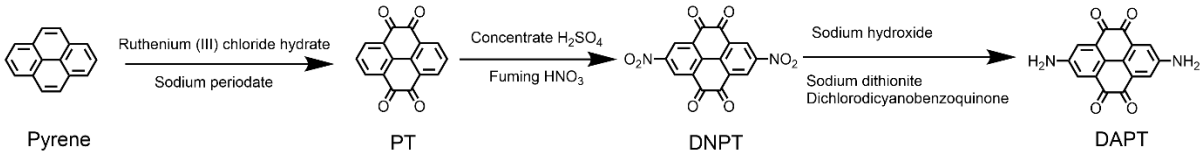

Scheme 5-1. Synthetic routes of small molecules PT, DNPT and DAPT.

5.4.2.1 Synthesis of Pyrene-4,5,9,10-tetraone (PT)

PT was synthesised using a previously reported method.[4,5] In a 500 ml round flask equipped with a condenser and a stirrer bar, pyrene (20 mM, 4.0 g) was dissolved in a mixture of 80 mL dichloromethane and 80 mL acetonitrile. Then, sodium periodate (164 mM, 35.0 g), 100 mL H_2O, and Ruthenium (III) chloride hydrate (0.42 mM, 0.5 g) was added to the mixture. The reaction mixture was stirred at 35-40 ˚C overnight. After the reaction, the suspension was removed by filtration, and the precipitate was washed with copious amounts of DCM. The filtrate was extracted by DCM several times. A yellow solid was obtained by rotary evaporation of the organic solution. Then, the crude product was recrystallized from chloroform to give 1.2 g PT (22.9 %, yield). ^{1}H NMR (400 MHz, DMSO-d_6, ppm): 8.33 (d, *J*=7.5, 2H), 7.75 (t, *J*=7.5,

1H). ^{13}C NMR (100 MHz, DMSO-d_6, δ [ppm]): 177.5, 134.6, 134.0, 131.8, 130.7. HRMS (EIS): calcd for ([$C_{16}H_6O_4$]+Na)+: m/z = 285.206; found: 285.0162.

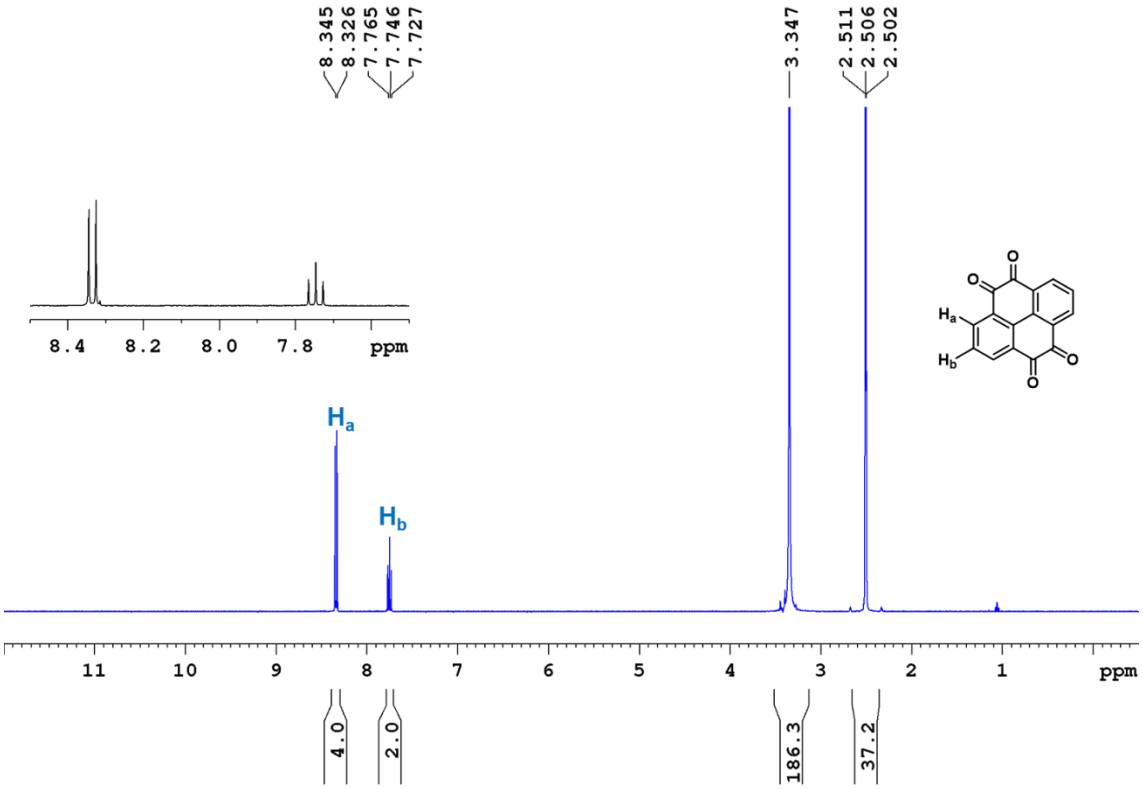

Figure 5-1. ^{1}H NMR (400 MHz, DMSO-d_6) spectrum of PT.

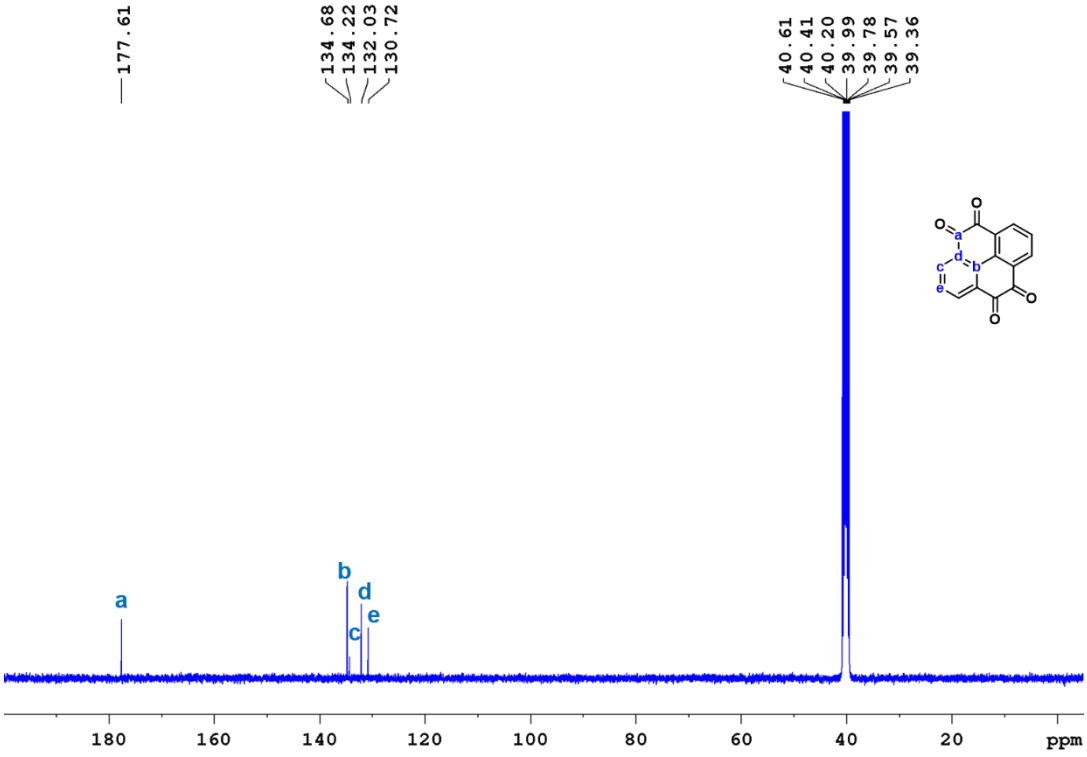

Figure 5-2. ^{13}C NMR (100 MHz, DMSO-d_6) spectrum of PT.

5.4.2.2 Synthesis of 2,7-Dinitropyrene-4,5,9,10-tetraone (DNPT)

DNPT was synthesised according to the reported protocol. PT (2 mM, 524 mg) was added into a 20 mL mixture of sulfuric acid and fuming nitric acid (4:1, v/v) and then the mixture was heated at 110 ˚C overnight. Then, the reaction mixture cooled down to room temperature and was poured into 200 mL ice water. Followed by neutralization by adding saturated $NaHCO_3$ solution. Then, the yellow precipitate was collected by filtering and washing with water several times. After dried in vacuum at 65 ˚C for 24 h, 457 mg yellow DNPT was obtained (65 %, yield). ^{1}H NMR (400 MHz, DMSO-d_6, ppm): 8.89 (s, 1H). ^{13}C NMR (100 MHz, DMSO-d_6, δ [ppm]): 174.9, 149.2, 136.3, 134.4, 126.4. HRMS (EIS): calcd for ($[C_{16}H_4N_2O_8]$+Na)$^+$: m/z = 374.986; found: 374.9857.

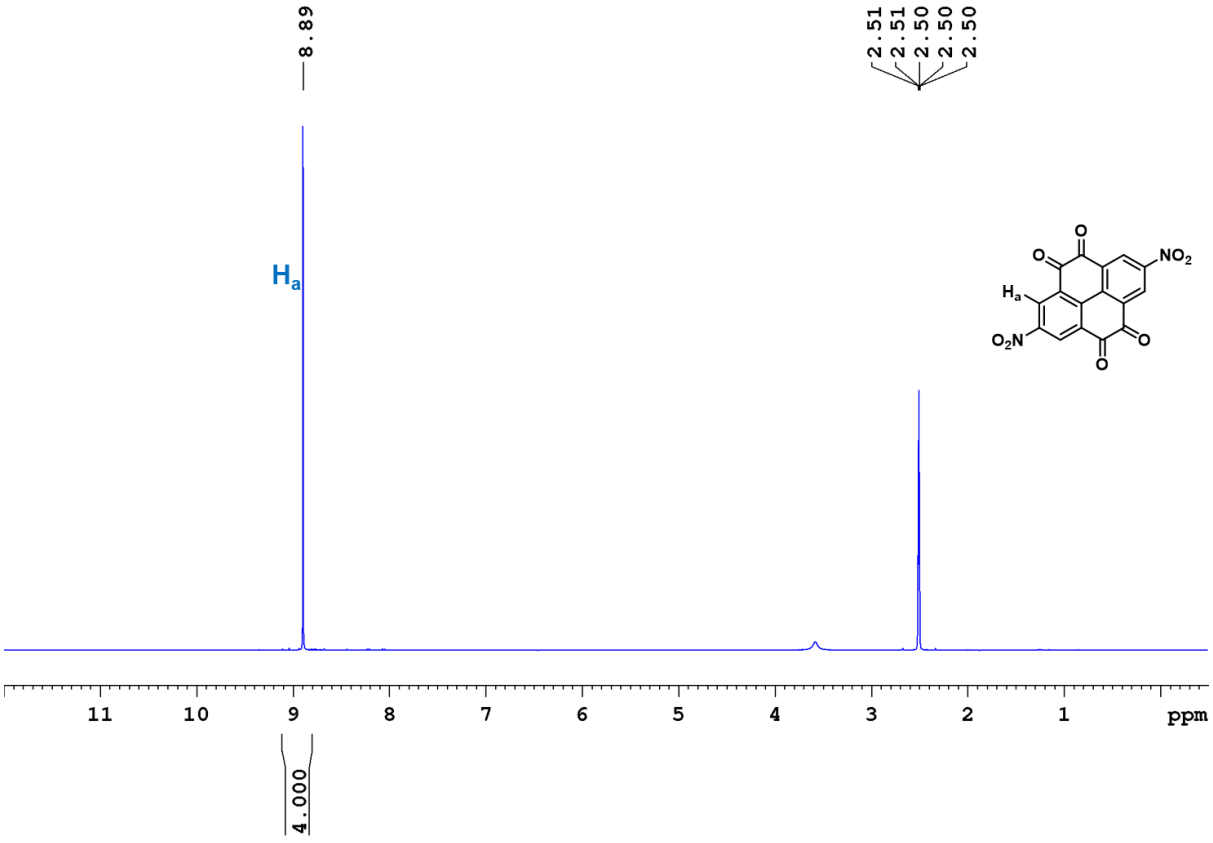

Figure 5-3. ^{1}H NMR (400 MHz, DMSO-d_6) spectrum of DNPT.

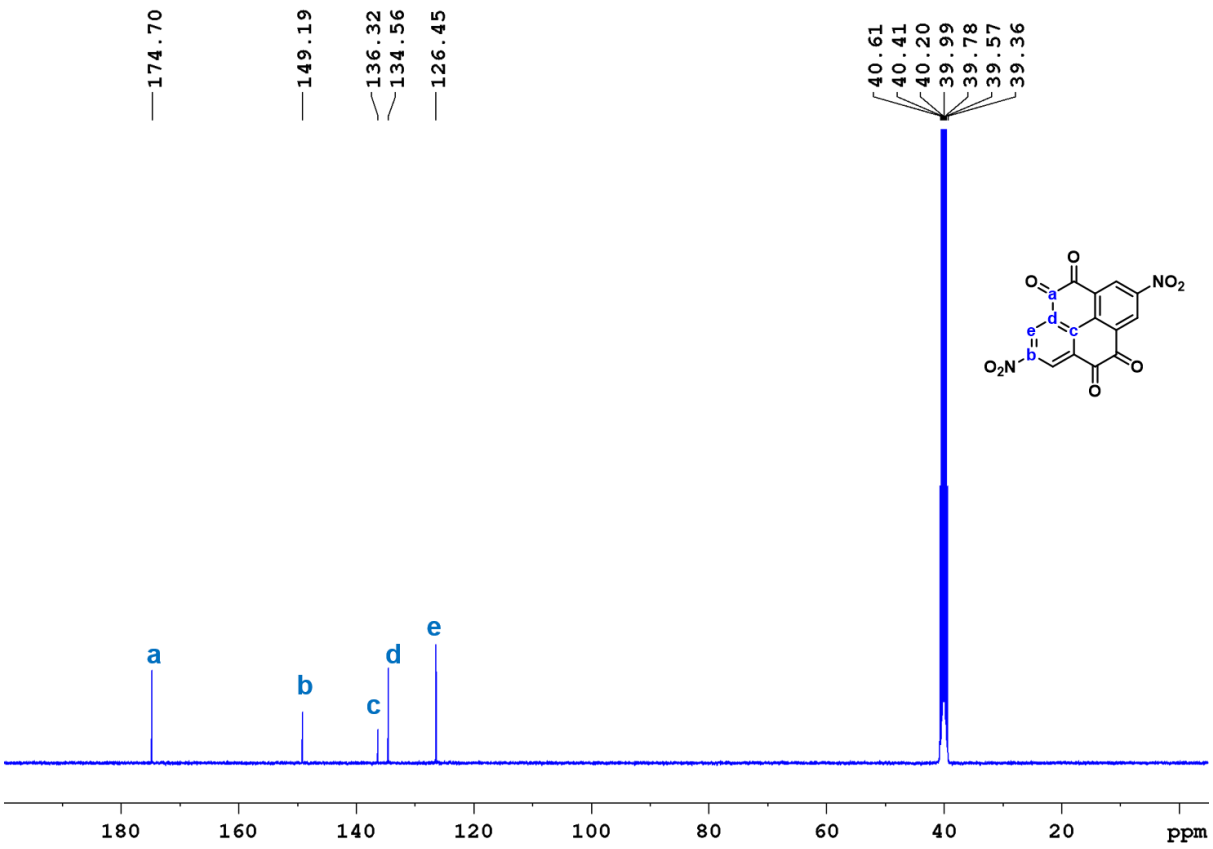

Figure 5-4. ^{13}C NMR (100 MHz, DMSO-d_6) spectrum of DNPT.

5.4.2.3 Synthesis of 2,7-Diaminopyrene-4,5,9,10-tetraone (DAPT)

DNPT (1 g, 2.8 mmol) was added in a 500mL two-necked flask. sodium hydroxide (8.9 g, 224 mmol), water (150 mL), and sodium dithionite (4.4 g, 25.5 mmol) were added one by one and heat at 50 ^{o}C, stirring for 15 min, the reaction mixture is poured into saturated ammonium chloride solution (500 mL), filtered, and washed with water to obtain a black powder, vacuum dried at room temperature overnight to obtain a crude product, and then the crude product (457 mg) and dichlorodicyanobenzoquinone (1.5 g) and methanol (30 mL) were mixed, stirred at 35 ^{o}C for 15 h, the reaction solution was diluted with ethyl acetate (60 mL), filtered with suction, Washing with ethyl acid gave a black solid (442 mg, yield 54%). ^{1}H NMR (400 MHz, DMSO-d_6, ppm): 7.37 (s, 4H), 5.96 (s, 4). ^{13}C NMR (100 MHz, DMSO-d_6, δ [ppm]): 178.8, 149.1, 131.2, 124.9, 119.3.

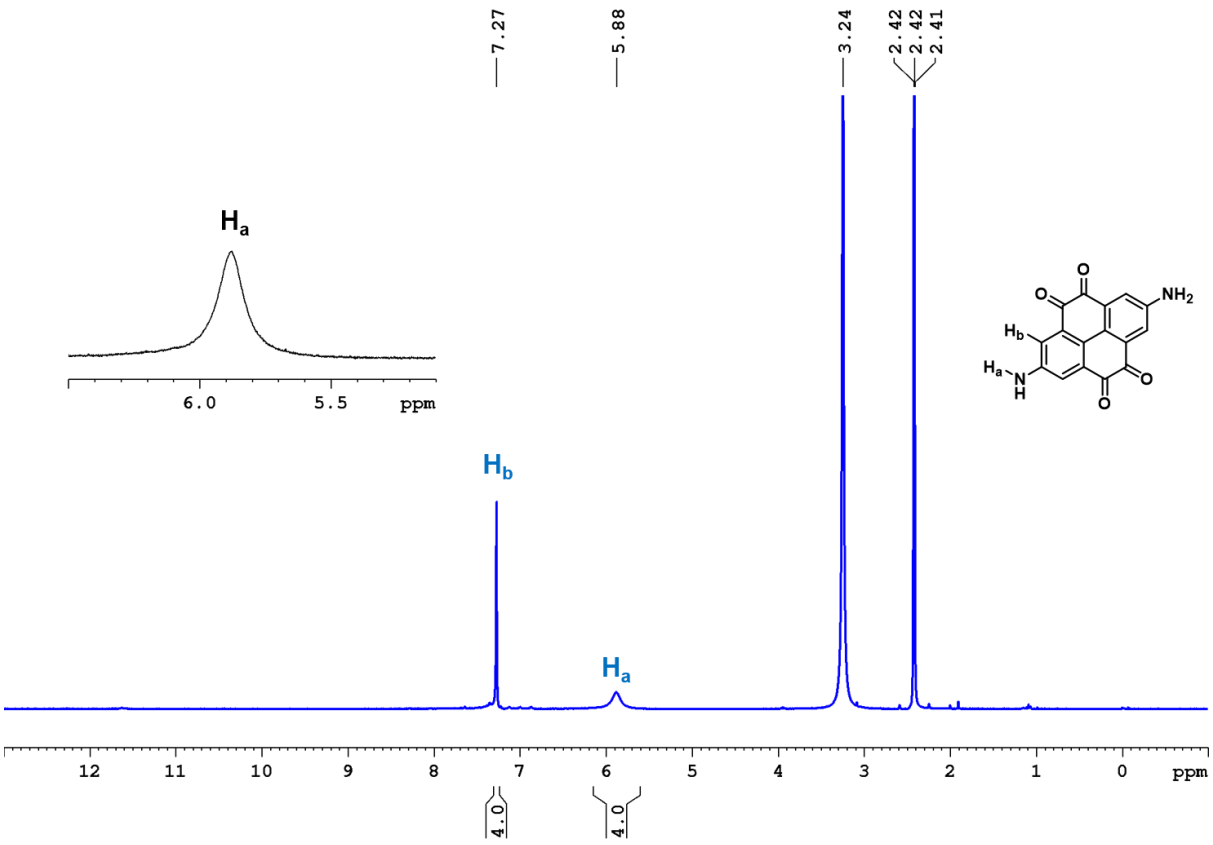

Figure 5-5. ^{1}H NMR (400 MHz, DMSO-d_6) spectrum of DAPT.

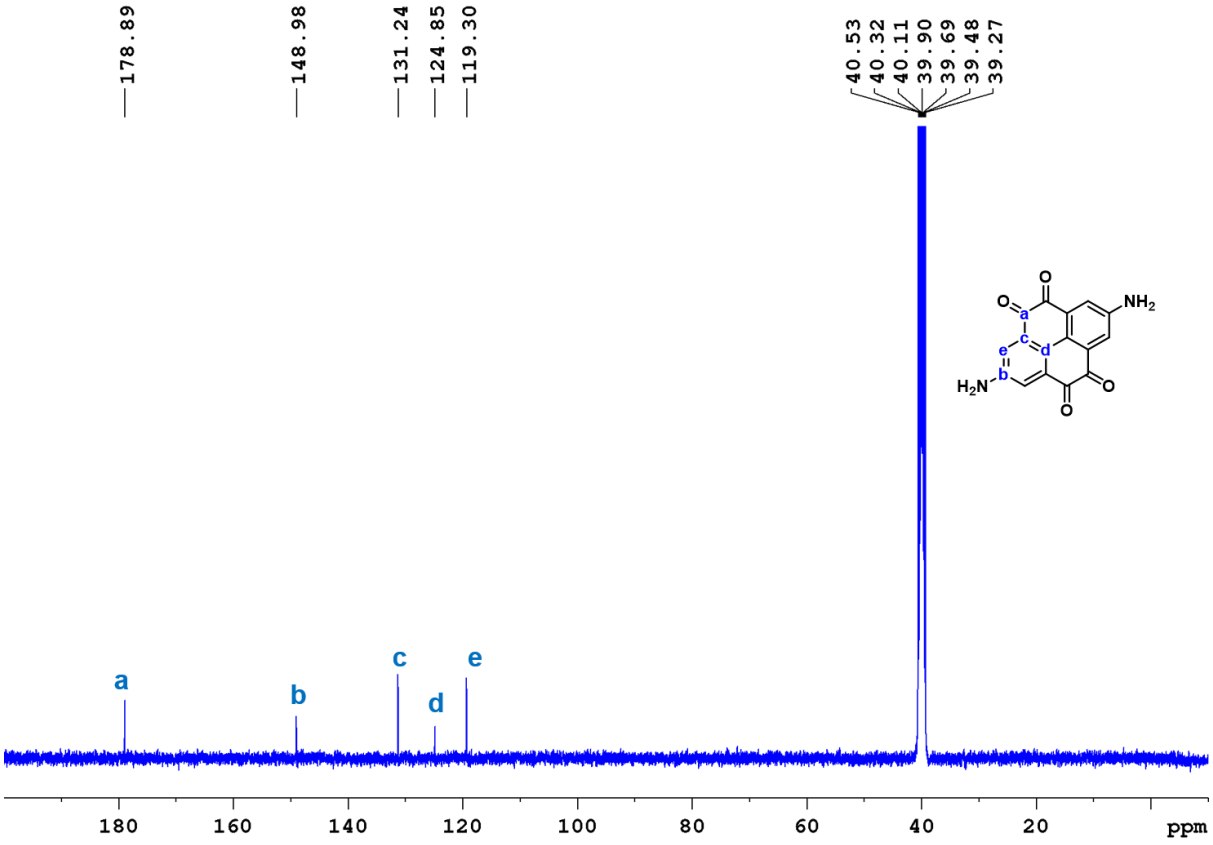

Figure 5-6. ^{13}C NMR (100 MHz, DMSO-d_6) spectrum of DAPT.

5.4.3 Synthesis of COFs Powders

5.4.3.1 Synthesis of PT-COF

1,3,5-triformylphloroglucinol (TFG) (10.5 mg, 0.05 mmol), 2,7-diaminopyrene-4,5,9,10-tetraone (DAPT) (21.9 mg, 0.075 mmol), mesitylene (0.2 mL), 1,4-dioxane (0.8 mL), and aqueous acetic acid (0.2 mL, 6 M) were added to a 10 mL Pyrex tube (outer × inner diameter = 1.3 × 1.0 cm with a length 15 cm). This mixture was homogenized by sonication for 10 minutes and the Pyrex glass tube was subjected to three freeze-pump-thaw cycles and evacuated to an internal pressure of 100 mTorr. The tube was sealed off and then placed in a thermal oven at 120 °C for 3 days. The black precipitate was collected by filtration and washed with DMF, DMSO, and acetone. The resulting solid was dried and then subjected to Soxhlet extraction with methanol as the solvent for 24 hours to remove the trapped guest molecules. The powder was collected and dried under reduced pressure at 85°C to afford PT-COF as a black powder (28.2 mg, 95%).

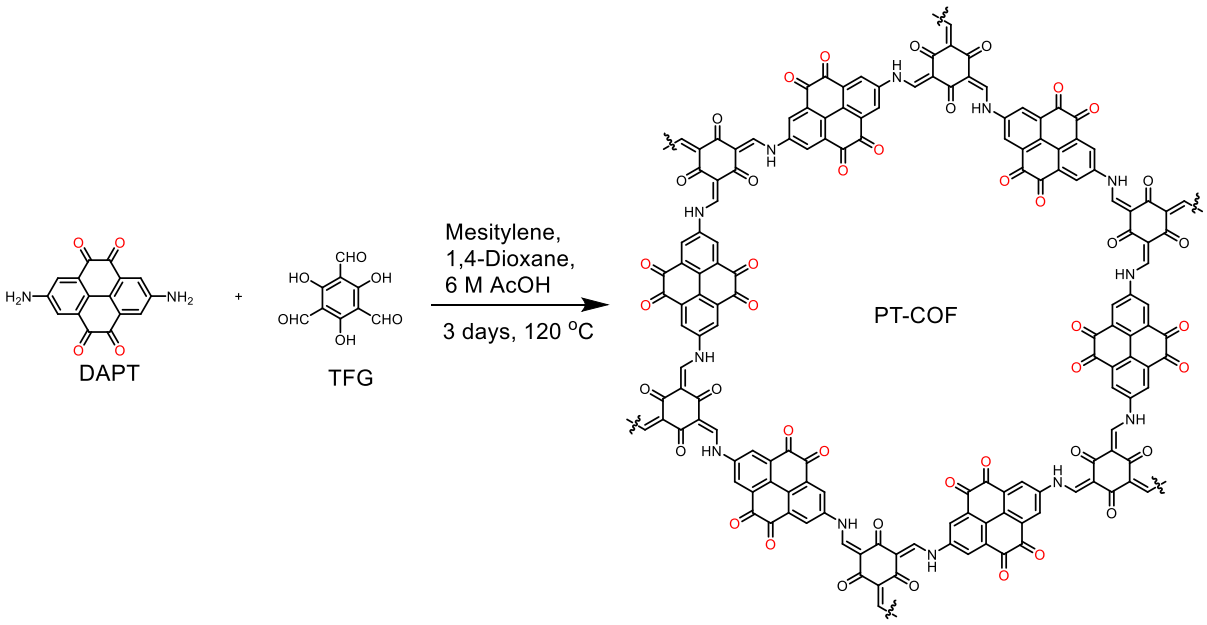

Scheme 5-2. Reaction scheme for the synthesis of PT-COF.

5.4.3.2 Synthesis of PT-COFX

A 10 mL Pyrex tube (outer × inner diameter = 1.3 × 1.0 cm with a length 15 cm) was charged with TFG (10.5 mg, 0.05 mmol), DAPT (21.9 mg, 0.075 mmol), CNT (10, 30, 50 wt% of the composite based on the yield of the PT-COF), mesitylene (0.9 mL), 1,4-dioxane (0.3 mL), and

aqueous acetic acid (0.1 mL, 3 M). This mixture was homogenized by sonication for 30 minutes and the Pyrex glass tube was subjected to three freeze-pump-thaw cycles and evacuated to an internal pressure of 100 mTorr. The tube was sealed off and then placed in an oven at 120 °C for 3 days. The black precipitate was collected by filtration and washed with DMF (3 × 5 mL), DMSO (3 × 5 mL), and acetone (3 × 5 mL). The resulting solid was dried and then subjected to Soxhlet extraction with methanol as the solvent for 24 hours to remove the trapped guest molecules. The powder was collected and dried under reduced pressure at 85°C to give PT-COFX as a black powder. The yields calculated for PI10, PI30, and PI50 were 95, 92, and 89%, respectively.

5.4.5 Optimisation of Experimental Conditions

Based on the synthesis of our previous β-ketoenamine-linked COF in Chapter 4, we initially attempted to synthesise PT-COF in a mesitylene and 1,4-dioxane solvent system and grow a crystalline COF structure (Table 5-1).

Table 5-1. Synthesis of PT-COF under different conditions

Entry[a]	Solvent (ml)	Acetic acid	Reaction temperature (°C)	Yield (%)	Crystallinity
1	Mesitylene/1,4-dioxane (0.9:0.3)	0.1 ml, 3M	120	91	Crystalline
2	1,4-Dioxane (1.0)	0.2 ml, 6M	120	91	Crystalline
3	Mesitylene/1,4-dioxane (0.2:0.8)	0.2 ml, 6M	120	95	Crystalline (high)

[a]Aldehyde (0.05 mmol), diamine (0.075 mmol), 3 d.

5.4.6 Theoretical Specific Capacity Calculation

The repeating unit in PT-COF consists of 1/2 of an A unit (M_A) and 1/3 of a B unit (M_B) (Figure 5-7). Hence, the molecular weight of the repeating unit cell in PT-COF is 198.02 g mol^{-1} ($C_{11}H_4NO_3$). The number of electrons (*n*) involved in the repeating unit is equal to 1, assuming 4 electrons are involved in each phenanthrenequinone unit. Therefore, using Equation 1-2, the theoretical capacity of PT-COF is calculated to be 271 mAh g^{-1}.

The specific capacities of the PT-COFX composites were calculated based on the mass of the PT-COF in the composite. However, both PT-COF and CNT contribute to the overall capacity of the electrode, so the total specific capacity of the PT-COFX composites was calculated using Equation 5-2:

$$C_{\mathrm{PT-COFX}} = \frac{a \times m \times C_{\mathrm{PT-COF}} + \mathrm{b} \times m \times C_{\mathrm{CNT}}}{a \times m} \qquad \textbf{(Equation 5-2)}$$

Where, $C_{\mathrm{PT\text{-}COFX}}$ and $C_{\mathrm{PT\text{-}COF}}$ are the specific capacities of PT-COFX and PT-COF, respectively, in the composite electrodes. C_{CNT} is the specific capacity of pure CNT (13 mAh g^{-1}) without PT-COF and m is the mass of the PT-COFX. a and b are the contents of PT-COF and CNT in the PT-COFX, such that $a+b=1$. Therefore, the capacity contribution of CNT in the PT-COFX is $C_{\mathrm{PT\text{-}COFX}}$-$C_{\mathrm{PT\text{-}COF}}$ = $(b \times C_{\mathrm{CNT}})/a$

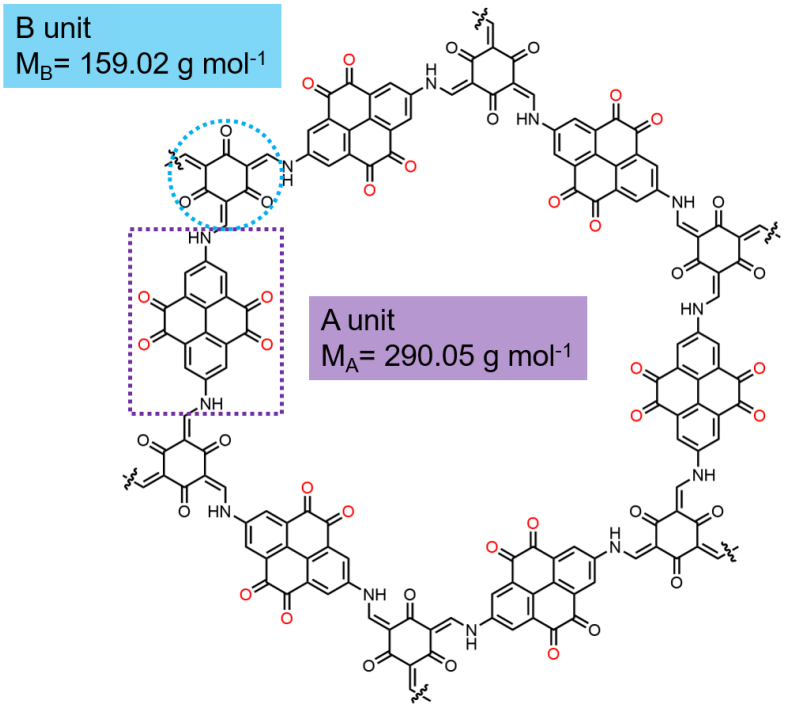

Figure 5-7. Chemical structure of PT-COF.

Table 5-3. Capacity contribution of CNT in PT-COFX.

Sample	Calculation of capacity contribution of CNT in PT-COFX (mAh g^{-1})
PT-COF10	0.1×13/0.9 = 1
PT-COF30	0.3×13/0.7 = 6
PT-COF50	0.5×13/0.5 = 13

5.4.7 Electrochemical Test Protocol

In PT-COF electrode, the mass ratio of active materials (PT-COF): carbon black: PVDF is 6: 3: 1. In the PT-COFX electrode, the mass ratio of active materials (PT-COF): carbon black: PVDF is 7: 2: 1. In the coin cells, PT-COF/PT-COFX was used as the working positive electrode, lithium as the counter electrode, and 1 M LiTFSI in DOL and DME (1:1 v/v) as the electrolyte solution.

Please see Chapter 2 (Section 2.2 Electrochemical Measurements) for the electrochemical test protocol.

5.5 PT-COF Design, Synthesis, and Characterisation

PT-COF was synthesised by one step Schiff-base condensation reaction of TFG with 2,7-diaminopyrene-4,5,9,10-tetraone (DAPT) in a 2:3 stoichiometric molar ration. The reagents were dispersed in a mixture solvent of mesitylene and 1,4-dioxane (1:4, v:v) by sonication 15 mins. Then the reagents were heated at 120 °C for 3 days. After filtration, the product was washed with DMF, DMSO, and then by Soxhlet using methanol. Finally, the product was dried at 80 °C under vacuum to afford the product in a yield of 95% (Scheme 5-2, see section 5.4.5.1 for detailed reaction conditions). The condensation reaction is followed by an irreversible keto-enol tautomerization, which enhances the chemical stability of the COF.[6]

The crystalline structure of the product was confirmed by PXRD. As shown in Figure 5-8, the PXRD pattern of PT-COF exhibits good crystallinity with an intense peak at 3.4°, which corresponds to (110) reflection planes. The experimental PXRD pattern of PT-COF is more consistent with the simulated PXRD pattern of the aligned AA stacked model, rather than the staggered AB stacking (Figure 5-9). A Pawley refinement also confirmed that the PXRD data was consistent with PT-COF having the same hexagonal *P*6/*m* symmetry ($a = b = 30.068$ Å, $c = 3.553$ Å, $V = 2784.09$ Å^3) and comparable dimensions to the eclipsed A-A stacked model.

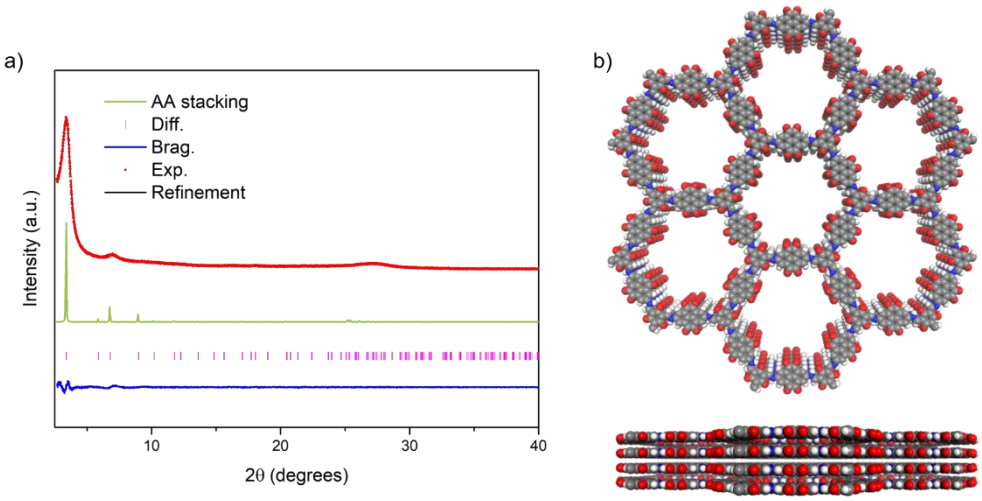

Figure 5-8. (a) PXRD pattern fitting of PT-COF with Pawley refinement (Cu-Kα). Red circles: experimental PXRD pattern, black line: fitting pattern, blue curve: difference between experimental and refinement, magenta bars: reflection positions, green curve: XRD pattern of simulated AA stacking model, R_p = 2.21%, R_{wp} = 3.17% (*P*6/*m*, *a* = *b* = 30.068 Å, *c* = 3.553 Å, *V* = 2784.09 Å^3). (b) Structural models for PT-COF with perfectly eclipsed AA stacking patterns, shown parallel to the pore channel along the crystallographic *c* axis (top) and parallel to the hexagonal layers (bottom). Grey, white, red, and blue atoms represent carbon, hydrogen, oxygen, and nitrogen, respectively.

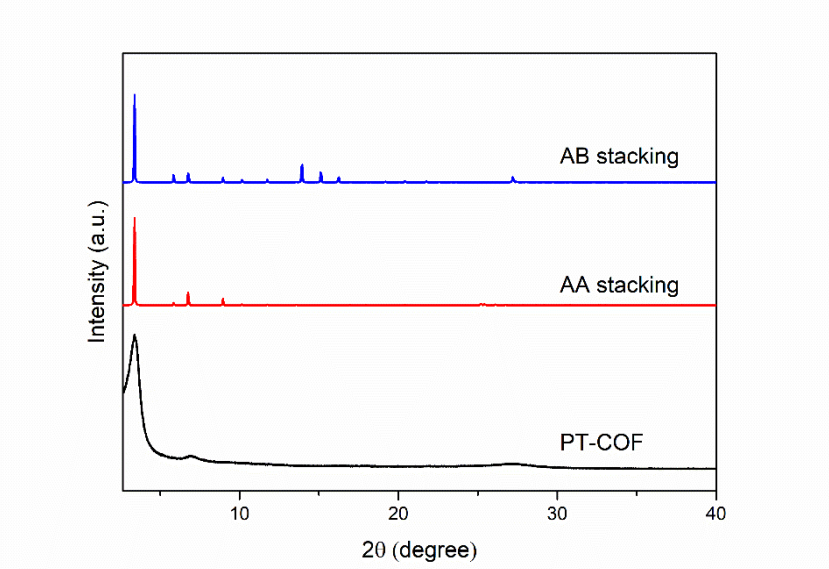

Figure 5-9. Experimental PXRD pattern of PT-COF and the simulated PXRD pattern for A-A and A-B stacking model.

The chemical structure of PT-COF was confirmed by ^{13}C CP-MAS solid-state NMR spectroscopy and FT-IR spectroscopy (Figure 5-10). The peaks observed at 147 and 108 ppm are assigned to the enamine carbon (=CNH) and α-enamine carbon, respectively, indicating the formation of β-ketoenamine- linked materials.[7] FT-IR spectrum of PT-COF show two characteristic peaks at 1259 and 1675 cm^{-1}, which were assigned to the stretching vibrations of β-ketoenamine C−N moieties and C=O of the DAPT unit, respectively (Figure 5-10). υ_{N-H} at 3470, 3437, 3367, and 3342 cm^{-1} in the FT-IR spectra of the DAPT precursor were not observed in the PT-COF, indicating the consumption of the DAPT in the reaction.

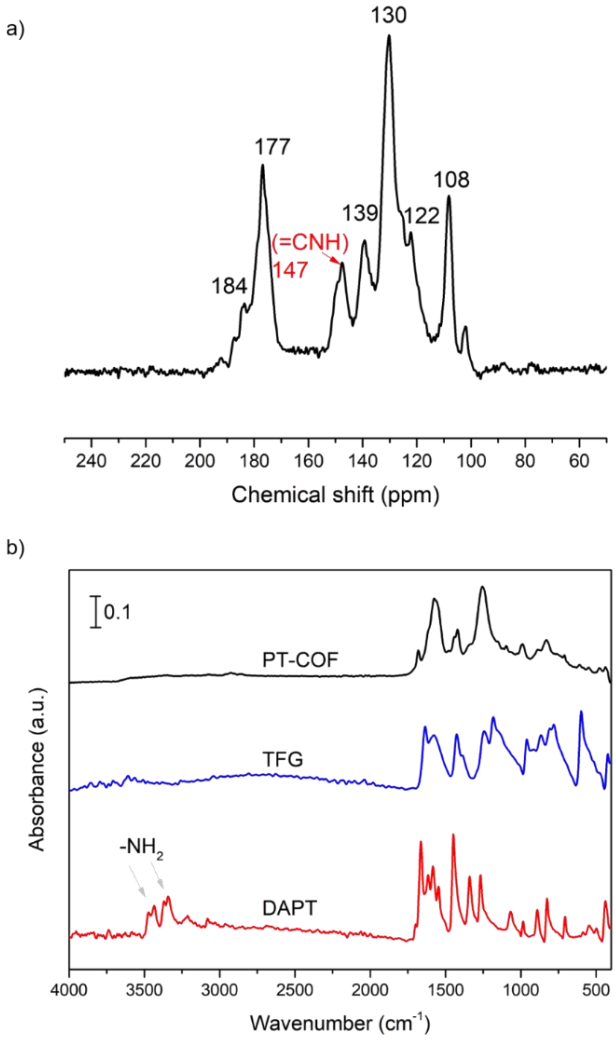

Figure 5-10. (a) ^{13}C solid-state NMR CP/MAS spectrum of PT-COF; (b) FT-IR spectra of TFG, DAPT, PT-COF.

The surface area and porosity of PT-COF were measured by N_2 adsorption-desorption analysis at 77.3 K. The N_2 adsorption-desorption profile of PT-COF is a type II isotherm (Figure 5-11). The isotherm displayed a sharp rise in the low-pressure range (P/P_0 = 0 – 0.01), indicating a microporous character of PT-COF. A relative loss at 0.5 – 1.0 P/P_0 was observed, implying the presence of the mesopores in the material. The SA_{BET} of PT-COF is 432 $m^2\ g^{-1}$. The pore size distribution of PT-COF derived by fitting nonlocal density functional theory (NL-DFT) models to the N_2 isotherms was 1.8 nm (Figure 5-11), which is close to the pore size in the A-A stacked model (~ 2.3 nm). The pore size of PT-COF is bigger than the electrolyte components. The molecule sizes of electrolyte components DOL, DME, and LiTFSI are 0.38, 0.73, and 0.72 nm, respectively. It means that the electrolyte can facilely transport in the micropores of 1.8 nm. The PXRD pattern of PT-COF is identical before and after gas sorption (Figure 5-12). It means the crystalline framework of PT-COF is stable during the gas sorption test.

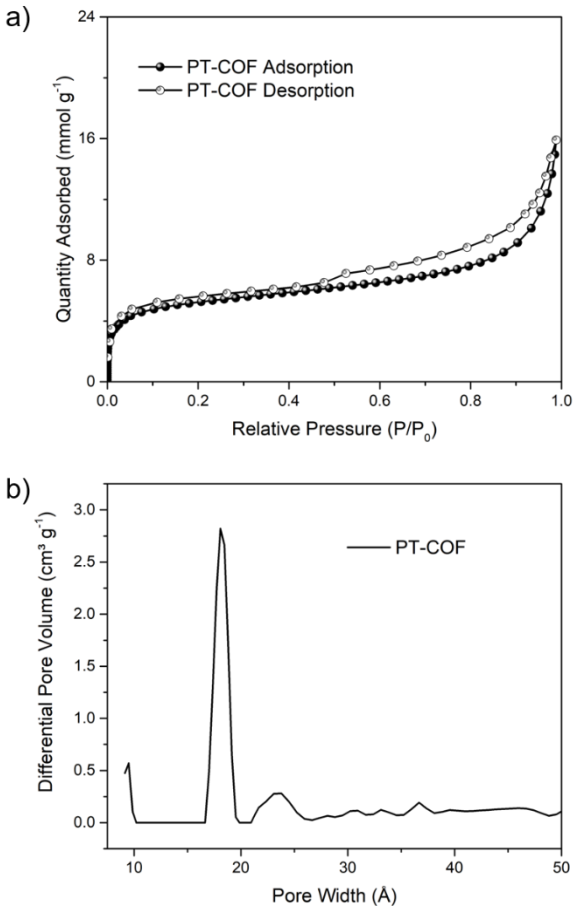

Figure 5-11. (a) N_2 sorption isotherms of PT-COF (77.3 K, solid symbols = adsorption; open symbols = desorption); (b) Pore size distribution plots of PT-COF (calculated by NL-DFT for pillared clay).

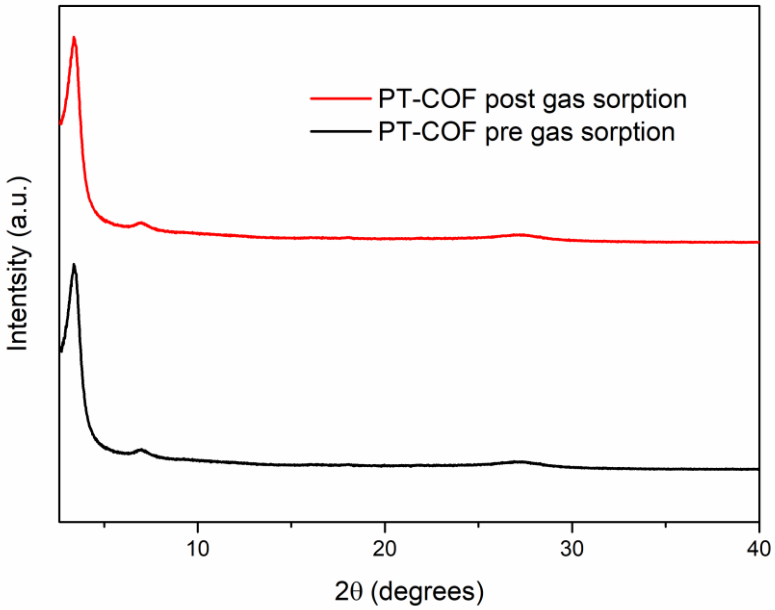

Figure 5-12. PXRD pattern of PT-COF before and after gas sorption test.

The morphologies of PT-COF were recorded by SEM. PT-COF displays an intergrown plate-like morphology in the SEM images (Figure 5-13). TEM further confirmed the crystalline structure of the PT-COF. The TEM images showed that PT-COF has an ordered structure with hexagonal pores oriented along its crystallographic *c* axis (area outlined in yellow, Figure 5-14).

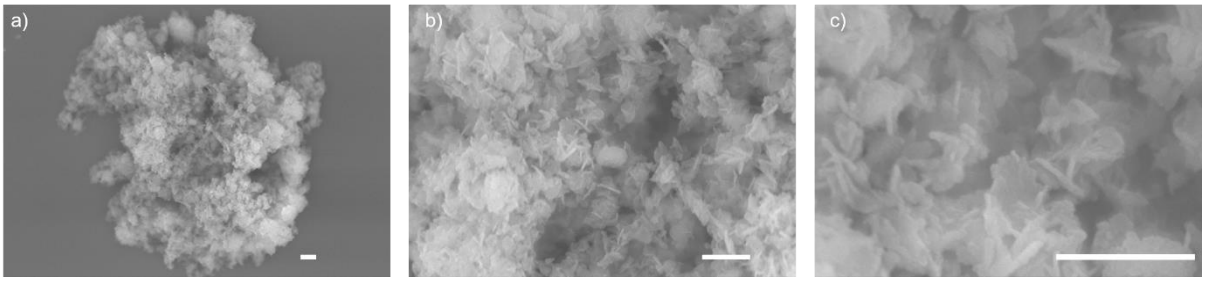

Figure 5-13. SEM images of PT-COF, scale bar: 1 μm.

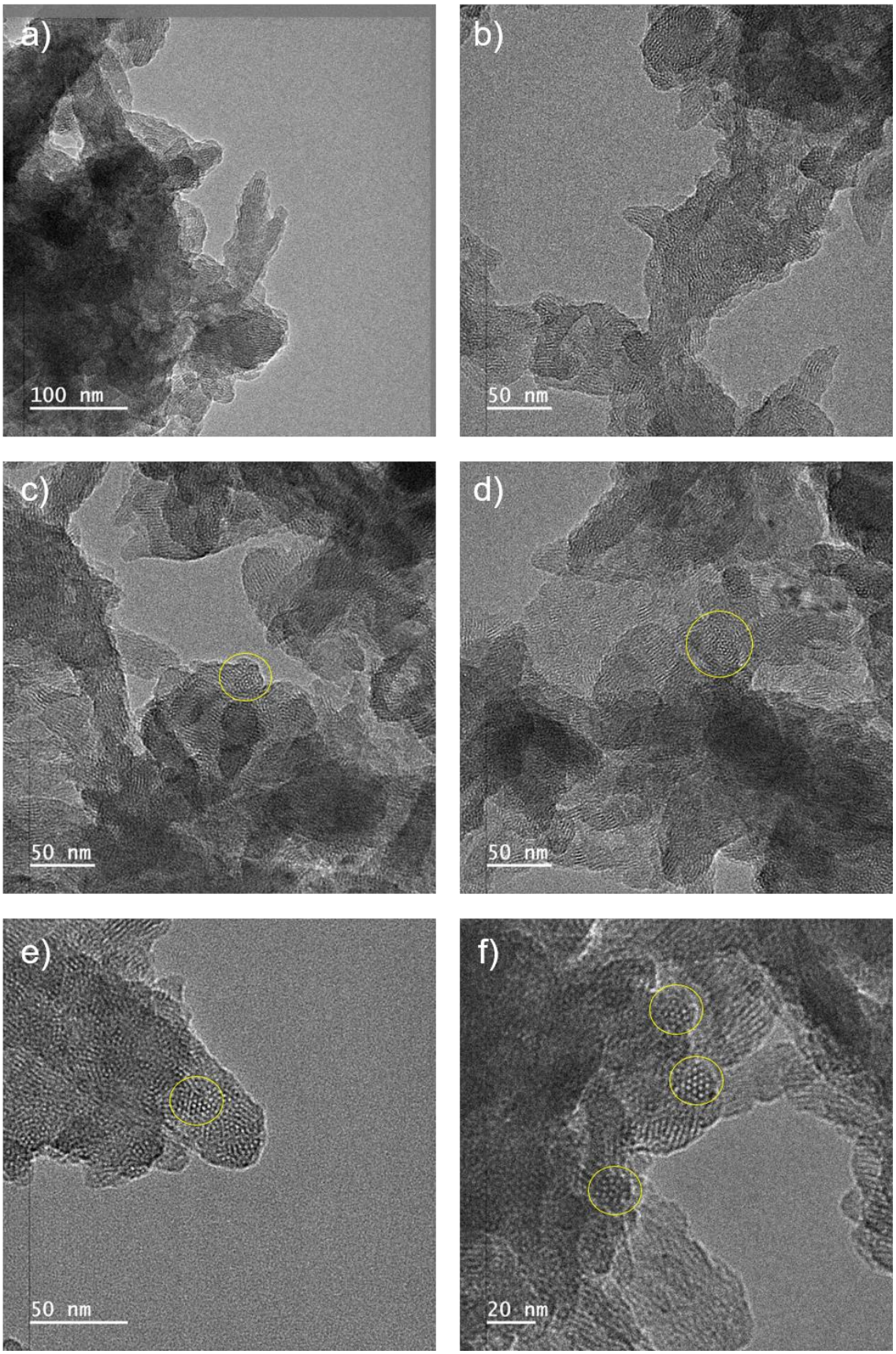

Figure 5-14. TEM images of PT-COF. The yellow circle outlined the ordered pore structure.

Chemical stability is an important requirement for electrode stability for battery application. PT-COF exhibited good chemical stability against various solvents, like water, hydrochloride acid, *N*,*N*-dimethylformamide and *N*-methyl-2-pyrrolidone. PT-COF showed identical PXRD pattern and FT-IR spectra (Figure 5-15) before and after exposure to the above solvents for 48 hours. The results showed that PT-COF kept good crystallinity and did not show structural decomposition, indicating good chemical stability.

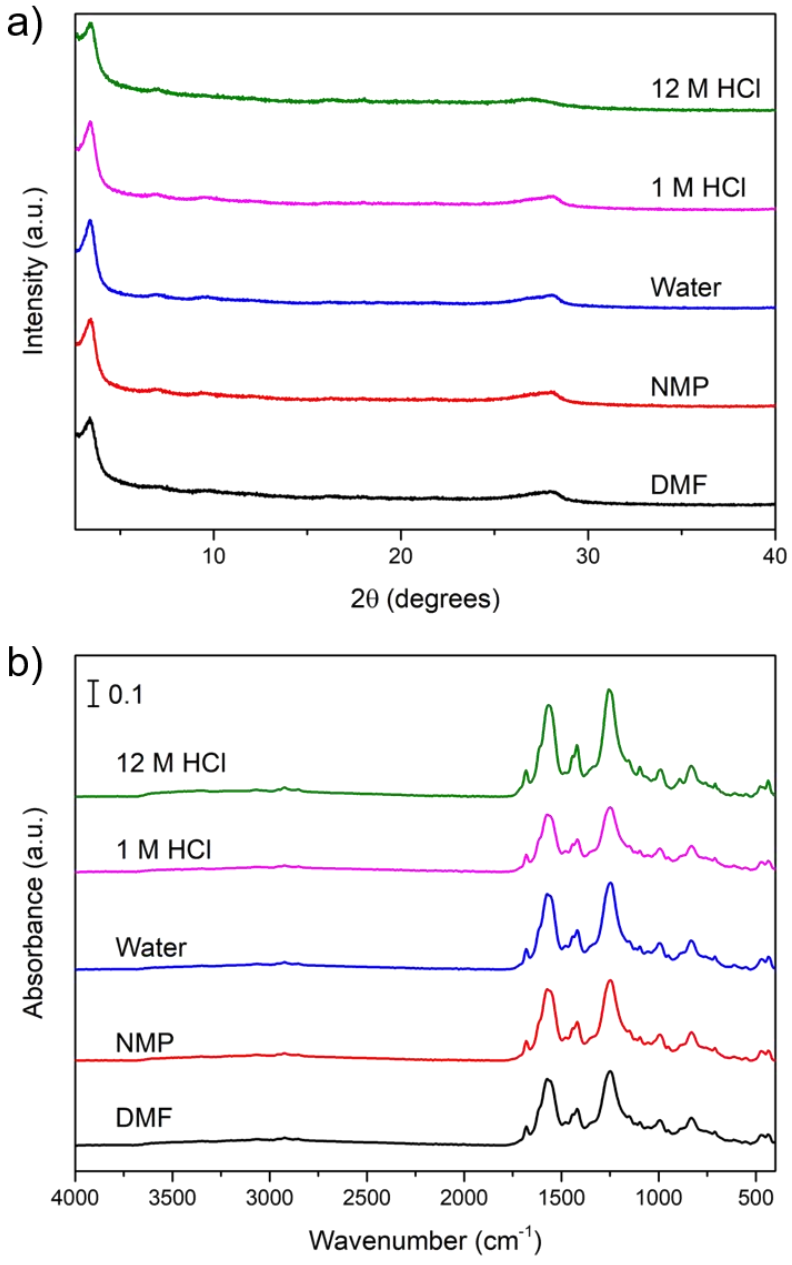

Figure 5-15. (a) PXRD and (b) FT-IR spectra of PT-COF after exposure to water, aqueous acid, *N*-dimethylformamide, and *N*-methyl-2-pyrrolidone for 24 hours.

5.6 PT-COF and CNT Composite Design, Synthesis and Characterisation

After synthesising PT-COF, a series of PT-COF composites was synthesised using the same synthetic method, but with CNT added into the reaction mixture (Scheme 5-3). In the preparation of the composite, a 2:3 stoichiometric molar ration of TFG with DAPT was dispersed in a mixture of mesitylene and 1,4-dioxane (1:4 v/v). CNT was added to the reaction mixture, followed by sonication for 30 min to ensure the reaction precursors were well mixed. Then, the reaction reagents were heated at 120 °C for 3 days. After filtration, the product was washed with DMF, DMSO, acetone, and then by Soxhlet with methanol. Finally, the product was dried at 80 °C under vacuum and got yield above 90%. In total, four samples were synthesised using the same method: PT-COF and CNT composite with 10, 30, and 50 wt.% CNT (The amount of CNT is calculated based on the 95% yield of PT-COF yield from the composite reaction). The composites are named PT-COFX, where X = 10, 30, and 50 wt.% of CNT.

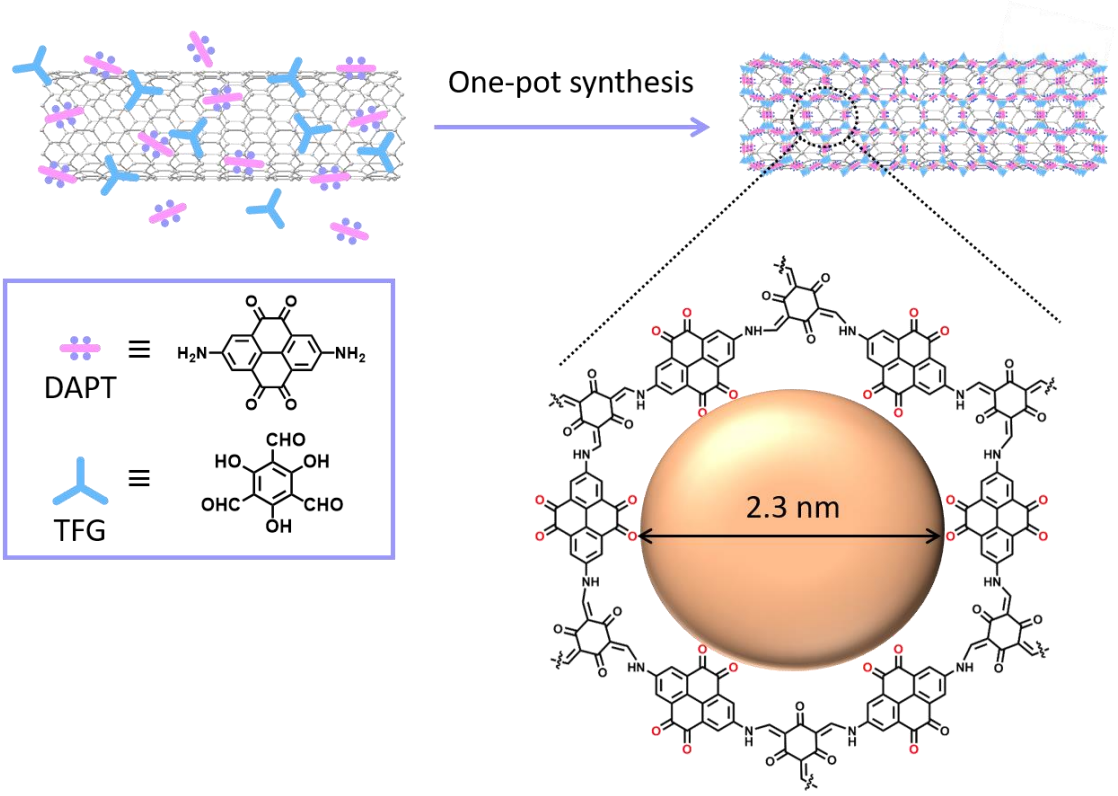

Scheme 5-3. Scheme showing the synthesis of PT-COF and CNT composite.

To confirm the crystallinity of the PT-COF composites, PXRD measurements were performed on all the composites. As shown in Figure 5-16a, the PXRD patterns of PT-COF10 and PT-COF30 display good crystallinity with an intense peak at 3.4°, which corresponds to (110) reflection. The addition of CNT decreases the crystallinity of PT-COFX. It was found that 50 wt% CNT is the threshold limit of crystallinity. The PXRD patterns indicated that PT-COF kept the same structure in the PT-COFX composites. FT-IR was used to characterise the chemical structure of PT-COF composites (Figure 5-16). The characteristic N-H peaks, $\upsilon_{N\text{-}H}$ at 3470, 3437, 3367, and 3342 cm^{-1}, were not observed in the IR spectra of the composites. New peaks at 1259 and 1675 cm^{-1} belong to the β-ketoenamine C−N moieties and C=C stretching vibrations appeared. The IR spectra indicated that the reaction occurred successfully and the PT-COF in the composite was in its keto form. The IR spectra in Figure 5-16b have not been normalised, so the intensity of the peaks differ with different sample amounts used.

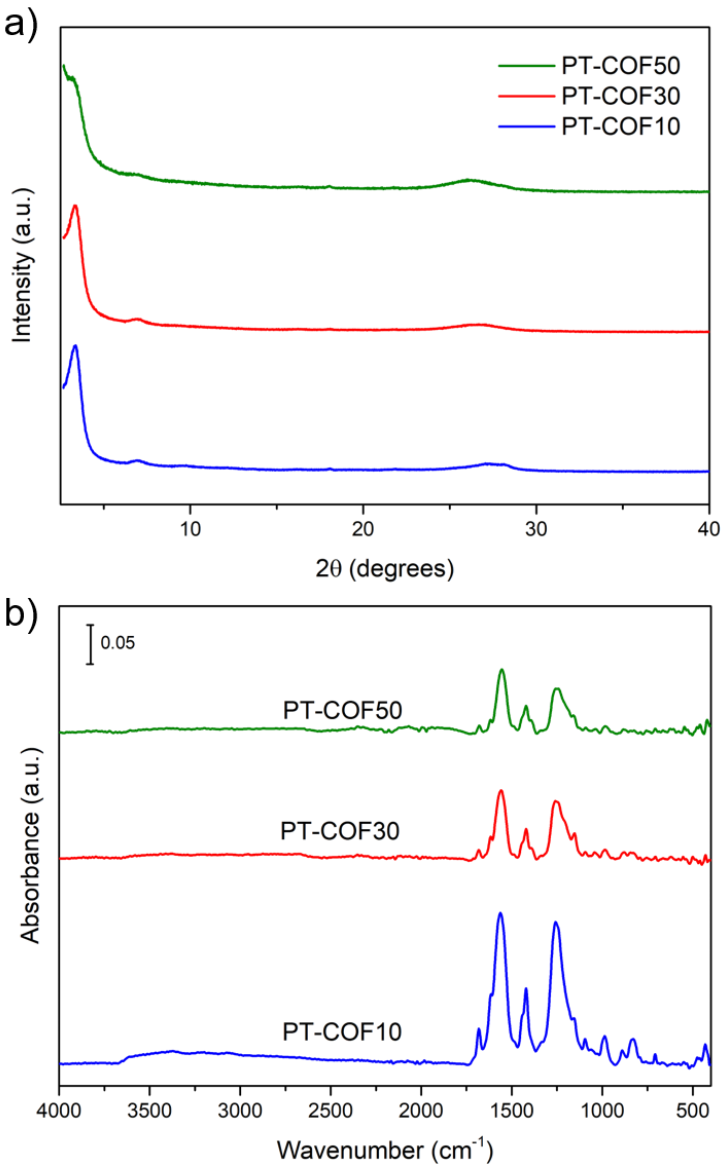

Figure 5-16. (a) PXRD pattern and (b) FT-IR spectra of PT-COF10, PT-COF30, and PT-COF50.

The BET surface areas and porosity parameters of PT-COFX composites were studied by N_2 sorption. Figure 5-17 presents the nitrogen sorption isotherms and pore distribution curves of the PT-COFX composites. As shown in Figure 5-17, all the PT-COFX composites showed type II isotherms. There is steep adsorption at a low relative pressure ($P/P_0 \approx 0.01$) indicates that these composites possess micropores. The hysteresis loop at the medium pressure region ($P/P_0 = 0.4–0.7$) reveals that mesopores exist in the materials. The adsorption isotherm increases steeply at higher relative pressure, which can be ascribed to macroporosity. That is because of

the presence of CNT, and a positive collection between the ratio of CNT and the N_2 uptake at high pressure was observed. The SA_{BET} of PT-COFXs increased first then decreased as the wt.% of CNT increased from 10 to 50wt.% (Table 5-2). This may be because the presence of CNT increased the crystallinity of the PT-COF in the PT-COF10 and PT-COF30, however, the exceed of CNT in PT-COF50 decreased the crystallinity of the PT-COF in the composite.

The pore size distribution (Figure 5-17, calculated by NL-DFT for pillared clay) also confirms the presence of micropores and mesopores. All the PT-COFX composites have pores with an average width of 1.8 nm, which is larger than the diameter of Li-ion (1.52 Å). Therefore, the open channels are beneficial for Li-ion transport within the composites. The detailed BET surface areas and pore volumes of the PT-COF, PT-COFX, and CNT are listed in Table 5-2.

Table 5-2. Surface areas and pore properties of PT-COF, the PT-COF composites and CNT.

Sample	SA_{BET}[a] ($m^2\ g^{-1}$)	Total pore volume[b] ($cm^3\ g^{-1}$)
PT-COF	432	0.172
PT-COF10	450	0.171
PT-COF30	473	0.176
PT-COF50	318	0.098
CNT	247	0.322

[a]Surface area calculated from the N_2 adsorption isotherms at 77.3 K using the BET equation;
[b]Pore volume calculated from the nitrogen isotherm at P/P_0 = 0.99, 77.3 K.

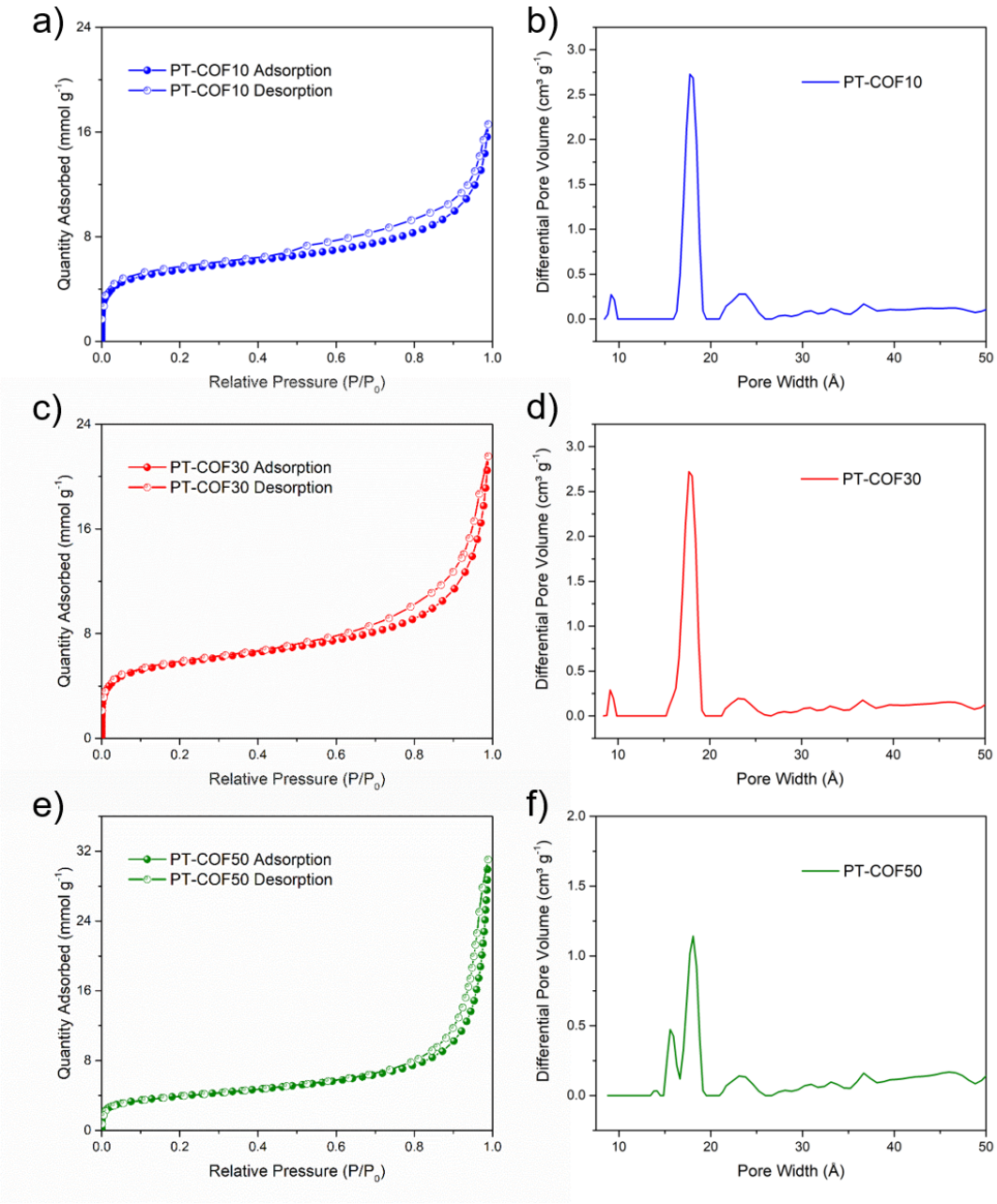

Figure 5-17. (a,c,e) N_2 sorption isotherms of PT-COFX composites, and CNT (77.3 K, solid symbols = adsorption; open symbols = desorption); (b,d,f) Pore size distribution plots of the PT-COFX composites (calculated by NL-DFT for pillared clay).

TEM was employed to characterise the structure of the PT-COFX composites. In Figure 5-18, it was found that tubular core-shell structures in PT-COFX with the COF structure grown around the external surface of the CNT. The ordered structure with hexagonal pores oriented along its crystallographic *c* axis of the COF in the composite can be observed in the TEM

images, implying that the COF layers retain their crystallinity. The thickness of the COF layer around the CNT decreases with the increasing amount of CNT in the composite. The morphologies of the PT-COFX composites were recorded by SEM (Figure 5-19). In PT-COF10, the COF is integrated with CNT. While PT-COF30 and PT-COF50 appear to retain bulk CNT morphology. The thickness of COF layers decreases with the increase of CNT mass weight maybe because there are more CNT surfaces for the COFs to grow on. With thinner COF layers in the composite, the ion transport pathway is shortened and more electrochemical redox-active sites are available. So, thinner COF layers are beneficial for electrochemical performance.

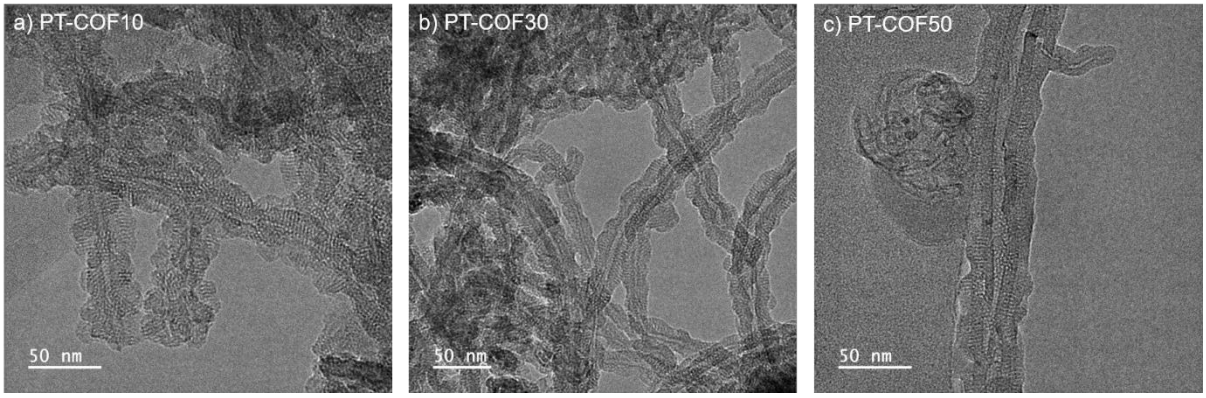

Figure 5-18. TEM images of (a) PT-COF10; (b) PT -COF30; (c) PT -COF50.

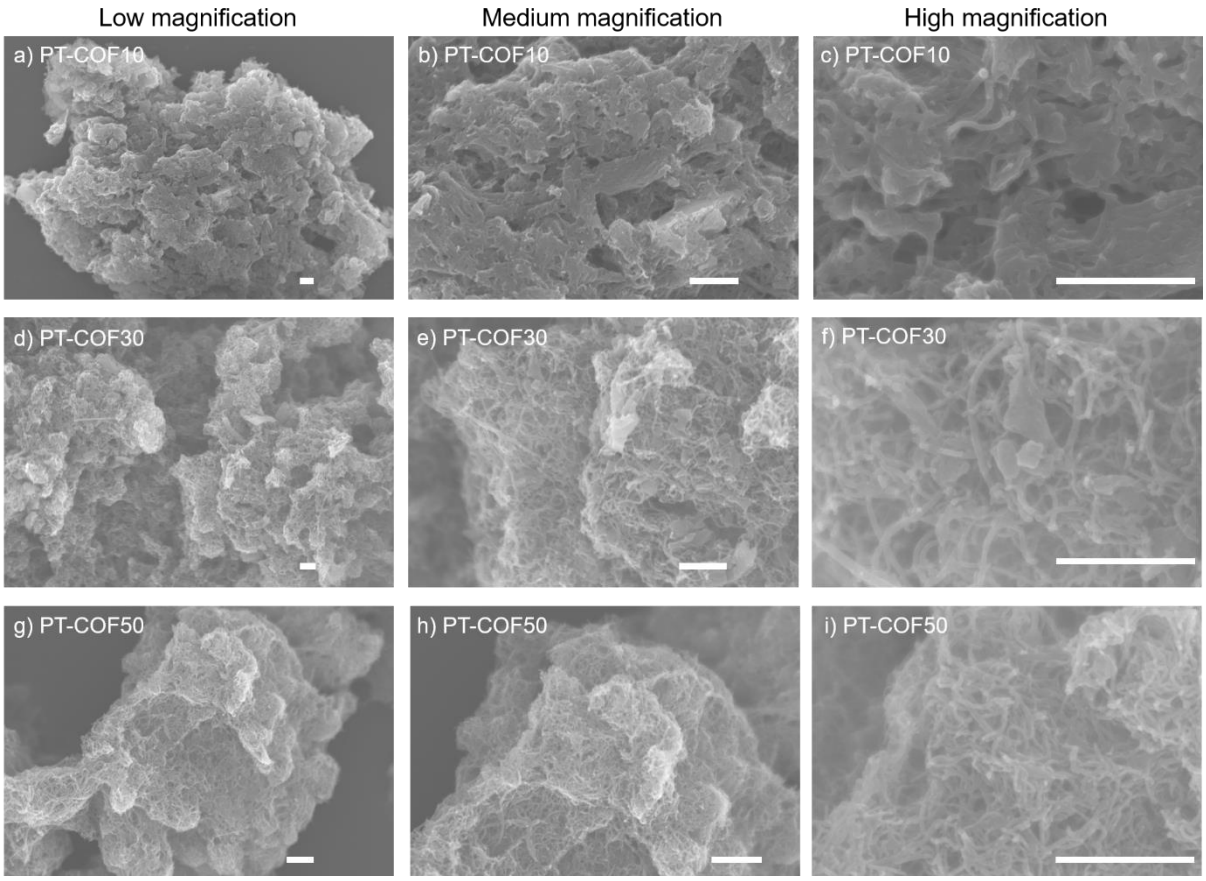

Figure 5-19. SEM images of PT -COF10 (a-c), PT -COF30 and (d-f), PT -COF50 (g-i); scale bar: 1 μm.

5.7 Energy Storage Performance of PT-COFX

The PT-COF is studied as a positive electrode for Li-ion coin cells with lithium metal as the counter electrode. Two electrolytes include 1 M LiTFSI in DOL and DME (1:1 v/v) and 1 M $LiPF_6$ in EC and DMC (1:1 v/v) were investigated. As shown in Figure 5-20, the PT-COF based positive electrode in carbonate-based electrolyte exhibits an initial capacity of 190 mA h g^{-1} but rapidly fades to 60 mAh g^{-1} within 50 cycles at the current density of 100 mA g^{-1}. This phenomenon may cause by the undesired side reaction of the active site with the carbonated-based electrolyte.[8] To improve the electrochemical performance of the PT-COF based cathodes, the electrolyte of LiTFSI in DOL/DME (1: 1 v/v) was used as an alternative to $LiPF_6$ since LiTFSI shows more ionic nature than $LiPF_6$.[9] In contrast, PT-COF in LiTFSI shows good cycling performance. The cathode retains the capacity of 193 mAh g^{-1} even after 100 cycles (Figure 5-21c). Therefore, the ether-based electrolyte is used for the rest of the tests.

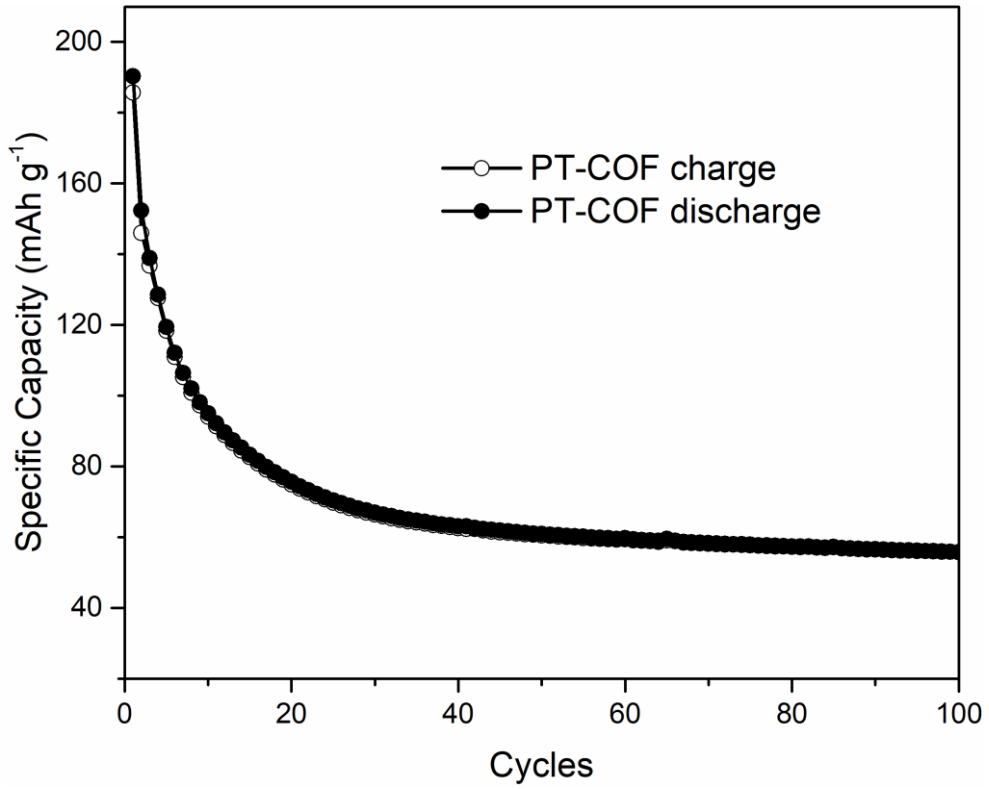

Figure 5-20. Cycling performance of PT-COF in a conventional Li-ion battery electrolyte (1 M $LiPF_6$ in EC/DMC (1:1 v/v) over 100 cycles at 100 mA g^{-1} operated in the voltage range of 1.5-3.5 V.

CV of PT-COF and PT-COFX was performed in the coin cells at 0.1 mV s^{-1} in a potential window of 1.5 -3.5 V (Figure 5-21a). In the CV profiles, all the curves have similar shapes. Two obvious separated redox peaks were present at 2.8 and 2.3 V. Further, with the increasing amount of CNT in the composite, the peak current densities and integral charge (based on the mass of PT-COF active material) increased. PT-COF50 has the highest integral charge area, implying more efficient utilisation of redox-active sites in PT-COF50 compared to PT-COF. This may be because the charge transport within the composite electrode was improved by the adding of CNT.

Galvanostatic charge-discharge tests were performed in a voltage window of 1.5 to 3.5 V for all Li-ion coin cells (Figure 5-21b). The sloping plateaus in the galvanostatic charge/discharge curves consist of their CV profile, corresponding to the reversible oxidisation/reduction of the carbonyl groups. The average discharge potential calculated from the PT-COF and PT-COFX composite is about 2.55 V, which is higher than most of the reported carbonyl functional group

based electrodes.[8,10–13] PT-COF delivered a specific capacity of 193 mAh g^{-1} at 200 mA g^{-1}, corresponding to 71% of its theoretical capacity of 271 mAh g^{-1} (see Section 5.4.7 for calculation details of the theoretical specific capacity). The specific capacity of PT-COF10, PT-COF30, and PT-COF50 at the current density of 200 mA g^{-1} are 225, 267, and 280 mAh g^{-1}, respectively. The capacity contribution of CNT in the PT-COF composites is 1, 6, and 13 mAh g^{-1} for PT-COF10, PT-COF30, and PT-COF50, respectively (see section 5.4.8 for the detailed calculation). The utilisation of redox-active sites (exclude the capacity contribution of CNT) increases to 83, 96, and 98% for PT-COF10, PT-COF30, and PT-COF50, respectively. Moreover, PT-COF and PT-COFX composites electrode all retain a nearly constant capacity after 150 cycles and their Coulombic efficiencies are *ca.* 100%, which implies good electrochemical stability (Figure 5-21c).

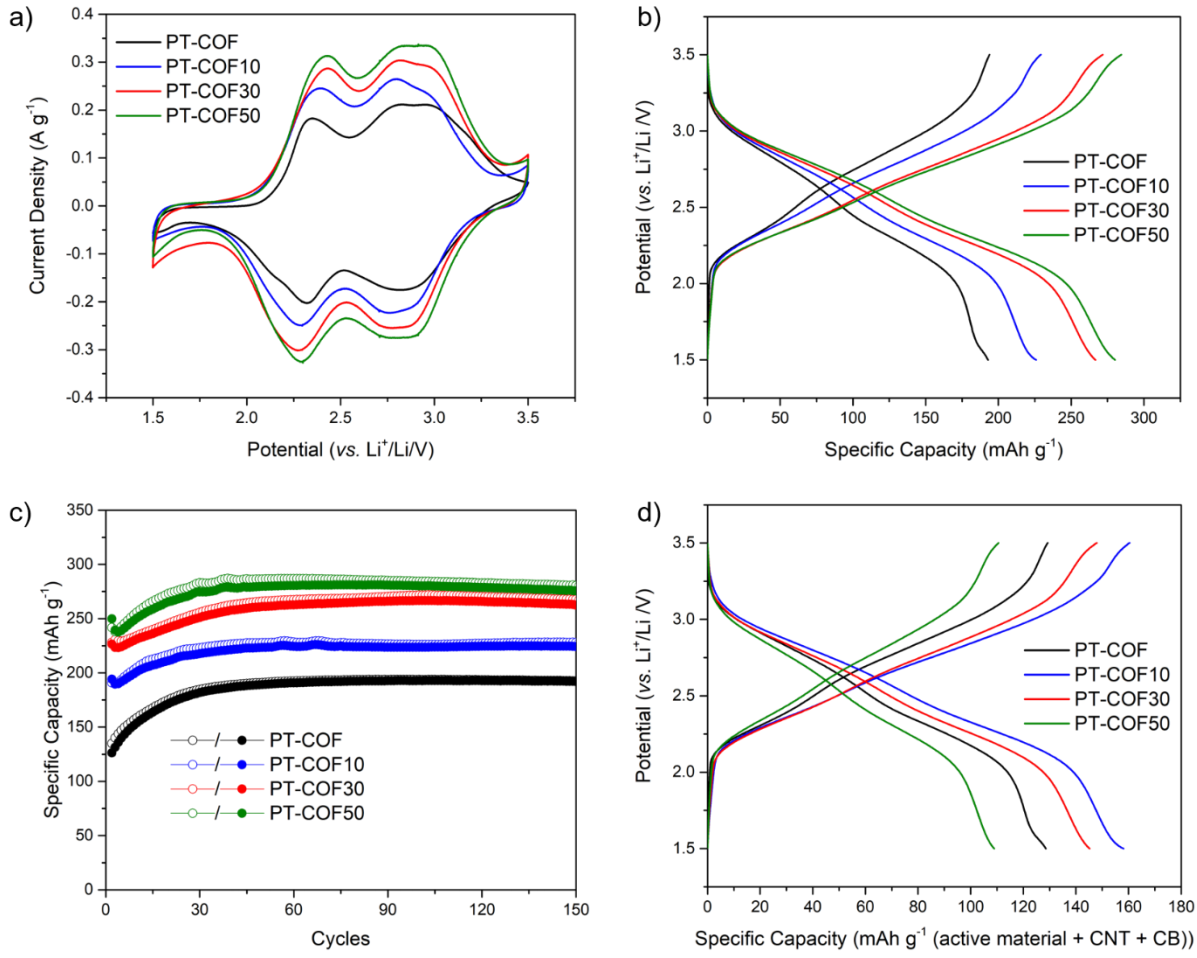

Figure 5-21. (a) Cyclic voltammetry profiles at a scan rate of 0.5 mV s^{-1}; (b) Charge-discharge profiles at 200 mA g^{-1}; (c) Cycling performances over 150 cycles at 200 mA g^{-1}; (d) Charge-discharge profiles (based on active material, CNT, and carbon black (CB)) at 200 mA g^{-1} for PT-COF, PT-COF10, PT-COF30, and PT-COF50.

DAPT-based positive electrodes exhibit a capacity of 345 mAh g^{-1} at the current density of 100 mA g^{-1}, corresponding to 94% of its theoretical specific capacity of 367 mAh g^{-1}) (Figure 5-22). The capacity is higher than that of the PT-COF and PT-COFX composite electrodes. However, the capacity of the DAPT monomer drops rapidly to 40 mAh g^{-1} in 50 cycles because DAPT is soluble in the organic electrolyte.

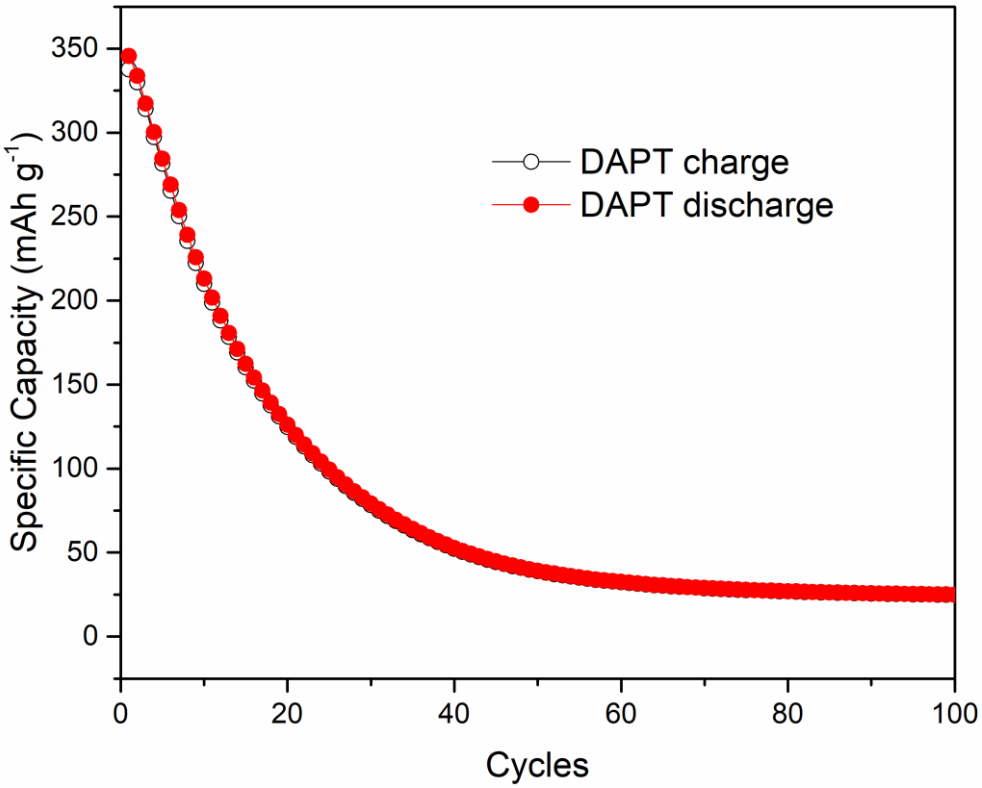

Figure 5-22. Cycling performance of the DAPT monomer over 100 cycles at 100 mA g^{-1} operated in the voltage range of 1.5-3.5 V.

To clarify the capacity contributions of CNT and carbon black towards the overall performance, their electrochemical performance was tested as well. The electrodes of CNT and carbon black exhibit capacities of 13 and 2 mAh g^{-1} under 200 mA g^{-1}, when the electrode is made from CNT: PVDF (9:1 by mass) and carbon black: PVDF (9:1 by mass) (Figure 5-23). CNT electrode showed a capacity indicating that CNT can accommodate Li-ions.

The capacity of the PT-COF50 electrode is higher than that of the typical positive electrode materials used in commercial cells.[14–18] However, the capacity of the PT-COFX cells is only about 150 mAh g^{-1} when calculated based on the summing mass of the active material and conductive additives (Figure 5-21d). PT-COF50 shows a capacity of 109 mAh g^{-1} when

considering the mass of the whole electrode, which is the lowest capacity in the PT-COF and PT-COFX composites electrode. It demonstrated that adding too many conductive additives is a poor strategy for practical cells. As we are doing the fundamental research and focusing on the electrochemical properties of PT-COF active material, all gravimetric capacities and currents are normalised to the mass of the active material (PT-COF), except for Figure 5-21d, in which the galvanostatic charge/discharge profiles are based on the mass of the whole electrode in the cell.

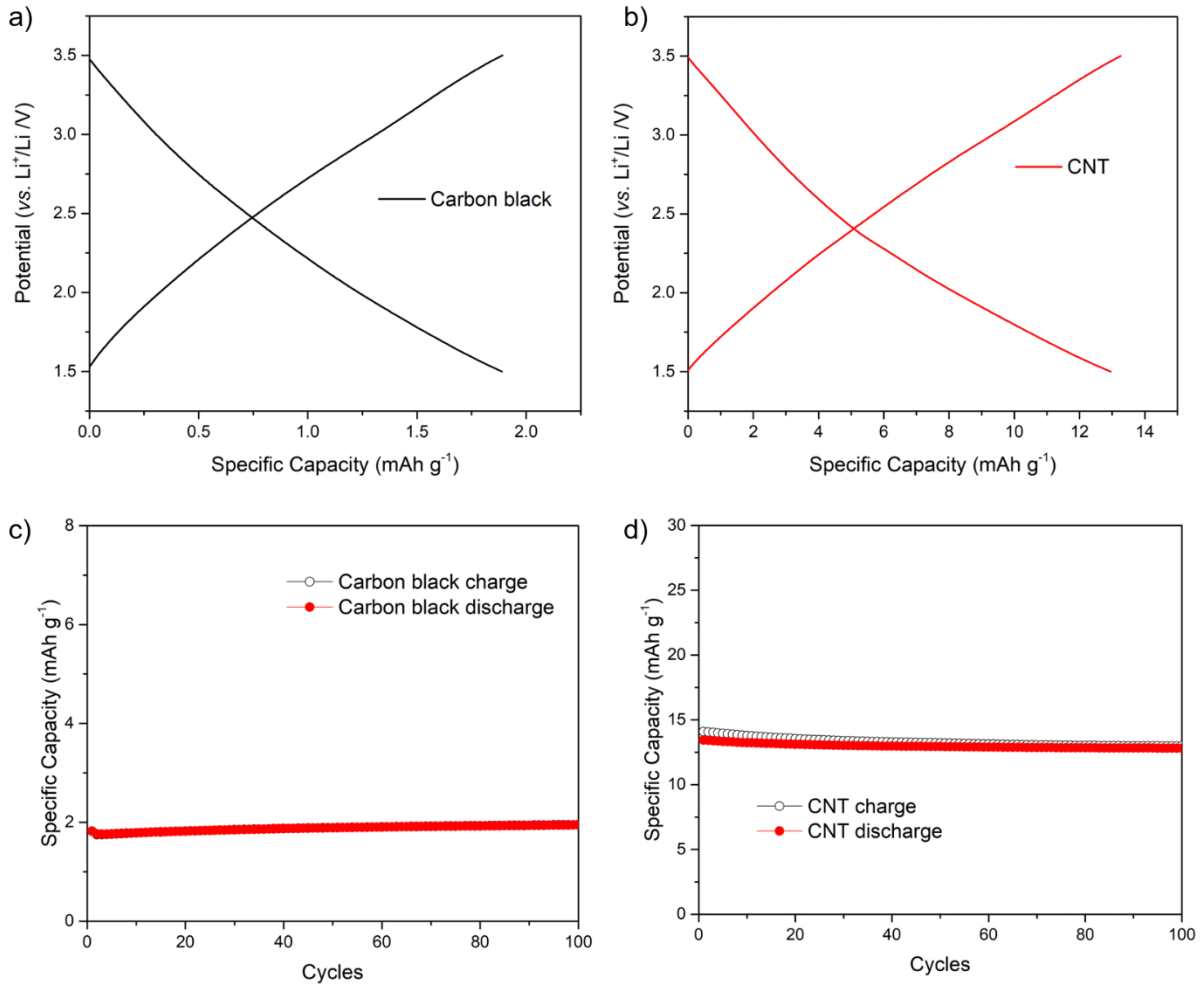

Figure 5-23. (a) Galvanostatic charge/discharge curve of carbon black electrode at 200 mA g^{-1}; (b) Galvanostatic charge/discharge curve of CNT electrode at 200 mA g^{-1}; (c) Cycling performance over 100 cycles for carbon black electrode at 200 mA g^{-1} operated in the voltage range of 1.5-3.5 V; (d) Cycling performance over 100 cycles for CNT electrode at 200 mA g^{-1} operated in the voltage range of 1.5-3.5V.

The rate performance of PT-COF and the PT-COFX composites were then studied under different current densities over the range of 200 to 5000 mA g^{-1} (Figure 5-24). The capacity of PT-COF50 is less dependent on the current density with a capacity retention of 79% at 5000 mA g^{-1} (18.5 C). In addition, the capacity of all composites recovered to the initial values once the current was reduced back to 200 mA g^{-1}. The utilisation of the carbonyl redox-active sites is 77%, even at a high current density of 5000 mA g^{-1}. These results indicate good rate performance. The rate capability of PT-COF50 is also comparable to those of the recently reported COF cathodes. For example, PPTODB, which contains the same electrochemical redox motif with PT-COF, had a capacity retention of less than 50% at 1500 mA g^{-1}.[19] A poly(imide-benzoquinone) COF (PIBN-G) has a capacity of 271 mAh g^{-1} at 0.1 C, showed a 73% of the capacity at 10 C.[11]

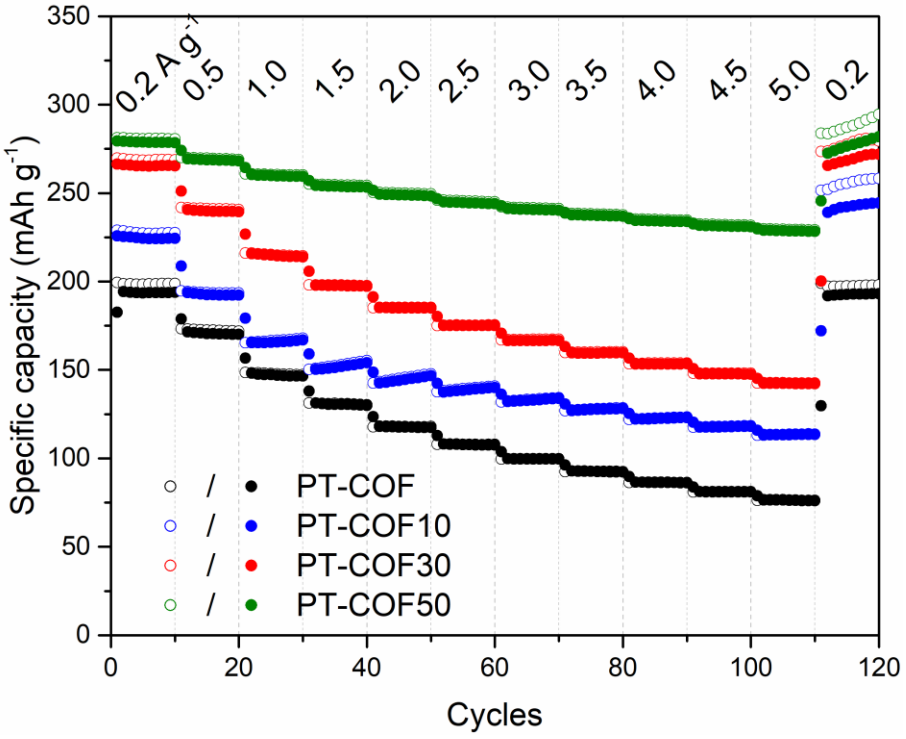

Figure 5-24. Rate performance of PT-COF, PT-COF10, PT-COF30, and PT-COF50. The open symbols represent the charge capacity and the solid symbols represent discharge capacity.

To investigate the Li^+ storage sites during discharging process, the *ex situ* FT-IR spectra of the PT-COF electrode were recorded. The lithiated and delithiated electrodes were recovered from the cycled cells. The recovered electrodes were washed by DOL and dried under reduced pressure at room temperature, and FT-IR spectra were then recorded inside the glovebox. As

in the IR spectra (Figure 5-25a), the character peak of the C=O (1675 cm^{-1}) groups in the DAPT structure, as assigned earlier in the DAPT monomer and PT-COF (Figure 5-10), disappeared when discharged to 1.5 V. While a new signal at 1460 cm^{-1} corresponds to the lithium enolate groups (C−O−Li) appeared when the electrode is fully discharged.[20] The pristine and fully recharged electrode have identical IR spectra, implying the reversible and stable electrochemical reactions based on the C=O bonds during the charge−discharge process. Based on these results we proposed a mechanism as outlined in Figure 5-25b that involves redox reactions of carbonyl groups in DAPT. This is consistent with previous reports that have also suggested that four carbonyl groups of DAPT moieties participate in the redox reactions.[21–23]

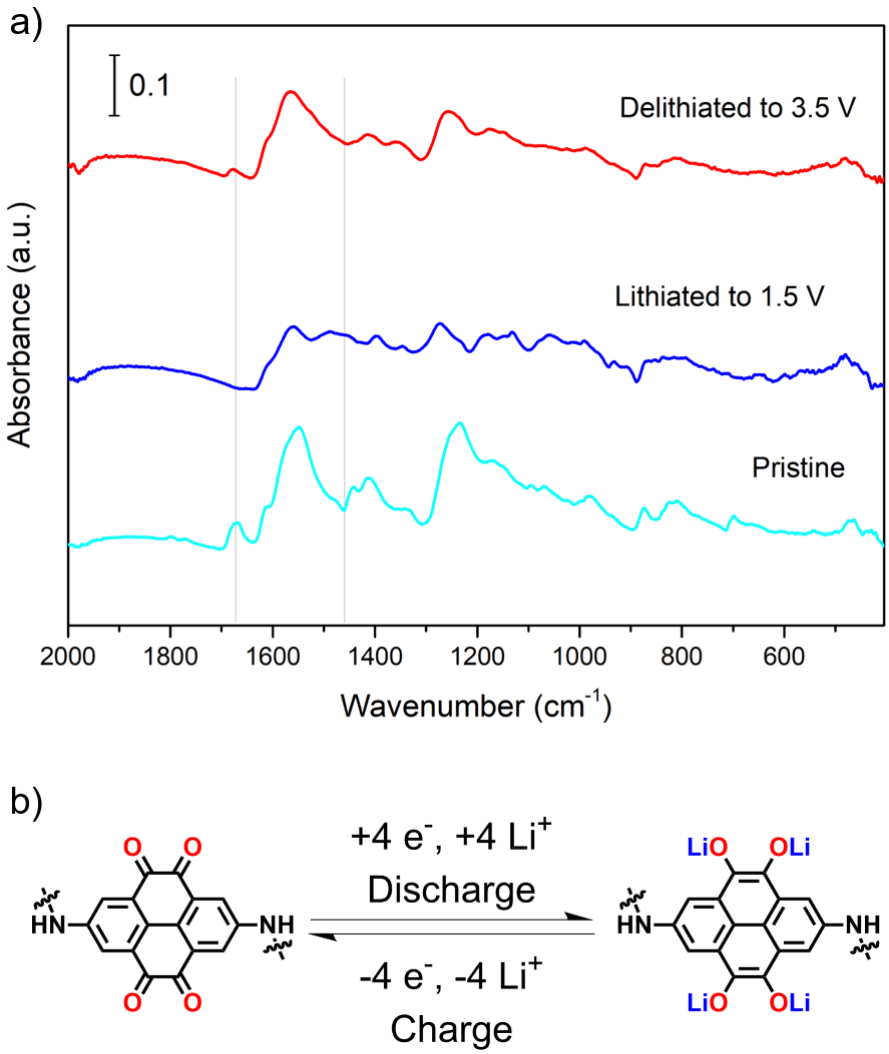

Figure 5-25. (a) FT-IR spectra of PT-COF electrode materials at different states of lithiation/delithiation (pristine, lithiated to 1.5 V and delithiated to 3.5 V); (b) Proposed reversible electrochemical redox mechanism of PT-COF during the lithiation/delithiation process.

5.8 Conclusion

A COF composite with rich electrochemical redox-active carbonyl groups was synthesised, using the strategy of *in situ* polycondensation on CNTs. By optimising the proportions of the COF and the CNTs in the reaction mixture, thinner layers of crystalline COFs could be fabricated on the surface of CNT that leads to highly improved charge transfer and efficiently electrochemical accessibility of active sites in the PT-COFX. Therefore, the largest capacity of 280 mAh g^{-1} at 200 mA g^{-1} for PT-COF50, corresponding to 98% utilisation of the redox-active sites, was obtained, which is the highest value so far among COF-based electrode materials. This remarkable performance was made possible by the four redox-active sites per unit within the PT-COF, with the core-shell nanotube structure shown to have greatly improved accessibility of active sites.

5.9 Reference

(1) Nokami, T.; Matsuo, T.; Inatomi, Y.; Hojo, N.; Tsukagoshi, T.; Yoshizawa, H.; Shimizu, A.; Kuramoto, H.; Komae, K.; Tsuyama, H.; Yoshida, J. I. Polymer-Bound Pyrene-4,5,9,10-Tetraone for Fast-Charge and -Discharge Lithium-Ion Batteries with High Capacity. *J. Am. Chem. Soc.* **2012**, *134* (48), 19694–19700.

(2) Li, M.; Liu, J.; Li, Y.; Xing, G.; Yu, X.; Peng, C.; Chen, L. Skeleton Engineering of Isostructural 2D Covalent Organic Frameworks: Orthoquinone Redox-Active Sites Enhanced Energy Storage. *CCS Chem.* **2021**, *3* (2), 696–706.

(3) Wang, H.; Wang, H.; Wang, H.; Yao, C. J.; Nie, H. J.; Wang, K. Z.; Zhong, Y. W.; Chen, P.; Mei, S.; Zhang, Q.; Zhang, Q. Recent Progress in Carbonyl-Based Organic Polymers as Promising Electrode Materials for Lithium-Ion Batteries (LIBs). *J. Mater. Chem. A* **2020**, *8* (24), 11906–11922.

(4) Letizia, J. A.; Cronin, S.; Ortiz, R. P.; Facchetti, A.; Ratner, M. A.; Marks, T. J. Phenacyl-Thiophene and Quinone Semiconductors Designed for Solution Processability and Air-Stability in High Mobility n-Channel Field-Effect Transistors. *Chem. A Eur. J.* **2010**, *16* (6), 1911–1928.

(5) Xing, Q.; Song, K.; Liang, T.; Liu, Q.; Sun, W. H.; Redshaw, C. Synthesis, Characterization and Ethylene Polymerization Behaviour of Binuclear Nickel Halides Bearing 4,5,9,10-Tetra(Arylimino)Pyrenylidenes. *Dalt. Trans.* **2014**, *43* (21), 7830–7837.

(6) Kandambeth, S.; Mallick, A.; Lukose, B.; Mane, M. V.; Heine, T.; Banerjee, R. Construction of Crystalline 2D Covalent Organic Frameworks with Remarkable Chemical (Acid/Base) Stability via a Combined Reversible and Irreversible Route. *J. Am. Chem. Soc.* **2012**, *134* (48), 19524–19527.

(7) Deblase, C. R.; Silberstein, K. E.; Truong, T.-T.; Abruñ, H. D.; Dichtel, W. R. β-Ketoenamine-Linked Covalent Organic Frameworks Capable of Pseudocapacitive Energy Storage. *J. Am. Chem. Soc* **2013**, *135*, 16821–16824.

(8) Shi, Y.; Tang, H.; Jiang, S.; Kayser, L. V; Li, M.; Liu, F.; Ji, F.; Lipomi, D. J.; Ong, S. P.; Chen, Z. Understanding the Electrochemical Properties of Naphthalene Diimide: Implication for Stable and High-Rate Lithium-Ion Battery Electrodes. *Chem. Mater.* **2018**, *30* (10), 3508–3517.

(9) Dahbi, M.; Ghamouss, F.; Tran-Van, F.; Lemordant, D.; Anouti, M. Comparative Study of EC/DMC LiTFSI and $LiPF_6$ Electrolytes for Electrochemical Storage. *J. Power*

Sources **2011**, *196* (22), 9743–9750.

(10) Vitaku, E.; Gannett, C. N.; Carpenter, K. L.; Shen, L.; Abruña, H. D.; Dichtel, W. R. Phenazine-Based Covalent Organic Framework Cathode Materials with High Energy and Power Densities. *J. Am. Chem. Soc.* **2020**, *142* (1), 16–20.

(11) Luo, Z.; Liu, L.; Ning, J.; Lei, K.; Lu, Y.; Li, F.; Chen, J. A Microporous Covalent-Organic Framework with Abundant Accessible Carbonyl Groups for Lithium-Ion Batteries. *Angew. Chem. Int. Ed.* **2018**, *57* (30), 9443–9446.

(12) Zhang, K.; Guo, C.; Zhao, Q.; Niu, Z.; Chen, J. High-Performance Organic Lithium Batteries with an Ether-Based Electrolyte and 9,10-Anthraquinone (AQ)/CMK-3 Cathode. *Adv. Sci.* **2015**, *2* (5), 1500018.

(13) Zhao, G.; Li, H.; Gao, Z.; Xu, L.; Mei, Z.; Cai, S.; Liu, T.; Yang, X.; Guo, H.; Sun, X. Dual-Active-Center of Polyimide and Triazine Modified Atomic-Layer Covalent Organic Frameworks for High-Performance Li Storage. *Adv. Funct. Mater.* **2021**, 2101019.

(14) Yamada, A.; Chung, S. C.; Hinokuma, K. Optimized $LiFePO_4$ for Lithium Battery Cathodes. *J. Electrochem. Soc.* **2001**, *148* (3), A224.

(15) Lee, M. J.; Lee, S.; Oh, P.; Kim, Y.; Cho, J. High Performance $LiMn_2O_4$ Cathode Materials Grown with Epitaxial Layered Nanostructure for Li-Ion Batteries. *Nano Lett.* **2014**, *14* (2), 993–999.

(16) Hu, Y. S.; Guo, Y. G.; Dominko, R.; Gaberscek, M.; Jamnik, J.; Maier, J. Improved Electrode Performance of Porous $LiFePO_4$ Using RuO_2 as an Oxidic Nanoscale Interconnect. *Adv. Mater.* **2007**, *19* (15), 1963–1966.

(17) Qi, P.; Han, Y.; Zhou, J.; Fu, X.; Li, S.; Zhao, J.; Wang, L.; Fan, X.; Feng, X.; Wang, B. MOF Derived Composites for Cathode Protection: Coatings of $LiCoO_2$ from UiO-66 and MIL-53 as Ultra-Stable Cathodes. *Chem. Commun.* **2015**, *51* (62), 12391–12394.

(18) Wu, F.; Tian, J.; Su, Y.; Wang, J.; Zhang, C.; Bao, L.; He, T.; Li, J.; Chen, S. Effect of Ni2+ Content on Lithium/Nickel Disorder for Ni-Rich Cathode Materials. *ACS Appl. Mater. Interfaces* **2015**, *7* (14), 7702–7708.

(19) Yao, C. J.; Wu, Z.; Xie, J.; Yu, F.; Guo, W.; Xu, Z. J.; Li, D. S.; Zhang, S.; Zhang, Q. Two-Dimensional (2D) Covalent Organic Framework as Efficient Cathode for Binder-Free Lithium-Ion Battery. *ChemSusChem* **2020**, *13* (9), 2457–2463.

(20) Ba, Z.; Wang, Z.; Luo, M.; Li, H. B.; Li, Y.; Huang, T.; Dong, J.; Zhang, Q.; Zhao, X. Benzoquinone-Based Polyimide Derivatives as High-Capacity and Stable Organic Cathodes for Lithium-Ion Batteries. *ACS Appl. Mater. Interfaces* **2020**, *12* (1), 807–817.

(21) Wang, H.; Yao, C.-J.; Nie, H.-J.; Wang, K.-Z.; Zhong, Y.-W.; Chen, P.; Mei, S.; Zhang, Q. Recent Progress in Carbonyl-Based Organic Polymers as Promising Electrode Materials for Lithium-Ion Batteries (LIBs). *J. Mater. Chem. A* **2020**, *8* (24), 11906–11922.

(22) Liang, Y.; Zhang, P.; Chen, J. Function-Oriented Design of Conjugated Carbonyl Compound Electrodes for High Energy Lithium Batteries. *Chem. Sci.* **2013**, *4* (3), 1330–1337.

(23) Nokami, T.; Matsuo, T.; Inatomi, Y.; Hojo, N.; Tsukagoshi, T.; Yoshizawa, H.; Shimizu, A.; Kuramoto, H.; Komae, K.; Tsuyama, H.; Yoshida, J.-I. *J. Am. Chem. Soc.* **2012**, *134*, 48.

Chapter 6

Summary and Outlook

6.1 Summary

In this thesis, electrochemically redox-active polyimide and *β*-ketoenamine covalent organic frameworks (COFs) were synthesised by polycondensation and utilised as the positive electrode material within Li-ion cells. The electrochemical performances of the polyimide and the COFs, such as average discharge potential, specific capacity, cycling performance, rate performance, were systematically studied. The structures were designed to incorporate electrochemically active groups to enhance their performance and *in situ* growth conditions were used to combine the polyimide and COFs with the conductive carbon. Structure-performance relationships were then investigated and it was shown that the performance of the carbonyl-containing polymers could be enhanced by designing the chemical structure and the morphology. Wherein, the key design parameter for the chemical structure is to get more electrochemically redox-active groups into the structure unit.

In **Chapter 3**, a non-porous polyimide (**PI**) was synthesised and its performance in an electrode was studied. **PI** by itself had a negligible specific capacity so to improve the utilisation of the redox-active sites, a series of **PIX** composites (**PI10, PI30**, and **PI50**, where "X" value refers to either 10, 30 and 50 = wt.% of reduced graphene oxide (rGO)) was synthesised by *in situ* polycondensation on rGO. The increased surface area of the composites and the reduced particle size of the polyimide polymer in the composites was shown to lead to a dramatic enhancement of the accessible electrochemically active surface area and improved both electron transfer and Li^+ ion transport to the redox-active carbonyl groups. It was found that the **PIX** composites had improved electrochemical performance. This improved the utilisation of the redox-active sites from 2.2% in **PI** to 86% in **PI50**. In the composite electrode, **PI50** was also shown to have the largest capacity of 172 mAh g^{-1} at 500 mA g^{-1} and retained 80% of its initial capacity after 9000 cycles at 2000 mA g^{-1}.

In **Chapter 4**, *β*-ketoenamine COF composites (DAPQ-COFX) were synthesised through *in situ* polycondensation on CNTs. The *in situ* growth method was shown to yield composites with a unique tube-type core-shell structure. The COF with uniform 1D channels was shown to be beneficial for ion diffusion and the intimate contact between the COF and the CNT increased charge transfer. By optimising the DAPQ-COFX (where X = 10, 30, and 50 wt.% of CNT) resulted in the synthesis of composites with thinner COF layers. DAPQ-COF50, which had the thinnest COF layer of about 5 nm was shown to have the highest number of electrochemical redox-active sites accessible and shorter pathways for ion transport. DAPQ-

COF50 was shown to have 95% utilisation of its redox-active sites and exhibited excellent ultra-high rate performance, retaining 58% of its capacity at 50000 mA g^{-1} (320 C). This indicated that the DAPQ-COF50 positive electrode could be fully recharged within 11 seconds. The rate capability of DAPQ-COF50 exceeds all other previously reported carbonyl-contained organic electrodes by an order of magnitude. DAPQ-COF50 also exhibits an estimated power density of 110 kW kg^{-1}, which is comparable to values achieved by electrochemical capacitors.

In **Chapter 5**, a *β*-ketoenamine COF (PT-COF) with a high theoretical capacity of 271 mAh g^{-1} was synthesised. PT-COF exhibits a 79% utilisation of the redox-active sites. To further improve the utilisation of active sites in PT-COF, a series of PT-COFX (where X = 10, 30, and 50 wt.% of CNT) composites was prepared using the same strategy reported in Chapter 4. PT-COF50 shows 98% utilisation of the redox-active site and had a capacity of 280 mAh g^{-1} at 200 mA g^{-1}, which is the highest capacity of the COF-based cathode materials reported in the literature to date.

6.2 Outlook

It remains challenging, both in terms of research and commercialisation, to produce organic electrode materials. Organic materials usually have a much lower mass density compared to inorganic materials because organic electrodes consist of light elements such as C, H, N, O, S. The densities of reported organic electrode materials are typically low (1-2 g cm^{-3}), which is not a problem when we are just concerned about the specific energy in Wh kg^{-1}. However, for energy storage devices emphasizing the energy density in Wh dm^{-3}, such as rechargeable lithium-ion, used in mobile phones and electric vehicles, this is the limitation. However organic Li-ion cells may find application within large-scale grid batteries, where volume is less of a limitation and as demonstrated within the thesis the significant power capability that can be achieved is a possible major advantage. The poor electronic conductivity of carbonyl-containing polymeric electrode materials seriously hinders the full utilisation of the active sites, which limits the rate of performance of the active materials. When large amounts of conductive carbon additives are used to improve the conductivity, it leads to low mass loadings of active material and low specific energy. Thus, organic electrode materials are more likely to be applied in fields where energy density is less important than gravimetric energy density. It is worthy to do a systermtic study to compare the effect of different conductive additives (such as rGO, CNT and carbon nanofiber) on the electrochemical performance including discharge

capacity, average discharge potential, cycling stability. Furthermore, batteries with organic electrode materials still suffer from safety issues. For the majority of organic electrode materials, especially n-type organics, Li metals or alloys are used as the negative electrode and lithium source, which brings about safety problems in practical use.[1] Since Li–S and Li–O_2 batteries also face this problem, there have been many attempts at Li surface protection[2] or lithium powder/carbon composite anodes tried to solve this problem.[3,4] Due to safety issues, the use of organic liquid electrolytes is another risk, the research on solid-state batteries is a promising way to solve the safety problems caused by organic liquid electrolytes.

To satisfy the rapidly increasing demand for batteries, the development aim of the next-generation battery is to invent ultra-high performance batteries that are safe, affordable, and sustainable, with a long lifetime. The core lies in the discovery of high-performance materials and components that enable the creation of batteries with higher energy and power. Therefore, accelerated discovery and design of battery materials by high-throughput automated synthesis combination with autonomous data analysis and data mining, as well as AI and machine learning is the trend in the future.

In a battery, degenerative processes cannot be suppressed completely, and external factors, such as extreme temperatures, mechanical stress, excessive power during operation, or simply ageing will, over time, be detrimental to battery performance. From the perspectives of sustainability, economic efficiency, and reliability, new ways need to be found to increase safety and lifetime, particularly in critical applications. Also, for a greener and more sustainable battery industry, the recycling of batteries is a project that needs to be considered.

6.3 Reference

(1) Winter, M.; Barnett, B.; Xu, K. Before Li Ion Batteries. *Chem. Rev.* **2018**, *118* (23), 11433–11456.

(2) Umeda, G. A.; Menke, E.; Richard, M.; Stamm, K. L.; Wudl, F.; Dunn, B. Protection of Lithium Metal Surfaces Using Tetraethoxysilane. *J. Mater. Chem.* **2011**, *21* (5), 1593–1599.

(3) Jang, B. Z.; Liu, C.; Neff, D.; Yu, Z.; Wang, M. C.; Xiong, W.; Zhang, A. Graphene Surface-Enabled Lithium Ion-Exchanging Cells: Next-Generation High-Power Energy Storage Devices. *Nano Lett.* **2011**, *11* (9), 3785–3791.

(4) Cao, W. J.; Zheng, J. P. Li-Ion Capacitors with Carbon Cathode and Hard Carbon/Stabilized Lithium Metal Powder Anode Electrodes. *J. Power Sources* **2012**, *213*, 180–185.